GLOBAL IONOSPHERIC MODEL DEVELOPMENT AND UTILISATION FOR NOVEL RADIO SYSTEMS.

by

LUKE NUGENT, BSc. MSc.

A thesis submitted to
The University of Birmingham

For the Degree
DOCTOR OF PHILOSOPHY

Space Environment and Radio Engineering Group
School of Engineering
College of Engineering and Physical Sciences
University of Birmingham
February 2024

ABSTRACT

Global ionospheric models have a wide range of uses in addition to developing the understanding and characterisation of the ionosphere. Two examples of these uses are explored within this work, both of which use ionospheric models to predict ionospheric impacts to radio transmissions as they pass through the ionosphere. The first example is the impact of the ionosphere on High Frequency (HF) propagation, namely in the context of a multistatic over-the-horizon radar (OTHR) simulation. By ray tracing through output from an ionospheric model, the sensitivity of a simulated multistatic OTHR (MOTHR) has been compared to the sensitivity of a simulated, conventional monostatic OTHR configuration. The MOTHR requires a target signal to be detected by the monostatic receiver and at least one bistatic receiver simultaneously. This makes it possible for a target velocity to be determined from a single radar sweep, and makes it easier to distinguish the signal scattered by the target from the signal scattered by illuminated terrain or water waves. The region for which targets could be detected by the MOTHR was very similar to the coverage area for a monostatic OTHR configuration. The monostatic configuration could detect smaller targets than the MOTHR configuration; however, the loss of sensitivity was not severe for most locations, and small targets could still be detected with the MOTHR.

The second example is the impact of the ionosphere on Ultra High Frequency (UHF) propagation, focusing on the impact of ionospheric irregularities on Global Navigation Satellite System (GNSS) transmissions. Transmissions passing through regions with sudden changes in plasma density can result in rapid fluctuations of signal amplitude or phase, referred to as ionospheric scintillation. These sudden changes in plasma density take the form of plasma bubbles at low latitudes, which can considerably degrade GNSS performance in that region. A

novel method to forecast the scintillation due to plasma bubbles at low latitudes has been developed. This method is shown to have forecasting skill as good as, or better than, an existing method when using output from the same physics-based ionospheric model. Modelled electron densities are used to determine a proxy for vertical plasma drift (PVPD) speeds at the post-sunset magnetic equator, which are used as an indicator of whether scintillation will occur. PVPD forecasting using a global ensemble data assimilation ionospheric model is shown to have a significant improvement in forecasting skill compared to PVPD forecasting with the physics-based model for a single test case. A methodology to use ensembles of PVPD values to produce probabilistic scintillation forecasts is also discussed.

The accuracy of HF ray tracing and scintillation forecasting within this work are dependent on the quality of the ionospheric specification. Furthermore, excellent ionospheric specification would be crucial for, e.g., coordinate registration in an operational MOTHR. A technique to potentially improve the accuracy of an ensemble data assimilation model of the ionosphere by increasing variability between ensemble members is described. Additional variability between ensemble members can be generated by adding perturbations to lower boundary horizontal wind speeds. It is shown that lower boundary perturbations impact ionospheric conditions at higher altitudes, and can increase the range of modelled ionospheric conditions.

To,

William, Patrick, Jon, Tom, Peter, Colin, Sylvester, Paul,
Christopher, David, Matt, Peter, Jodie & Ncuti

ACKNOWLEDGEMENTS

This work was supported by an EPSRC Research Grant and the UK Met Office. Thanks are also given to the Defence Science Technology Laboratory (Dstl), whose research projects provided further support for some sections of this work.

There are several people I wish to thank for their support up to and including the work within this thesis. My Mum for her never-ending encouragement throughout my life. Grandad Jim, who I know would have been immensely proud. My secondary school science teacher, Mr Gwynn, for providing fantastic opportunities which helped to stoke my childhood fascination with science. Of course, my wonderful wife and children, Louise, Freyja and Clara, for their patience and understanding.

My PhD was with the SERENE group at the University of Birmingham. My thanks go to Matthew Angling, my initial PhD supervisor, for his advice and feedback which helped me to develop vital skills for my research career. I appreciate how fortunate I have been to work within a group of supportive, collaborative, interesting people, and am grateful to each member for making it such a pleasure. Particular thanks go to Paul Cannon for his insightful and useful suggestions and enjoyable conversations. Also, to Joeal Subash, Gareth Dorrian, and Elizabeth Donegan-Lawley, for their willing ears whenever I needed someone to bounce ideas off.

Finally, I wish to express my immense gratitude to Sean Elvidge. Initially as my mentor, and subsequently as my PhD supervisor, you have provided enormous amounts of support. Whether

highlighting opportunities or interesting papers, discussing topics from cosmology to lower league football, or lending an ear when I need one, you have made my PhD a fantastic experience. Thank you.

TABLE OF CONTENTS

LIST OF FIGURES

LIST OF TABLES

LIST OF ABBREVIATIONS

AENeAS	Advanced Ensemble electron density (Ne) Assimilation System
AUC	Area under the ROC curve
CCIR	International Radio Consultative Committee
CIT	Coherent integration time
DA	Data assimilation
DIR	Dwell illumination region
EA	Equatorial anomaly
EIC	Equatorial ionisation crests
EnKF	Ensemble Kalman filter
EPB	Equatorial plasma bubble
F10.7	Solar flux at a wavelength of 10.7 cm
FAIM	Fully Analytic Ionosphere Model
FIRI	Faraday-International Reference Ionosphere
FIRIC	FAIM IRI Combination model
FPR	False positive rate
GNSS	Global Navigation Satellite System
GPS	Global Positioning System
GSWM	Global Scale Wave Model
h'F	F layer virtual height
HF	High frequency
h_{max}	Height of peak electron density
IRI	International Reference Ionosphere
IS	Ionospheric specification
ISM	Ionospheric Scintillation Monitor
ITU-R	International Telecommunication Union Radiocommunication Sector
KDE	Kernel density estimation
Kp	Indicator of planetary geomagnetic activity
LBC	Lower boundary condition

LETKF	Local ensemble transform Kalman filter
LT	Local time
M(3000)F2	Ratio of MUF(3000) to the F2 layer critical frequency
MDRCS	Minimum detectable radar cross section
MDTSN	Monthly mean of the daily total sunspot number
MOSWOC	Met Office Space Weather Operations Centre
MOTHR	Multistatic over the horizon radar
MUF(3000)	Maximum useable frequency which can be used to transmit a signal from a ground transmitter to a ground receiver 3000 km from the transmitter
N_{max}	Peak electron density
OTHR	Over the horizon radar
PDF	Probability density function
PRE	Pre-reversal enhancement
PVPD	Proxy for vertical plasma drift
R_{12}	Twelve month smoothed sunspot number
RCS	Radar cross section
RGF	Randomly generated forecast
ROC	Receiver operating characteristic
RTGR	Rayleigh-Taylor growth rate
S4	Indicator of amplitude scintillation
$S4_{90}$	Hourly 90^{th} percentile of one minute S4 observations
SD	Standard deviation
TEC	Total electron content
TIE-GCM	Thermosphere-Ionosphere-Electrodynamics General Circulation Model
TPR	True positive rate
UT	Universal time
YI	Youden's index, also known as the Peirce skill score

1. INTRODUCTION

Models of the ionised component of the Earth's upper atmosphere (the ionosphere) have been developed to aid the understanding of the physical processes and development of structures within the medium. However, the specification of ionospheric characteristics has many other uses, some of which can help to mitigate risk for industries which are dependent on ionospheric radio propagation such as satellite communications and high frequency (HF) communications. The ionosphere can impact communications in several ways. For example, a transmission which passes through plasma irregularities can result in rapid fluctuations of the signal amplitude or phase, referred to as scintillation. Strong scintillation can present a risk for users who require a continuous connection to satellite signals, e.g. Global Navigation Satellite Systems (GNSS). However, it is possible to capitalize on some ionospheric effects. For example, ionospheric reflection can result in the ability for HF signals to be transmitted to locations which are too far away for direct line-of-sight communications due to the curvature of the Earth. The reflection of HF transmissions is also used for skywave over-the-horizon radar (OTHR), enabling the detection of targets which are too distant for conventional line-of-sight radar. Typically, OTHR configurations are described as monostatic if the transmitter and receiver are co-located. However, to avoid direct transmitter-receiver communication the transmitter and receiver may be in separate locations (e.g. 100 km distance) for which the transmitter-target and receiver-target directions are very similar, which we refer to as pseudo-monostatic. Transmitter-receiver distances can be significantly greater, with different viewing angles to the target. This is referred to as a bistatic OTHR configuration.

In Section 5, simulations of an OTHR are produced by simulating the propagation of radio waves (ray tracing) through the ionosphere using output from a global ionospheric model. The concept of a multistatic OTHR (MOTHR) is introduced, in which the OTHR configuration uses a single transmitter and multiple receivers. An advantage of a MOTHR (compared to a monostatic or bistatic configuration) is the ability to estimate target velocities from a single radar sweep by combining target radial speeds (calculated from the Doppler shift of the received signal from the target) from multiple receive sites. The transmitted signal will not only be scattered by the target, but also by the land, sea, etc. in the region around the target which has been illuminated. This signal scattered by the surrounding terrain, etc. can also be detected by the receiver and is referred to as clutter. A further advantage of having multiple receivers in a MOTHR is that they make it less likely that a target signal will remain undetected due to clutter when the signal is detected at multiple receivers simultaneously, due to the different target Doppler shifts at each receiver. The area of coverage and sensitivity of a MOTHR will be compared to a conventional pseudo-monostatic configuration, to determine the viability of the MOTHR concept.

The magnitude of the ionospheric refraction (and likelihood of reflection) of signals within the ionosphere decreases as the transmission frequency increases. Global Navigation Satellite Systems (GNSS) communications (such as the Global Positioning System) are a widely used form of trans-ionospheric communications. However, these communications have transmission frequencies which are far higher than the HF frequencies used for OTHR. Therefore, the propagation path deviations due to ionospheric refraction are very small. However, GNSS (and other) communications can be impacted by other ionospheric effects, such as the rapid fluctuation of signal amplitude and phase (referred to as scintillation) when a transmission

passes through a region with sudden changes in plasma density. A physics-based global ionospheric model is used within this work to forecast ionospheric scintillation at low-latitudes. A novel method to predict the occurrence of scintillation is described in Section 6, which uses model output to generate a proxy for vertical plasma drift (PVPD) at the magnetic equator. PVPD values are then used as an indicator for whether low-latitude scintillation will occur during the subsequent evening. PVPD forecasting is compared to an existing method which uses model output to calculate Rayleigh-Taylor growth rates (RTGRs), which are also used as an indicator of subsequent scintillation. PVPD forecasts only require electron density model output at the magnetic equator, whereas RTGR forecasts require a greater number of output variables for a far greater number of locations. Several test cases will be considered, including test cases used in the literature to demonstrate RTGR forecasting skill, to determine whether PVPD forecasting can match or outperform RTGR forecasting when using output from the same ionospheric model despite the additional complexity of the RTGR method. PVPD forecasting skill is also assessed for PVPDs generated using an ensemble data assimilation ionospheric model, rather than a physics-based model. Techniques to develop probabilistic PVPD forecasts using output from the ensemble data assimilation model are also discussed in Section 7.

The accuracy of HF ray tracing for simulations of OTHR and the forecasting skill of PVPD forecasting are both dependent on the accuracy of the ionospheric specification. The inclusion of data assimilation within the ionospheric modelling provides the opportunity to improve the ionospheric specification and, therefore, the ray tracing accuracy and PVPD forecasting skill. The ensemble data assimilation ionospheric model within this work uses geomagnetic and solar activity indices to produce variability between ensemble members. An important consideration

for this ensemble model is that the range of ensemble members spans close to the full range of possible ionospheres. In Section 8, changes are made to the background model lower boundary wind speeds to determine whether changes in ionospheric conditions are produced at higher altitudes. A technique to add randomly generated perturbations to lower boundary winds is introduced, which produces localised variability and may also include large-scale structures. Test cases are considered for different combinations of season, solar activity and geomagnetic activity, to determine the changes to electron density profile peak values and associated heights for a range of environmental conditions. If the range of ionospheric conditions which can be produced by the data assimilation model can be expanded using lower boundary wind perturbations, it may be possible to increase the accuracy of the ionospheric specification of the data assimilation model and, therefore, the accuracy of OTHR modelling and scintillation forecasting using output from this model.

2. EARTH'S UPPER ATMOSPHERE

2.1. The Neutral Atmosphere

2.1.1. Vertical Structure

The vertical structure of Earth's atmosphere can be separated into distinct layers by considering the behaviour of certain characteristics. The change in temperature with altitude can be used to separate the atmosphere into the troposphere, stratosphere, mesosphere and thermosphere (Figure 1). The troposphere is the lowest of these layers, extending from the ground to around 10 km. In the troposphere the temperature decreases with altitude. Extending from the top of the troposphere to about 50 km is the stratosphere, in which temperatures tend to increase with altitude. The mesosphere extends from the top of the stratosphere to about 85 km and is characterised by decreasing temperature with altitude. The thermosphere extends from the top

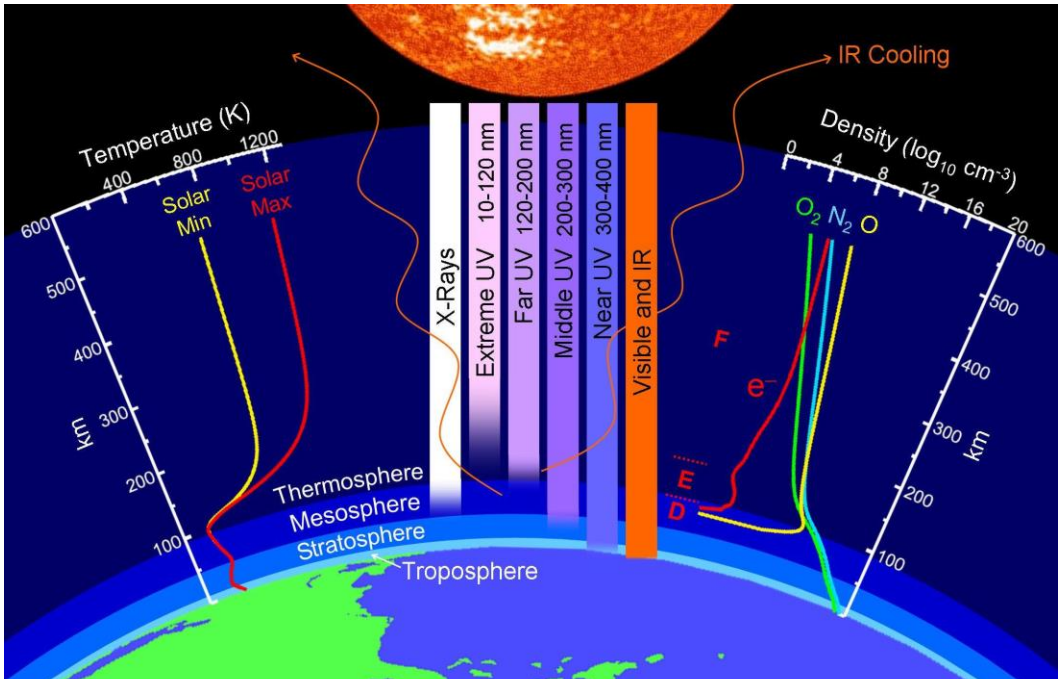

Figure 1. Properties of Earth's atmosphere (Emmert, 2010).

of the mesosphere to between 500 and 1000 km depending on solar activity. In this region the temperature tends to increase with altitude, with temperatures in the upper thermosphere reaching over 1000 K during periods of high solar activity.

Neutral density tends to decrease with altitude. Up to around 90 km, the neutral species are well mixed and in proportions which do not tend to change significantly with altitude (about 78% molecular nitrogen, 21% molecular oxygen, 1% argon, 0.04% carbon dioxide and trace amounts of other species). This region is defined as the homosphere. Above the homosphere the lower neutral density results in less frequent collisions between molecules. Neutral species do not remain well mixed and neutral composition varies with altitude. Without frequent collisions, neutral species can separate into layers in which different species dominate; this region is defined as the heterosphere. The layers depend on species mass, with higher mass species settling in layers below lower mass species. Molecules can also be ionised, primarily by absorbing energy from solar radiation. At higher altitudes the density of the atmosphere is lower so recombination of charged species will be at a slower rate than at lower altitudes. As a result, species which are uncommon at lower altitudes can be found in abundance at higher altitudes. For example, atomic oxygen tends to be the most common species from about 180 km up to between 600 and 800 km (Figure 1), depending on solar activity. Above the atomic oxygen layer the dominant species are hydrogen and helium. The charged and neutral species within the Earth's atmosphere are engaged in a complex interplay, driven by factors such as the behaviour of charged particles within the Earth's magnetic field and the motion of neutral particles due to atmospheric tides and winds.

2.1.2. Tidal Winds

As the atmosphere absorbs radiation from the Sun during the day a difference in temperature is apparent between the dayside and night-side of the Earth. This difference in temperature (and pressure) results in neutral tidal winds within the thermosphere and other atmospheric layers. The point at which the temperature is greatest corresponds to the relative position of the Sun, so moves around the Earth once each day or, more accurately, the tide remains stationary relative to the direction of the Sun while the Earth rotates beneath it. These winds are classed as diurnal migrating tides. Migrating tides due to harmonics related to this solar diurnal tide are also present. The semi-diurnal migrating tide (12-hour tide) also makes a significant contribution to overall tidal winds. However, migrating tides with smaller periods (e.g. 8 hours, 6 hours) generally have smaller amplitude than the diurnal and semi-diurnal migrating tide. Tides which do not travel westward with the apparent motion of the Sun are described as non-migrating tides. However, non-migrating tides are not necessarily static with respect to the Earth's surface. Convective cloud systems in the upper troposphere at tropical latitudes are an important contributing factor to some non-migrating tides (Hagan & Forbes, 2003). Other non-migrating tides can be generated by interactions between planetary tides and Rossby waves (planetary waves generated by the Coriolis effect due to the Earth's rotation; Rossby, 1939) or interactions between planetary tides (Mayr et al., 2005). Atmospheric tidal winds are discussed in great depth by, for example, (Lindzen & Chapman, 1969).

2.2. The Ionosphere

2.2.1. Ionisation and Recombination

When solar radiation is absorbed by neutral atoms and molecules in Earth's atmosphere it can result in electrically charged ions and free electrons (Eccles, 1912). A photon absorbed by an electron associated with an atom or molecule excites the electron. The excited states and unexcited (ground) state of the electron correspond to specific energy levels. A photon can be absorbed by the electron if the photon energy is equal to the energy required to excite the electron from its current state to a more excited state. A photon can also be absorbed if the photon energy is greater than the energy required to overcome the attractive force between a negatively charged electron and it's positively charged nucleus. The absorption of the photon converts the atom or molecule into a positively charged ion and a free electron. This process is called photoionisation; the atom or molecule has been ionised. In Table 1 ionisation energies and corresponding photoionisation wavelengths are displayed for common ionospheric ions. These wavelengths correspond to the extreme ultraviolet (EUV) range of the electromagnetic spectrum apart from nitrogen monoxide which corresponds to far ultraviolet (FUV), i.e. ionisation occurs when the atmosphere is subjected to FUV, EUV, X rays, and gamma rays. Atoms and molecules can also be ionised during collisions with energetic particles (Schunk & Nagy, 2009). Kinetic energy is transferred from the energetic particle during the collision; if enough energy is transferred, ionisation takes place.

Interactions between free electrons and positively charged ions can result in recombination of electrons and ions to form neutral particles. The dominant reactions for recombination in the E region are (Bates & Massey, 1946; Hargreaves, 1992):

Table 1. Ionisation energies and corresponding photoionisation wavelengths of common ionosphere species. Adapted from (Hargreaves, 1992).

Species	Ionisation energy (eV)	Photoionisation wavelength (nm)
NO	9.25	134.0
O_2	12.07	102.7
H_2O	12.60	98.5
H	13.60	91.2
O	13.61	91.1
N	14.54	85.3
H_2	15.41	80.4
N_2	15.58	79.6
He	24.58	50.4

$$\begin{aligned} \mathrm{e} + \mathrm{O}_2^+ &\rightarrow \mathrm{O} + \mathrm{O} \\ \mathrm{e} + \mathrm{N}_2^+ &\rightarrow \mathrm{N} + \mathrm{N} \\ \mathrm{e} + \mathrm{NO}^+ &\rightarrow \mathrm{N} + \mathrm{O}\,, \end{aligned} \tag{2.1}$$

where e is a free electron, O and N are neutral atoms of oxygen and nitrogen respectively, and O_2^+, N_2^+ and NO^+ are positively charged ions of molecular oxygen, nitrogen, and nitric oxide respectively. In the F region the dominant ion species is O^+. However, for O^+ electron attachment recombination is very slow. Instead, in the F region, O^+ will exchange charge with

neutral O_2 or N_2 molecules, to produce O_2^+ and NO^+ ions which can recombine with electrons in the same manner as the E region (Bates & Massey, 1946; Hargreaves, 1992).

A further discussion of ionisation and recombination processes within the ionosphere is provided by, for example, Hargreaves (1992).

2.2.2. Ionospheric Vertical Structure and Characterisation

The ionosphere can be separated into distinct layers (Appleton, 1927), referred to as the D, E, F1, and F2 layers, by considering the variation of electron density with altitude (Figure 2). The bottom of the D layer (the lowest ionospheric layer) is from an altitude of ~50 km. The

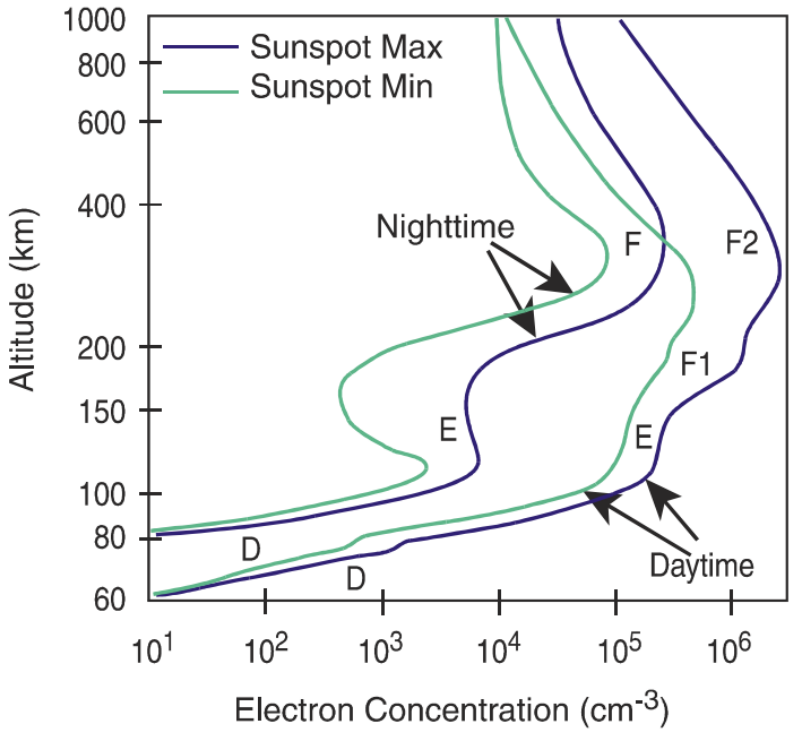

Figure 2. A representation of ionospheric vertical structure and the variability due to time of day and solar activity (Angling et al., 2013).

ionospheric structure is dependent on local time: at night the D layer effectively disappears (Mitra & Syam, 1935) and the F1 and F2 layers combine to form a single F layer (Appleton, 1933). Electron density profiles, and the resulting propagation of radio waves through the ionosphere, are dependent on solar activity (Plendl, 1932), as increased solar activity tends to increase the rate at which ionisation occurs. Solar output varies according to the (on average) eleven-year solar cycle (Schwabe, 1844) as shown by the variability of the F10.7 solar flux (solar flux with a wavelength of 10.7 cm, used as an indicator of solar activity) in Figure 3. There is also local variability of solar flux within the ionosphere on diurnal and annual timescales due to the Earth's rotation and seasonal effects. Ionospheric conditions are heavily dependent on solar flux variability; the maximum diurnal ionospheric electron content has been shown to be linearly dependent on solar flux, although this relationship becomes non-linear when solar flux is high (Balan et al., 1993). Following sunset electron densities tend to reduce

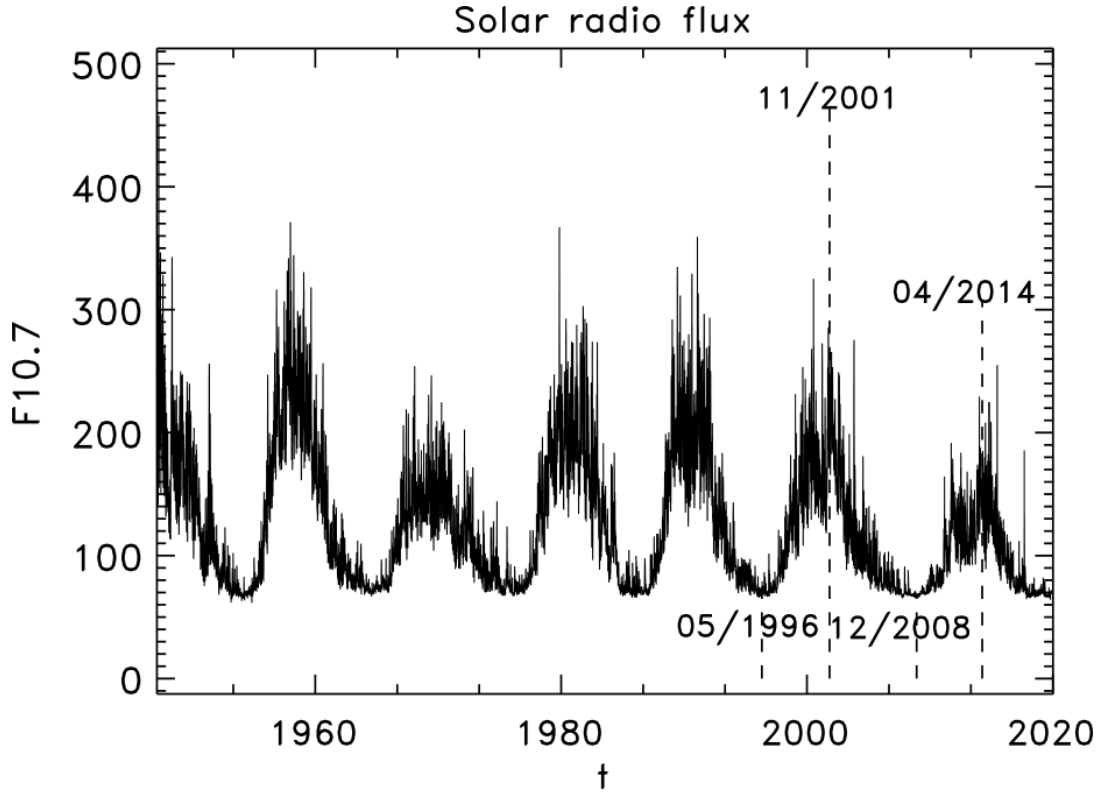

Figure 3. Daily F10.7 solar flux values from 1947 to 2019 (Du, 2020).

as ions and electrons recombine to form neutral species. There are also seasonal effects due to the change in hemisphere tilted towards the Sun throughout the year.

Examples of electron density profiles for daytime and night-time during periods of high and low solar activity are shown in Figure 2. The electron density peak value within the F2 layer (NmF2) and the altitude of the F2 peak electron density (hmF2) also vary according to environmental conditions such as solar activity and time of day. Electron density peak values and heights for other layers use the same form of notation, e.g. hmE for the height of the peak electron density in the E layer and NmF1 for the peak electron density in the F1 layer, etc. Electron density profiles can also vary by latitude, due to effects which are localised to particularly latitudinal sectors.

2.3. Low Latitude Ionospheric Variability

2.3.1. Plasma and the Neutral Wind

The ionosphere is engaged in a complex, dynamic interplay with the neutral atmosphere. Neutral atmospheric winds can drive ionospheric plasma transport, which in turn can generate electric fields (Richmond et al., 1976). As the electric fields are generated by converting the mechanical energy of the wind into electrical energy in a manner similar to that of a dynamo, the electric fields are referred to as dynamo electric fields. A short summary of dynamo electric fields shall now be provided. However, an in-depth discussion of these processes is discussed by, for example, Hargreaves (1992). Ions and electrons can be driven by neutral winds. However, unless the ion-neutral (or electron-neutral) collision frequency is sufficiently large, plasma motion is also influenced by Earth's magnetic field. A neutral wind with a velocity

component perpendicular to magnetic field lines, *U*, can be considered to provide a force, *F*, acting upon the charged particles such that

$$F = m\nu U\,, \tag{2.2}$$

where m is the mass of the charged particle and ν is the ion-neutral (or electron-neutral) collision frequency. Each collision will transfer momentum to the charged particles in the direction of the neutral wind. If the collision frequency is sufficiently high, the charged particles are driven along with the neutral wind. However, this is not the case for lower collision frequencies. If there is no wind or other additional forces acting on charged particles in a uniform magnetic field, the charged particles tend to exhibit circular motion relative to the magnetic field line. The frequency of this circular motion (gyrofrequency) is inversely proportional to the mass of the particle, so the gyrofrequency is far greater for an electron than for an ion (by a factor of $\sim 1800 m_i$, where m_i is the atomic weight of the ion). When a force (such as the neutral wind) is applied to charged particles in a magnetic field, this circular motion is disrupted. The circular motion is in opposite directions for particles with positive and negative charge. As a result, for low collision frequencies, the neutral wind can cause the ions and electrons to be driven in opposite directions in the line perpendicular to the neutral wind and the magnetic field directions (Figure 4). The average angle, θ, between the neutral wind direction and the velocity of a charged particle in the presence of a magnetic field due to the neutral wind is given by

$$\tan\theta = \frac{\omega}{\nu}\,, \tag{2.3}$$

where ω is the gyrofrequency of the charged particle and ν is the collision frequency between the charged and neutral particles. In the E region, the ion gyrofrequency is much smaller than the ion-neutral collision rate. However, the electron gyrofrequency is far greater than the electron-neutral collision frequency. As a result, the ions move in a direction close to that of the neutral winds whereas electrons move in a direction nearly perpendicular to the neutral winds. The wind component parallel to the magnetic field lines can drive plasma along magnetic field lines, thereby producing an uplift or depression of plasma at locations where the magnetic field lines are not horizontal (i.e. away from the magnetic equator).

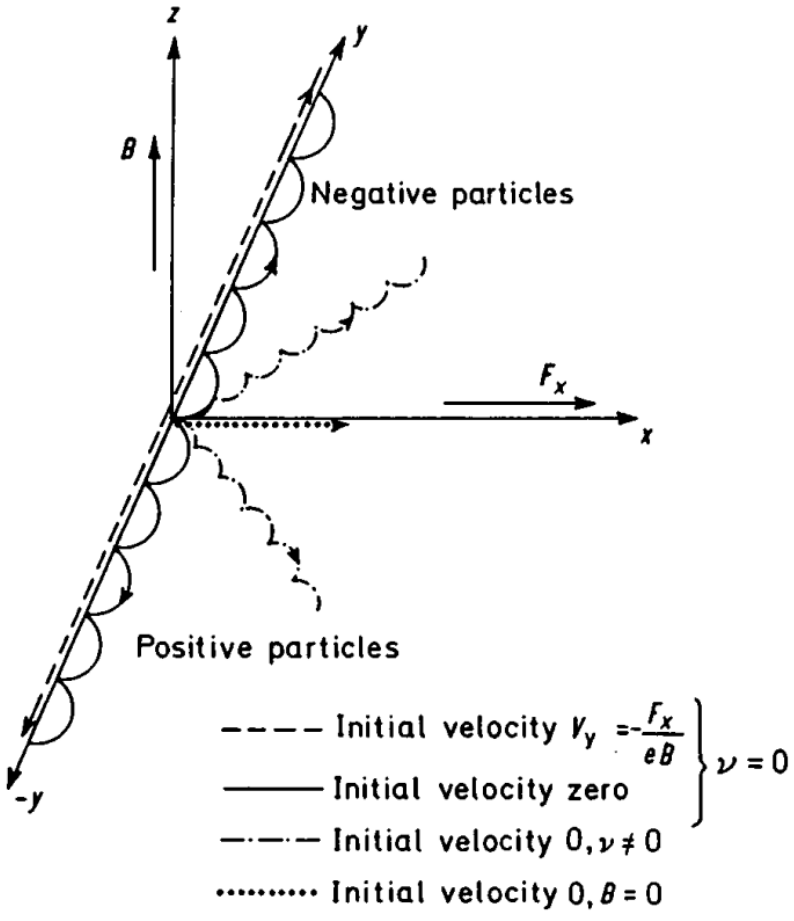

Figure 4. Charged particle motions in a magnetic field (B) when driven by a force (F_x) due to neutral winds and collision frequency, v (Hargreaves, 1992).

2.3.2. E x B Drift

The presence of perpendicular magnetic and electric fields results in transport of positive and negative particles in the same direction (Gunn, 1930), referred to as **E×B** drift. At the magnetic equator the magnetic field and dynamo electric field are effectively horizontal and perpendicular, with an eastward electric field during the day and a westward electric field at night. The resulting **E×B** drift is, therefore, upwards during the day and downwards at night (D. F. Martyn, 1953; Woodman, 1970). The **E×B** drift velocity $\boldsymbol{v}$ is given by (Gunn, 1930)

$$\boldsymbol{v} = \frac{\mathbf{E} \times \mathbf{B}}{|\mathbf{B}|^2}, \tag{2.4}$$

where **E** and **B** are the electric and magnetic fields respectively.

E region dynamo electric fields generated by neutral winds are propagated to the F region due to the high conductivity along magnetic field lines (Farley, 1960). An increase in F region eastward zonal wind speeds across the day-night terminator (King-Hele & Walker, 1977) contribute to an enhancement in upwards **E×B** drift speeds in the evening before the **E×B** drift reverses direction (Rishbeth, 1971), referred to as the pre-reversal enhancement (PRE). The magnitude of the PRE has a seasonal dependence (Fejer et al., 1991) due to steep conductivity gradients at the day-night terminator when the terminator and magnetic field directions are misaligned (Figure 5).

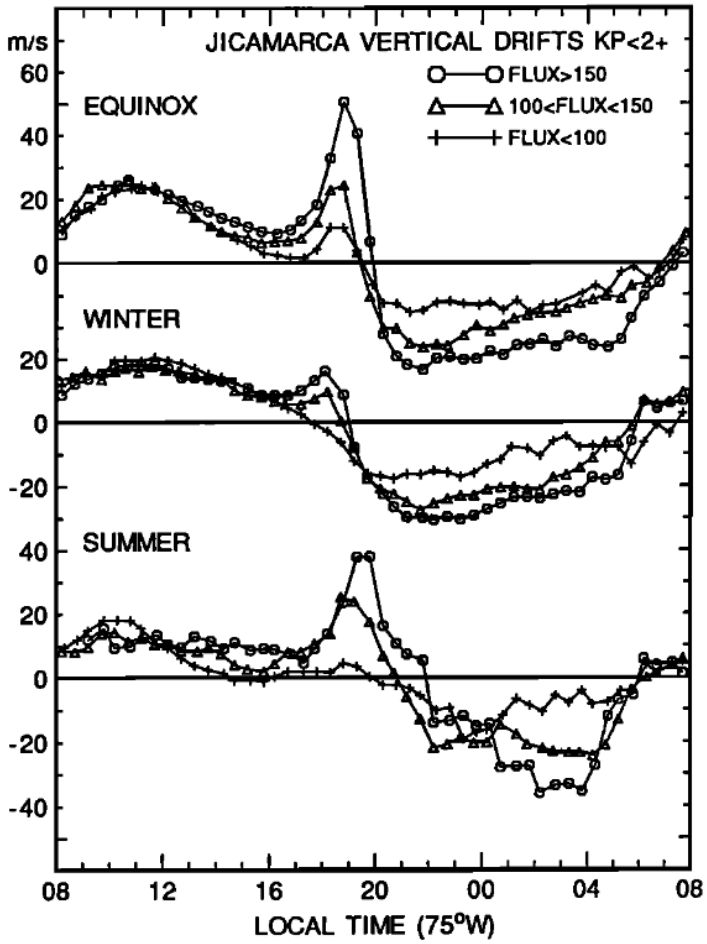

Figure 5. Observations of the pre-reversal enhancement of vertical plasma drift at low latitudes for three levels of F10.7 solar flux (Fejer et al., 1991).

2.3.3. Equatorial Anomaly

At higher altitudes the daytime upwards motion of plasma at the geomagnetic equator eventually succumbs to gravity and the magnetic field, and starts to drift downwards. However, the downwards plasma motion follows magnetic field lines north and south as it returns towards the Earth's surface (Figure 6). This "fountain effect" results in a depletion of plasma density in the F2 region at the magnetic equator and an enhancement of the F2 layer to the north and

south of the magnetic equator (Appleton, 1946). This deviation from electron density increasing with decreasing latitude is known as the Equatorial (or Appleton) Anomaly (EA). The peak F2 enhancement, or equatorial ionisation crests (EIC), occur approximately 15° latitude north and south of the magnetic equator. As the atmospheric density decreases with increasing altitude, the rate of recombination of ions and electrons will also decrease with increasing altitude. As a result, the EIC can persist and still be observed in the night-time region (Martyn, 1956).

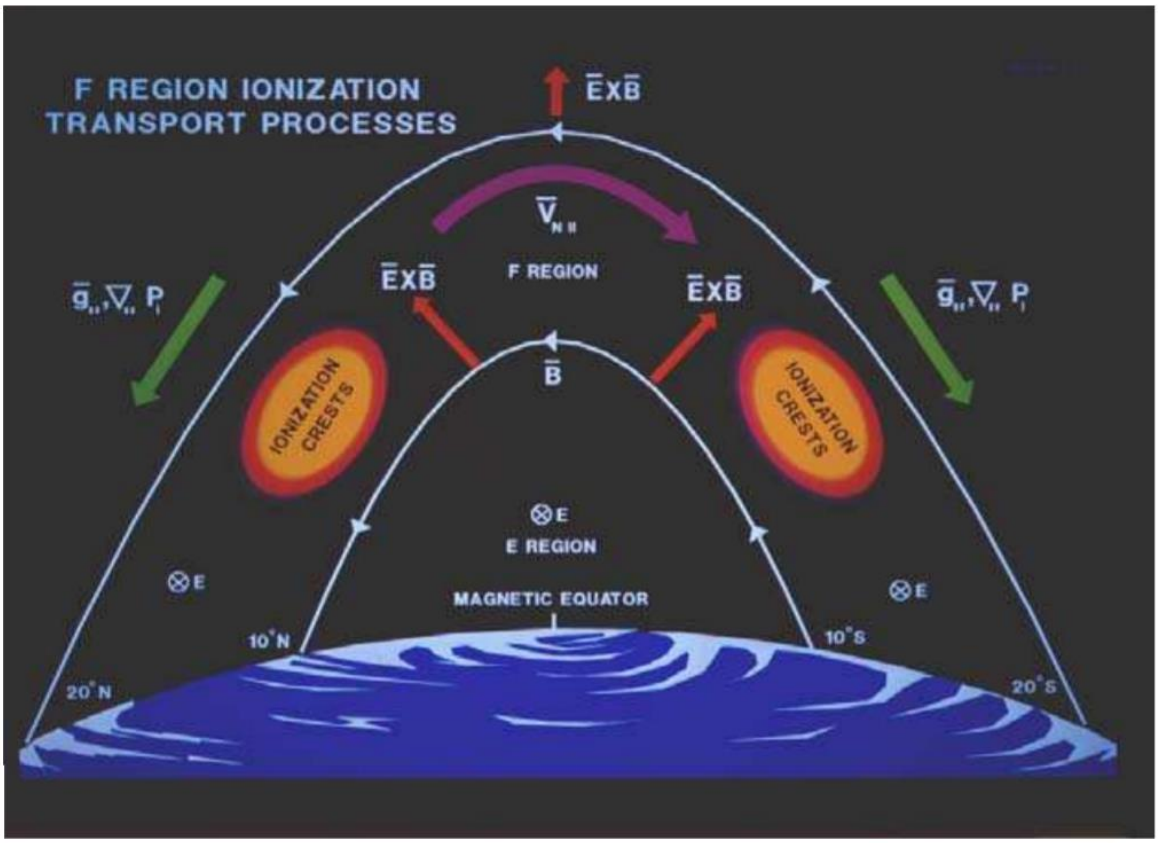

Figure 6. Diagram showing plasma transport processes which produce the equatorial anomaly, with ionisation crests approximately 15° north and south of the magnetic equator (de La Beaujardière, 2004).

2.3.4. Equatorial Plasma Bubbles

Within a fluid, a higher density layer situated above a lower density layer will result in regions where the low density fluid extends upwards into the high density layer. Also, high density fluid sinks into the low density layer (Figure 7). This is not necessarily because the low density layer is unable to provide sufficient force to support the high density layer: rather, it is due to imperfections in the boundary between the two layers. If a region of the boundary is higher than the average boundary plane, the lower density fluid which is above the average boundary plane will experience more pressure than would have been required to maintain the boundary between the two layers in the average boundary plane. As a result, the lower density fluid will rise into the higher density fluid, forcing higher density fluid aside during this upwards progress. Regions of the boundary below the boundary average contain higher density fluid, which requires more pressure to support it than the average pressure at the boundary. As a result, the higher density fluid sinks downwards through the lower density fluid. The instability of such a

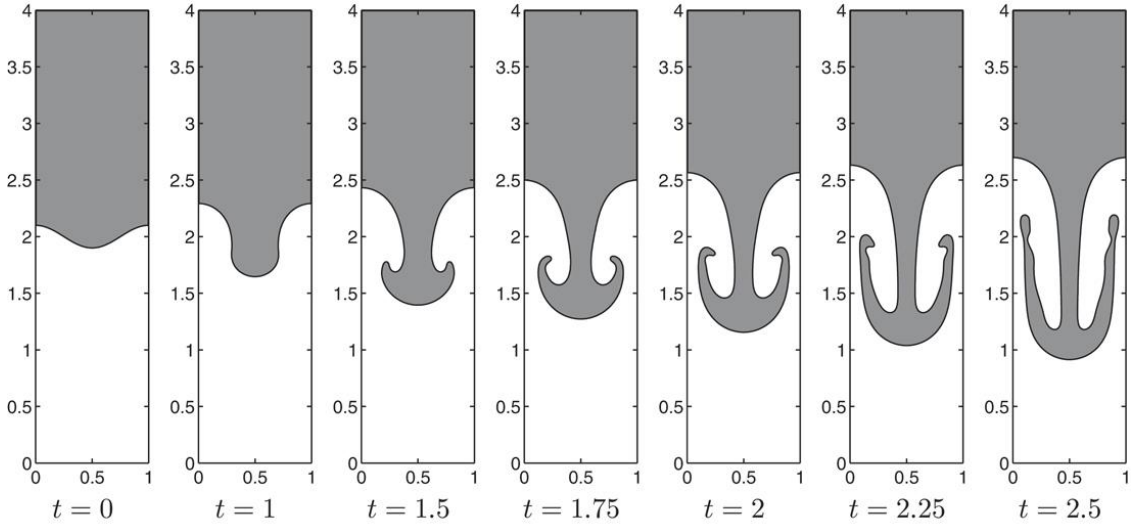

Figure 7. Simulation of a Rayleigh-Taylor instability which can develop when a denser fluid (grey) is above a lighter fluid (white). Adapted from (Lee et al., 2011)

system was investigated and described by Lord Rayleigh (Rayleigh, 1882) and, following later work by Sir Geoffrey Ingram Taylor, is described as a Rayleigh-Taylor instability.

Without ionisation from solar radiation the electron density starts to decrease after sunset due to recombination of ions and electrons. At higher altitudes the atmosphere continues absorbing solar radiation for some time after the Sun has set at lower altitudes, due to the curvature of the Earth. Furthermore, the atmospheric density is lower at higher altitudes, so ion-electron collisions are less frequent than at lower altitudes. Therefore, recombination can occur more rapidly after sunset at lower altitudes, which can increase the rate at which electron density increases with altitude in the lower ionosphere. If the boundary between layers corresponding to specific electron densities is perturbed, the Rayleigh-Taylor instability can be initiated thereby creating bubbles or plumes of lower electron density (Figure 8) which rapidly rise hundreds of kilometres into the region of higher electron density (Woodman & La Hoz, 1976). The northward magnetic field and downwards gravitational force causes an eastward drift of charged particles in a process similar to that of $\mathbf{E}\times\mathbf{B}$ drift (referred to as $\mathbf{g}\times\mathbf{B}$ drift, as the plasma transport is due to gravity and the magnetic field). If a longitudinal wave (such as a gravity wave which has propagated up from the lower atmosphere) with sufficient amplitude were to develop across the boundary between layers of higher and lower electron densities, ions and electrons could accumulate on either side of each wave trough or crest. This creates an electric field which results in vertical drift, increasing the altitude of the boundary wave crests and decreasing the altitude of the wave troughs. The increased wave amplitude serves to transport lower density plasma upwards, generating the plasma depletion within the higher density plasma region above (Ott, 1978; Sultan, 1996). These density irregularities regularly form at low latitudes and are known as Equatorial Plasma Bubbles (EPBs).

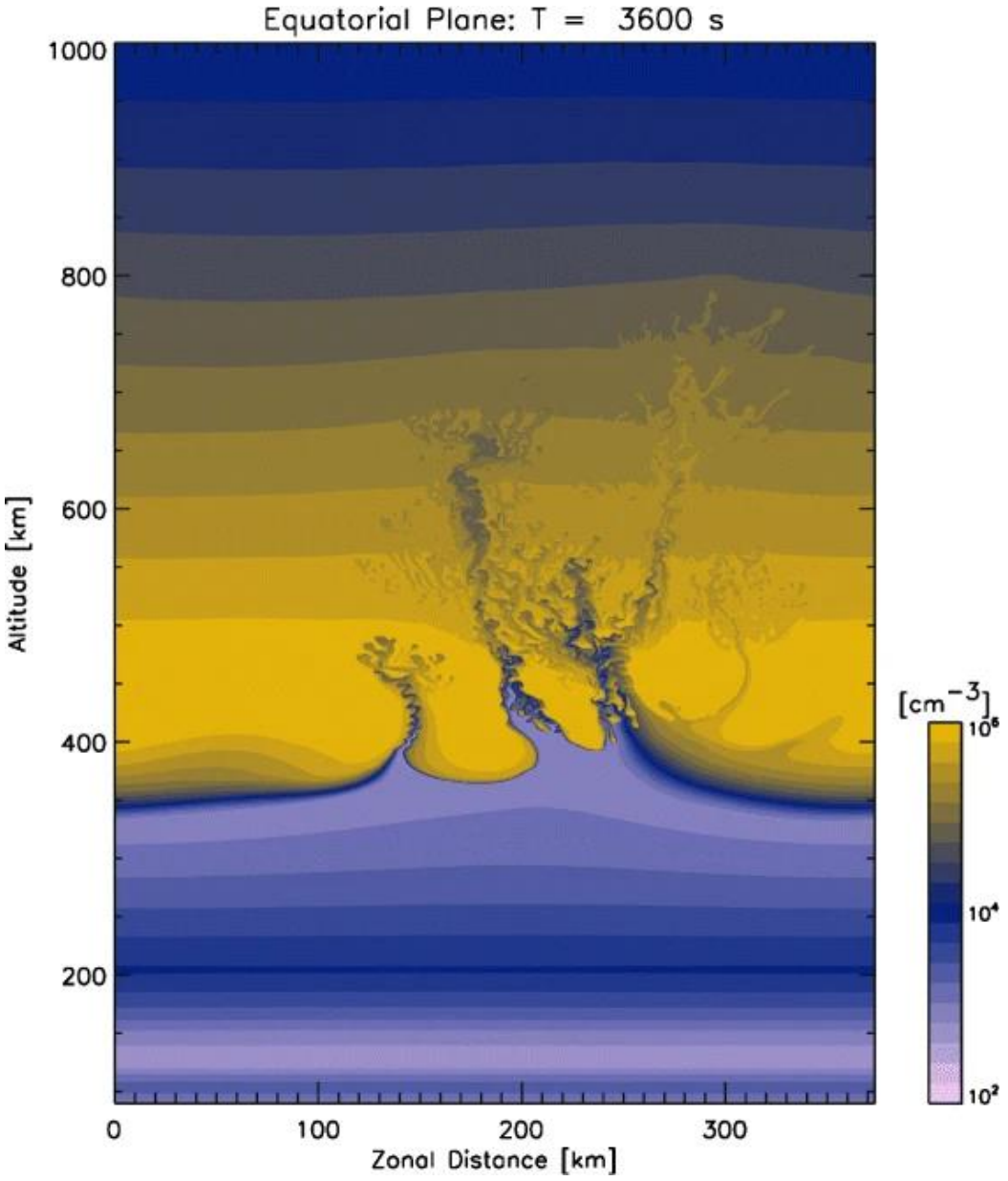

Figure 8. Numerical simulation of equatorial plasma bubbles (Yokoyama, 2017).

2.4. Ionospheric Impacts to Communications

Satellite communications, such as those from Global Navigation Satellite Systems, are essential for many of the technical advancements enjoyed by modern society and are critical for many

industries (Hapgood, 2017; Hapgood et al., 2021). However, transmissions which travel into or pass through the ionosphere can be impacted by variability of plasma density along the transmission path. In the ionosphere, electrons will oscillate with an angular frequency which is dependent on the square root of the electron density. The angular plasma frequency (ω_P) of the ionosphere at a chosen location can be defined from Tonks and Langmuir (1929) as

$$\omega_p^2 = \frac{N_e q_e^2}{\epsilon_0 m_e}, \tag{2.5}$$

where N_e is the electron density at the chosen location ($\mathrm{e^-/m^3}$), q_e is the magnitude of the electric charge of an electron (1.6×10^{-19} C), ϵ_0 is the permittivity of free space (8.85×10^{-12} $\mathrm{C^2/(N\ m^2)}$), and m_e is the mass of an electron (9.11×10^{-31} kg).

Alternatively, the (linear) plasma frequency (f_P) in Hz can be defined as

$$f_p^2 = \left(\frac{\omega_p}{2\pi}\right)^2. \tag{2.6}$$

Therefore, substituting values for q_e, ϵ_0, and m_e, f_p can be approximated as

$$f_p \approx \sqrt{80.6\, N_e} \tag{2.7}$$

or

$$f_p \approx 9\sqrt{N_e}, \tag{2.8}$$

as reported by Tonks and Langmuir (1929) following conversion to SI units. For a vertical column extending through an ionospheric layer, the critical frequency is the maximum plasma frequency within the column. The critical frequency provides an approximation of the maximum vertically transmitted frequency which would be refracted by the ionosphere back to the ground. The critical frequency (of the ordinary (*o)* wave; the difference between *o* and *x* waves is discussed in Section 2.4.1) of a layer is denoted by the prefix fo (e.g. foE for the E layer and foF2 for the F2 layer).

Electron densities in the D region are considerably lower than in the E and F region. However, in the D region the higher neutral densities (compared to the F region) result in higher propagation path losses due to absorption in this region and the E region. Zawdie et al. (2017) provide an example of this behaviour for a simulated 5 MHz *x*-mode vertical wave (Figure 9). The approximate boundaries of the D, E, and F regions for an IRI-2016 daytime electron density profile (top left) are shown in the top middle and top right plots as dashed horizontal lines. It can be seen that the D and E region contribute more to the daytime total attenuation (top right) than the F region. Zawdie et al. (2017) reported that in this example the D, E, and F regions produce approximately 30%, 60%, and 10% of the total attenuation respectively. Therefore, accurate representation of the D and E regions can be an important factor when determining total signal loss along the ray path.

Two forms of ionospheric impacts to trans-ionospheric signals will be a focus of this work: refraction (and reflection) of the transmission path, and ionospheric scintillation.

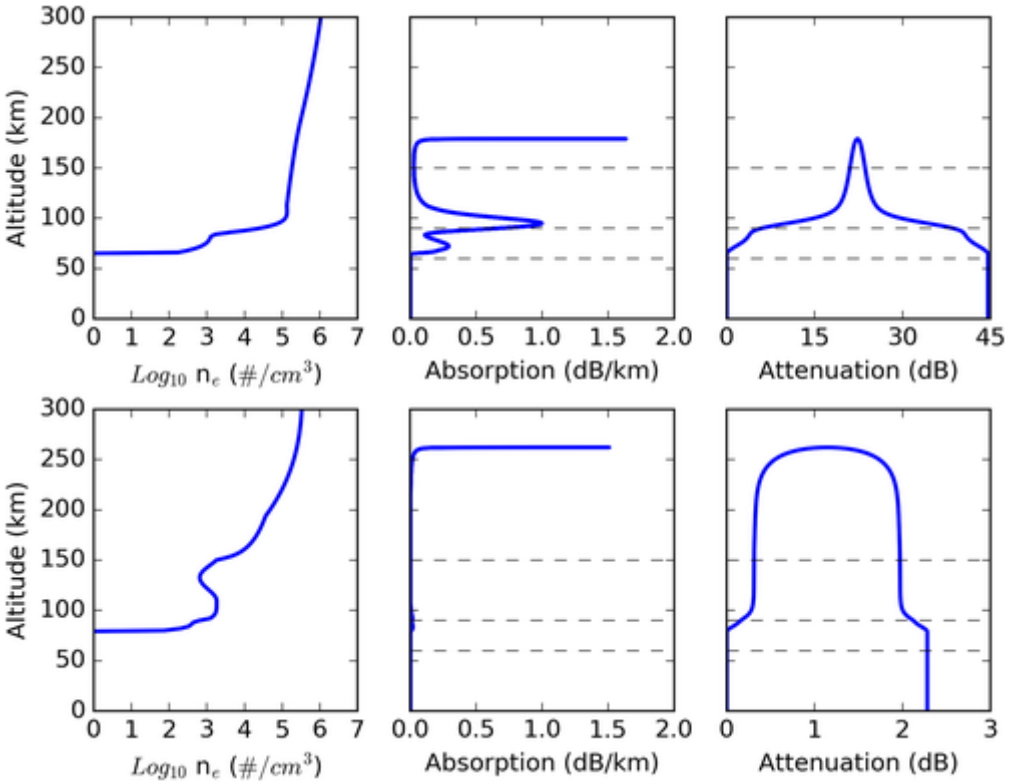

Figure 9. Electron density profile (left), absorption (middle) and total attenuation (right) for a simulated 5 MHz vertical X-mode wave at 28°N, 0°E during the day (top) and night (bottom) of 14 March 2010 (Zawdie et al., 2017).

2.4.1. Refraction

When electromagnetic radiation passes from one medium to another, a difference between the refractive indices of the two media will result in a change of direction of the radiation. According to Snell's law, this can be described by

$$\mu_1 \sin\theta_1 = \mu_2 \sin\theta_2 \,, \tag{2.9}$$

where μ_i is the refractive index of the ith medium, and θ_i is the angle in the ith medium between the direction of propagation and the normal of the boundary between the media. The refractive index μ_i can be defined as

$$\mu_i = \frac{c}{v_i}, \tag{2.10}$$

where v_i is the phase speed of the electromagnetic wave in medium i, and c is the speed of light in a vacuum. Therefore, if the angle of incidence in medium 1 and the refractive indices (or electromagnetic wave phase speeds) of medium 1 and 2 are known, the angle of incidence in medium 2 can be determined by

$$\sin\theta_2 = \frac{n_1}{n_2}\sin\theta_1 = \frac{v_2}{v_1}\sin\theta_1 . \tag{2.11}$$

The Appleton-Hartree-Lassen (Appleton, 1932; Hartree, 1929; Lassen, 1926) equation, also referred to as the Appleton-Hartree, or Appleton-Lassen equation, permits calculation of the refractive index of ionospheric plasma when including collisions and the effects of the Earth's magnetic field. The Appleton-Hartree-Lassen equation can be written as (Hargreaves, 1992):

$$\mu^2 = 1 - \frac{X}{1 - iZ - \frac{Y_T^2}{2(1-X-iZ)} \pm \left(\frac{Y_T^4}{4(1-X-iZ)^2} + Y_L^2\right)^{1/2}}, \tag{2.12}$$

with

$$X = \frac{N_e q^2}{\varepsilon_0 m_e \omega^2}, \tag{2.13}$$

$$Y_T = \frac{qB_T}{m_e \omega}, \tag{2.14}$$

$$Y_L = \frac{qB_L}{m_e \omega}, \tag{2.15}$$

$$Z = \frac{\upsilon}{\omega}, \tag{2.16}$$

where B_T and B_L are the components of the magnetic field which are perpendicular and parallel respectively to the ray path direction, N_e is the electron density, υ is the electron-neutral collision frequency, q and m_e are the charge and mass of an electron respectively, ω is the angular (radians per second) transmission frequency, and $i = \sqrt{-1}$. Note that two refractive indices are provided. The magnetic field effectively splits the transmission wave into two distinct waves. The refractive index differs for these two waves, so the ray path propagation directions may differ significantly. If we consider the special case in which the ray path travels perpendicular to the magnetic field, $Y_L = B_L = 0$, and the Appleton-Hartree-Lassen equation reduces to

$$\mu^2 = 1 - \frac{X}{1 - iZ - \frac{Y_T^2}{2(1 - X - iZ)} \pm \frac{Y_T^2}{2(1 - X - iZ)}}. \tag{2.17}$$

Note that in this special case the refractive index produced using the positive term in the denominator corresponds to the refractive index when no magnetic field is present. The mode using the positive term (for any transmission direction with respect to the Earth's magnetic field) is referred to as the ordinary mode (*o*-mode), whereas the negative term corresponds to

the extraordinary mode (*x*-mode). Also note that when the magnetic field and collisions are ignored, $B_T = B_L = \upsilon = 0$, and the Appleton-Hartree-Lassen equation reduces to

$$\mu^2 = 1 - X = 1 - \frac{N_e q^2}{\varepsilon_0 m_e \omega^2}. \tag{2.18}$$

Therefore, substituting from equation 2.1, in a plasma which is cold (i.e. neglecting thermal effects), collisionless, and is not in the presence of a magnetic field, the refractive index μ is given by:

$$\mu = \sqrt{1 - \frac{\omega_p^2}{\omega^2}}, \tag{2.19}$$

which can also be written as

$$\mu = \sqrt{1 - \frac{f_p^2}{f^2}}, \tag{2.20}$$

where f is the linear (Hz) transmission frequency respectively, and ω_p and f_p are the angular and linear plasma frequency respectively. By substituting from equation 2.3 the refractive index can, therefore, be approximated as

$$\mu \approx \sqrt{1 - \frac{80.6\ N_e}{f^2}}. \tag{2.21}$$

A key point to note here is that $\mu < 1$. Therefore, when travelling through a region with increasing plasma density, a ray will be refracted away from the normal of the boundary between two plasma densities. Conversely, when travelling through regions with decreasing plasma density the plasma the ray will be refracted towards the normal of the boundary. This ionospheric effect provides the opportunity for skywave propagation, in which a ray is transmitted at an oblique angle into the ionosphere. The ray is refracted by the ionosphere and can reach a point at which total internal reflection occurs, returning to the ground at locations which may be too distant to transmit to via direct line-of sight methods. This forms the basis of an over the horizon radar (OTHR) system, which will be discussed further in Sections 4 and 5.

2.4.2. Ionospheric Scintillation

Another important factor for ground-satellite communications transmitted through the low and high latitude ionosphere is whether the transmission passes through plasma irregularities, such as equatorial plasma bubbles (EPBs). At the boundary of the EPB there is a steep electron density gradient. Smaller scale electron density perturbations are likely to be present at the boundary and within the EPB due to the non-linear nature of the Rayleigh-Taylor instability producing additional structure within these regions. The presence of electron density irregularities can impact the ionospheric refractive index. Transmissions passing through these electron density irregularities may experience rapid fluctuations of phase and amplitude due to refractive and diffractive effects; these fluctuations are referred to as scintillation. A recent discussion of scintillation theory and models is provided by Materassi et al. (2019). Scintillation increases transmission noise and, if scintillation is sufficiently intense, can cause breaks in

communication (Kintner et al., 2007). The increasing dependence on trans-ionospheric communications such as Global Navigation Satellite System (GNSS) receivers (e.g. Global Positioning System (GPS) receivers) has made these communications critical for a range of industries (Hapgood, 2017). Scintillation can result in a loss of lock between GPS satellites and receivers, and cause reductions in accuracy for GPS positioning information (Béniguel et al., 2004).

Low and high latitude scintillation is driven by different processes. Low-latitude scintillation from EPBs depends on magnetic field lines being horizontal at the magnetic equator to produce **E**×**B** drift due to the dynamo electric field. In high latitude regions these circumstances are not reproduced. However, scintillation can be produced by other methods. For example, strong plasma density gradients can be produced at high latitudes during particle precipitation events (Santimay Basu et al., 1988; Makarevich et al., 2021). However, only forecasting of low-latitude amplitude scintillation will be considered within this work. Low-latitude amplitude scintillation tends to be greatest when the irregularity size along the transmission path is on the order of the radius of the transmission's first Fresnel zone (Yeh & Liu, 1982). The first Fresnel zone defines the region around a ray path for which the distance travelled by a ray which is reflected at this point travels $\frac{\lambda}{2}$ further than the unreflected ray path, i.e. the region for which reflection produces the greatest destructive interference as it is out of phase with the original signal by half the transmission wavelength $\left(\frac{\lambda}{2}\right)$. The radius of the Fresnel zone varies along the transmission ray path, with the greatest radius occurring at the midpoint between the transmitter and receiver. The radius of the first Fresnel zone (R_F) is given by

$$R_F = \left(\frac{DD'\lambda}{D + D'}\right)^{\frac{1}{2}}, \tag{2.22}$$

where D is the distance between the irregularity and the receiver, D' is the distance between the irregularity and the transmitter, and λ is the transmission wavelength. A method for modelling scintillation due to weak scattering treats the ionosphere as a thin phase screen at a chosen altitude. For example, consider a receiver at a fixed location on the ground which receives GPS signals at frequency L_1 (1575.42 MHz, corresponding to a wavelength of about 19 cm) from a satellite orbiting directly above the receiver at an altitude of 20,000 km. At an altitude of 400 km the radius of the first Fresnel zone is

$$R_F = \left(\frac{19600 \times 400 \times 10^6 \times 0.19}{20000 \times 10^3}\right)^{\frac{1}{2}} \approx 273 \text{ m}. \tag{2.23}$$

If an irregularity such as an EPB completely covers the Fresnel zone at a particular altitude, the signal will have a change in phase compared to a signal with no irregularities within the Fresnel zone, which results in a change to the signal direction. However, in the absence of significant plasma density gradients within the irregularity, the change in phase will be reasonably similar along the signal wave front. Therefore, the change in direction is similar across the wave front and the signal remains consistent with the original transmission apart from the change in phase. However, in the presence of small irregularities which do not cover all of the Fresnel zone, there can be significant differences to the phase across the wave front due to significant differences in plasma density within irregularities compared to the surrounding region. The change of phase produces small changes in direction across the wave front. At the ground, the

convergence of the signal from different regions within the wave front at the irregularity altitude can produce constructive or destructive interference due to the differences in phase from the source in the wave front at the irregularity altitude. Therefore, there will be variation in the received signal amplitude at different locations on the ground. When the thickness of the irregularity is also considered, variability in amplitude (as well as phase) can be present across the wave front as it leaves the irregularity (particularly for irregularities with stronger scattering strength), contributing further to variability in the received amplitude at different locations on the ground. If the transmitter, receiver, and ionospheric features were fixed in space, the signal amplitude and phase would vary by ground receiver location but would remain constant in time. However, even for a fixed ground receiver and a satellite in geostationary orbit, the bulk motion of the ionosphere and irregularity drift result in variability of the signal phase and amplitude with time at a receiver location. Small scale irregularities can, therefore, produce the rapid fluctuations of amplitude and phase defined as scintillation. As the size of the Fresnel zone is dependent on the wavelength, scintillation effects are also dependent on the transmission frequency. For example, the radius of the Fresnel zone for frequency L_1 at 400 km was determined to be 273 m. Many plasma irregularities will have size in excess of 1 km, so will have less of an impact at GPS frequencies. However, lower frequencies with a larger Fresnel zone (as the radius of the Fresnel zone at an altitude is proportional to the square root of the wavelength, or the inverse square root of the frequency) are more likely to be impacted by scintillation due to larger plasma irregularities. Therefore, lower frequencies tend to encounter scintillation more often than higher frequencies. In this work the focus will be on amplitude scintillation of GPS transmissions at low latitudes.

2.5. Ionospheric Observations

There are numerous methods and techniques for probing the ionosphere. Three of these techniques contribute directly towards work within this thesis and are described below.

2.5.1. Ionosondes

A vertical ionosonde can provide observations of the ionosphere directly above it by sweeping through a range of transmission frequencies and observing the time taken for the vertical signal to be refracted back down to the ionosonde. The results can be displayed on an ionogram which reveals several useful ionospheric characteristics (Figure 10). The virtual height is obtained by assuming that the transmission is reflected at a single point in the ionosphere but experiences no other path deviation (i.e. assuming that the peak height of the transmission path is $0.5ct$, where t is the time taken and c is the speed of light). However, the true peak height will be lower than the virtual height as the plasma density is non-zero along the transmission path below the point of reflection. Each curve on the ionogram is associated with an ionospheric layer. The height associated with the lowest point on the curve corresponds to the virtual height for that layer, e.g. the virtual height of the E layer is shown as h'E in Figure 10. The frequency associated with the peak of the curve corresponds to the critical frequency already described, e.g. the critical frequency of the E layer is shown as foE in Figure 10. The ordinary (*o*-mode) and extraordinary (*x*-mode) waves are shown in Figure 10 in green and red respectively. Software such as the Automatic Real-Time Ionogram Scaler with True height (ARTIST) can be used to autoscale ionosonde output to determine the electron density profile at the ionosonde location (Galkin et al., 2008). However, care must be taken when drawing conclusions based on autoscaled output, as such software is not infallible (Themens et al., 2022). Hand scaling of

ionograms can be used to avoid common autoscaling errors. The colocation of the ionosonde transmitter and receiver is not essential. Non-vertical ionosondes are referred to as oblique ionosondes (Sartori, 2021), and can provide information about electron densities along the skywave paths between the transmitter and receiver.

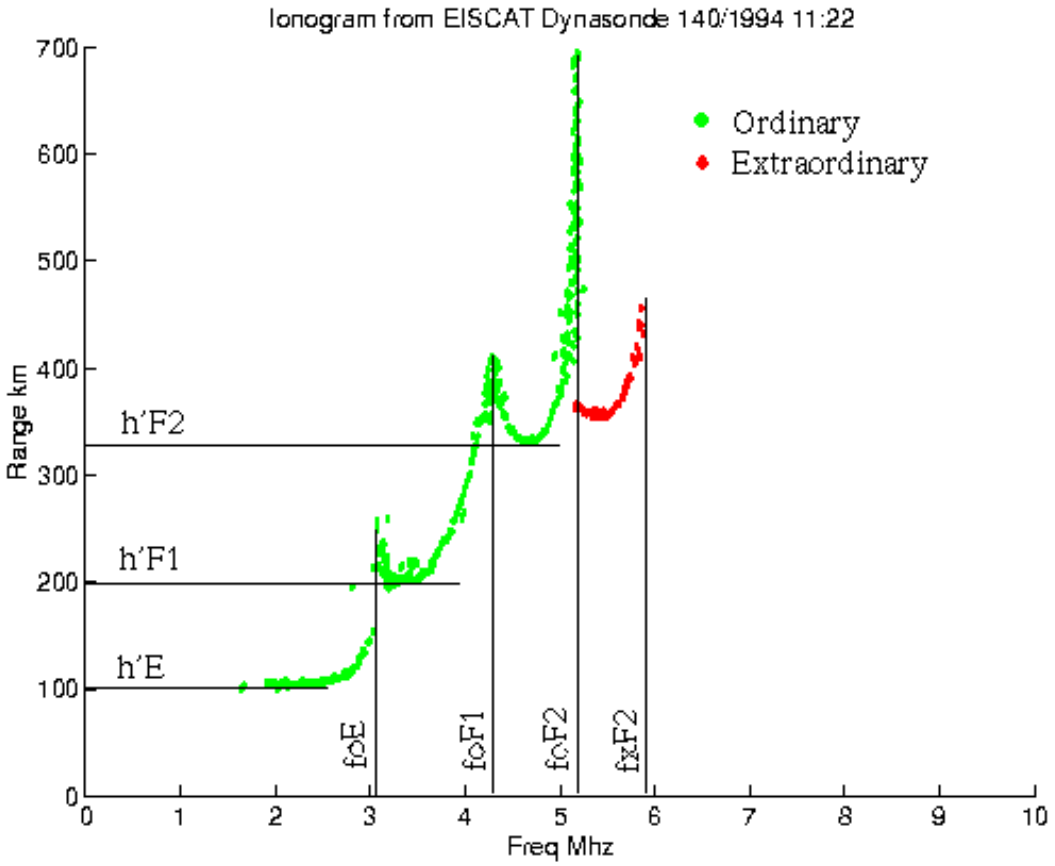

Figure 10. Example ionogram (Davis, 1996).

2.5.2. GNSS TEC Observations

The TEC for a ray path represents the integrated electron density along the path. A key aspect of modern GNSS systems (such as GPS) when determining TEC observations is the use of two or more satellite transmission frequencies which can be detected by the receiver. The

pseudorange (R) of the transmission is an approximation of the distance between the transmitter and receiver, given by

$$R = ct\,, \tag{2.24}$$

where c is the speed of light in a vacuum and t is the time of flight. The pseudorange is an overestimation of the true distance due to ionospheric effects on the transmission, and is dependent on the frequency used. However, by determining the pseudorange for two frequencies, an estimation of the TEC along the transmission path can be determined. Similarly, TEC can be determined using the difference in phase between the two signals. However, the difference in phase does not provide a definitive TEC value. Rather, a TEC value is produced which is of the form

$$TEC_{phase} = \alpha + 2\pi\beta\,, \tag{2.25}$$

for some unknown value β. An advantage of calculating the TEC_{phase} is that it is considerably less susceptible to noise than the TEC value determined from the pseudorange (TEC_{range}). Commonly, a combination of the TEC_{phase} and TEC_{range} observations are used to provide a smoothed TEC value. The TEC_{range} and TEC_{phase} (when inherent biases and the phase ambiguity have been removed) are given by

$$TEC_{range} = \frac{f_1^2 f_2^2}{40.3 \times 10^{16}(f_2^2 - f_1^2)}(R_1 - R_2)\,, \tag{2.26}$$

$$TEC_{phase} = \frac{f_1^2 f_2^2}{40.3 \times 10^{16}(f_2^2 - f_1^2)}(\Phi_2 - \Phi_1)\,, \qquad (2.27)$$

where TEC is in TEC units (10^{16} electrons per m^2) and f_i are the transmission frequencies used for the observations (in Hz). R_i (metres) and Φ_i (metres) are the pseudorange and phase range observations respectively associated with frequency f_i. Frequencies commonly used for GPS TEC observations are L_1 (1575.42 MHz) and L_2 (1227.6 MHz). Therefore, using these frequencies we have

$$TEC_{range} = 9.52(R_2 - R_1)\,, \qquad (2.28)$$

$$TEC_{phase} = 9.52(\Phi_1 - \Phi_2)\,, \qquad (2.29)$$

where R_1 and Φ_1 are the pseudorange and phase for frequency L_1, and R_2 and Φ_2 are the pseudorange and phase for frequency L_2. Methods to create smoothed TEC observations using TEC_{range} and TEC_{phase}, and an in-depth discussion of techniques to generate total electron content (TEC) observations, are provided by Liu et al. (2005).

2.5.3. Ionospheric Scintillation Monitors

A commonly used indicator of amplitude scintillation is the S4 index (Briggs & Parkin, 1963), given by the normalised standard deviation of the signal intensity, i.e.

$$S4 = \sqrt{\frac{\langle I^2 \rangle - \langle I \rangle^2}{\langle I \rangle^2}}, \qquad (2.30)$$

where I is the signal intensity of a transmission over a chosen period (commonly 60 seconds). The S4 index is a useful indicator of scintillation as it is relatively straightforward to compute and, as S4 can be determined using a single receiver such as a GPS receiver, data is widely available across many regions. However, S4 does not provide specific information about irregularity size or strength, as the transmission path direction relative to the magnetic field direction (and, therefore, the axes along which an irregularity may be elongated) can impact the strength of the S4 observation.

Ionospheric Scintillation Monitors (ISMs) such as those operated by the Australian Space Weather Services (Australian Bureau of Meteorology Space Weather Services, 2022), use GPS receivers to detect scintillation occurrences and strength. In this work the Space Weather Services (SWS) ISM located in Vanimo, Papua New Guinea will be used to provide observations of low-latitude scintillation. A dual-frequency (L_1 and L_2) GPS receiver with sampling rate of 50 Hz provides scintillation observations for transmissions from several satellites. Output for each detected satellite is provided every one minute, including observations of S4, a satellite identifier number and the azimuth and elevation of the satellite. ISM observations of S4 will be used to determine the accuracy of low-latitude scintillation forecasting.

3. IONOSPHERIC MODELLING

The development of ionospheric models plays a key role in the effort to mitigate ionospheric effects and to continue improving the understanding of ionospheric physics and processes. Ionospheric models can be classed as empirical, physics-based, or data assimilation models. Empirical models use observations of the ionosphere to build a climatology of ionospheric conditions. A key advantage of empirical models is that they tend to be computationally cheap compared to physics-based and data assimilation models (Forootan et al., 2023). Empirical models have played an important role in the development of the current understanding of the ionosphere. However, the climatological nature of output from an empirical model makes these models unsuitable for nowcasts or forecasts of day-to-day ionospheric variability. Physics-based models use the underlying physical equations relevant to the ionosphere to propagate ionospheric conditions forward in time. When the underlying physics is modelled accurately, physics-based models would be expected to provide greater accuracy for the nowcasting and forecasting of day-to-day ionospheric variability (Lin et al., 2017). However, assumptions, simplifications and incomplete physics within physics-based modelling, as well as numerical errors and uncertainty in appropriate values for key parameters, can be detrimental to the model forecasting accuracy (Schunk et al., 2012). A key issue for nowcasting and forecasting with physics-based models is the determination of the initial conditions to use. Even if all of the underlying physics were able to be modelled perfectly, the model cannot provide a truly accurate short-term forecast if the model initial conditions do not accurately reflect the real ionospheric conditions at that time (Schunk et al., 2012). Furthermore, inaccurate representations of boundary conditions can have significant impacts to modelled ionospheric conditions. For example, the solar flux is a model boundary condition which will affect ionisation rates and, therefore, electron and ion densities. The solar flux can also impact

recombination rates. For example, increased solar activity results in larger densities of vibrationally excited N_2 which increases the recombination rate of O^+ (Liu et al., 2011). One way to overcome some of the problems due to inaccurate boundary and initial conditions is to combine output from an ionospheric model with ionospheric observations: a process referred to as data assimilation (DA). DA models can use empirical or physics-based models as the background model, and several DA techniques exist to combine the model output with observations, such as Kalman filters (Kalman, 1960), ensemble Kalman filters (Evensen, 1994), optimal interpolation (Daley, 1991), variational analysis (Courtier, 1998; Eyre, 1989; Parrish & Derber, 1992), and particle filters (Gordon et al., 1993). When an observation value is available, a key consideration is to estimate the uncertainty of the observation value compared to the background model. If the observation and model output represent the same variable, the DA model output can then be a weighted combination of the observation value and background model values. It is also possible to use observations of one ionospheric variable to estimate the appropriate change to make to a different variable within the background model output, if the covariance between the two variables is known or can be estimated.

A number of ionospheric models are under active development around the world. Here specific focus is given to six models: NeQuick2 (Section 3.1), FIRI (Section 3.2), IRI (Section 3.3), FIRIC (Section 3.4), TIE-GCM (Section 3.5), and AENeAS (Section 3.6).

3.1. NeQuick2

NeQuick2 was developed at the Aeronomy and Radiopropagation Laboratory of the Abdus Salam International Centre for Theoretical Physics (ICTP), Trieste, Italy and at the Institute for

Geophysics, Astrophysics and Meteorology of the University of Graz, Austria (Nava et al., 2008). NeQuick2 is the second generation of the NeQuick model and is an empirical global model of ionospheric electron densities. Electron density profiles are designed to be numerically integrable to permit calculation of TEC along any transmitter-receiver path. The NeQuick lower boundary is at an altitude of 90 km. Electron densities below 90 km are considerably lower than at higher altitudes such as in the F region, so the absence of lower altitude electron densities is not significant for modelling of TEC. NeQuick2 electron density profiles from the lower boundary to hmF2 are constructed using the sum of five semi-Epstein layers (Rawer, 1982) with anchor points at the peaks of the E, F1 and F2 layers. One further semi-Epstein layer with a height-dependent layer thickness parameter describes electron densities above the F2 peak, to altitudes of 20,000 km or more. The electron density at altitude h can be modelled in an Epstein layer $(N_{Epstein})$ as

$$N_{Epstein} = \frac{4\,Nmax}{\left(1 + \exp\left(\frac{h - hmax}{B}\right)\right)^2} \exp\left(\frac{h - hmax}{B}\right), \quad (3.1)$$

where $Nmax$ is the peak electron density within the layer, $hmax$ is the peak height, and B is the layer thickness parameter. An Epstein layer is used to describe each of the E region bottomside and topside, the F1 region bottomside and topside, and the F2 layer bottomside. Correction factors are applied to $Nmax$ for the bottomside and topside of the E and F1 regions to ensure that E and F1 region peak densities are correct once all five Epstein layers have been summed. A "fadeout" function is applied to each $h - hmax$ term in the E and F1 regions to ensure that multiple peaks are not produced in the F2 layer.

The $M(3000)F2$ is the ratio of $MUF(3000)$ to $foF2$ (critical frequency of the F2 layer), where $MUF(3000)$ is the maximum useable frequency (MHz) which can be used to transmit a signal from a ground transmitter to a ground receiver 3000 km from the transmitter. Monthly median values of $foF2$ and $M(3000)F2$ are determined using the International Telecommunication Union Radiocommunication Sector (ITU-R) coefficients (Jones & Gallet, 1962), previously known as the International Radio Consultative Committee (CCIR). $foF2$ and $M(3000)F2$ are used to determine, for example, the F2 bottomside layer thickness and $hmF2$. $hmF2$ calculations also require the solar zenith angle (the angle between the vertical and the direction of the sun) and the F10.7 solar flux (solar flux with a wavelength of 10.7 cm, used as an indicator of solar activity). The $F10.7$ solar flux is required as a model input. $F10.7$ values between 63.7 and 193 solar flux units (sfu) may be chosen, and NeQuick determines the twelve month smoothed sunspot number (R_{12}) from the $F10.7$ using

$$R_{12} = \sqrt{167273 + 1123.6(F10.7 - 63.7)} - 408.99\,, \qquad (3.2)$$

as, for example, R_{12} is required for the ITU-R coefficients.

A full description of NeQuick2 is provided by Nava et al. (2008) and references therein. Within this work the University of Birmingham adaptation of NeQuick2 described by Angling et al. (2018) is used. The updates to NeQuick2 included in the University of Birmingham version are:

- Maximum accepted F10.7 input value extended beyond 193 sfu
- Day of month included as input. Output is a linear interpolation of the monthly median values provided by NeQuick2

- hmE (height of the peak electron density in the E layer) is set equal to 110 km rather than 120 km
- Bottomside taper using a tanh function included to avoid a discontinuity at the NeQuick2 lower boundary (90 km)

3.2. FIRI

The Faraday-International Reference Ionosphere (FIRI; Friedrich et al., 2018) is a semi-empirical model of the lower ionosphere (60-150 km). FIRI uses a simple, steady-state ion-chemical model of the lower ionosphere. Adjustments to modelled electron densities are made using ionospheric observations obtained using sounding rockets. The adjustments made are dependent on altitude, latitude, solar zenith angle, day of year, and solar activity (F10.7 solar flux). Output is provided as a database of 1980 electron density profiles, for eleven solar zenith angles (0°, 30°, 45°, 60°, 75°, 80°, 85°, 90°, 95°, 100°, and 130°), five latitudes (0°, 15°, 30°, 45° and 60°), and three levels of solar activity (F10.7 = 75, 130 and 200) for the middle of each calendar month. Output is only applicable to the northern hemisphere. For southern hemisphere output, six months are added to the day of year for northern hemisphere values.

3.3. IRI

The International Reference Ionosphere (IRI) is an empirical model of the ionosphere which is recognised as the international standard (TS 16457) for ionospheric modelling (ISO, 2009). In this work the 2016 edition of IRI (IRI-2016) is used. IRI source code is available at irimodel.org, and an online version of IRI-2016 is available at

ccmc.gsfc.nasa.gov/modelweb/models/iri2016_vitmo.php. An overview of IRI-2016 is provided by (Bilitza, 2018) and references therein. Model development began in the 1960s, sponsored by the Committee on Space Research (COSPAR) and the International Union of Radio Science (URSI). Ionospheric data has been accumulated over many years from several sources, with current sources of data for IRI including ionosondes, topside sounders, incoherent scatter radars and low earth orbit GPS radio occultation for electron densities, and in situ satellite observations and incoherent scatter radars for electron and ion densities and temperatures. IRI output provides monthly averages (median values) of ion densities and composition (75-2000 km), ion and electron temperatures (60-2500 km), and electron densities (65-2000 km during the day, 80-2000 km at night). Output can also include vertical TEC to a user-specified altitude, and equatorial vertical ion drift. IRI requires input including geomagnetic (Ap, Kp) and solar indices (R_{12}, and the daily, 81 day average and 12 month average F10.7). IRI also requires IG_{12} input, an indicator of solar activity derived from midday foF2 measurements from a network of ionosondes. However, if a date for model output is provided these values can be determined from an internal database. The D, E, F1 and F2 peak plasma frequency/electron density and peak height can be specified if desired, as well as the $M(3000)F2$. If not specified, these parameters will be determined by the model.

Several options are available for underlying models used within IRI-2016 to determine ionospheric features. These options, and the model default options, are listed in Table 2. A more recent version of IRI (IRI-2020) has since been released. However, IRI-2016, including the default options for IRI-2016 listed in Table 2, is used for IRI output within this work.

Table 2. Selectable model options and default options for IRI-2016.

IRI-2016 selectable parameters	Model options (default in **bold**)
Sunspot number (R_{12}), ionospheric index (IG_{12}) daily and 81-day average F10.7 solar flux	**Determined from an internal database if date selected is between 1952 and current date**
Ne topside	**NeQuick** (Nava et al., 2008) IRI01-corr (Bilitza, 2004). IRI2001 (Bent et al., 1972)
Ne F-peak	**URSI** (Fox & McNamara, 1988) CCIR (Jones & Gallet, 1962)
F-peak storm model	**On** Off
F-peak height	**AMTB2013** (Altadill et al., 2013) SHU-2015 (Shubin, 2015) BSE-1979 (Bilitza et al., 1979)
Bottomside thickness	**ABT-2009** (Altadill et al., 2009) Bil-2000 (Bilitza et al., 2000) Gul-1987 (Gulyaeva, 1987)
F1 occurrence probability	**Scotto-1997 no L** (Scotto et al., 1998) Scotto-1997 with L (with F1 ledges) IRI-95 (DuCharme et al., 1973)
Auroral boundaries	**On** Off

E-peak auroral storm model	**Off** On
D-region model	**IRI-95** (Danilov et al., 1995) FT-2001 (Friedrich & Torkar, 2001)
Te topside	**TBT2012+SA** (Truhlik et al., 2012): includes correction term for solar activity TBT-2012 (Truhlik et al., 2012) BIL-1995 (Brace & Theis, 1981)
Ion composition	**RBV10/TBT15** (Třísková et al., 2003; Truhlik et al., 2015) DS95/DY85 (Danilov & Smirnova, 1995; Danilov & Yaichnikov, 1985)

IRI has been used for decades to build up an understanding of ionospheric conditions and processes (Bilitza, 2018). However, as previously discussed, the climatological nature of IRI is a limiting factor when attempting to forecast day-to-day variability within the ionosphere. Even when data assimilation is incorporated into IRI to allow a good representation of initial conditions, these conditions must swiftly return to climatology in the absence of further information when conditions are propagated forward in time in real time forecasting. Therefore, IRI with data assimilation can be a useful tool for nowcasting but is less effective for forecasting.

3.4. FIRIC

The FAIM (Fully Analytic Ionosphere Model; Anderson et al., 1989) IRI Combination model (FIRIC; Coleman, 1997) by Coleman has been in continuous development since the 1990s. The motivation for the development of FIRIC was to create an ionospheric model suitable for ionospheric ray tracing. A key requirement for ray tracing is that the electron density profile and the first and second derivative of the electron density profile (with electron density as a function of altitude) must be continuous to permit calculation of the ray path. To ensure this is possible, the ray tracer used within this work fits splines to vertical electron density profiles. However, this can result in unphysical output from the ray tracer if electron density profiles include sudden changes of gradient or discontinuities. FIRIC has been designed to provide electron density profiles suitable for the ray tracer. However, this is not necessarily the case for other numerical models such as IRI. Models, such as NeQuick 2, which fit functions to empirical anchor points may be more likely to provide suitable electron density profiles for ray tracing. However, the lower boundary of NeQuick is at 90 km. Therefore, the D region is not included, which is important for ray tracing due to high levels of signal attenuation within the D and E regions.

The FIRIC electron density profiles below the peak are described by the sum of four Chapman layers. The electron density within a Chapman layer (N_e) can be expressed as (e.g. Hargreaves, 1992)

$$\begin{aligned} N_e &= N_p Chap(\alpha, z) \\ &= N_p \exp\left(\alpha\left(1 - z - \sec\chi \exp(-z)\right)\right), \end{aligned} \tag{3.3}$$

with

$$z = \frac{r - r_p}{H}, \tag{3.4}$$

where N_p is the peak electron density within the Chapman layer, α is the recombination coefficient, χ is the solar zenith angle, r is the distance from the Earth's centre to the electron density location (i.e. altitude + Earth's radius), r_p is the distance from the Earth's centre to the altitude of the peak electron density within the Chapman layer, and H is the scale height. In the E and F1 layers α is set equal to 0.5 (referred to as α-Chapman layer functions), and in the D and F2 layers α is equal to 1 (referred to as β-Chapman layer functions). Therefore, the plasma frequency (MHz) at height h (which is below hmF2) is described using

$$\begin{aligned} f_p^2 = {} & c_1 Chap(1, z_1) + c_2 Chap\left(\frac{1}{2}, z_2\right) \\ & + c_3 Chap\left(\frac{1}{2}, z_3\right) + c_4 Chap(1, z_4), \end{aligned} \tag{3.5}$$

with

$$z_1 = \sqrt{2}\frac{h - hmD}{ymD}, \tag{3.6}$$

$$z_2 = 2\frac{h - hmE}{ymE}, \tag{3.7}$$

$$z_3 = 2\frac{h - hmF1}{ymF1}, \tag{3.8}$$

$$z_4 = \sqrt{2}\frac{h - hmF2}{ymF2}, \tag{3.9}$$

so, e.g.,

$$c_2 Chap\left(\frac{1}{2}, z_2\right) = c_2 \cdot \exp\left(\frac{1}{2}\left(1 - 2\frac{h - hmE}{ymE} - \sec\chi \exp\left(-2\frac{h - hmE}{ymE}\right)\right)\right). \tag{3.10}$$

The peak height for each bottomside layer is defined as

$$hmD = 78 \text{ km}, \tag{3.11}$$

$$hmE = 110 \text{ km}, \tag{3.12}$$

$$hmF1 = 0.65hmE + 0.35hmF2, \tag{3.13}$$

$$hmF2 = \frac{1490}{M3000 + D} - 176, \tag{3.14}$$

with

$$D = (0.00232\, R_{12} + 0.222)\frac{1 - \left(\frac{R_{12}}{150}\right)\exp\left(\frac{-\theta_{gm}^2}{1600}\right)}{\frac{foF2}{foE} - 1.2 + 0.0116\exp(0.0239\, R_{12})} + \frac{0.096}{150}(R_{12} - 25), \tag{3.15}$$

where θ_{gm} is the geomagnetic latitude, and foE and foF2 are the critical plasma frequencies in the E region and F2 region respectively. The value for hmD was determined by taking the mean hmD from the database of FIRI (Section 3.2) electron density profiles. The hmE value is the same as in the version of NeQuick described in (Angling et al., 2018). The method used to determine $hmF2$ is the same as in the BSE-1979 (Bilitza et al., 1979) option available within IRI (Section 3.3). The semi-thickness for each bottomside layer is defined as

$$ymD = 10\,, \tag{3.16}$$

$$ymE = 18 + \frac{R_{12}}{50}\,, \tag{3.17}$$

$$ymF1 = \frac{hmF1}{4}\,, \tag{3.18}$$

$$ymF2 = \frac{hmF2 - hmE}{2}\,. \tag{3.19}$$

The value for ymD was determined by taking the mean ymD from the database of FIRI (Section 3.2) electron density profiles, in the same manner as for hmD. $ymF1$ is determined in the same manner as the RADARC ionospheric model (Thomason et al., 1979), and $ymF2$ is determined in a similar manner to that used by NeQuick (Section 3.1) to calculate the bottomside F1 layer semi-thickness $\left(\frac{hmF1-hmE}{2}\right)$. A scaling coefficient, c_i, is applied to each Chapman layer. c_1 is given by

$$c_1 = f_o D^2\,, \tag{3.20}$$

where f_oD is the peak plasma frequency in the D layer. Scaling coefficients c_2, c_3 and c_4 are chosen such that the modelled plasma frequency matches the E, F1 and F2 layer peak plasma frequencies at the peak frequency heights, i.e.

$$f_p(hmE) = foE\,, \tag{3.21}$$

$$f_p(hmF1) = foF1\,, \tag{3.22}$$

$$f_p(hmF2) = foF2\,. \tag{3.23}$$

Peak plasma frequencies in the D, E, and F1 layers are given by

$$f_p = (A + B \times R_{12}) \cos(\chi)^p \cos(\chi_{12})^q\,, \tag{3.24}$$

where χ is the solar zenith angle, and χ_{12} is the solar zenith angle at midday local time. Values for parameters A, B, p and q are chosen to obtain peak frequencies in the D and E regions which are similar to those provided by the FIRI model. Peak plasma frequencies for the F2 layer are obtained from the ITU-R (CCIR) coefficients (Jones & Gallet, 1962) in the same manner as IRI and NeQuick2.

For plasma frequencies above the peak, the F2 layer is represented by an α-Chapman layer function to improve accuracy (Pignalberi et al., 2018), with

$$z_{4top} = 2\frac{h - hmF2}{ymF2_{top}}\,, \tag{3.25}$$

and $ymF2_{top} = 78.6$ km. Topside plasma frequencies are, therefore, modelled using

$$f_p^2 = c_1 Chap(1, z_1) + c_2 Chap\left(\frac{1}{2}, z_2\right) + c_3 Chap\left(\frac{1}{2}, z_3\right) + c_4 Chap\left(\frac{1}{2}, z_{4top}\right). \quad (3.26)$$

Further corrections can also be provided by FIRIC to account for auroral plasma frequencies and geomagnetic storms. However, these corrections are not required within this work.

3.5. TIE-GCM

The Thermosphere-Ionosphere-Electrodynamics General Circulation Model (TIE-GCM) is a physics-based model of the ionosphere and thermosphere (Qian et al., 2014; Richmond et al., 1992) developed by the National Center for Atmospheric Research (NCAR). TIE-GCM provides a self-consistent representation of the thermosphere and ionosphere, including interactions between the two (such as dynamo electric fields). The three-dimensional momentum, energy, and continuity equations are solved at each time step for both neutral and ion species, using a 3-dimensional grid consisting of latitude, longitude and height, with the height defined by a log-pressure coordinate system. The pressure level, z, is given by

$$z = \ln\left({}^{p_0}/_{p}\right), \quad (3.27)$$

where p is the pressure, and with reference pressure $p_0 = 5 \times 10^{-7}$ hPa (hectopascals). The lower boundary of TIE-GCM corresponds to $z = -7$ which equates to a geopotential height of

approximately 97 km. Geopotential height is a measure of height which takes into account the variation of gravitational force with altitude and latitude by taking the integral of the gravitational force from mean sea level to the specified height and dividing by the gravitational force at mean sea level. The pressure level $z = 7$ marks the upper boundary of TIE-GCM, which corresponds to between 500 and 700 km geopotential height depending on solar activity.

TIE-GCM input includes F10.7 solar flux and global geomagnetic activity (Kp index) as well as temperatures, wind velocities and geopotential heights at each grid point on the lower boundary. The lower boundary consists of a background field and input files representing perturbations from the background. The default background field is a spatially and temporally constant field with geopotential height, neutral temperature, and wind velocity of 96.37229 km, 181.0 K, and 0 ms^{-1}, respectively. Other backgrounds can be selected, which provide climatologies of lower boundary conditions from the Climatological Tidal Model of the Thermosphere (Oberheide et al., 2011), the Mass Spectrometer and Incoherent Scatter data thermospheric model (Hedin, 1987), the Horizontal Wind Model (Hedin et al., 1988) or data from the Upper Atmosphere Research Satellite (UARS). The default method for perturbing the homogeneous background field is to use Global Scale Wave Model (Hagan et al., 1993) output. The GSWM solves the linearised and extended Navier-Stokes equations to provide perturbations from the background field in the form of migrating and non-migrating diurnal and semi-diurnal tides. TIE-GCM can also use perturbation input from other sources such as the Sounding of the Atmosphere using Broadband Emission Radiometry (SABER) on-board the Thermosphere Ionosphere Mesosphere Energetics and Dynamics (TIMED) satellite (Yee et al., 2003), or wind speeds from the High Resolution Doppler Imager (Hays et al., 1993) on-board the UARS. Alternatively, tides can be specified using eigenfunctions of Laplace's equation for

tidal motion known as Hough functions (Hough, 1897, 1898). In this work GSWM output is used to determine lower boundary conditions.

Electron densities, electric potentials, geometric heights (elevation above sea level) and geopotential heights are available as output at every latitude-longitude 2-D grid point on the pressure level interfaces; however, most model output is reported at the midpoints between pressure level interfaces (NCAR High Altitude Observatory, 2016). Further output available includes: neutral, ion and electron temperatures; zonal (east-west), meridional (north-south) and vertical neutral winds and ion drifts; vertical atmospheric motion; Joule heating (heating generated by an electric current); height-integrated Joule heating; vertical total electron content (TEC); the critical frequency of the F2 layer (foF2); the zonal, meridional and vertical electric current density and components of the electric and magnetic fields; the magnitude of the magnetic field; the total heating; carbon dioxide and nitric oxide cooling; the densities of individual species (atomic and molecular oxygen, atomic and molecular oxygen ions, atomic nitrogen in its ground and excited states, molecular nitrogen, nitric oxide, helium and argon) and the total neutral density. TIE-GCM is publicly available in both 2.5° and 5° resolution, and has also been developed for 1.25° and 0.625° resolution (Dang et al., 2021). Some differences between the 2.5° and 5° resolution versions are shown in Table 3. In this work TIE-GCM at 2.5° resolution is used.

Table 3. Features of 2.5° and 5° TIE-GCM v2.0 resolutions.

TIE-GCM resolution	5° resolution	2.5° resolution
Latitude	5° steps	2.5° steps
Longitude	5° steps	2.5° steps
Height (log pressure: -7 to +7)	0.5 steps	0.25 steps
GSWM tides available for lower boundary	Diurnal and semi diurnal migrating tides	Diurnal and semi-diurnal migrating and non-migrating tides
Default model time step	60 seconds	30 seconds

3.6. AENeAS

The Advanced Ensemble electron density (Ne) Assimilation System (AENeAS; Elvidge & Angling, 2019) is a data assimilation model of the ionosphere and thermosphere. AENeAS assimilates GNSS total electron content (TEC), true height ionosonde, radio occultation, and altimeter observations using a variant of the ensemble Kalman filter (Evensen, 1994) called the Local Ensemble Transform Kalman Filter (LETKF; Hunt et al., 2007), and propagates ionospheric and thermospheric conditions forward in time using the physics-based TIE-GCM (Section 3.5) model. NeQuick2 (Section 3.1) electron density profiles are smoothly attached to the TIE-GCM upper boundary (~500-700 km depending on solar activity) to provide continuous electron density profiles up to 20,000 km.

Conventional Ensemble Kalman Filters (EnKFs) combine an ensemble of initial (background) states with observations, thereby producing an ensemble of updated (analysis) states, which

should be closer to the true conditions. AENeAS uses the Local Ensemble Transform Kalman Filter which, like other Kalman filter methods, consists of an update step to assimilate observations and a prediction step to propagate the conditions forward in time. The LETKF equations used within AENeAS for the update step are:

$$\mathbf{A} = \mathbf{X}_b \widetilde{\mathbf{A}} (\mathbf{X}_b)^T \,, \tag{3.28}$$

$$\bar{\mathbf{x}}_a = \bar{\mathbf{x}}_b + \mathbf{X}_b \mathbf{w}_a \,, \tag{3.29}$$

$$\mathbf{X}_a = \mathbf{X}_b \left((k-1) \widetilde{\mathbf{A}} \right)^{\frac{1}{2}} . \tag{3.30}$$

Descriptions of variables within these equations are provided in Table 4.

Once the update step has been completed, a prediction step is performed to propagate the analysis state forward in time to the next time step. TIE-GCM is used to propagate each ensemble member 15 minutes forward in time from the analysis state. The resulting ensemble forms the new ensemble of background states in the next time step.

The use of LETKF avoids the requirement of calculating the full background error covariance matrix required for traditional Kalman filters (Kalman, 1960). The computational cost of a standard EnKF is $O\left(s^3 + s^2 k + k^2 (s+m)\right)$, where m, s, and k are the dimension of the state vector, the number of observations, and the number of ensemble members, respectively. However, the computational cost of the LETKF is $O\left(k^3 + k^2 s + k(s+m)\right)$ and, generally (for AENeAS), $k \ll s$ (Elvidge, 2019). LETKF only assimilates observations from locations which are within predetermined boundaries in relation to each model grid point (i.e. only

Table 4. Sizes and descriptions of variables within the LETKF equations used by AENeAS.

Name	Size	Description
M	Integer	Number of variables (each variable is one species, temperature, etc. at one latitude-longitude-pressure height grid point)
K	Integer	Number of ensemble members
S	Integer	Number of observations to be assimilated
$\bar{\mathbf{x}}_b$	$m \times 1$	The mean of the background ensemble (before data assimilation (DA) takes place), i.e. one element of $\bar{\mathbf{x}}_b$ represents the mean of the k values (one from each ensemble member) for one variable
$\mathbf{X}_b$	$m \times k$	The deviation from the background ensemble mean for each variable within each background ensemble member
$\bar{\mathbf{x}}_a$	$m \times 1$	The mean of the analysis ensemble, i.e. the mean of the ensemble members after the update step
$\mathbf{X}_a$	$m \times k$	The deviation from the analysis ensemble mean for each variable within each analysis ensemble member
$\mathbf{A}$	$m \times m$	Analysis (updated values) error covariance matrix
$\mathbf{w}_a$	$k \times 1$	$\mathbf{w}_a = \widetilde{\mathbf{A}}(\mathbf{Y}_b)^T\mathbf{O}^{-1}(\boldsymbol{y_0} - \bar{\boldsymbol{y}}_b)$. Matrix used to update ensemble mean.
$\widetilde{\mathbf{A}}$	$k \times k$	$\widetilde{\mathbf{A}} = [(k-1)\mathbf{I} + (\mathbf{Y}_b)^T\mathbf{O}^{-1}\mathbf{Y}_b]^{-1}$. Matrix used to update perturbations from the ensemble mean. **I** is the identity matrix. Note that calculation of $\widetilde{\mathbf{A}}$ requires the inversion of a matrix. However, the inversion is performed on a square matrix with size $k \times k$ whereas with traditional Kalman filters the inversion is performed on a matrix with size $s \times s$. In AENeAS the number of observations to be assimilated (s) will generally be far greater than the number of ensemble members (k).
$\boldsymbol{y_0}$	$s \times 1$	Observation values
$\mathbf{Y}_b$	$s \times k$	$\mathbf{Y}_b = \mathbf{H}\mathbf{X}_b$. The background perturbations from the mean, transformed by the observation operator **H** from variable space to observation space (reducing the matrix size from $m \times k$ to $s \times k$)
$\bar{\mathbf{y}}_b$	$s \times 1$	The mean background values transformed from variable space to observation space
$\mathbf{O}$	$s \times s$	Observation error covariance matrix. Observations are assumed to be independent, so $\mathbf{O}$ is a diagonal matrix. Therefore, calculating the inverse of $\mathbf{O}$ (which is required for $\mathbf{w}_a$ and $\widetilde{\mathbf{A}}$) is very straightforward and computationally cheap

observations which are “local” to the grid point location are included within observations to be assimilated at that grid point). This helps to avoid spurious correlations between parameters and observations in distant locations. A disadvantage of the LETKF (compared to standard EnKFs) is that an observation vector and observation covariance matrix must be determined for each localisation region. However, these observation vectors and covariance matrices will be far smaller than the global vector and covariance matrix required for standard EnKFs, and a key advantage of localisation is that implementation of parallelisation is straightforward. A cartoon of this localisation of observations is provided in Figure 11.

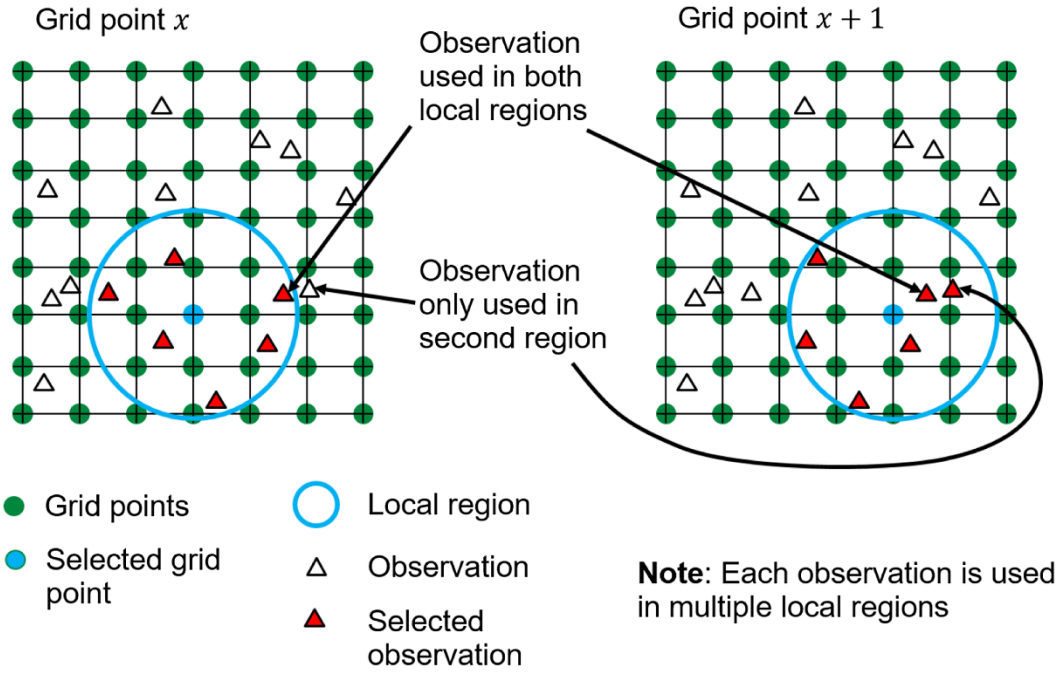

Figure 11. Example of data assimilation which only includes data sources from within a chosen range from each grid point (Elvidge & Angling, 2019). The blue grid point in each plot is the grid point for which data assimilation is being carried out. The blue circle represents the boundary of the region in which observations are included for data assimilation (for one grid point). Triangles represent observation locations, with red triangles representing observations included in the data assimilation for the relevant grid point.

For the prediction step, AENeAS uses TIE-GCM to propagate conditions forward in time. Once the update step has been completed, TIE-GCM input driver values are chosen randomly from predetermined probability distributions. TIE-GCM is driven by the level of solar and geomagnetic activity, provided in the form of indices F10.7 (solar flux) and Kp (indicator of geomagnetic activity). The Kp value is used to determine the cross-tail electric potential (CTP) and the hemispheric power (HP; an indicator of auroral activity given by the total power in the auroral zones which has been transferred from the kinetic energy of charged magnetospheric or solar wind particles) TIE-GCM input values, using

$$HP = \begin{cases} 16.82e^{(0.32\,Kp)} - 4.86\,, & (Kp \leq 7) \\ 153.13 + \dfrac{146.87}{2}(Kp - 7) & (Kp > 7) \end{cases} \tag{3.31}$$

$$CTP = 15 + 15Kp + 0.8Kp^2\,. \tag{3.32}$$

An important consideration for the LETKF is whether each new ensemble member contributes to the estimation of the true state. To achieve this the ensemble member conditions should span the range of possible states. Also, each new ensemble member should be orthogonal to the existing ensemble members, i.e. each new ensemble member cannot be made up of a linear combination of existing ensemble members. In an effort to make orthogonality of ensemble members and greater possible spread of ensemble member conditions more likely, AENeAS stochastically selects both the HP and the CTP values rather than calculating them from one randomly selected Kp value (Lee, 2013). The HP and CTP values are determined by considering historical Kp data to find the discrete conditional probability distribution of $P(Kp_{t=1}|Kp_{t=0})$. Let the current Kp value be i. By considering all historical cases when Kp = i, the proportion of cases for which the next Kp value was j is determined for all possible values

of j. A Kp value is randomly drawn from this discrete probability distribution and is used to calculate the HP for the next timestep. Another Kp value is randomly drawn to determine the CTP. The F10.7 for the next timestep is calculated in a similar manner, by determining the probability distribution of $P(F10.7_{t=1}|F10.7_{t=0})$. AENeAS lower boundary conditions are represented using output from the Global Scale Wave Model (Hagan et al., 1993).

4. INTRODUCTION TO OVER THE HORIZON RADAR

4.1. Theory

As discussed in Section 2, detrimental impacts to communications can occur when passing through the ionosphere; however, it is possible to capitalize on some ionospheric effects such as ionospheric reflection. Skywave Over the Horizon Radar (OTHR) is a method of target detection which, as the name suggests, is able to detect targets sufficiently distant that direct line-of-sight observations are not possible due to the curvature of the Earth (Headrick & Skolnik, 1974). A transmitted signal is directed into the ionosphere where, if the initial elevation and frequency are not too high, the signal can be reflected back down to the ground with a dwell illumination region (DIR; the area on the Earth's surface illuminated by the radar) which is "over the horizon" from the transmitter (Figure 12). Land terrain, sea waves, or potential targets of interest present in the DIR can scatter some of the transmitted signal back into the ionosphere,

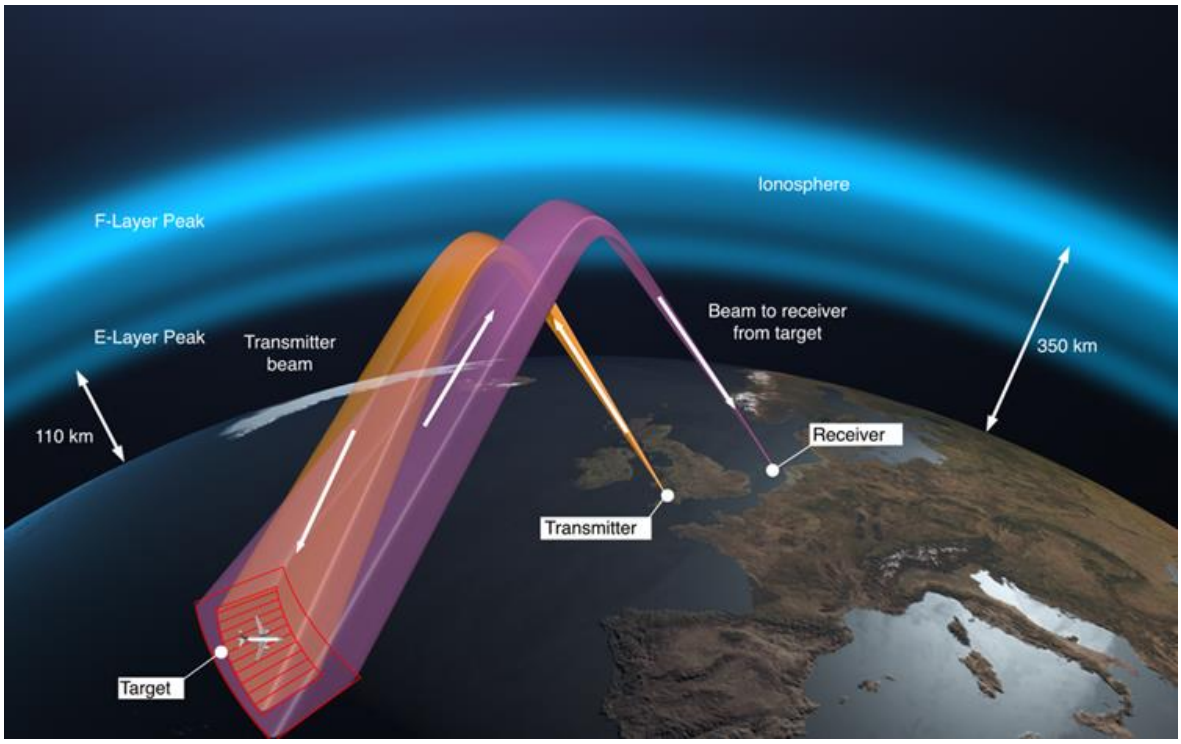

Figure 12. Cartoon of an over the horizon radar. Copyright University of Birmingham.

where it can be reflected back down to the ground in a region which includes the location of the OTHR receiver. Unwanted signals received by a radar are referred to as “clutter”. Therefore, scattered signal from terrain or sea waves may be referred to as “ground clutter” or “sea clutter”, which consists of the integrated signal scattered from all terrain or waves in the DIR to the receiver. A necessary aspect of OTHR is, therefore, the ability to distinguish a target of interest from the clutter. This can be achieved if the signal from the target has been Doppler shifted (Skolnik, 1990). If, for example, a target is travelling over land toward or away from the transmitter and receiver, the signal which is scattered by the target will be Doppler shifted. The terrain surrounding the target is stationary so produces clutter which is centred on a Doppler shift of zero. There is some spread of the land clutter line into non-zero Doppler shifts, for example due to ionospheric motion along the ray paths. If the Doppler shift of the target is sufficient to fall outside of the clutter line, the target will be far easier to detect as the signal strength only needs to be greater than the noise, rather than noise plus clutter. It is possible to detect targets in a clutter dominated environment, however the clutter strength is dependent on the type of terrain (e.g. mountainous regions or cities will generally produce stronger clutter strength than smoother terrain for a backscattered signal; e.g. Fabrizio, 2013). Clutter lines from DIRs over water exhibit different behaviour. If the water is still then backscattered clutter strength will be very low as most of the signal will be forward-scattered (e.g. Fabrizio, 2013). If, however, the water is not still, two clutter lines (or Bragg lines) may be produced (Barrick, 1971; Crombie, 1955) which are approximately equidistant from zero Doppler shift (unless the radial speeds of water surface currents are high). An example of sea clutter returns is provided in Figure 13, showing a pair of Bragg lines roughly equidistant from zero Doppler shift.

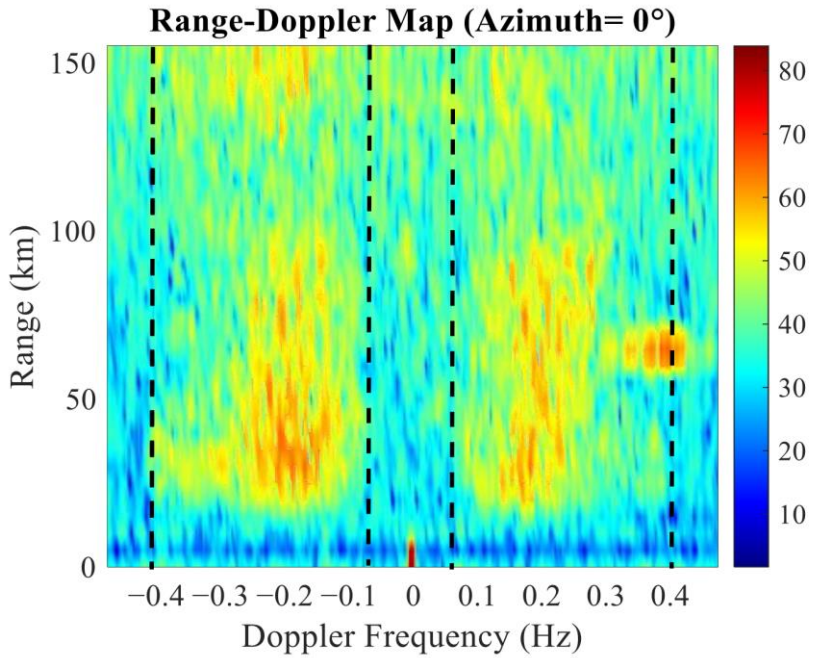

Figure 13. Sea clutter returns from a high frequency surface wave radar. Two clutter lines (Bragg lines) with Doppler spread are formed, which are shown within the vertical dashed lines (Guo et al., 2021).

The ray path peak altitude is dependent not only on electron density (Section 2.4), but also the elevation angle and frequency of the transmitted signal, as discussed by (for example) Fabrizio (2013). Generally, the higher the initial elevation and frequency, the greater the electron density required to refract the signal sufficiently to return it to the ground, as demonstrated in Figure 14 for a fixed frequency. Therefore, if the electron density along the ray path is not sufficiently high the ray will pass through the ionosphere. Also, if using a fixed frequency and sweeping through elevations, ray paths will have peaks at different altitudes for the same frequency (Figure 14). Ray paths with low and high initial elevations may reach the ground at the same location, but propagation paths with peaks at lower altitudes will generally have shorter group path range. The group path range (GP) is given by:

$$GP = c \cdot T_g \,, \tag{4.1}$$

where c is the speed of light and T_g is the time taken for the signal to reach a location from the transmitter, so GP is an indicator of the distance travelled along the ray path. Although lower propagation paths will generally result in lower GP when the transmission reaches the target or receiver, the propagation path losses can be greater for lower propagation paths, particularly if the transmission refraction is such that the ray path spends more time in the D and E region. This is due to higher neutral densities in these regions (compared to the F region), which will produce higher rates of signal absorption (Zawdie et al., 2017). Multiple propagation paths can also be generated by interactions with the Earth's magnetic field (creating ordinary and extraordinary ray paths). However, in this discussion the magnetic field will not be considered.

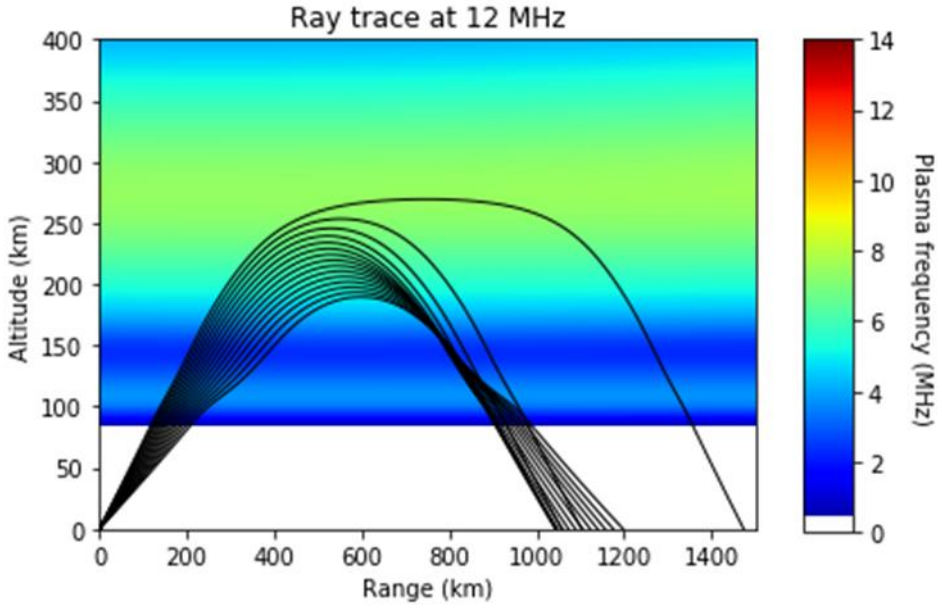

Figure 14. Example of ray tracing through a modelled ionosphere.

4.1.1. Monostatic Configuration

In a monostatic OTHR configuration the transmitter and receiver are co-located. A pulsed waveform can be used to ensure that there is no direct transmitter-to-receiver signal, however, use of a continuous waveform permits higher radar sensitivity (Fabrizio, 2019). A distance of around 100 km between the transmitter and receiver is generally sufficient to permit use of a continuous waveform without a direct transmitter-to-receiver signal (Basler, 1997). As this transmitter-receiver distance is much smaller than the distances to locations being observed by the radar, this configuration is referred to as pseudo-monostatic or quasi-monostatic. For ease, in this subsection we will assume a monostatic configuration in which the transmitter and receiver are co-located.

In a monostatic configuration, for a direct line-of-sight radar, the Doppler shift or Doppler frequency (f_D) of the signal scattered from a target is given by (Barlow, 1949) :

$$f_D = \frac{2v_R}{\lambda}\left(1 + \frac{v_R}{c} + \frac{v_R^2}{c^2} + \frac{v_R^3}{c^3} + \cdots\right), \tag{4.2}$$

where v_R is the radial speed of the target with respect to the transmitter/receiver location and look angle, λ is the wavelength of the transmitted signal and c is the speed of light in a vacuum. The Doppler shift occurs on the transmitter-target and target-receiver ray paths, thereby producing the factor of two. For skywave propagation, there are also Doppler frequency contributions from temporal changes to ionospheric conditions along the ray path (e.g. due to ionospheric motion). The Doppler shift (δf) experienced by radio waves propagating through a slowly varying ionosphere in which collisions are neglected is given by (Davies et al., 1962):

$$\delta f = -\frac{f}{c}\frac{dP}{dt}, \tag{4.3}$$

where f is the frequency, c is the speed of light in a vacuum and $\frac{dP}{dt}$ is the rate of change of the phase path with time. The dependence of the Doppler frequency on the target radial speed can be problematic for target detection. For example, if a target is moving with direction perpendicular to the transmitter-target direction, the target's radial speed is zero. Therefore, the Doppler frequency is (assuming a constant ionosphere) also zero and, on land, the target will be within the single land clutter line, which is centred on a Doppler shift of zero.

In a monostatic configuration the transmitter-target and target-receiver ray paths will be very similar unless there are sudden changes in ionospheric conditions along the ray paths. As such, the number of viable propagation paths, n_p, will produce at least n_p distinct sets of landing points (when no landing point regions overlap, i.e. the propagation path is the same for both the transmitter-target and target-receiver legs), and up to ${n_p}^2$ distinct sets of ray path landing points corresponding to each possible combination of n_p outward ray paths and n_p return ray paths (if all landing point regions overlap for at least one location). When some of these sets of landing points overlap, multiple propagation paths provide coverage for a particular region. For example, if two propagation modes are possible in a region, four sets of landing points can be produced. One set corresponds to ray paths with the lower propagation mode on both the transmitter-target and target-receiver ray paths. One set will correspond to ray paths with the higher propagation mode for both the transmitter-target and target-receiver ray paths. The remaining two sets will correspond to the lower propagation mode on one leg and the higher on

the other. As such, the group paths in these two sets (with a monostatic configuration) will be very similar to each other, and will fall between the other two sets of group paths. The integrated propagation path losses will be dependent on the magnitude of the group path. However, ray paths with extended regions within the D and E region will have higher losses due to absorption resulting from higher neutral densities (and, therefore, higher ion-neutral collision frequencies) within these regions. Therefore, the propagation mode with the lowest group path is not always the propagation mode with the lowest propagation path losses.

4.1.2. Bistatic Configuration

When the transmitter and receiver are not co-located the scenario becomes a little more complicated. The maximum possible number of propagation mode combinations (n_m) is now given by

$$n_m = n_{Tp} \cdot n_{Rp} \,, \tag{4.4}$$

where n_{Tp} and n_{Rp} are the number of viable propagation modes for the transmitter-target and target-receiver ray paths respectively. The minimum number of viable propagation mode combinations is zero, as it is possible for the sets of transmitter-target landing point ground ranges and receiver-target landing point ground ranges to include no overlapping regions for transmitter-target and receiver-target illumination regions (assuming that the set of all target-receiver and all receiver-target ray paths for a particular target location can be considered to be identical but in the opposite direction). In regions for which multiple propagation paths are possible for both the transmitter-target and target-receiver legs, the range of landing point

ground ranges resulting from the combination of, for example, an E region transmitter-target propagation mode and F1 region target-receiver propagation mode is likely to be distinct from the combination of a F1 region transmitter-target propagation mode and E region target-receiver propagation mode (whereas in the monostatic configuration these would be very similar). This is due to target-receiver ground ranges which may be different from the transmitter-target ground ranges, and differing ionospheric conditions along the transmitter-target and target-receiver ray paths. An example of group paths from different bistatic combinations of propagation modes is shown in Figure 15, with two viable propagation modes for one leg and

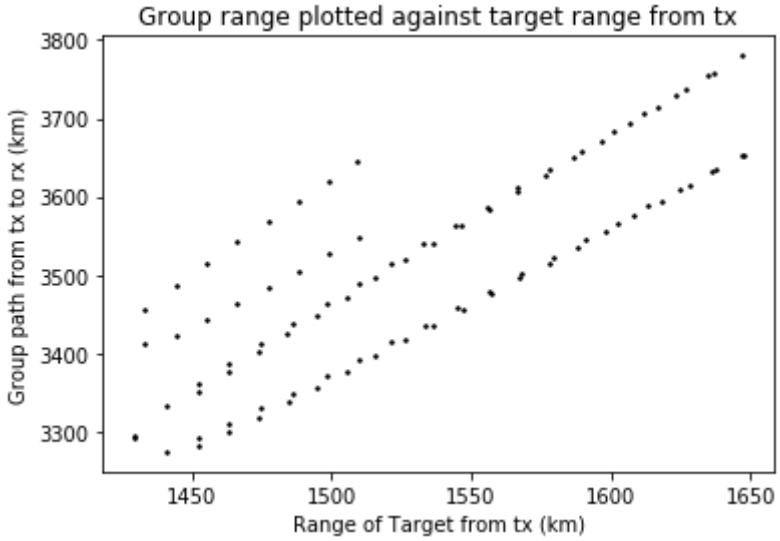

Figure 15. Example of multiple propagation modes in a modelled bistatic OTHR configuration. One leg has two propagation modes which are viable over the full range of ground ranges from the transmitter (tx) shown. The other leg has three viable propagation modes. Two of these produce ray paths with very similar transmitter-target-receiver (rx) group paths and are viable over the full range of ground ranges shown. The third propagation mode is only viable for ground ranges between about 1430 and 1520 km, so for ground ranges of 1430-1520 km there are six viable propagation mode combinations whereas ground ranges of 1520-1650 km have four viable propagation mode combinations.

three viable propagation modes for the other. As for the monostatic configuration, propagation path losses at each target location will be dependent on both the total group path and the distance along the ray path which is within lower altitudes with higher neutral densities.

4.1.3. Using Skip Zones to Avoid Direct Transmitter-Receiver Skywave Paths

One issue when using a bistatic configuration is the potential presence of direct transmitter-receiver skywave paths, i.e. a transmitted signal which is reflected by the ionosphere directly to the receiver location. The signal from these direct skywave paths will generally be much stronger than the signal from transmitter-target-receiver ray paths as the total group path will be smaller and the strength of the signal will not be diminished by the signal scattering at the target. As such, the OTHR would need to be sufficiently sensitive to distinguish the weak signal which has been scattered by the target from the stronger direct skywave signal. A way to avoid this issue is the use of skip zones. Skip zones are transmission frequency dependent regions surrounding the transmitter for which, for sufficiently high transmission frequencies, the transmission cannot be received by direct skywave propagation (e.g., Landeau et al., 1997).

To explain the existence of skip zones, we must first consider the critical frequency. For a vertical column extending through the ionosphere, the (vertical) critical frequency is the maximum plasma frequency within the column. The critical frequency provides an approximation of the maximum vertically transmitted frequency which would be reflected by the ionosphere back to the ground. Generally, if the transmission frequency is above the critical frequency a signal directed vertically upward will pass through the ionosphere and will not be reflected back to the ground. However, it may be possible for a signal with the same

transmission frequency to be refracted back to the ground if an initial elevation below 90° is chosen. Using the secant law, the critical frequency (f_c) when non-vertical initial elevations are used is given by

$$f_c = f_v \sec\theta \,, \tag{4.5}$$

where f_v is the vertical critical frequency and θ is the angle between the ray path and the vertical below the ionosphere (e.g., Fabrizio, 2013). This is an extremely simplified case in which collisions, the Earth's magnetic field and the curvature of the Earth are ignored. However, it is clear that when using the same frequency, lower initial elevations can result in the transmission being refracted back to Earth whereas higher elevations would result in the transmission passing through the ionosphere. As a result, when using a frequency which is above the vertical critical frequency, a "skip zone" around the transmitter location can be created. In the skip zone the transmitted signal cannot be refracted back down to the ground as the higher elevations which would allow the ray path to land at this location result in the ray path passing through the ionosphere. The skip zone is, therefore, a region containing the transmitter in which the transmitted signal cannot be detected via a skywave path. Higher transmission frequencies will generally produce larger skip zones, as the maximum useable initial elevation will be lower when using higher frequencies.

Skip zones can be used to avoid direct transmitter-receiver skywave paths. For chosen transmitter and receiver locations, if a sufficiently high transmission frequency is used the receiver location will lie within the transmitter skip zone (Figure 16). The minimum frequency for which the receiver lies within the transmitter skip zone can be referred to as the skip

frequency. By only using transmission frequencies above the skip frequency the presence of a direct transmitter-receiver skywave path can be avoided. However, the skip frequency is dependent on ionospheric conditions and will, therefore, be dependent on factors such as solar activity, season, and time of day.

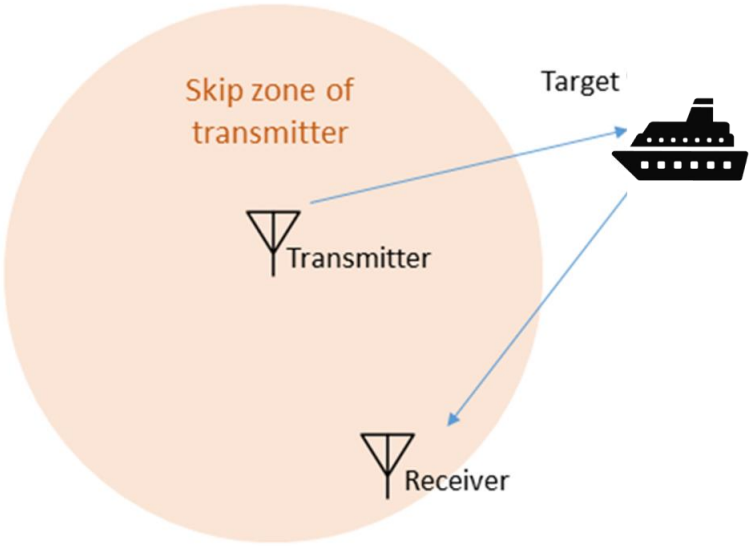

Figure 16. The skip zone of a transmitter.

4.1.4. Minimum Detectable Radar Cross Sections

As with line-of-sight radars, the radar cross section (RCS) of a target is a contributing factor to the success or failure of target detection. The RCS is dependent on the size, orientation, and construction material of the target, and is also dependent on the transmission frequency. For example, for OTHR frequencies, a large ship may have RCS between 25 and 50 dB m^2 depending on the orientation of the ship with respect to the direction of the transmitted beam. To determine the effectiveness of an OTHR system in a particular location and set of

ionospheric conditions, the minimum detectable radar cross section (MDRCS) can be determined. The MDRCS represents the smallest RCS which is able to be detected when using a selected frequency, i.e. the smallest RCS such that the received signal will exceed the noise. To determine the MDRCS we must first consider the over-the-horizon form of the radar equation (Skolnik, 1990) for signal to noise ratio (SNR), where

$$SNR = \frac{P_T \times G_T \times G_R \times CIT \times \lambda^2 \times \sigma \times F_p}{N \times L \times (4\pi)^3 \times R^4}, \tag{4.6}$$

where P_T is the transmitted power (W), G_T and G_R are the transmitter and receiver antenna gain respectively, CIT is the coherent integration time (s; the radar dwell time allowed for Doppler processing), λ is the transmission wavelength (m), σ is the target radar cross section (m^2), N is the noise power per Hz (W s), L is the combined transmission path and systems losses, and R is the distance along the transmitter-target-receiver path (assuming a monostatic configuration). F_p is the propagation factor, resulting from several phenomena including multipath effects and focussing or defocussing of rays, which in favourable conditions can increase the SNR by 3-6 dB (Fabrizio, 2013). It should be noted that the OTHR equation represents the SNR when clutter is not present. By rearranging the OTHR equation, we can determine the minimum radar cross section (σ_{min}) required to ensure that the signal is at least equal to the noise ($SNR = 1$), such that

$$\sigma_{min} = \frac{N \times L \times (4\pi)^3 \times R^4}{P_T \times G_T \times G_R \times CIT \times \lambda^2 \times F_p}. \tag{4.7}$$

The free space path loss, $\left(\frac{4\pi R}{\lambda}\right)^2$, for the transmitter-target ray path, the free space path loss for the target-receiver ray path, propagation path losses due to ionospheric absorption (from L), and propagation factor effects can be combined into a single variable, $TgLoss$, which represents the integrated total losses along the transmitter-target-receiver path. Therefore, σ_{min} can also be described by

$$\sigma_{min} = \frac{\lambda^2 \times TgLoss \times N \times L_S}{4\pi \times CIT \times G_T \times G_R \times P_T}, \tag{4.8}$$

where L_S is the system losses. It can be seen that the size of RCSs which are able to be detected by an OTHR system are dependent on the ray path propagation losses (and, therefore, the ionospheric conditions) and noise, including system losses. However, by increasing the coherent integration time, transmitter or receiver gain, or transmitted power, smaller targets are able to be detected.

4.2. Operational OTHR Systems

Skywave OTHR systems are known to have been developed in several countries including the US (Thomason, 2003), Australia (Wise, 2004), and France (Bazin et al., 2006). For example, the Jindalee Operational Radar Network (JORN) is a network of three OTHRs in Australia which are used for surveillance, primarily of the region to the north of Australia (Holdsworth et al., 2022). As described by Fabrizio (2013), skywave OTHR systems may use initial transmission elevations from about 5 to 45 degrees. This elevation range, along with the azimuthal beamwidth, determines the size of the DIR. A typical DIR can have ground range

depth of 500 to 1000 km and cross range of 200 to 500 km. However, as described by (for example) Fabrizio (2013), the DIR can be separated into grid cells to permit finer resolution when detecting targets. Grid cells have cross range length (Δx) given by:

$$\Delta x = r\Delta\theta\,, \tag{4.9}$$

where r is the ground range from the transmitter to the grid cell border (to calculate the DIR arc length at this ground range) and $\Delta\theta$ is the azimuthal cell size resolution, given by:

$$\Delta\theta = \frac{\lambda}{L}\,, \tag{4.10}$$

where λ is the transmission wavelength and L is the length of the receiver. The grid cell ground range depth size (Δy) is given by:

$$\Delta y = \frac{c}{2B}\,, \tag{4.11}$$

where c is the speed of light and B is the transmission bandwidth. Therefore, the cross range resolution is dependent on the size of the receiver whereas the ground range resolution is only dependent on the transmission bandwidth. A difficult issue to overcome with operational OTHR systems is that of coordinate registration, i.e. determining the location of the ray path landing point (for terrain and targets on the ground). One way to overcome this issue when using a monostatic configuration is to take advantage of identifiable geographical features in the area of interest (Washburn, 1971) such as coastlines (Anderson, 1995). As previously discussed,

land clutter consists of a single clutter line whereas sea clutter has two distinct clutter lines. Therefore, the transition from one to two clutter lines (or vice versa) can be used to determine the geographical coordinates of the radar signal if the direction of transmission is known. Alternatively, if current ionospheric conditions are known, estimations can be made of ray path landing point locations and, therefore, target locations. One method used to estimate ionospheric conditions along the ray path is to use instrumentation such as an ionosonde to determine conditions at one (or more) location. Ideally, if using one vertical sounder, this would be located roughly halfway between the transmitter and the area of interest for illumination to enable estimation of plasma frequencies at the desired ray path peak location, thereby providing an estimate of elevations and transmission frequencies which will illuminate the desired location. If ionospheric conditions are similar along the ray path then an ionosonde location away from the peak is not necessarily problematic. Oblique sounders may also be used to determine ionospheric conditions at particular locations along the ray path. This approach may, however, be less successful when ionospheric conditions are more variable along the ray path, such as at high latitudes, when part of the ray path is within low-latitude regions impacted by the equatorial fountain effect, or when the ray path crosses or is close to the day-night terminator. Alternatively, an ionospheric model can be used to estimate ionospheric conditions along the ray path, particularly in locations where observations are not available. With a representation of ionospheric plasma frequencies or electron densities, ray paths can be traced through the modelled or observed ionospheric conditions to determine estimations of where the landing points of the ray paths will be when using the operational system. Other useful information such as propagation path losses can also be estimated. The accuracy of ray tracing will increase as the accuracy of the ionospheric specification increases; therefore, the use of an

accurate ionospheric model, such as a high-quality data assimilation ionospheric model (e.g. AENeAS; section 3.6), would be beneficial to increase the accuracy of ionospheric ray tracing.

4.3. Ray Tracing

4.3.1. Virtual Path Ray Tracing

Work on predicting ray paths through the ionosphere, or ray tracing, has been ongoing for about a century. The Breit-Tuve theorem (Breit & Tuve, 1926) shows that the group path of a ray which is reflected by the ionosphere (Figure 17: path ABC) is equal to the group path of an imaginary straight reflected path in a vacuum with the same initial elevation from the transmitter and which is reflected at the virtual height (Figure 17: path ADC), known as the virtual path. Martyn's theorem (Martyn, 1935) shows that the group path of an oblique ray path (P') can be well approximated using the group path of a vertical ray which is reflected by the same ionospheric layer (P'_V), such that

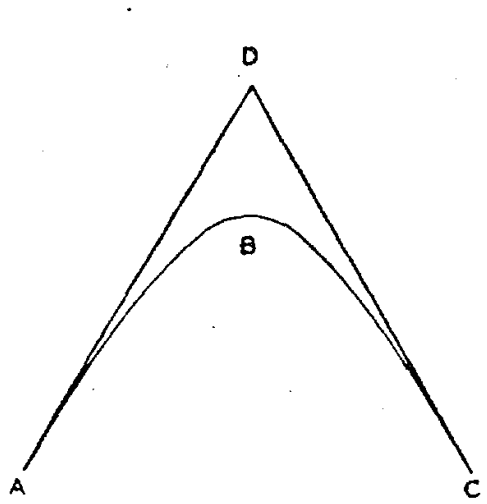

Figure 17. Ray path and virtual ray path with identical group paths (Breit & Tuve, 1926).

$$P' = \frac{1}{\cos i_o} P'_V \,, \tag{4.12}$$

where i_o is the oblique ray path angle of incidence with the ionosphere (i.e. $i_o + \beta_0 = \frac{\pi}{2}$ when the curvature of the Earth is ignored, where β_0 is the initial transmission elevation). However, if using the same frequency the peak height and virtual height of a vertical ray path will be lower than for an oblique ray path. The secant law provides a good approximation of the frequency required to obtain a vertical ray path (f_v) which has peak height and virtual height equal to the oblique ray path peak height and virtual height, given by

$$f_v = \frac{f_o}{\sec i_o} \,, \tag{4.13}$$

where f_o is the frequency used for the oblique ray path (this method can be used for both ordinary (*o*-mode) and extraordinary (*x*-mode) ray paths). Therefore, under the assumption that ionospheric densities are horizontally layered (so electron density profiles are identical along the ray path) and ignoring the curvature of the Earth, the group path is given by

$$P' = \frac{2h_v}{\cos i_o} \,, \tag{4.14}$$

where h_v is the virtual height of the vertical ray path when using frequency f_v. The distance (D) between the transmitter and the landing point is, therefore,

$$D = \frac{2h_v}{\tan \beta_0}. \tag{4.15}$$

In this way, the use of a vertical ionosonde can provide an estimation of the location of the ray path landing point. However, over longer distances ignoring the curvature of the Earth will result in larger errors for this estimation.

In Figure 18, although not to scale, the geometrical problem of including the Earth's curvature is shown. The transmission is sent from point A, has peak virtual height at C and returns to the ground at D. We see from Figure 18 that

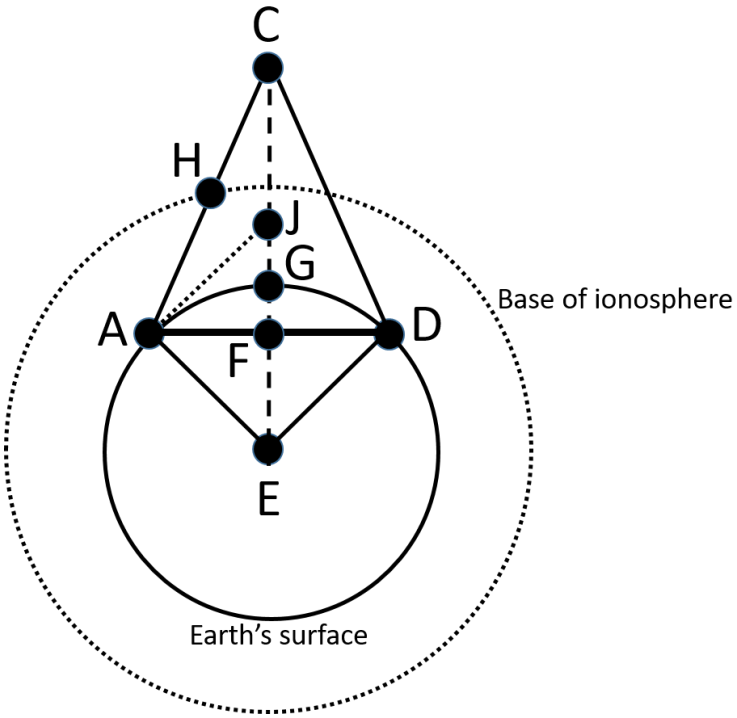

Figure 18. Cartoon of the geometrical problem of calculating transmitter-target ground ranges when the curvature of the Earth is incorporated (not to scale).

$$\tan i_O = \frac{a}{2(z_v + h)}, \tag{4.16}$$

where i_O is the oblique angle at the virtual peak (angle $A\hat{C}F$), a is the chord length AD (i.e. $\frac{1}{2}a$ is the length AF), z_v is the virtual height (CG), and h is the smallest distance from the centre of the chord to the circumference (FG). We can write $h = r - b$, where r is the radius of the Earth (i.e. EG) and b is the distance from the centre of the Earth (E) to the mid-point of the chord (F). b can be defined as

$$b = r\cos\theta\,, \tag{4.17}$$

where θ is the angle $A\hat{E}F$, and $\frac{1}{2}a$ can be defined as

$$\frac{1}{2}a = r\sin\theta\,. \tag{4.18}$$

Therefore,

$$h = r - r\cos\theta = r(1 - \cos\theta)\,, \tag{4.19}$$

so

$$\tan i_O = \frac{r\sin\theta}{z_v + r(1 - \cos\theta)}, \tag{4.20}$$

as provided by Smith (1937).

The ground range between A and D is simply the length of the arc between these two points which are both on the circumference of a circle (the Earth's surface, assumed to be spherical). The ground range (D_G) is, therefore, given by

$$D_G = r \cdot 2\theta \,, \tag{4.21}$$

as θ is the angle $A\hat{E}F$ (in radians) which is half the angle $A\hat{E}D$. Therefore,

$$\theta = \frac{D_G}{2r} \,, \tag{4.22}$$

or, with the ground range in km and the oblique angle in degrees,

$$\theta = \frac{180\ D_G}{2\pi r} \approx \frac{D_G}{222.4} \,. \tag{4.23}$$

This was also provided by Smith (1937), but was incorrectly reported as $\frac{222.4}{D_G}$.

Alternatively, the geometry of Figure 18 can be used to provide the ground range as a function of initial elevation and peak virtual height. The line of sight along the ground from the transmitter is shown as line AJ. Therefore, the initial elevation angle from the transmitter, β_0, is the angle $C\hat{A}J$. By considering the triangle with vertices at A, C, and E, and using the sine rule,

$$\frac{r + z_v}{\sin\left(\beta_0 + \frac{\pi}{2}\right)} = \frac{r}{\sin\left(\pi - \theta - \left[\beta_0 + \frac{\pi}{2}\right]\right)}, \tag{4.24}$$

as angle $C\hat{A}E$ is $\beta_0 + \frac{\pi}{2}$ and, therefore, angle $A\hat{C}E$ is $\pi - \theta - \left[\beta_0 + \frac{\pi}{2}\right]$, as angle $A\hat{E}C$ = angle $A\hat{E}F = \theta$. Therefore,

$$\theta = \frac{\pi}{2} - \beta_0 - \arcsin\left(\frac{r\sin\left(\beta_0 + \frac{\pi}{2}\right)}{r + z_v}\right), \tag{4.25}$$

and, from equation 4.20, the ground range (D_G) is given by

$$D_G = 2r\left(\frac{\pi}{2} - \beta_0 - \arcsin\left(\frac{r\sin\left(\beta_0 + \frac{\pi}{2}\right)}{r + z_v}\right)\right). \tag{4.26}$$

Rather than calculating the distance directly in this way, the group path can also be used to estimate the ground range between the transmitter and a target as, using the Breit-Tuve theorem, the "time of flight" of the ray path from transmitter to target to receiver can be used to determine the group path with the assumption that the ray is travelling at the speed of light in a vacuum. If ionospheric conditions at the locations of the ray path peaks are known this can provide an estimate of the target location. The methods described do, however, require knowledge of the oblique angle of the ray at the base of the ionosphere. As shown in Figure 18, the oblique angle at the virtual peak ($A\hat{C}F$) is not the same as the oblique angle at the base of the ionosphere (point H) when the Earth's curvature is considered, as the ionosphere is not parallel with the

chord AD. Therefore, a correction factor is required when using the secant law to determine the appropriate frequency for a vertical sounder to use for estimating the oblique virtual peak (Smith, 1939).

4.3.2. Analytical Ray Tracing

An alternative method, which provides greater accuracy, is analytical ray tracing, in which equations can be used to describe the electron density profile along the ray path (De Voogt, 1953). Equations are then used to describe properties of the ray path as it progresses within the ionosphere. Therefore, the closer the model ionosphere is to current ionospheric conditions, the greater the accuracy of the analytical ray tracing. A key advantage of ray tracing compared to the methods discussed so far is that estimations of propagation path losses may be significantly more accurate as the ray path through the model ionosphere is more accurate than using the virtual path (assuming that the ionospheric model is a reasonable representation of true conditions). This is particularly important in the D and E region as the propagation path losses can be high in these regions (Section 2.4; Zawdie et al., 2017) due to the presence of higher neutral densities.

If the refractive index can be described as a function, it may be possible to use Snell's law to analytically determine the path the ray takes as it passes through the model ionosphere. Consider a very small increment of the ray path within the ionosphere, such that the ray path can be considered to be straight along the increment. Let the increase (on the upward leg) in altitude along this increment be ∂r and let i represent the angle between the ray and the normal to the ionosphere at the end of the increment. As discussed, if the spherical nature of the

ionosphere is ignored then the virtual path from the ground to the peak is such that (Smith, 1937)

$$\tan i_O = \frac{r \sin\theta}{z_v + r(1 - \cos\theta)}. \tag{4.27}$$

However, using the same method for the small increment, we have

$$\tan i = \frac{r_h \sin\partial\theta}{\partial r + r_h(1 - \cos\partial\theta)}, \tag{4.28}$$

where $\partial\theta$ is the angle at the Earth's centre between the start and end of the increment, and r_h is the distance from the Earth's centre to the start of the increment. As the increment is small, $\partial\theta$ is very small. As $\partial\theta \to 0$, $\sin\partial\theta \to \theta$ and $\cos\partial\theta \to 1$. Therefore, using the small-angle approximations:

$$\tan i \approx \frac{r_h \partial\theta}{\partial r}, \tag{4.29}$$

when the increment is small. Using this approach, but with angle β such that β is the angle between the ray path and the tangent to the ionospheric layer at the start of the increment, Croft and Hoogansian (1968) described a method to provide exact values (for the modelled ionosphere) for the ray position, group path, and phase path along the ray path. The increment is now described using

$$\tan\beta = \frac{\partial r}{r_h \partial\theta}. \tag{4.30}$$

Using Bouger's rule, in a spherically symmetric ionosphere (and ignoring collisions and the Earth's magnetic field), $r_h \mu \cos\beta$ is constant along the ray path, where μ is the refractive index. Therefore,

$$r_h \mu \cos\beta = r_0 \mu_0 \cos\beta_0 , \tag{4.31}$$

where r_0 is the Earth's radius, μ_0 is the refractive index at the ground, and β_0 is the initial elevation angle. The refractive index in free space is one. Therefore,

$$\cos\beta = \frac{r_0 \cos\beta_0}{r_h \mu}, \tag{4.32}$$

and

$$\sin\beta = \sqrt{1 - \left(\frac{r_0 \cos\beta_0}{r_h \mu}\right)^2}. \tag{4.33}$$

Therefore, the ground range for the ray path increment (∂D_G) is given by

$$\partial D_G = r_0 \partial\theta , \tag{4.34}$$

$$= r_0 \frac{\partial r \cos\beta}{r_h \sin\beta} ,$$

$$= \frac{r_0 \partial r}{r_h} \cdot \frac{r_0 \cos\beta_0}{r_h \mu \sqrt{1 - \left(\frac{r_0 \cos\beta_0}{r_h \mu}\right)^2}} ,$$

$$= \frac{{r_0}^2 \cos\beta_0}{r_h \sqrt{{r_h}^2 \mu^2 - {r_0}^2 \cos^2\beta_0}} \, \partial r ,$$

and the ground range for the total ray path from the transmitter to the landing point (D_G) is given by

$$D_G = 2 \int_{r_0}^{r_t} \frac{{r_0}^2 \cos\beta_0}{r \sqrt{r^2 \mu^2 - {r_0}^2 \cos^2\beta_0}} \, dr , \qquad (4.35)$$

where r_t is the distance from the Earth's centre to the ray path peak. The group path and phase path can be obtained using similar approaches. Appleton and Beynon (1940) defined the square of the refractive index as

$$\mu^2 = 1 - \frac{2 f_c^2 y}{f^2 y_m} + \frac{f_c^2 y^2}{f^2 y_m^2} , \qquad (4.36)$$

where f_c is the critical frequency of the ionospheric layer, f is the operating frequency, y_m is the layer semi-thickness, and y is the height above the base of the layer. Substitution into equation 4.34, and incorporating a simplification (as the distance from the ground to the base of the ionospheric layer is very small compared to the Earth's radius) provides an analytic

approximation of ray path characteristics. The refractive index is related to the electron density such that

$$\mu^2 = \frac{N_e}{F^2 N_m}, \tag{4.37}$$

where N_m is the peak electron density within the ionospheric layer, and $F = \frac{f}{f_c}$. Therefore, the parabolic function used by Appleton and Beynon to describe the electron density within the layer is

$$N_e = N_m \left(\frac{2}{y_m} y - \frac{1}{y_m^2} y^2 \right), \tag{4.38}$$

or equivalently, using the notation of Croft and Hoogansian (1968),

$$N_e = N_m \left[1 - \left(\frac{r - r_m}{y_m} \right)^2 \right], \tag{4.39}$$

where r is the radial distance from the Earth's centre, and r_m is the radial distance from the Earth's centre to the peak electron density within the layer. However, a key development from Croft and Hoogansian (1968) was to choose a quasi-parabolic function to describe the electron density within an ionospheric layer such that an exact analytic solution could be found for the ground range, group path, and phase path. Describing the electron density with

$$N_e = N_m \left[1 - \left(\frac{r - r_m}{y_m}\right)^2 \left(\frac{r_b}{r}\right)^2\right], \tag{4.40}$$

where r_b is the radial distance from the Earth's centre to the base of the layer, results in μ^2 defined as

$$\mu^2 = 1 - \frac{1}{F^2} + \left(\frac{r_m - r}{F\ y_m}\right)^2 \left(\frac{r_b}{r}\right)^2 \tag{4.41}$$

within the ionospheric layer. Allowing $\mu^2 = 1$ below the base of the ionosphere provides a sum of two integrals for ground range, group path and phase path which can be solved analytically, such as the solution

$$D_G = 2r_0 \left\{(\gamma - \beta_0) - \frac{r_0 \cos\beta_0}{2\sqrt{C}} \ln \frac{B^2 - 4AC}{4C\left(\sin\gamma + \frac{1}{r_b}\sqrt{C} + \frac{1}{2\sqrt{C}}B\right)^2}\right\} \tag{4.42}$$

provided by Croft and Hoogansian (1968), where

$$A = 1 - \frac{1}{F^2} + \left(\frac{r_b}{F\ y_m}\right)^2, \tag{4.43}$$

$$B = -\frac{2r_m r_b^2}{F^2 y_m^2}, \tag{4.44}$$

$$C = \left(\frac{r_b r_m}{F\ y_m}\right)^2 - r_0^2 \cos^2\beta_0, \tag{4.45}$$

and γ is the angle between the ray and the base of the ionosphere, such that

$$\cos\gamma = \frac{r_0}{r_b}\cos\beta_0\ , \tag{4.46}$$

which can be determined using the sine rule for the triangle with vertices at the Earth's centre, the transmitter location, and the point at which the ray path meets the base of the ionosphere, i.e.

$$\frac{\sin\left(\frac{\pi}{2}-\gamma\right)}{r_0} = \frac{\sin\left(\beta_0+\frac{\pi}{2}\right)}{r_b}. \tag{4.47}$$

This approach was developed further by Dyson and Bennett (1988) by representing the electron density profile using multiple quasi-parabolic segments (QPS). This permitted profiles which could more accurately represent ionospheric conditions but which were still able to solved analytically. To avoid erratic behaviour when the ray moves from one QPS to another, QPS electron density values and gradients at the end of a QPS would match the value and gradient at the end of the adjoining QPS (i.e. the profile and the first derivative of the profile are both continuous). This was developed further by Chen et al. (1992) to include a perturbation value which provided an approximation of the *x*-mode ray characteristics.

A fundamental issue with the approaches discussed so far is the dependency on a spherically symmetrical ionosphere. As previously discussed, in a real ionosphere the electron density profile may vary significantly along the ray path, which will result in horizontal electron density gradients (Elvidge, 2022). One method used to address this issue and introduce horizontal

plasma density gradients to the model ionosphere is to shift the centre of the spherically symmetric model ionosphere so it is no longer collocated with the Earth's centre. By shifting and tilting the Earth up to the base of the ionosphere, or shifting and tilting the ionosphere, horizontal and vertical gradients can be produced (e.g., Folkestad, 1968). As the model ionosphere is still spherically symmetrical, Bouger's rule holds so exact analytic solutions are possible. However, this approach will not necessarily provide vertical and horizontal gradients which are an accurate reflection of real current ionospheric conditions. An alternative approach to incorporate variability along the ray path is the Segment Method Analytical Ray Tracing (SMART) technique, which involved separating the ray path within the ionosphere into several distinct sections (Norman & Cannon, 1997). At the start of a section, a QPS model is fitted to a modelled or observed (or combination of both) electron density profile using the method described by Chen et al. (1990). This QPS is used to determine the ray path behaviour within the section. Within the section the ionosphere is assumed to be spherically symmetrical so analytic solutions within the section can be obtained. This method is applied at each section boundary, with the ray path behaviour at the end of a section used to determine the initial ray path elevation at the beginning of the next section. Therefore, if the QPS electron density profiles are assumed to be accurate, the model accuracy improves with an increasing number of sections. This 2-dimensional approach improved accuracy by considering horizontal gradients along the ray path. However, this was later extended to a pseudo 3-dimensional approach (Norman et al., 2012) which also took into account horizontal gradients transverse to the ray path, including the resulting azimuthal variation of the ray path.

An alternative method for ray tracing is referred to as numerical ray tracing. Analytic ray tracing can provide a relatively computationally cheap approach (compared to numerical ray tracing)

which provides an acceptable level of accuracy for many processes; however, numerical ray tracing can provide greater accuracy if required.

4.3.3. Numerical Ray Tracing

The Haselgrove equations (Haselgrove & Haselgrove, 1960; Haselgrove, 1957, 1963) provide the basis for a numerical calculation of ray paths through a model ionosphere, which also takes the Earth's magnetic field into account. The equations provided by Haselgrove (1963) are:

$$\frac{dx_i}{dt} = Ju_i - KYv_i \,, \tag{4.48}$$

$$\frac{du_i}{dt} = L\frac{\partial X}{\partial x_i} + \sum_j \left(Ku_j + MYv_j\right)\frac{\partial Y_j}{\partial x_i}, \tag{4.49}$$

with

$$J = 2\{2(1 - X - Y^2)p + Y(1 + (\mathbf{v}\cdot\mathbf{u})^2)\}\,, \tag{4.50}$$

$$K = -2X(\mathbf{u}\cdot\mathbf{v})(pY - 1)\,, \tag{4.51}$$

$$L = Y(1 - Y^2)p^2 - 2(1 - X - Y^2)p - Y\,, \tag{4.52}$$

$$M = 2Xp(Py - 1)\,, \tag{4.53}$$

where x_1, x_2, and x_3 are the Cartesian coordinates of a point on the ray path, $\mathbf{u} = (u_1, u_2, u_3)$ is a vector parallel to the wave path normal (i.e. the direction of propagation at point (x_1, x_2, x_3)), $\mathbf{Y} = (Y_1, Y_2, Y_3)$ is a vector parallel to the Earth's magnetic field, which has length $Y = \frac{F_H}{F}$, where F_H and F are the gyrofrequency and transmission frequency, $X = \frac{{F_c}^2}{F^2}$ where F_c

is the plasma frequency, and t is a dummy variable. The parameter p is derived from the Appleton-Hartree equation, such that

$$(1 - X - Y^2)p^2 + Y(1 + (\mathbf{v} \cdot \mathbf{u})^2)p - (\mathbf{v} \cdot \mathbf{u})^2 = 0\,. \qquad (4.54)$$

The positive and negative roots in the solution to the quadratic for p represent the ordinary and extraordinary rays respectively. The Haselgrove equations involve the application of Hamiltonian equations to propagation through a model ionosphere. However, Coleman (2008) showed that the Haselgrove equations could also be derived directly from Maxwell's equations.

A key advantage of numerical ray tracing is that the model ionosphere does not need to be represented by functions. Rather, the ionosphere can be represented by a grid of plasma frequency values obtained from an ionospheric model, observations, or combination of both. Therefore, the model ionosphere can provide a more accurate representation of true ionospheric conditions. As mentioned, a further advantage of this method is the inclusion of effects due to the Earth's magnetic field. Haselgrove's equations are still used in modern numerical ray tracing methods and toolboxes, such as the Provision of High-frequency Raytracing Laboratory for Propagation studies (PHaRLAP; e.g. Cervera & Harris, 2014). An example of PHaRLAP output using the 3D engine based on Haselgrove's equations with Cartesian coordinates is shown in Figure 19. Another 3D model developed by Jones and Stephenson (Jones & Stephenson, 1975) uses a time-varying adaptation of the Haselgrove equations with spherical polar coordinates. These models have been used as the basis for many studies, and several later models are based on the Jones and Stephenson model, e.g. the IONOspheric Ray Tracing (IONORT) model (Azzarone et al., 2012).

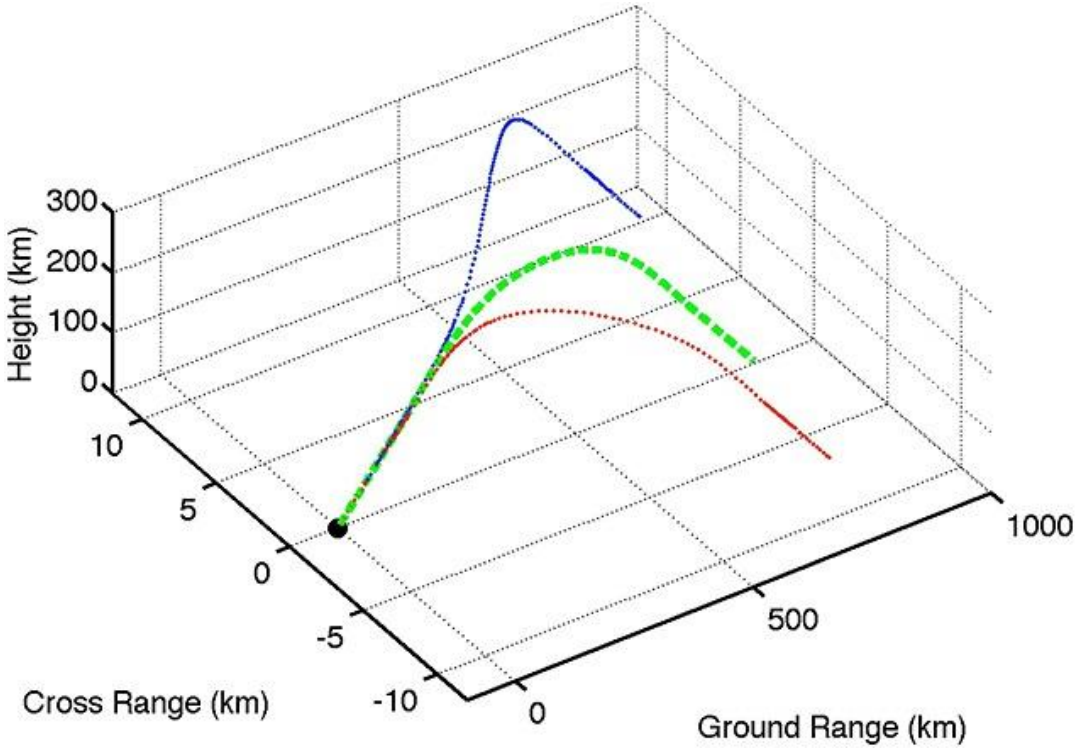

Figure 19. Example output of 3D ray tracing from PHaRLAP (Cervera & Harris, 2014). The green line represents the ray path when the Earth's magnetic field is ignored. The blue and red lines show the o-mode and x-mode ray paths respectively.

A significant disadvantage of 3D ray tracing with Haslegrove's equations is the computational expense. With the continuing improvement in computational speed, in recent decades the use of numerical ray tracing has become more viable. However, for an operational OTHR system some operations can require ray tracing for many rays in near-real time. The computational expense of 3D numerical ray tracing can, therefore, be prohibitive, which has been a driving factor in the continued development of analytical ray tracing techniques described in Section 4.3.2. For the same reason, there has also been a focus in recent decades in developing numerical ray tracing approaches which are less computationally intensive. Coleman (1998)

developed a 2D numerical ray tracing method which was much faster than 3D methods. The change in position of points along the ray path are described by

$$\frac{d(\delta Q)}{d\theta} = \frac{r}{\sqrt{\mu^2 - Q^2}}\left[\frac{\delta r}{2r}\left(\frac{\partial \mu^2}{\partial r} + \frac{\partial^2 \mu^2}{\partial r^2}\right) - \left(\frac{1}{2(\mu^2 - Q^2)}\frac{\partial \mu^2}{\partial r} - \frac{1}{r}\right)\left(\frac{\delta r}{2}\frac{\partial \mu^2}{\partial r} - Q\delta Q\right)\right], \tag{4.55}$$

$$\frac{d(\delta r)}{d\theta} = \frac{r}{\sqrt{\mu^2 - Q^2}}\left[\frac{\delta r Q}{r} + \delta Q - \frac{Q}{\mu^2 - Q^2}\left(\frac{\delta r}{2}\frac{\partial \mu^2}{\partial r} - Q\delta Q\right)\right], \tag{4.56}$$

where $Q = \mu \frac{dr}{d\theta}\left(\left(\frac{dr}{d\theta}\right)^2 + r^2\right)^{-1/2}$, r is the distance from the Earth's centre, θ is the angular coordinate along the great circle path, δQ and δr are the variations in Q and r, and μ is the refractive index. To account for the Earth's magnetic field a correction factor can be used. For example, when determining the group path for the ordinary and extraordinary modes the correction factor C_G, given by

$$C_G = \pm\left(\frac{f_H^L}{2f}\right)(P' - P)\,, \tag{4.57}$$

is added to the group path with no magnetic field, where f_H^L is the longitudinal gyrofrequency at the ray path midpoint, f is the operating frequency, P' is the group path, and P is the phase path. This approach was generally able to achieve levels of accuracy comparable with 3D numerical ray tracing; however, in more extreme examples (e.g. ray paths travelling through ionospheric disturbances) there is a notable reduction in accuracy. It should also be noted that, as this approach is two-dimensional, azimuthal variations between the ordinary mode and

extraordinary mode ray paths (as seen in Figure 19) and azimuthal variations due to transverse horizontal gradients in plasma density will not be captured. PHaRLAP provides users with the ability to produce ray paths using analytical ray tracing, 2D numerical ray tracing using the approach by Coleman (1998), and 3D numerical ray tracing as previously described. In this work an OTHR model incorporating an updated version of Coleman's 2D ray tracing will be used to test the viability of a multistatic OTHR configuration.

5. ASSESSING THE VIABILITY OF A MULTISTATIC OVER THE HORIZON RADAR

5.1. Multistatic Over the Horizon Radar

As discussed in Section 4.1, Doppler shifts to the scattered signal from a target can be used to separate the target signal from the background clutter; however, as the Doppler shift is dependent on the target-transmitter and target-receiver radial speeds, it is possible for a target to accidentally or deliberately maintain a course which results in the target signal remaining within clutter lines. Detection of the scattered signal by multiple receivers in different locations would make "hiding" in the clutter far more difficult as the target signal Doppler shift would be different at each receiver location. This approach would also provide the opportunity to determine the target velocity. The Doppler shift detected at a receiver is an indicator of the radial speed, which is dependent on the transmitter-target-receiver geometry; however, this radial speed does not provide the target velocity on a single radar sweep. For example, for a particular radial speed with a co-located transmitter and receiver, a target may be travelling directly toward the transmitter and receiver at the observed radial speed or could be travelling in a different direction at a higher speed. However, as the transmitter location is fixed, consideration of observed Doppler shifts at multiple receiver sites permits calculation of the target velocity from a single radar sweep.

The development of an operational multistatic over the horizon radar (MOTHR) system, i.e. an OTHR system with multiple receivers, would involve many challenges. A conventional over the horizon radar (OTHR) configuration for target detection can involve a transmitter with array length exceeding 100m and receivers with lengths which can exceed 1 km. The identification of viable locations for several of these large structures would clearly be problematic. To address

this issue, an alternative approach to the conventional OTHR configuration has been proposed. Rather than one large transmitter and multiple enormous receivers, the proposed approach will require one very large transmitter and multiple receivers which are very small and cheap. Within this work the model transmitter is assumed to be 2.5 km in length and is capable of a transmitting power of 2 MW. The receivers are assumed to be simple dipole receivers with 0 dB of gain. An advantage of using such small receivers is that they will be easily relocatable. Receivers could even be placed on small ships, thereby providing a network of receivers which could be redeployed whenever required to provide OTHR coverage in regions of interest. It should be noted that coordinate registration for bistatic configurations will be far more difficult than for a monostatic configuration. The availability of a very accurate ionospheric model (such as a real-time data assimilation model) will, therefore, be vital for the successful operation of the MOTHR. It would also be sensible for one of the receivers to be positioned in a pseudo-monostatic configuration (e.g. located about 100 km from the transmitter) as coordinate registration will be less problematic for this receiver. In this work the pseudo-monostatic receiver is also assumed to have 0 dB of gain. However, in an operational system the construction of a larger array for the pseudo-monostatic receiver (and any others which are not intended to be relocatable) would enable the detection of smaller targets.

5.2. Over the Horizon Radar Modelling

In this work an OTHR model developed by C.J. Coleman will be used to test the viability of the MOTHR concept. Ray tracing is performed through output from an ionospheric model (FIRIC: Section 3.4) using a 2D numerical approach based on the method described by Coleman (1998). This provides output including the ground range from the transmitter, altitude,

group path, phase path, and propagation path losses at multiple points along the ray path. Ray paths are produced for a chosen frequency and transmitter bearing with initial elevations from 5° to 45° in 0.5° steps. Any ray path which has a peak altitude greater than 120 km and returns to the ground is included in the analysis. The ray tracing output at the ray path landing point (i.e. altitude = 0) is stored. The minimum and maximum landing point ground ranges from all considered initial elevations are determined. Model output will be provided for a fixed number (51 by default) of equally spaced landing point locations (model target locations) between the location of the minimum ground range landing point and the location of the maximum ground range landing point. For each of the target locations, ray tracing is performed from the receiver in the direction of the target location (using the assumption that the target-receiver and receiver-target ray paths are identical) in the manner described for the transmitter-target ray paths. Ray paths using each pair of subsequent transmitter-target initial elevations are considered in turn. Once a pair of landing point ground ranges is found such that the target ground range lies between the two ray path ground ranges, linear interpolation is performed on the ray tracing output to determine the group path, phase path, and propagation path losses at the target location. This is repeated for each pair of subsequent initial elevations, with each successful pair providing output for the target location using a different propagation mode. This approach is repeated for the receiver-target ray paths. The combined output of the transmitter-target and receiver-target output provides the group paths, ray paths, and propagation path losses for the transmitter-target-receiver paths, using each successful combination of transmitter-target and receiver-target propagation modes. The propagation path losses are then used to calculate the minimum detectable radar cross section (MDRCS), i.e. the smallest target radar cross section which can be detected. From equation 4.7, when system losses are disregarded and following conversion to dB m^2, the MDRCS is given by

$$MDRCS = 10\ log_{10}\left(\frac{\lambda^2 \times TgLoss \times N}{4\pi \times CIT \times G_T \times G_R \times P_T}\right). \qquad (5.1)$$

The model provides output for up to 51 target locations (as some target locations may not have any viable receiver-target propagation modes), showing the transmitter-target-receiver MDRCS value for each combination of viable transmitter-target and receiver-target propagation modes. Figure 20 and Figure 21 show examples of OTHR model output for MDRCS values and group paths respectively for a bistatic configuration at midday (local time).

In this work only one-hop skywave propagation is considered (i.e. all paths are of the form transmitter-ionosphere-target-ionosphere-receiver) and receiver locations are assumed to be remote. The frequency dependent galactic noise and external noise at the receiver site are calculated using the Radio Noise Model (RNM) developed by Coleman. External noise at a remote location (n_x) with the RNM corresponds closely to noise for a "quiet rural" site (Figure 22) from the International Telecommunication Union model (ITU, 2019), and is given by

$$n_x = 40 - 12.16 \ln\left(\frac{f}{3}\right), \qquad (5.2)$$

for frequency f (MHz). Galactic noise (n_g) from the RNM is given by

$$n_g = 39 - 9.555 \ln\left(\frac{f}{3}\right), \qquad (5.3)$$

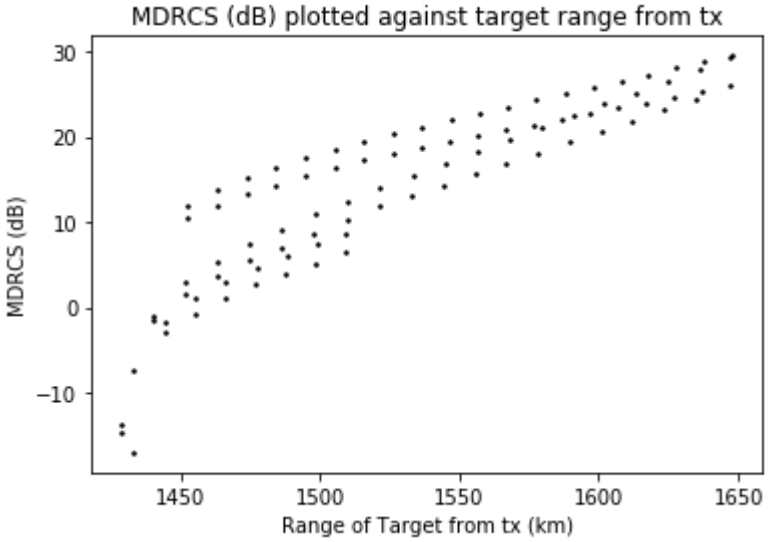

Figure 20. MDRCS (dB m^2) at 1200 LT on a frequency of 13 MHz.

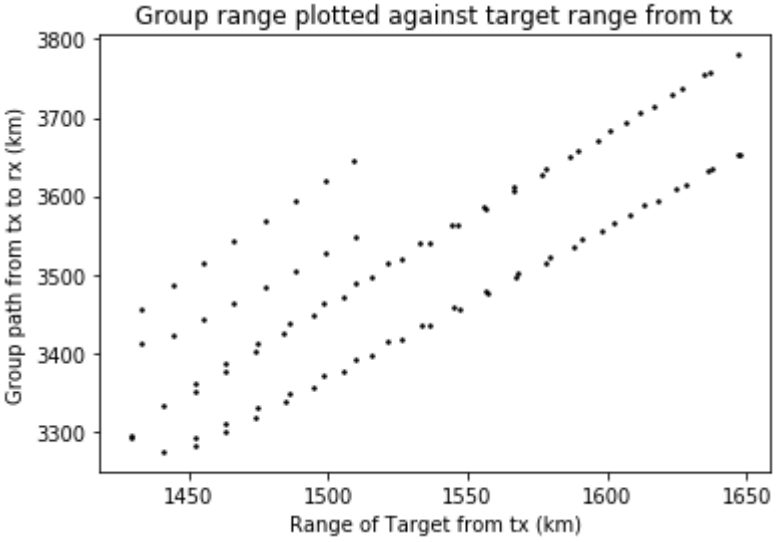

Figure 21. Group path at 1200 LT on a frequency of 13 MHz.

which differs by no more than 2 dB from the International Telecommunication Union (ITU) model (Figure 23) and is comparable with the external noise at a RNM remote and ITU quiet rural site. The ionospheric model used for ray tracing is the FIRIC model, described in Section

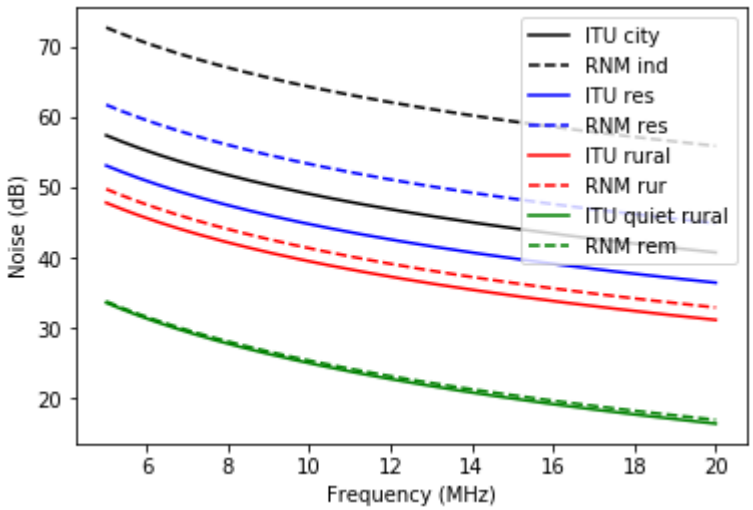

Figure 22. Environmental noise at the receiver site as determined using the ITU model (ITU, 2019) *and the RNM by Coleman. RNM noise values for a remote (rem) location with RNM (green dashed line) corresponds closely to a quiet rural location with the ITU model (green solid line). Noise power (dB W) per Hz is obtained by subtracting 204 dB.*

3.4. To gain an understanding of OTHR performance for a range of environmental conditions, MDRCS values will be considered for ionospheric conditions representative of March, June, September and December, at 0000 UT and 1200 UT, and with low and high solar activity (F10.7 = 80 and F10.7 = 160). FIRIC input includes the smoothed 12 month sunspot number (R_{12}) as an indicator of solar activity. Conversion from F10.7 to R_{12} is performed using the method applied within the NeQuick model, where

$$R_{12} = \sqrt{167273 + 1123.6(F10.7 - 63.7)} - 408.99\,. \qquad (5.4)$$

Therefore, low and high solar activity conditions will be represented using R_{12} = 21.8 and R_{12} = 115.9 respectively.

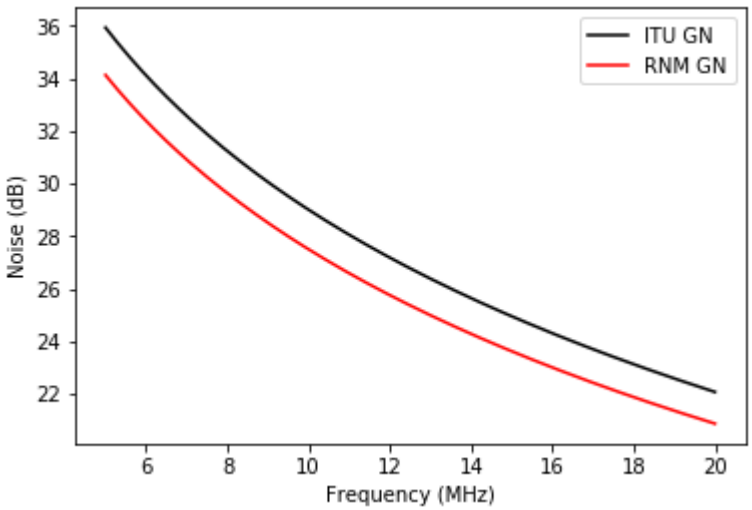

Figure 23. Galactic noise (GN) values from the ITU model (ITU, 2019) *and the RNM.*

For a chosen frequency, when using elevations with landing points close to the edge of the skip zone, the signal strength can be increased due to a phenomenon known as skip focussing (or leading edge focussing). This occurs due to the convergence of low and high elevation ray landing points at the edge of the skip zone. Skip focussing is a real, observable phenomena. However, as a target enters the skip zone the signal strength will decrease rapidly until the target is no longer detectable by the receiver. It is, therefore, important that when reporting the capability of an OTHR configuration, this performance is not dependent on skip focussing as the target may only be detectable for an extremely short period. To avoid this issue, the ray path landing point for the chosen frequency and bearing (from all initial elevations between 5° and 45°) which is closest to the transmitter is assumed to be representative of the edge of the skip zone. Only rays which land at least 50 km further from the transmitter than the edge of the skip zone are included in the analysis. Therefore, targets with RCS equal to the MDRCS will be detectable for the time it takes to travel a radial distance of 50 km towards the transmitter. For example, in the worst-case scenario in which the target is travelling directly towards the transmitter, a target travelling at Mach 1 would be observable for at least 2.5 minutes, whereas a hypersonic vehicle travelling at Mach 20 would be observable for at least seven seconds.

5.3. Maps of Minimum Detectable Radar Cross Sections: Multistatic Configuration with One Bistatic Receiver

Within this work a fictitious transmitter (tx) is positioned in Cornwall, England (-5.7°E, 50.1°N), with a pseudo-monostatic receiver located 100 km north-west of the transmitter. A bistatic receiver (R1) location is arbitrarily chosen as the location determined by travelling 500 km south-west from the transmitter and then travelling a further 500 km south-east (-6.0°E, 43.5°N). This bistatic configuration is shown in Figure 24, including an example target location and FIRIC ionospheric conditions representative of 1200 UT in June with low solar activity (F10.7 = 80). In this example the transmitter-target distance is greater than the target-receiver distance. Also, the critical frequency is generally greater along the target-receiver path than for the transmitter-target path. Therefore, ray path properties (e.g. propagation path losses) on the transmitter-target path may be significantly different from the properties on the target-receiver path. Ray tracing is performed for transmitter azimuths in 1° steps from 175° to 275°. A one degree latitude-longitude grid determines pixel size and location for maps of MDRCS and propagation path loss values. The minimum MDRCS or loss output value from all target locations within a pixel represents the smallest target which can be detected by the OTHR configuration at that location. Pixel minimum values are plotted on coverage maps, e.g. Figure 25. The example in Figure 25 shows MDRCS values which can be achieved in one test case (1200 UT in June with F10.7 = 80) when using one transmission frequency (10 MHz). Under these environmental conditions the skip frequency for the direct skywave tx-R1 path is 9.4 MHz. A frequency is chosen which is above the skip frequency to avoid a direct skywave path between the transmitter and receiver: in this example, 10 MHz. The left-hand plot shows MDRCS values which can be achieved when using the pseudo-monostatic configuration. The middle plot shows MDRCS values for the bistatic configuration with receiver R1. The right-

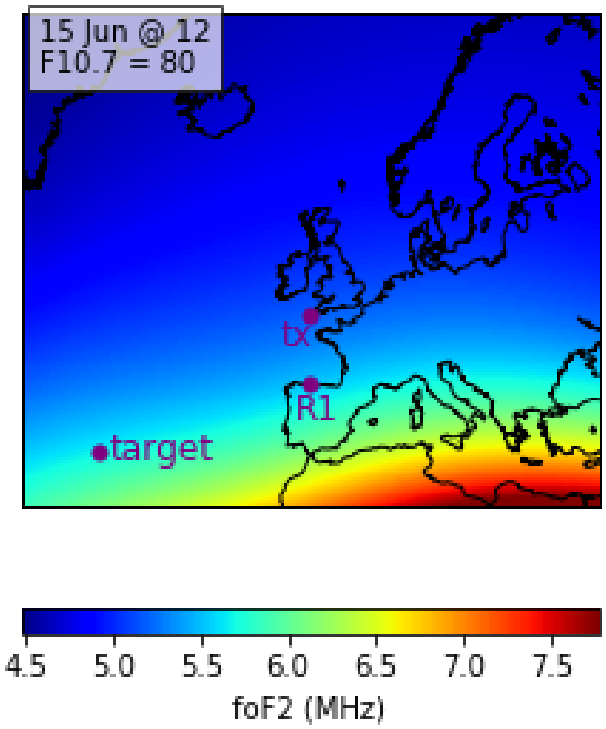

Figure 24. Bistatic OTHR configuration with transmitter (tx), bistatic receiver (R1), and an example target location. Ionospheric conditions shown are representative of 1200 UT in June with low solar activity (F10.7 solar flux = 80 sfu).

hand plot shows the maximum (worst) of the monostatic and bistatic MDRCS values at each location (i.e. the greater of the two pixel minimum values). This provides the minimum RCS which can be detected at a location by both the monostatic and bistatic receivers simultaneously. Figure 26 uses the same approach to display propagation path loss values. Monostatic OTHR coverage is available at all considered transmitter bearings for ground ranges from about 1000 km to less than 1500 km from the transmitter. The coverage area is reduced for the bistatic configuration in the region close to the receiver location as rays which have been scattered by the target are unable to be reflected to the receiver location (so effectively the receiver is within

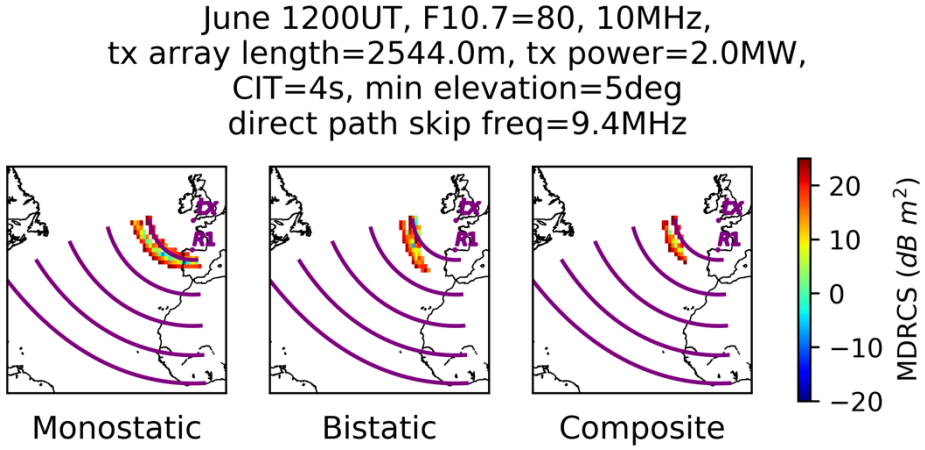

Figure 25. MDRCS values which can be detected by a pseudo-monostatic (left) and bistatic (middle) configuration at a frequency of 10 MHz. The lowest MDRCS which can be detected by both receivers simultaneously is also shown (right). Purple arcs represent points with distance 1000, 2000, 3000, 4000 and 5000 km from the transmitter. Ionospheric conditions are representative of 1200 UT in June with F10.7 solar flux of 80 sfu.

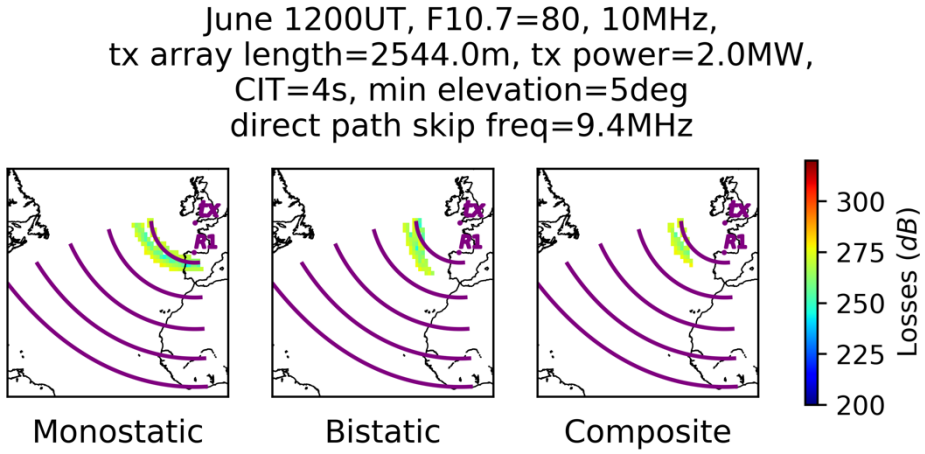

Figure 26. Lowest loss values for a pseudo-monostatic (left) and bistatic (middle) configuration at a frequency of 10 MHz. The lowest possible losses for both configurations simultaneously are also shown (right). The ionospheric conditions are identical to those used in Figure 25: 1200 UT in June with F10.7 = 80 sfu.

the skip zone of the target). It should, however, be noted that if the transmitter bearings used extended beyond 275° the coverage area for the bistatic configuration would be larger. The coverage area for both receivers simultaneously (composite) is reduced further, as some of the bistatic coverage area is outside the monostatic coverage area. OTHR coverage is now considered when multiple frequencies are available for use. Figure 27 shows MDRCS values which can be achieved when frequencies from 10 to 15 MHz (in 1 MHz steps) are available. Again, the performance of the monostatic (left), bistatic (middle), and multistatic (right) configurations are shown. However, note that the multistatic (composite) plot shows the MDRCS value that can be achieved by both the monostatic and bistatic receivers simultaneously when using the same frequency. Also, the coverage area is not indicative of the area in which target detection is possible at one instant in time (unless all considered frequencies could be used simultaneously). Rather, it is the area for which observations could be made if frequencies from 10 to 15 MHz are available. Figure 28 provides the frequency used at each location to obtain the MDRCS values in Figure 27. The lowest propagation path losses are displayed in Figure 29. Coverage for the monostatic configuration extends to ground ranges of about 2500 km or more for all considered transmitter bearings. The coverage area for the bistatic and composite configurations are similar to the monostatic coverage area apart from the region close to receiver R1. Also, the composite coverage area includes a large region in which targets with a RCS in excess of 5 dB m^2 can be detected by both receivers simultaneously. Figure 30, Figure 31, and Figure 32 show the MDRCS, best frequency, and loss maps when frequencies up to 20 MHz are available. Coverage now extends to ground ranges of 3500 km or more. Again, away from the edges of the coverage area, it is possible for both receivers to detect targets with RCS greater than 5 dB m^2 simultaneously.

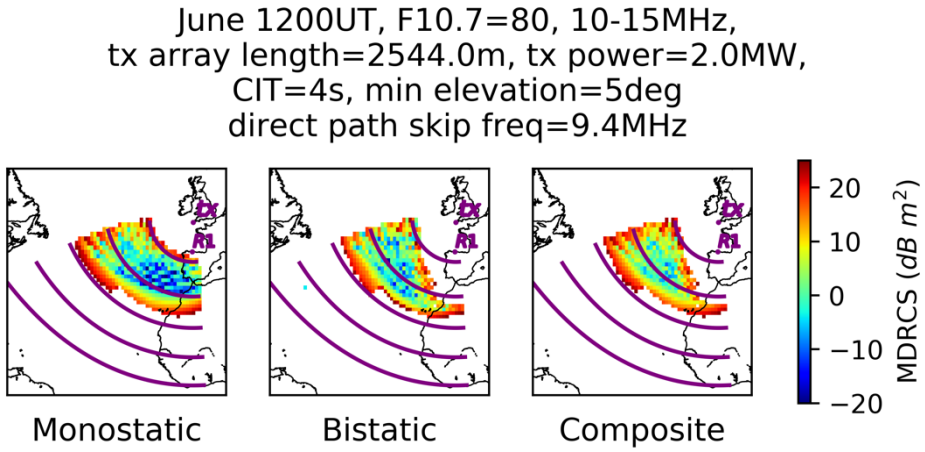

Figure 27. MDRCS values when a range of frequencies from 10 -15 MHz can be used in a pseudo-monostatic (left) and bistatic (middle) configuration. The best (lowest) MDRCS values that can be observed by both receivers when using the same frequency is also shown (right).

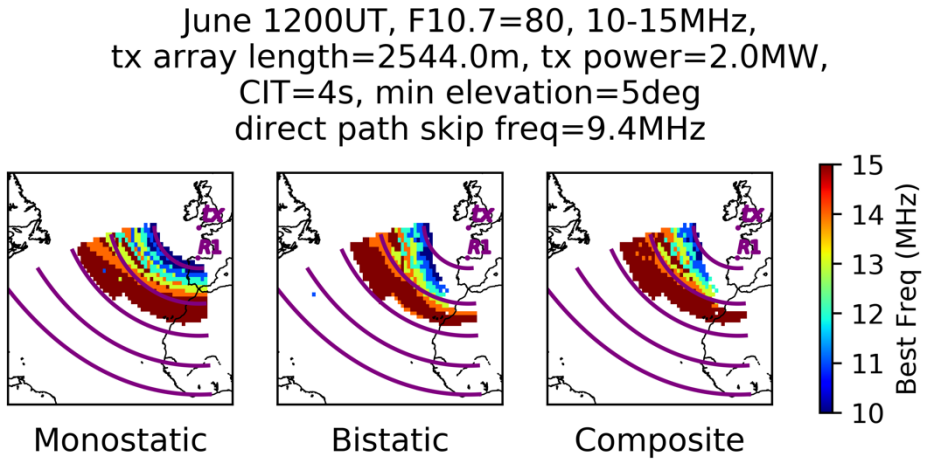

Figure 28. Frequencies used to obtain the lowest MDRCS values in Figure 27.

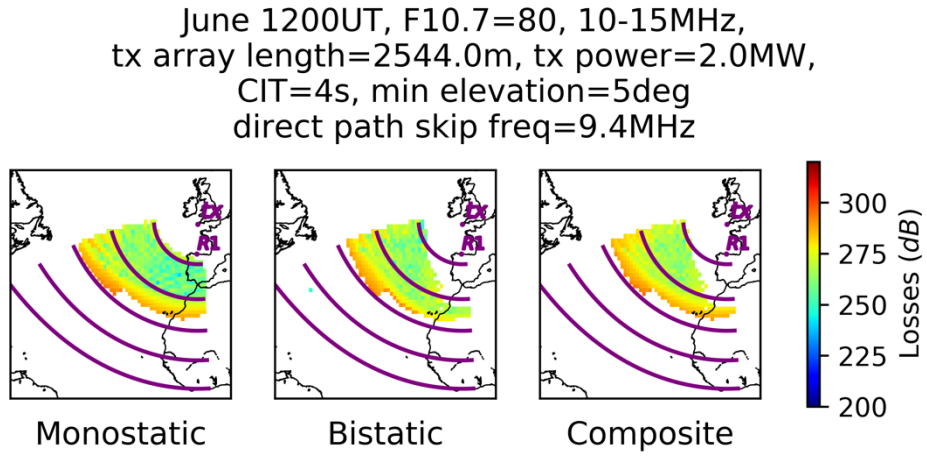

Figure 29. Minimum losses associated with the conditions for Figure 27 and Figure 28.

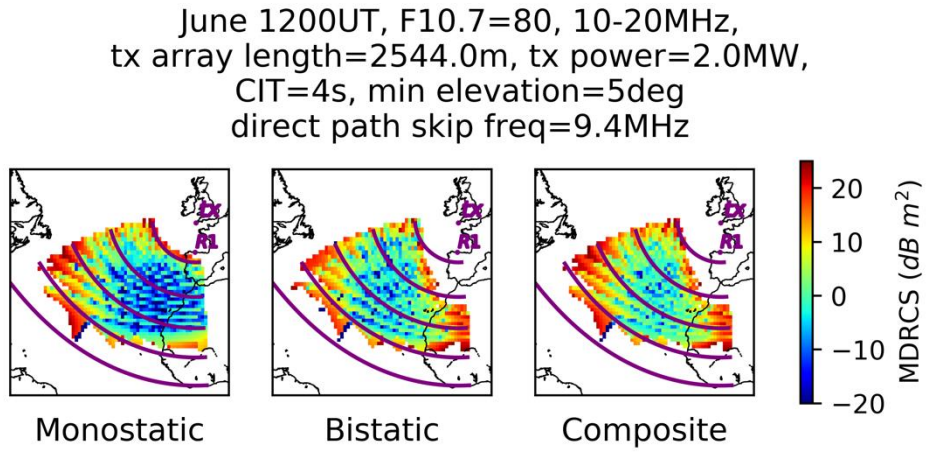

Figure 30. MDRCS values when a range of frequencies from 10-20 MHz can be used in a pseudo-monostatic (left) and R1 bistatic (middle) configuration. The best MDRCS values that can be observed by both receivers when using the same frequency is also shown (right).

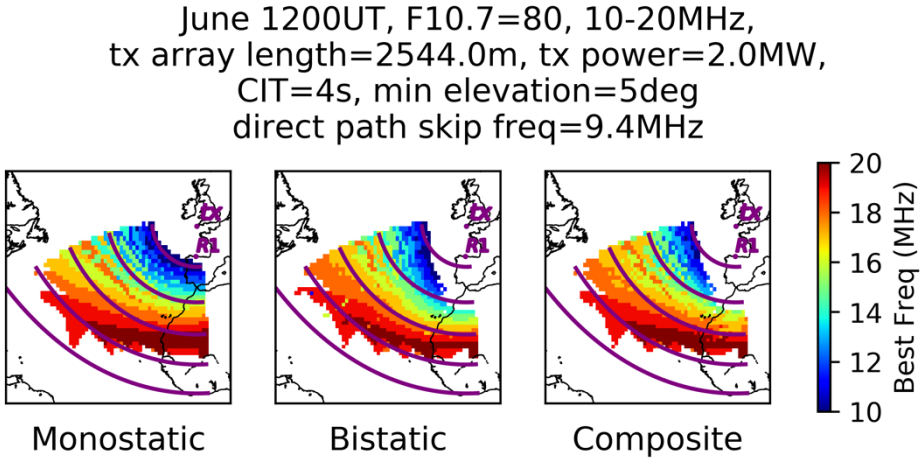

Figure 31. Frequencies used to obtain the lowest MDRCS values in Figure 30.

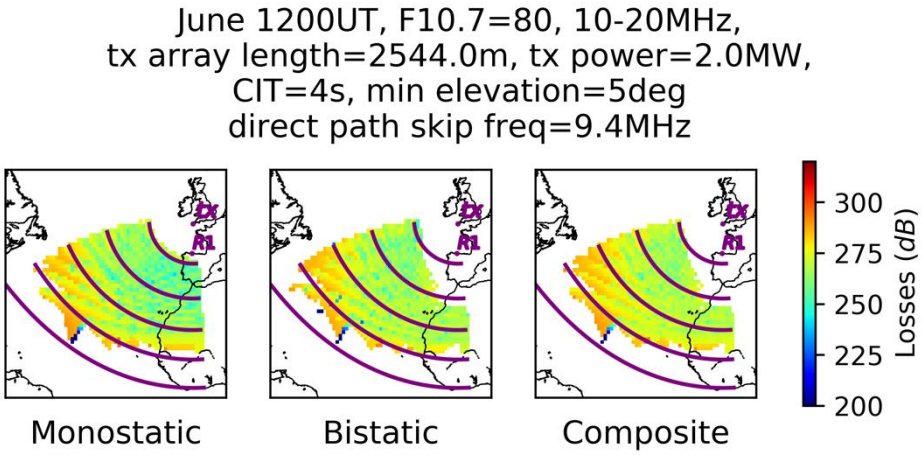

Figure 32. Minimum losses associated with the conditions for Figure 30 and Figure 31.

A second bistatic receiver, R2, is now included in the analysis. The location of R2 is chosen in a manner similar to R1, travelling 500 km south-west from the transmitter site followed by travelling 500 km north-west. Figure 33, Figure 34, and Figure 35 show OTHR coverage with the same environmental conditions and frequencies chosen previously (1200 UT in June with F10.7 = 80 and frequencies of 10-20 MHz), but using bistatic receiver R2 instead of R1. Note that good coverage is now possible for the bistatic and composite configurations in the region

close to receiver R1 for which bistatic or composite coverage was not possible when using receiver R1. Similarly, coverage is not possible close to receiver R2 when using receiver R2. However, coverage can be provided for this region when using receiver R1. This suggests that widespread coverage is possible when using multiple receivers located in different regions.

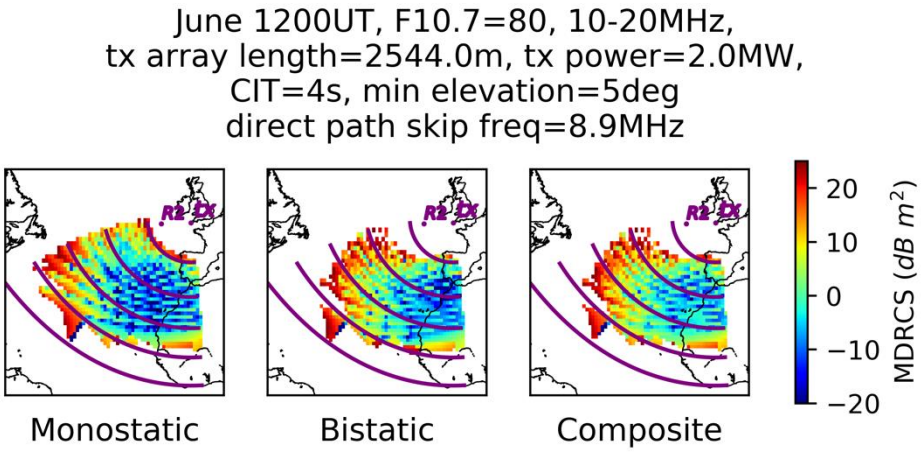

Figure 33. MDRCS values when a range of frequencies from 10-20 MHz can be used in a pseudo-monostatic (left) and R2 bistatic (middle) configuration. The best MDRCS values that can be observed by both receivers when using the same frequency is also shown (right).

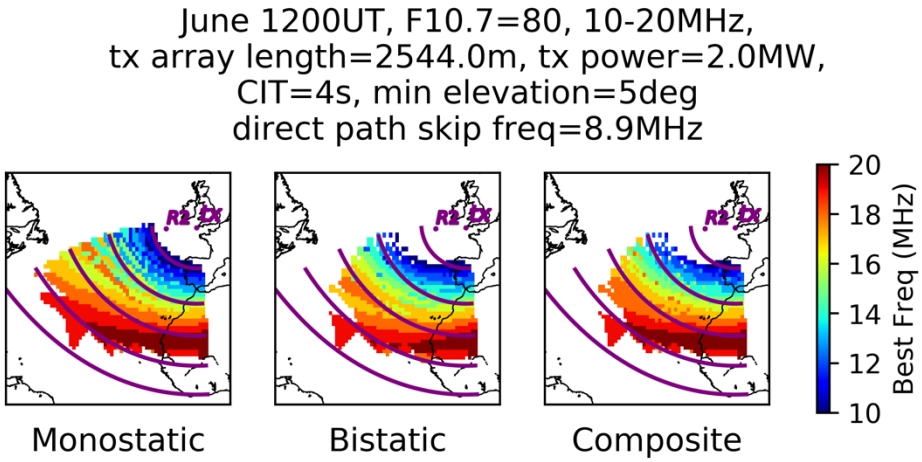

Figure 34. Frequencies used to obtain the lowest MDRCS values in Figure 33.

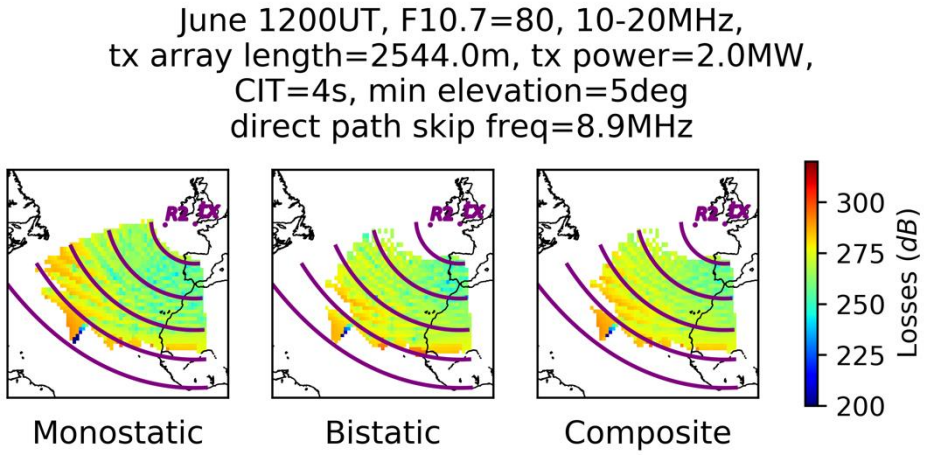

Figure 35. Minimum losses associated with the conditions for Figure 33 and Figure 34.

5.4. Maps of Minimum Detectable Radar Cross Sections: Multistatic Configuration with Two Bistatic Receivers

OTHR performance is now considered when the multistatic configuration consists of one transmitter and three receivers. The pseudo-monostatic receiver and bistatic receivers R1 and R2 are in the locations discussed in the previous subsection. However, the OTHR performance is now assessed for signals detected by the pseudo-monostatic receiver as well as either receiver R1 or receiver R2 simultaneously and using the same transmitted frequency. Target detection using two receivers simultaneously provides the benefits previously described, i.e. determination of target velocities and an increased likelihood of detecting targets against noise rather than noise plus clutter. The requirement of including the pseudo-monostatic receiver permits coordinate registration for the pseudo-monostatic configuration which is far less problematic than attempting coordinate registration independently for a bistatic configuration. The signal scattered by a single target which is detected by each receiver will have had identical

transmitter-target ray paths. A challenge of multiple return signals is identification of which monostatic target detection corresponds to each target detection by a bistatic receiver.

Figure 36 provides the MDRCSs which can be detected by both the pseudo-monostatic receiver and bistatic receiver R1 or R2 when using the same transmitted frequency. Conditions are identical to those in the previous subsection, i.e. 1200 UT in June with F10.7 = 80 sfu. Frequencies up to 20 MHz are considered, with the minimum transmission frequency used determined as the minimum frequency (in steps of 1 MHz) such that all receivers lie within the skip zone of the transmitter (in this test case the minimum frequency used is 10 MHz). Coverage is possible for nearly all locations (within the transmitter bearings considered) with distances (ground range) of between 1000 and 4000 km from the transmitter. Targets with RCS of 0 dB m^2 or greater are detectable by two receivers over much of this coverage area.

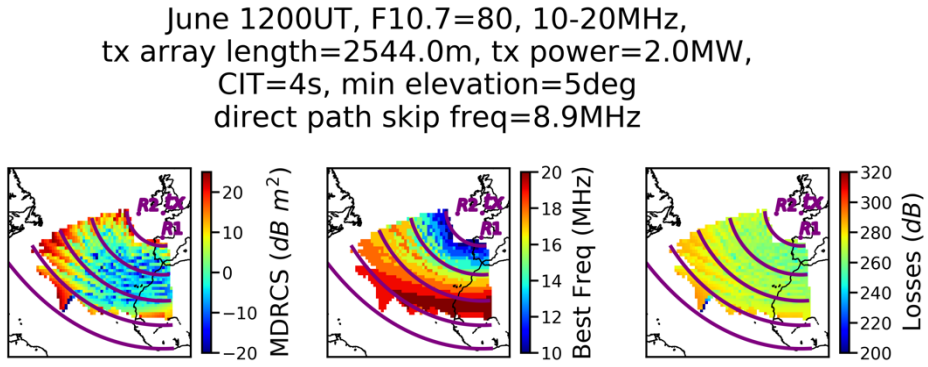

Figure 36. Lowest MDRCS achievable with both the pseudo-monostatic receiver and either receiver R1 or R2 (left) when using the same frequency. The frequency which produced the lowest MDRCS (middle) and lowest possible transmitter-receiver losses (right) for both the pseudo-monostatic and a bistatic receiver are also provided.

Alternative test cases will now be considered to determine how changes to ionospheric

conditions affect the MOTHR performance. One test case parameter (month, time of day, solar activity) will be adjusted in turn to provide a direct comparison with the MOTHR performance displayed in Figure 36. Test case conditions for Figure 36-Figure 39 are provided in Table 5. Details of the MOTHR coverage area and typical MDRCS values achievable within the coverage area are also provided, and can be viewed in the corresponding figures. As before, the lowest frequency used is determined as the lowest frequency which results in a skip zone which includes all three receiver locations. However, only frequencies of 4 MHz and above will be included in any analysis to avoid the inclusion of lower frequencies which would be difficult to use in a physical system.

Table 5. Ionospheric conditions for test cases considered in Figure 36-Figure 39. Changes in test conditions from the test case in Figure 36 are highlighted in yellow.

Figure No	Month	F10.7	Time of day	Coverage area minimum ground range	Coverage area maximum ground range	Typical MDRCS
Figure 36	June	80	1200 UT	~1000 km	~3500 - 4000 km	0 dB m^2
Figure 37	June	160	1200 UT	~1000 km	~3000 - 3500 km	0 dB m^2 (to ~3000 km)
Figure 38	December	80	1200 UT	~1000 km	~2500 km	-20 dB m^2
Figure 39	June	80	0000 UT	~1000 km	~3000 km	-20 dB m^2

Electron densities are generally greater during high solar activity, resulting in ray paths with low initial elevations (which generally travel to landing points with higher ground ranges)

having their peak height at lower altitudes. Therefore, during higher levels of solar activity (Figure 37) the maximum ground range for the coverage area has decreased compared to coverage during low solar activity (Figure 36). However, lower (better) MDRCS values can be observed for ground ranges ~1500-2500 km, again due to lower peak altitudes. Note, however, that the region for which the optimal frequency is 20 MHz is much larger during high solar activity. If the maximum transmission frequency was increased beyond 20 MHz the greater electron densities during high solar activity would support skywave propagation with higher frequencies during these times. This would be likely to extend the maximum ground range for the coverage area, and to reduce MDRCSs for ground ranges above 2500 km. Figure 38 shows MDRCSs for conditions representative of 1200 UT in December with F10.7 = 80 sfu. Higher peak electron densities (nearly as high as 1200 UT in June with F10.7 = 160 sfu) and lower peak electron density height compared to the daytime June test cases result in ray path peaks at much lower altitudes. The coverage area maximum ground range is reduced further in this test case. However, the lower peak altitudes result in shorter ray paths and considerably lower MDRCS values within the coverage area. As for the June test case with high solar activity, ionospheric conditions would appear to support skywave propagation with higher transmission frequencies. The coverage area in Figure 39 (0000 UT in June with F10.7 = 80 sfu) also presents a reduction in the coverage area maximum ground range and considerably lower MDRCS values when compared to the test case in Figure 36. During the night, lower altitudes in the ionosphere are no longer illuminated and recombination reduces electron densities. The D and E region effectively disappear and ray paths avoid the increase in propagation path losses due to these regions. Therefore, it is possible to achieve considerably lower MDRCS values during the night. In this test case the depletion of F region electron densities is much less severe so skywave propagation can still be supported in the F region. Note that skywave propagation is

not supported for frequencies above 17 MHz. Therefore, the reduction in peak plasma frequency (around 0.5 MHz compared to midday) is sufficient to reduce the maximum ground ranges for the coverage area, as higher peak plasma frequencies would support skywave propagation when using higher transmission frequencies with low initial elevations.

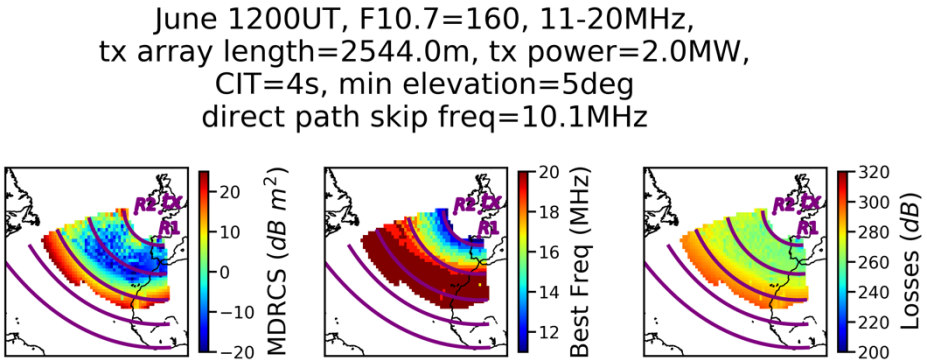

Figure 37. As Figure 36, but with increased solar activity (F10.7 = 160 sfu). Lowest MDRCS achievable with both the pseudo-monostatic receiver and either receiver R1 or R2 (left) when using the same frequency. The frequency which produced the lowest MDRCS (middle) and lowest possible transmitter-receiver losses (right) for both the pseudo-monostatic and a bistatic receiver are also provided.

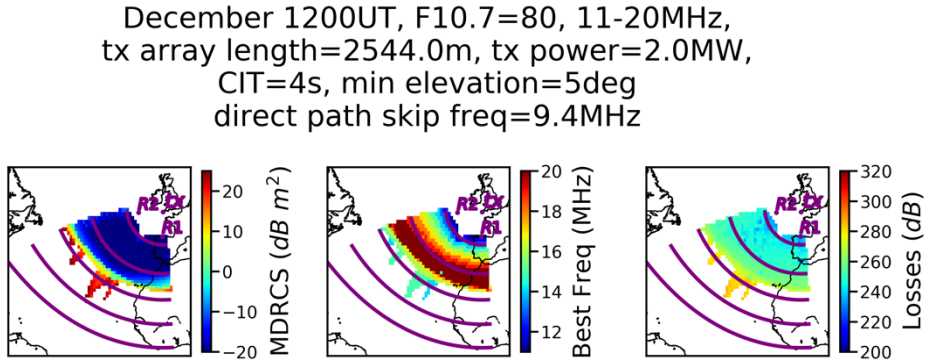

Figure 38. As Figure 36, but December. Lowest MDRCS achievable with both the pseudo-monostatic receiver and either receiver R1 or R2 (left) when using the same frequency. The frequency which produced the lowest MDRCS (middle) and lowest possible transmitter-receiver losses (right) for both the pseudo-monostatic and a bistatic receiver are also provided.

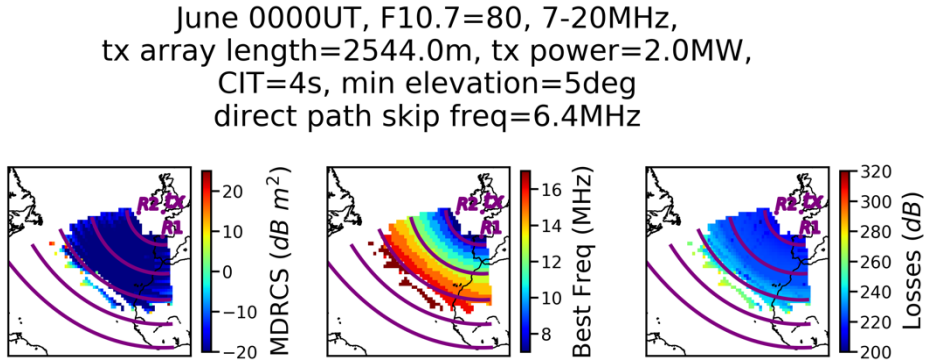

Figure 39. As Figure 36 but for 0000 UT. Lowest MDRCS achievable with both the pseudo-monostatic receiver and either receiver R1 or R2 (left) when using the same frequency. The frequency which produced the lowest MDRCS (middle) and lowest possible transmitter-receiver losses (right) for both the pseudo-monostatic and a bistatic receiver are also provided.

5.5. Worst Case MDRCS

Comparing MDRCS values and coverage areas for individual test cases can provide useful information about variability in MOTHR performance under specific ionospheric conditions. However, it would also be useful to consider what sort of performance could generally be expected regardless of season or time of day. To this end the worst case MDRCS is considered. MDRCS coverage maps are determined using the approach described in the previous subsection, for test cases which include every combination of season (March, June, September, December), time of day (0000 UT, 1200 UT) and F10.7 solar flux (80 sfu, 160 sfu) considered in this work. The worst (highest) MDRCS value corresponding to a pixel across all 16 test cases determines the worst-case scenario MDRCS for that location, providing an indication of the MOTHR performance which can generally be expected at all times (not including less common ionospheric conditions such as geomagnetic storms). MDRCS values of 0 dB m^2 or less are achievable for most locations with ground ranges between 1750 and 2500 km from the transmitter across all test cases (Figure 40, left). However, if 0000 UT in December with F10.7=80 is excluded this coverage area is increased (Figure 40, right). Targets with RCS greater than 0 dB m^2 are now detectable at most locations with ground range between 1250 and 2500 km from the transmitter. This demonstrates that the MOTHR configuration is capable of detecting a variety of targets, such as ships, aircraft, and smaller targets such as missiles. Figure 41 provides the OTHR performance when only the pseudo-monostatic receiver is used. It can be seen that coverage areas in Figure 41 are very similar to Figure 40. However, MDRCS values are 6-10 dB m^2 lower than MOTHR MDRCS values over a significant region of the coverage area. Therefore, A MOTHR configuration can be used without a loss of coverage area (compared to a monostatic configuration) for targets with RCS greater than 0 dB m^2. However, smaller targets could be detected by the pseudo-monostatic receiver alone when required.

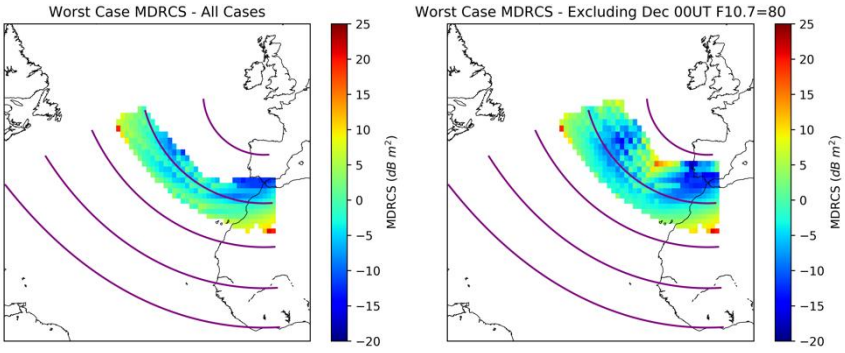

Figure 40. MDRCSs which are achievable using both the pseudo monostatic receiver and either bistatic receiver R1 or R2 at 0000 and 1200 UT in March, June, September, and December with F10.7 = 80 and F10.7 = 160 (left). MDRCS values for the same set of conditions but excluding 0000 UT in December with F10.7 = 80 are also shown (right).

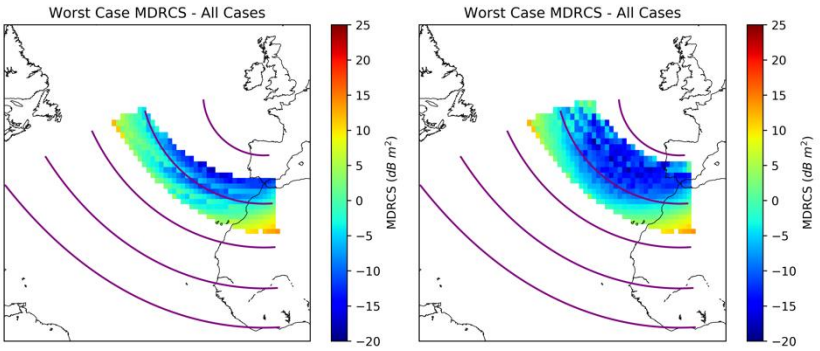

Figure 41. As Figure 40 but using only the pseudo-monostatic receiver. MDRCSs which are achievable using the pseudo-monostatic receiver at 0000 and 1200 UT in March, June, September, and December with F10.7 = 80 and F10.7 = 160 (left). MDRCS values for the same set of conditions but excluding 0000 UT in December with F10.7 = 80 are also shown (right).

As discussed in Section 5.1, it would be beneficial for the network to have relatively small receivers for ease of redeployment when desired. However, it should also be noted that using larger or more efficient receivers (compared to the simple dipole receivers with 0 dB of gain used in these simulations) will improve MOTHR performance further. A large-scale permanent

structure for a pseudo-monostatic receiver would also provide obvious benefits for the detection of smaller targets. Future work could include incorporating antenna and array gain patterns which provide better (and more realistic) antenna performance. This would impact the results discussed due to taking into account different transmitter and receiver gains when transmitting or receiving in different directions with respect to the orientation of the array.

It should be noted that within this work a monthly median climatological ionospheric model (FIRIC) has been used for ray tracing. Therefore, the ray tracing output and OTHR simulations discussed do not provide information about the variability of OTHR performance around these average conditions. Future work could include investigation into the variability of OTHR performance with, for example, ionospheric specification from AENeAS. This would provide useful insight into the true capabilities of a real OTHR system, such as the proportion of times for which the OTHR would be able to detect targets with a specified RCS.

6. USING AN IONOSPHERIC MODEL FOR LOW-LATITUDE SCINTILLATION FORECASTING

This chapter is an extended version of (Nugent et al., 2021).

In Sections 4 and 5 the effects of ionospheric refraction and reflection on HF transmissions have been discussed. However, the magnitude of propagation path deviation due to ionospheric refraction (and, therefore, the likelihood that ionospheric reflection takes place) is dependent on the transmission frequency. Global Navigation Satellite Systems (GNSS) transmissions, e.g. Global Positioning System (GPS) transmissions, are commonly used by many industries (Hapgood, 2017; Hapgood et al., 2021). The frequencies used for GNSS are much higher than HF frequencies, so the effects of ionospheric refraction on GNSS transmission paths are very small. However, as discussed in Section 2.4.2, GNSS communications (and other trans-ionospheric transmissions) can be impacted by ionospheric refraction and diffraction when passing through plasma irregularities, resulting in ionospheric scintillation.

6.1. Low-Latitude Scintillation Forecasting

At low-latitudes ionospheric scintillation can occur due to the presence of an equatorial plasma bubble (EPB: Section 2.3.4) on the transmission path. The development of equatorial plasma bubbles has been shown to be correlated with the magnitude of the pre-reversal enhancement (PRE) vertical plasma drift (Basu et al., 1996; Fejer et al., 1999; Kil et al., 2009). EPB occurrence has also been associated with the presence of atmospheric waves, such as gravity waves (Abdu et al., 2009; Tsunoda, 2010), which can produce the perturbations required to initiate the Rayleigh-Taylor instability as they propagate upwards from lower altitudes.

Anderson et al. (2004) suggested that the "seeding" mechanism for EPB generation can be considered to be present at all times, so the necessary and sufficient condition for EPB formation is a large PRE vertical plasma drift; however, later work has demonstrated that, whilst the probability of EPB generation increases with increasing PRE vertical plasma drift, large vertical plasma drifts do not guarantee the presence of EPBs (Huang & Hairston, 2015; Kil et al., 2009), possibly due to a lack of the perturbations required to initiate EPB generation.

In order to mitigate the effects of low-latitude scintillation several approaches have been developed to forecast the occurrence of plasma irregularities. Ionospheric observations have been used for regional scintillation forecasts by applying methods such as machine learning and data mining (e.g. Rezende et al., 2010) or by considering the temporal change of the observables and then propagating them forward in time using forecasts of irregularity drift (Groves et al., 1997). Observations used to forecast EPB generation/scintillation include S4 (Groves et al., 1997), total electron content (Sridharan et al., 2012; Sunda et al., 2017; Tanna et al., 2013), the virtual height associated with a specified plasma frequency (Anderson et al., 2004; Sousasantos et al., 2017), the minimum F layer virtual height (h'F; de Lima et al., 2014; Redmon et al., 2010; Rezende et al., 2010; Sridhar et al., 2017), the F2 layer *o*-mode critical frequency (foF2; Bagiya et al., 2014), ultraviolet spectographic imagery (Kelly et al., 2014), and coherent scatter radar and planar Langmuir probe observations of electron densities (Costa et al., 2011). A drawback of these approaches is the absence of significant antecedence because observations for a specified region generally need to be made around the time of local sunset. An alternative approach which allows greater antecedence is the use of an ionospheric model. A model also makes forecasting possible for regions with limited ionospheric observations such as over oceans.

Empirical ionospheric models can capture the global climatology of EPB formation, structure, longevity, and decay, including the resulting scintillation effects. There is, however, considerable day-to-day variability around this climatology. Retterer (2010) noted that their ionospheric plume model would not accurately predict ionospheric variability if it was driven only by empirical models. This is because, unless the empirical models were adequately parameterized, the output would represent averages or binnings that would suppress the day-to-day variability. Several empirical models have been shown to include inaccuracies when nowcasting or forecasting scintillation due to the description of conditions in terms of statistical parameters (Forte & Radicella, 2005; Hamel et al., 2014; Priyadarshi, 2015). A physics-based model may, therefore, be more successful at representing day-to-day variability when forecasting scintillation due to EPBs.

An existing scintillation forecasting technique using a physics-based model (TIE-GCM: Section 3.5) to calculate integrated field line Rayleigh-Taylor growth rates will be described. A second scintillation forecasting technique using ionosonde data to calculate a proxy for vertical plasma drift (PVPD) at the magnetic equator will also be described. For the first time the ionosonde PVPD technique has been adapted to use output from a physics-based model (Nugent et al., 2021), providing a simple and computationally cheap method for real-time scintillation forecasting which may prove attractive for operational use. Methods for comparing forecasting skill will be discussed, and the forecasting skill of the Rayleigh-Taylor growth rate and the PVPD forecasting methods will be compared using output from the same physics-based model (TIE-GCM). Finally, the improvement in PVPD forecasting skill when using a physics-based data assimilation model (AENeAS: Section 3.6) will be demonstrated for a single test case.

6.2. Scintillation Forecasting Using Rayleigh-Taylor Growth Rates

(Sultan, 1996) developed an expression to describe the ionospheric Rayleigh-Taylor instability growth rate (RTGR):

$$RTGR = \frac{\sum_P^F}{\sum_P^E + \sum_P^F}\left(V_P - U_L^P - \frac{g_e}{\nu_{eff}}\right)K^F - R_T\,, \qquad (6.1)$$

where $\sum_P^E$ and $\sum_P^F$ are the field line integrated E and F region Pedersen conductivities, V_P is the vertical (upwards) plasma drift speed at the magnetic equator, U_L^P is the integrated Pedersen conductivity-weighted neutral wind in the geomagnetic meridional and vertical plane, g_e is the acceleration due to gravity for a given altitude, ν_{eff} represents the F region ion-neutral collision frequency weighted by the electron density along the field line, K^F is the F region field line electron content height gradient, and R_T is the recombination rate integrated along the field line.

Carter et al. (Carter, Yizengaw, et al., 2014) used output from the TIE-GCM to calculate RTGRs for field lines passing over Vanimo, Papua New Guinea (141.3°E geographic longitude, -11.4°N magnetic latitude) during March and April 2000 and for multiple locations in March and April 2011 (Carter, Retterer, Yizengaw, Groves, et al., 2014). The daily maximum RTGR was used as a predictor for whether strong scintillation would be observed at that location. Carter et al. set the recombination rate (R_T) equal to zero, with K^F:

$$K^F = \frac{1}{N_e}\left(\frac{\partial N_e}{\partial h}\right). \quad (6.2)$$

Here h is the height and N_e is the integrated field line electron content. RTGR field line integration was conducted between an altitude of 125 km in one hemisphere to 125 km altitude in the other hemisphere, for field lines with peak altitudes of up to 600 km.

The dominant factor when calculating the daily maximum TIE-GCM RTGR is increased vertical plasma drift speed at the magnetic equator due to the PRE (Carter, Yizengaw, et al., 2014; Rajesh et al., 2017). Increases in geomagnetic activity limit the magnitude of TIE-GCM's enhancement of plasma drift speed thereby reducing TIE-GCM RTGR values (Carter, Yizengaw, et al., 2014). Days on which the maximum TIE-GCM RTGR value was low were found to correspond to days on which strong scintillation was not observed. Carter et al. (Carter, Yizengaw, et al., 2014) selected thresholds for the daily maximum RTGR and daily maximum hourly average of amplitude scintillation (S4) observations. The maximum S4 value for a chosen day was predicted to be above the S4 threshold only if the maximum RTGR value for that day was above the RTGR threshold. RTGR forecasting correctly predicted whether maximum S4 values would be above or below the S4 threshold on 48 of the 56 days considered. The Carter et al. approach demonstrated forecasting skill during seasons in which EPB generation was common; however, during seasons in which EPB generation was less frequent, RTGR forecasting performed worse than persistence forecasting at some locations (Carter, Retterer, Yizengaw, Wiens, et al., 2014).

Forecasting skill with TIE-GCM can be improved by using data assimilation (DA). This approach provides a more accurate representation of the ionospheric conditions so should produce more accurate forecasts. DA has been shown to improve the accuracy of the RTGR forecasting technique (Rajesh et al., 2017). However, results have only been published for a two day test scenario so it is not yet well validated. A drawback of incorporating DA is the increased computational expense of the background model.

6.3. Scintillation Forecasting Using a Proxy for Vertical Plasma Drift

Another approach for forecasting scintillation is the use of proxy vertical plasma drifts (PVPDs). Anderson et al. (2004) calculated PVPDs at the magnetic equator by determining the virtual height associated with a plasma frequency of 4 MHz ($\sim 2 \times 10^{11}$ e^-/m^3) and investigating the rate of change of this height. PVPD speeds greater than 20 ms^{-1} between 1830 and 2000 local time (LT) were found to correspond to strong scintillation observations (five minute average S4 > 0.5) during the subsequent evening (Anderson et al., 2004). Maximum PVPD speeds less than 20 ms^{-1} corresponded to days in which strong scintillation was not observed. This approach successfully predicted whether strong scintillation would occur on 84% of 300 consecutive days in 2001 and 2002. Two key limitations to this approach were that regional forecasts could not be produced until the observation window had commenced and the need for a local ionosonde.

Limited antecedence and the need for an ionosonde would be avoided if PVPD calculations used model output rather than ionosonde data. Since the change in virtual height of a 4 MHz ionosonde return signal can be represented by the change in altitude of electron density

2×10^{11} e^-/m^3 (assuming that the virtual height changes at the same rate as the true height), PVPD calculations using a model require only electron densities, their corresponding altitudes, and the interval between simulated observations. Therefore, it is straightforward to use output from a 3D ionospheric model to generate scintillation forecasts using PVPDs. In this study, the height of the 2×10^{11} e^-/m^3 electron density is determined using linear interpolation between vertically adjacent grid points. The maximum PVPD is determined by the largest change in height of the 2×10^{11} e^-/m^3 electron density between each consecutive 15-minute model time step from 1830 to 2000 LT. If the maximum PVPD speed at a location on the magnetic equator is greater than a specified threshold, a forecast for strong scintillation conditions in the subsequent evening is predicted for that longitude.

PVPD forecasting requires model output from one altitude profile per time step since only points at the magnetic equator are necessary for a forecast at that specific longitude. RTGR forecasting, however, needs a greater number of profiles per time step as model conditions are required at several locations along the magnetic field lines. PVPD values are calculated for 1830-2000 LT whereas RTGR forecasting calculates maximum daily RTGR values so a larger number of time steps are required. The complexity of the individual calculations required for PVPD and RTGR forecasting are similar, however, RTGR forecasting requires a greater number of calculations and TIE-GCM output corresponding to a greater number of variables, time steps, and grid points per time step. Once TIE-GCM output has been produced the calculation of PVPDs is, therefore, less complex and less computationally expensive than calculating RTGRs. However, the computational expense of the PVPD and RTGR calculations is significantly less than the expense of running a physics-based ionosphere-thermosphere model such as TIE-GCM or a data assimilation (DA) model such as AENeAS.

PVPD forecasting only requires electron densities and associated altitude as inputs whereas RTGR forecasting also requires Pedersen conductivity, neutral wind speed, and ion-neutral collision frequencies. Therefore, PVPD forecasting could be performed using output from an ionospheric DA model. However, the majority of currently existing DA models do not provide output for all variables required for RTGR forecasting.

6.4. Methods for Comparison of Scintillation Forecasting Skill

6.4.1. S4 Calculation

Various methods can be used to determine scintillation strength for a given evening from a set of amplitude scintillation (S4: Section 2.5.3) observations. Carter et al. (Carter, Yizengaw, et al., 2014) calculated the mean GPS S4 (with 5° minimum elevation) from the Vanimo Ionospheric Scintillation Monitor for each hour and used the maximum value to represent scintillation strength for that day. In later work (Carter, Retterer, Yizengaw, Groves, et al., 2014) the 90^{th} percentile of one minute S4 observations (30° minimum elevation) was calculated for each hour. The largest of these values ($S4_{90}$) represented scintillation strength for that evening. Maximum hourly average S4 values will be considered when comparing forecasting skill for Vanimo in March and April 2000 (Carter, Yizengaw, et al., 2014). $S4_{90}$ will be considered for Vanimo test cases, as well as test cases used in later work by Carter et al. (Carter, Retterer, Yizengaw, Groves, et al., 2014).

6.4.2. Performance Testing

RTGR forecasting has demonstrated forecasting skill including successfully predicting whether strong scintillation would occur at Vanimo, Papua New Guinea for 48 of the 56 days considered during March and April 2000 (Carter, Yizengaw, et al., 2014); however, this success was generated by retrospectively choosing thresholds to provide the optimal results, which would not be possible in an operational setting. A useful method for evaluating forecasting skill is the receiver operating characteristic (ROC) curve. A ROC curve keeps the observation threshold (S4) fixed while stepping through possible values for the predictor threshold (PVPD or RTGR). The true positive rate (TPR) and false positive rate (FPR) are calculated for each of the values for the predictor threshold. The TPR is the proportion of positive events (i.e. strong scintillation days) which were correctly predicted. The FPR is the proportion of negative events (i.e. weak scintillation days) which were incorrectly predicted to be a positive event. A ROC curve plots TPRs against FPRs (Figure 42a). The line $y = x$ indicates a forecasting method with no skill. A perfect model is represented by the line from (0,0) to (0,1) to (1,1). The area under the ROC curve (AUC) is equal to the probability that a model will rank a randomly chosen positive event higher than a randomly chosen negative event (i.e. the probability that a randomly chosen strong scintillation day will have a higher PVPD or RTGR than a randomly chosen weak scintillation day). Simply, if the predictor threshold is unknown, models with a larger AUC have greater forecasting skill and a model with no skill has AUC = 0.5 whereas a model with perfect skill has AUC = 1. Since the S4 threshold is fixed for an individual ROC curve, sets of ROC curves and AUCs can be calculated for a range of S4 threshold values (e.g. Figure 43a, Section 6.4.4). A further metric to determine forecasting skill using ROC curves is Youden's index (Youden, 1950), also known as the Peirce skill score (Peirce, 1884). The maximum Youden's index (YI)

value indicates the point on the ROC curve for which the model forecast skill improvement over random chance is greatest. YI is given by

$$YI = TPR - FPR\ , \tag{6.3}$$

which can be observed on a ROC plot as the vertical distance of a specific point on the ROC curve from the line representing no skill (the maximum YI is displayed for each forecasting method in Figure 42a). A maximum YI of 0 represents a method with no forecasting skill (as the skill is no better than chance) and a maximum YI of 1 represents a perfect model. The maximum YI can be calculated for a range of S4 threshold values (e.g. Figure 42b, Section 6.4.4) by inspection of the set of ROC curves generated using the same set of S4 thresholds.

6.4.3. Statistical Significance of Results

The methods described in Section 6.4.2 provide an assessment of the relative forecasting performance of the different approaches. It is also important to consider the absolute forecasting skill; i.e. whilst one approach may outperform the other, this is not useful if both approaches have little skill. The maximum YI is calculated from a wide range of PVPD or RTGR thresholds: if the S4 threshold is set so low or high that most observations fall into one class, any PVPD or RTGR threshold which is also particularly low or high may suggest higher forecasting skill than is actually present. The AUC may also be affected by low or high S4 thresholds. To address this, 100 randomly generated sequences of numbers were used as randomly generated forecasts (RGFs). If the PVPD and/or RTGR methods outperform at least 95 of these RGFs there is effectively 95% confidence that the method is more successful than

random chance. If more than five RGFs are capable of matching the performance of all considered forecasting methods for a chosen S4 threshold then the results for this threshold are not included in the analysis. For consistency the same 100 RGFs are used for each data set.

Statistical significance of results can be further impacted by small data sets. Each test case corresponds to a two month period and includes between 56 and 61 data points. Leave-one-out jackknifing (Quenouille, 1949) has been used to test whether small changes to a data set could have a large impact on results. One data point (one day) is removed from the data set and the model performance is calculated. This is repeatedly performed with each of the data points excluded in turn. The mean and standard deviation of these leave-one-out performance values are calculated. The mean and two standard deviations shown in Sections 6.4.4 and 6.4.5 effectively provides a ~95% confidence interval of forecasting skill for a specific S4 threshold when the data are subject to small variations.

6.4.4. Low-Latitude Scintillation Forecasting with TIE-GCM: Results

Carter et al. (Carter, Yizengaw, et al., 2014) showed that, using hourly average S4 values at Vanimo for 56 days in March and April 2000, RTGR forecasting could successfully predict that strong scintillation would occur on 17 days, successfully predict that strong scintillation would not occur on 31 days, predict strong scintillation which did not occur on 3 days, and predict that strong scintillation would not occur on 5 days for which strong scintillation was observed, i.e. whether strong scintillation would or would not occur was correctly predicted on 85.7% of days in the test case. This was achieved by predicting S4 would be greater than 0.244 when the daily maximum RTGR was greater than $0.625 \times 10^{-3} s^{-1}$. Using the same scintillation data and S4

threshold PVPD forecasting successfully predicted that strong scintillation would occur on 17 days, successfully predicted that strong scintillation would not occur on 29 days, predicted strong scintillation which did not occur on 5 days, and predicted that strong scintillation would not occur on 5 days for which strong scintillation was observed, i.e. whether strong scintillation would or would not occur was correctly predicted on 82.1% of days. This was achieved using a PVPD threshold of 18 ms^{-1} (i.e. there is a prediction of strong scintillation when the maximum PVPD speed is greater than 18 ms^{-1}).

Figure 42a displays a ROC plot for PVPD (blue) and RTGR (red) forecasting using TIE-GCM and persistence forecasting (green) for March and April 2000 at Vanimo, Papua New Guinea (141.3°E geographic longitude, -11.4°N magnetic latitude). Persistence forecasts were generated using the observed daily S4 value as the predictor value for the following day. In Figure 42a the maximum hourly average S4 threshold has been fixed using the value 0.244 that was retrospectively selected by Carter et al. (Carter, Yizengaw, et al., 2014). The maximum Youden's Index (YI) is indicated by a coloured circle for each forecasting method. There is not a significant difference between the overall performance of RTGR and PVPD forecasting; however, both the RTGR and PVPD forecasting methods clearly outperform persistence. In Figure 42b the maximum YIs corresponding to Figure 42a are presented for the range of S4 thresholds which resulted in PVPD, RTGR, or persistence forecasting outperforming at least 95 of 100 randomly generated forecasts (RGFs). In Figure 42b PVPD maximum YIs do not have a significant reduction in forecasting skill compared to RTGRs for any considered S4 thresholds, although the RTGR maximum YI is slightly higher than the PVPD maximum YI for the chosen S4 threshold of 0.244. Both PVPD and RTGR forecasting significantly outperform persistence forecasting for all considered S4 thresholds. Area under the ROC curves

(AUCs) are not displayed for this data set as at least 5% of the RGFs outperformed PVPD, RTGR, and persistence forecasting for all possible S4 thresholds. This suggests that an understanding of reasonable PVPD and RTGR thresholds to use is an important factor for forecasting skill if using the maximum hourly average to determine S4 values and thresholds.

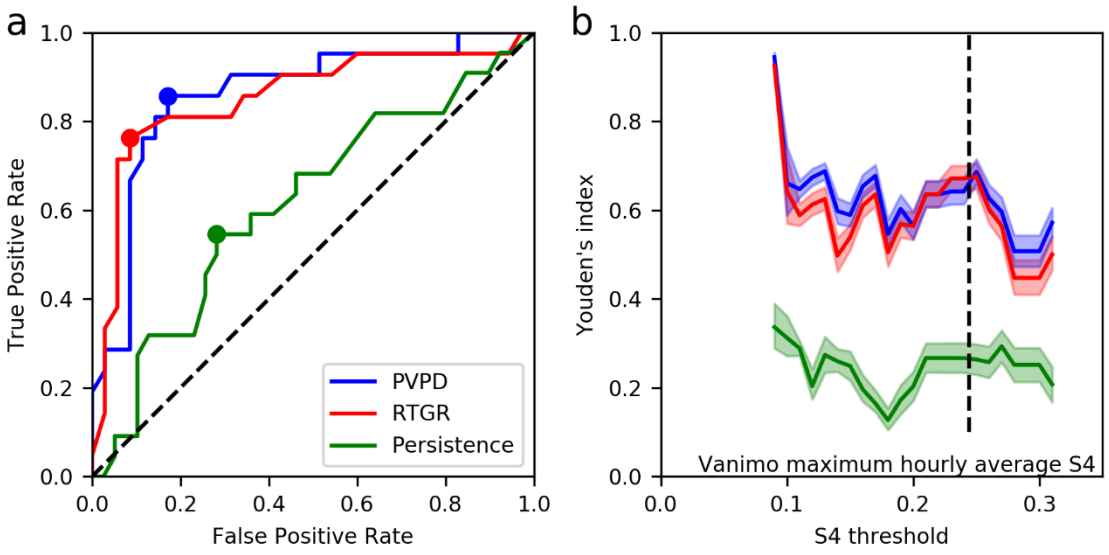

Figure 42. (a) ROC curve for scintillation forecasting performance using persistence forecasting (green), proxy vertical plasma drifts (PVPD, blue), and field line integrated Rayleigh-Taylor growth rates (RTGR, red) for 56 days in March and April 2000 at Vanimo, Papua New Guinea using the maximum hourly average S4. Coloured circles represent the point with the maximum Youden's index (YI). The black dashed line represents a model with no skill. The S4 threshold is set at 0.244. (b) The maximum YI values for a range of S4 thresholds. Coloured shaded regions represent the range of maximum YI values within the mean and two standard deviations from leave-one-out jackknifing (effectively a ~95% confidence interval of YI values subject to small changes in the data set). The vertical dashed line shows the S4 threshold 0.244 corresponding to the ROC curve in (a).

In Figure 43 the AUCs (Figure 43a) and maximum YIs (Figure 43b) are presented for the same conditions as Figure 42 when the maximum hourly 90th percentile of one minute S4 observations ($S4_{90}$) determines scintillation strength as used by Carter et al. (Carter, Retterer, Yizengaw, Groves, et al., 2014). In Figure 43a the horizontal black dashed line (AUC = 0.5) indicates no skill. In Figure 43a the range of S4 thresholds for which a forecasting approach outperforms 95% of RGFs is small. This provides further evidence that having an understanding of appropriate PVPD or RTGR thresholds to use is an important factor for the success of each approach. PVPD AUCs and maximum YIs are not significantly worse than RTGR AUCs or maximum YIs for all considered S4 thresholds at Vanimo, whether S4 is determined using the hourly average (Figure 42) or $S4_{90}$ (Figure 43).

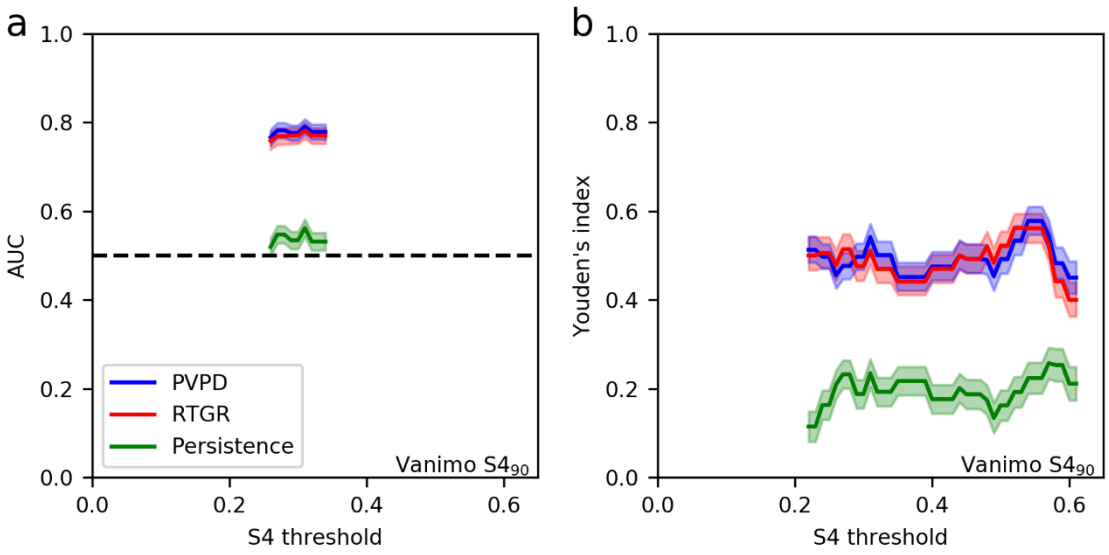

Figure 43. AUCs (a) and maximum Youden's index (b) for a range of $S4_{90}$ thresholds at Vanimo, Papua New Guinea for 56 days in March and April 2000.

Figure 44 and Figure 45 correspond to AUCs and maximum YIs respectively for $S4_{90}$ observations from March and April 2011 (Carter, Retterer, Yizengaw, Groves, et al., 2014) at

Ascension Island (geographic longitude (GLon) -14.4°E, magnetic latitude (MLat) -12.4°N), Calcutta (GLon 88.4°E, MLat 15.6°N), Guam (GLon 144.9°E, MLat 5.8°N), and Nairobi (GLon 36.8°E, MLat -10.8°N). PVPD forecasting performs as well or better than RTGR and persistence forecasting apart from AUCs at Ascension Island for $S4_{90}$ thresholds above 0.67 (Figure 44a), AUCs for very low $S4_{90}$ thresholds at Nairobi (Figure 44d), and maximum YIs

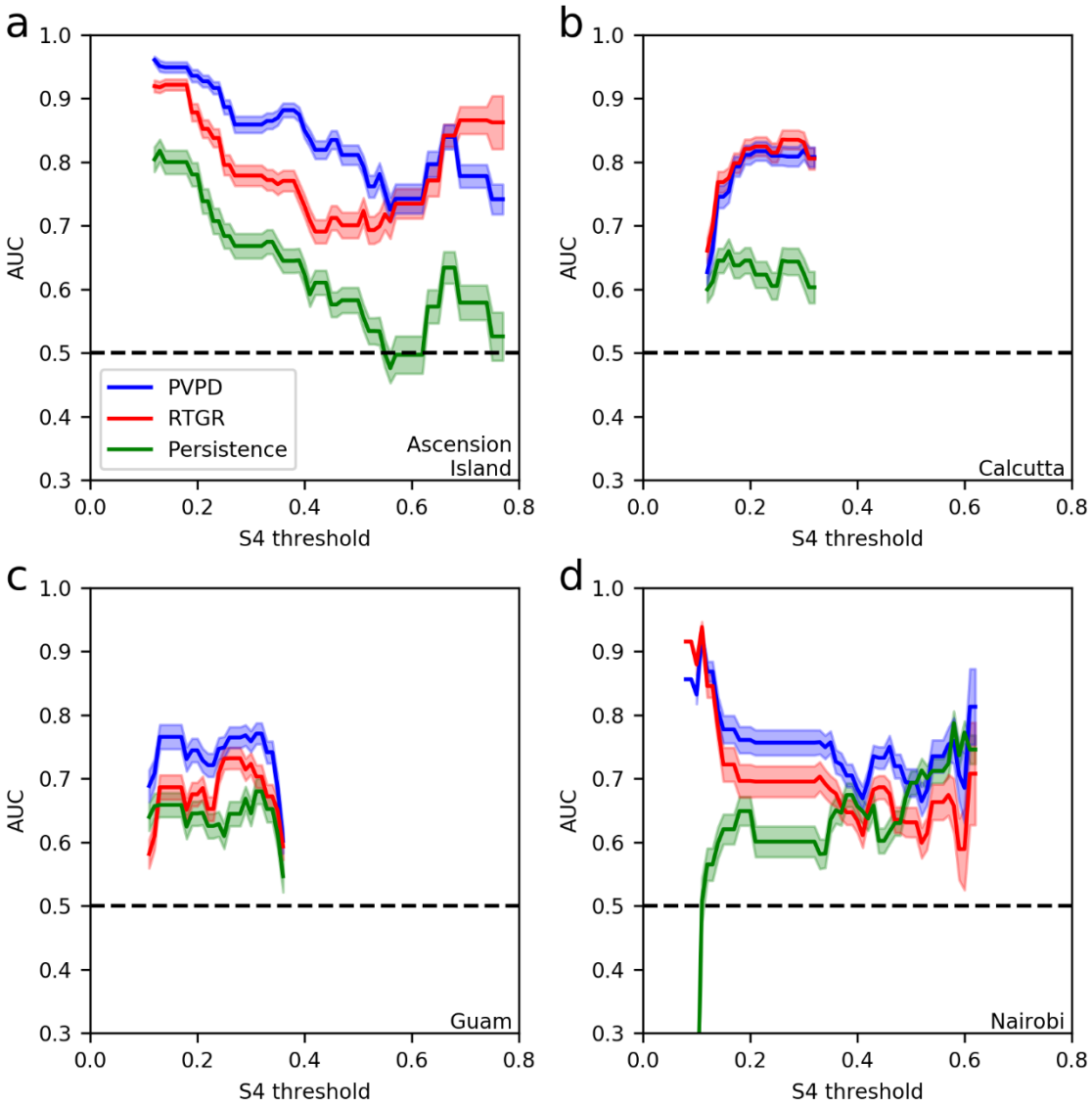

Figure 44. AUCs as in Figure 43a for a range of S490 thresholds at Ascension Island (a), Calcutta (b), Guam (c), and Nairobi (d) in March and April 2011.

for a very small range of $S4_{90}$ thresholds at Calcutta (Figure 45b). PVPD forecasting AUCs are significantly greater than both RTGR and persistence AUCs for all $S4_{90}$ thresholds below 0.55 at Ascension Island (Figure 44a), most $S4_{90}$ thresholds at Guam (Figure 44c), and most $S4_{90}$ thresholds between 0.15 and 0.49 at Nairobi (Figure 44d). PVPD forecasting maximum YIs are significantly greater than RTGR and persistence maximum YIs for all considered $S4_{90}$ thresholds at Ascension Island (Figure 45a) and Guam (Figure 45c).

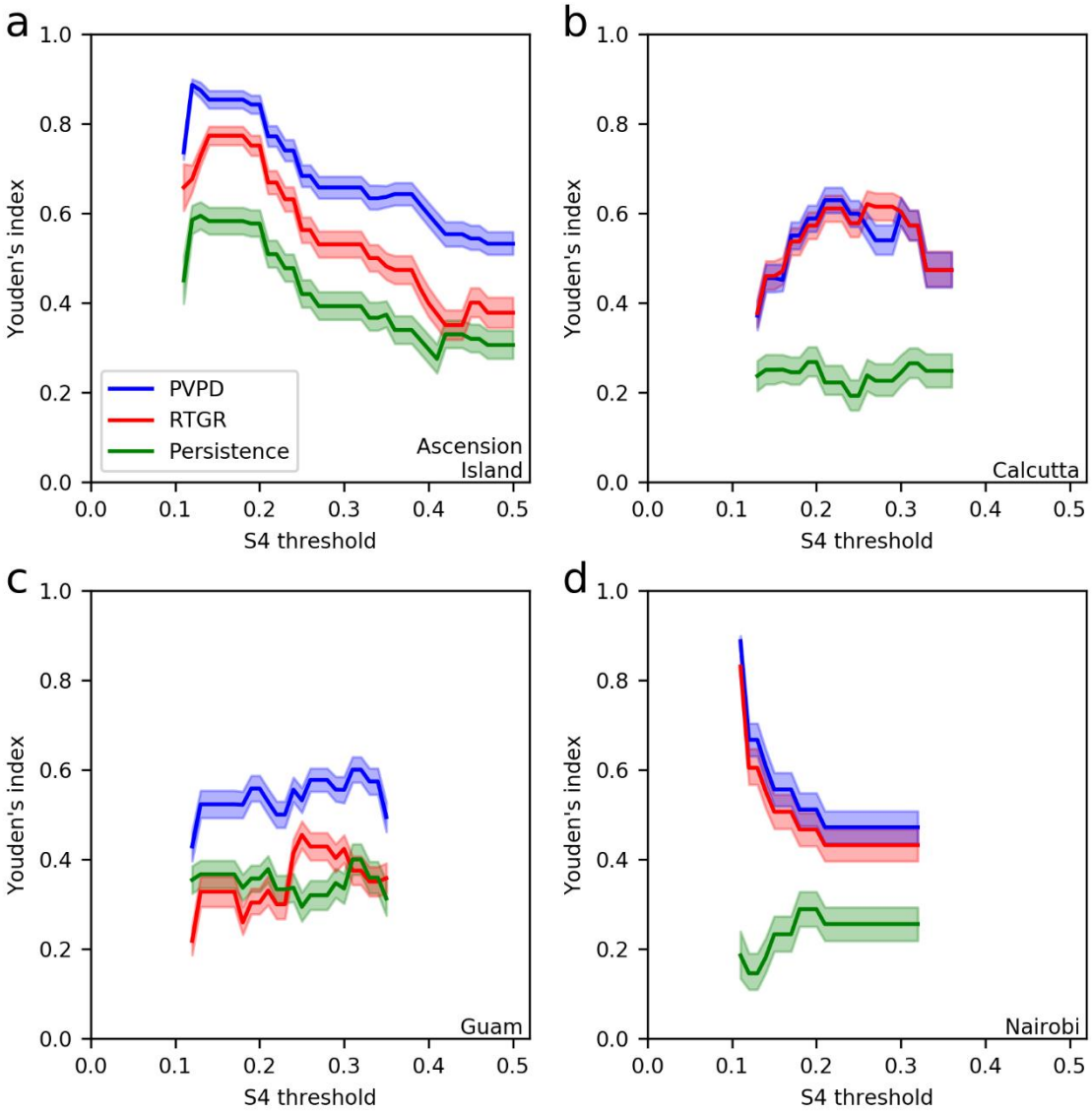

Figure 45. Maximum Youden's Index (YI) values corresponding to Figure 44.

Forecasting skill will be improved if suitable PVPD or RTGR thresholds are known prior to forecasting. However, these thresholds (and forecast success rates) are likely to vary under differing conditions such as longitude, season, and solar activity (Smith et al., 2016). The PVPD and RTGR threshold values which produced the maximum YI in the test cases considered are provided in Figure 46. There is a noticeable difference between the optimum PVPD thresholds for Vanimo when compared to the other four test cases. The Vanimo test case was for March and April 2000 whereas the other test cases were for March and April 2011. Solar activity was higher in March and April 2000 (monthly means of the daily total sunspot number (MDTSN) of 217.7 and 191.5) than in March and April 2011 (MDTSN of 78.6 and 76.1) suggesting that the optimum PVPD threshold may be dependent on solar activity. The optimum PVPD thresholds do not, however, appear to be heavily dependent on the choice of S4 threshold. In Figure 47 the maximum YIs are displayed for the Vanimo test case when the PVPD threshold is fixed at 18 ms^{-1} for all S4 thresholds. There is not a significant reduction in forecasting skill when compared to the RTGR forecasting skill. This behaviour is also seen in the other four test cases, apart from the small S4 range previously discussed at Calcutta (Figure 48).

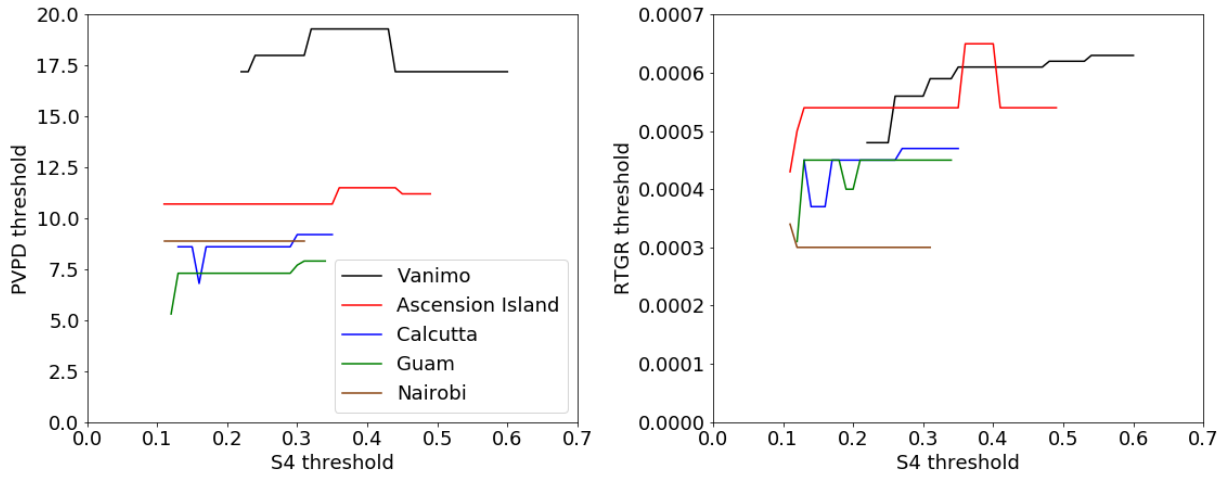

Figure 46. PVPD (left) and RTGR (right) thresholds used to obtain the maximum YI in the $S4_{90}$ test cases considered.

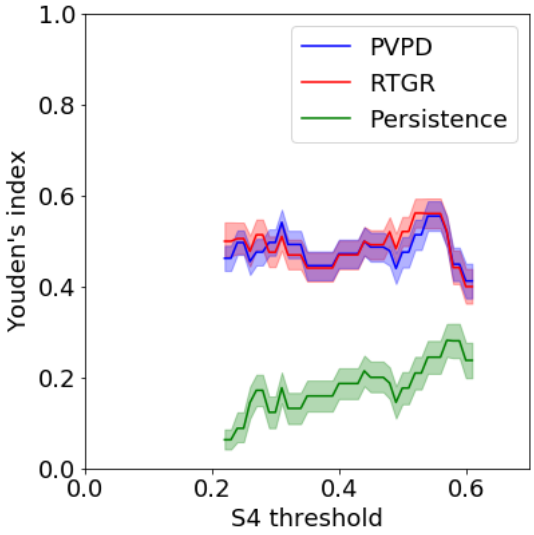

Figure 47. Maximum YIs at Vanimo in March and April 2000 when the PVPD threshold is fixed at 18 ms^{-1}.

The test cases discussed so far have previously been prsented by Carter et al. Further test cases are now considered. Carter, Yizengaw et al. (2014) used output from the Vanimo Ionospheric Scintillation Monitor (ISM) in March and April 2000 to test whether RTGR forecasting had skill. Vanimo ISM data is available from August 1999 to October 2000, March 2001 to October 2002, March 2003 to May 2004, October to December 2006, February 2007 to August 2008, and October 2008 to June 2009. We will now consider PVPD and RTGR forecasting performance during each pair of equinoctial (March and April, September and October) or solstitial (June and July, December and January) months within these periods.

The day-to-day variability of $S4_{90}$ daily maximum values from the Vanimo ISM shows a clear dependence on solar activity. *Figure 49* shows $S4_{90}$ daily maximum values from September 1999 to June 2009. Between 1999 and 2004 (top) solar activity was relatively high and there is clearly considerable day-to-day variability, with a quiet day background value roughly between

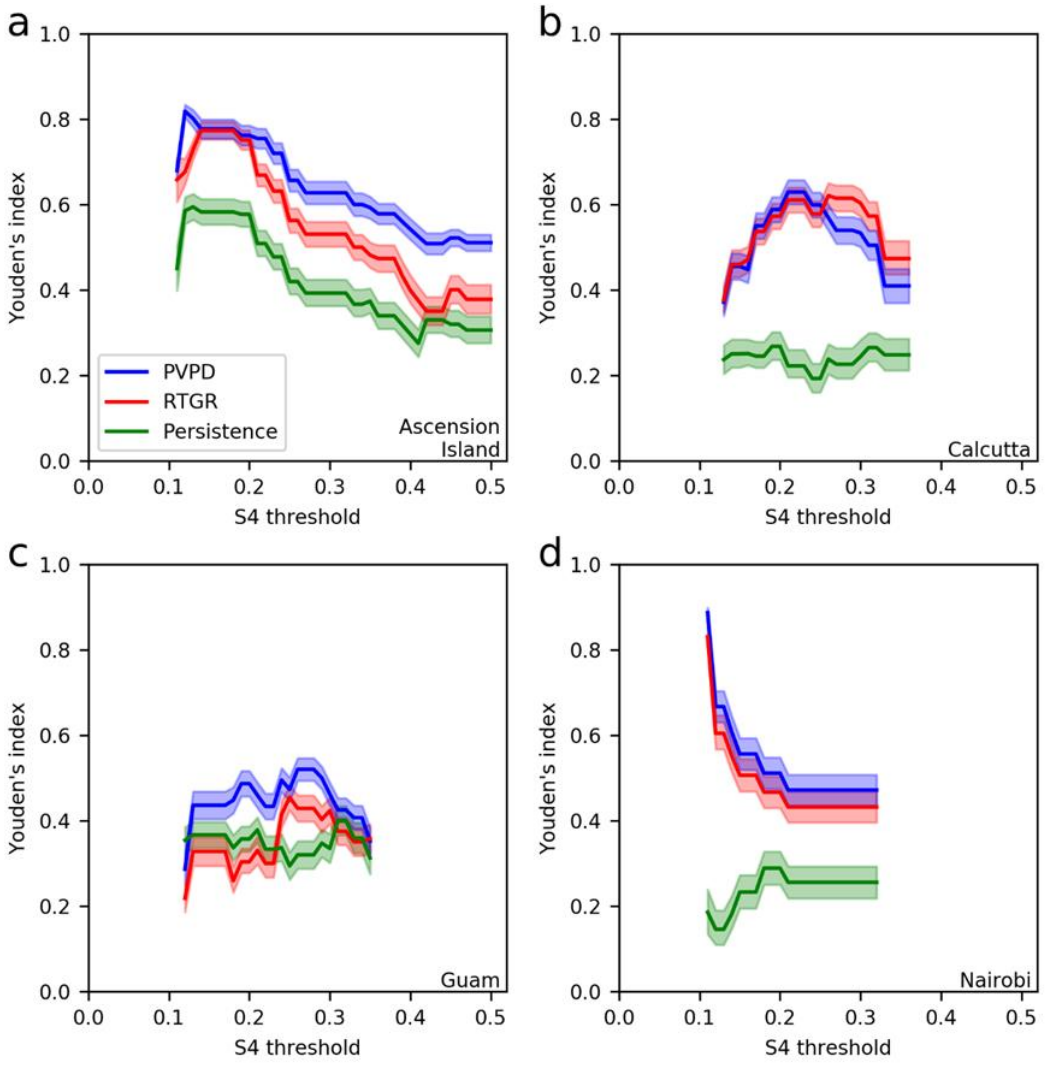

Figure 48. Maximum Youden's indices (YI) as for Figure 45 but with PVPD thresholds fixed for all S4 thresholds at a location. PVPD thresholds chosen were 11 (a), 9 (b), 7 (c), and 9 (d) ms^{-1} at Ascension Island, Calcutta, Guam, and Nairobi respectively.

0.15 and 0.25. Between 2006 and 2009 (bottom) solar activity was lower. The day-to-day $S4_{90}$ variability is small and $S4_{90}$ values tend to remain close to the quiet day background values seen between 1999 and 2004. Indeed, during all days on which the Vanimo ISM data is available

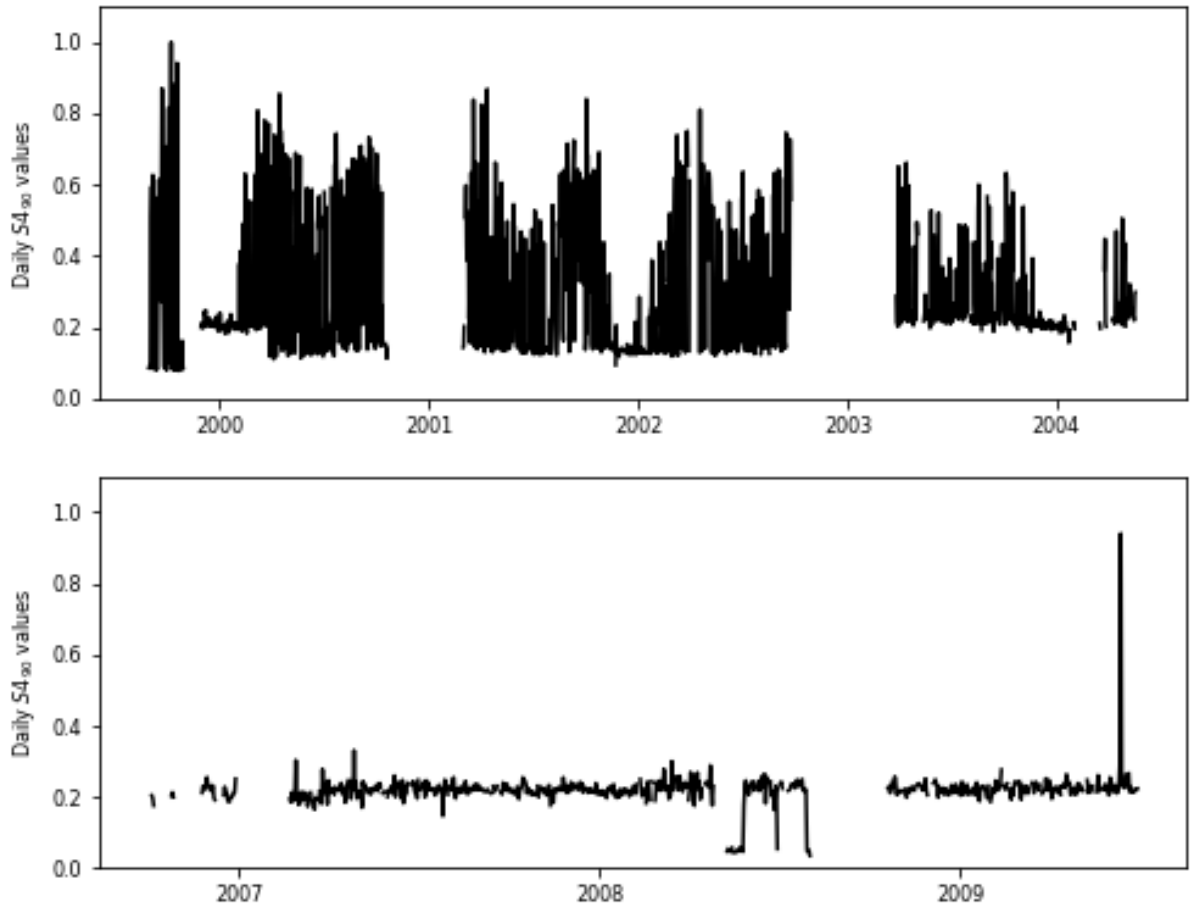

Figure 49. Daily $S4_{90}$ values for data available from the Vanimo Ionospheric Scintillation Monitor.

between 2006 and 2009, there were only 4 days on which the daily $S4_{90}$ value exceeded 0.3. Therefore, as persistent strong scintillation is not present in these years, analysis of forecasting skill for these years would be both pointless and misleading. This is also true for winter solstitial months (December and January) during high solar activity years. During the years considered (1999 to 2004), there was only one daily $S4_{90}$ value greater than 0.3 in December or January (no data are available for December 2000 and January 2001 or December 2002 and January 2003). Therefore, further test cases to be considered will include all equinoctial and June-July

Table 6. Number of days for which Vanimo ISM data is available in each two-month equinoctial and summer solstitial test case between 1999 and 2004. The monthly means of the daily total sunspot number are also provided.

Months	Days of available data	Monthly means of daily total sunspot numbers
Sep/Oct 1999	61	106.3, 168.7
Mar/Apr 2000	59 (56 used by Carter, Yizengaw, et al. (2014))	217.7, 191.5
Jun/Jul 2000	53	188.0, 244.3
Sep/Oct 2000	45	156.0, 141.6
Mar/Apr 2001	58	165.8, 161.7
Jun/Jul 2001	61	202.9, 123.0
Sep/Oct 2001	61	238.2, 194.1
Mar/Apr 2002	44	147.1, 186.9
Jun/Jul 2002	61	128.8, 161.0
Sep/Oct 2002	26	187.9, 151.2
Mar/Apr 2003	34	100.7, 97.9
Jun/Jul 2003	60	118.7, 128.3
Sep/Oct 2003	58	78.5, 97.8
Mar/Apr 2004	33	74.8, 59.2

pairs of months between 1999 and 2004 for which significant data gaps are not present. Table 6 provides the number of days for which S4 data is available during each of these pairs of months. Test cases in which over a third of days do not have data available will not be included

in the analysis. Results for March and April 2000 have already been discussed. Therefore, we will now consider forecasting skill for March and April in 2001 and 2002, September and October in 1999, 2000, 2001 and 2003, and June and July in 2000, 2001, 2002 and 2003. In Figure 50 the maximum PVPD, RTGR, and persistence forecasting YIs are shown for March and April in 2001 and 2002. As seen in the previously discussed test cases, PVPD forecasting skill is as good as or better than RTGR forecasting for all considered $S4_{90}$ thresholds. PVPD forecasting also outperforms persistence forecasting for all considered $S4_{90}$ thresholds. Figure 51 displays maximum YIs for September and October 1999, 2000, and 2001, and June and July 2002. In September and October 1999, 2000, and 2001 the PVPD and RTGR forecasting skill is very similar. In June and July 2002 PVPD forecasting outperforms RTGR and persistence forecasting. However, PVPD forecasting is only able to outperform 95% of random forecasts for a small range of $S4_{90}$ thresholds. The PVPD and RTGR thresholds used to obtain these results are shown in Figure 52. The optimal PVPD thresholds for March and April in 2001 and

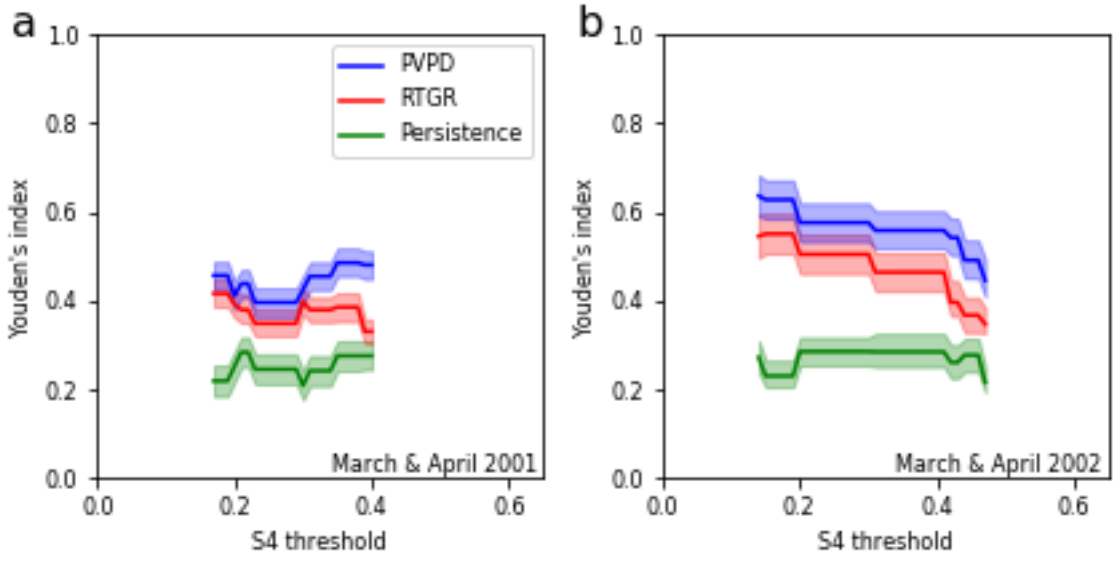

Figure 50. Maximum YIs at Vanimo in March and April 2001 (a) and 2002 (b).

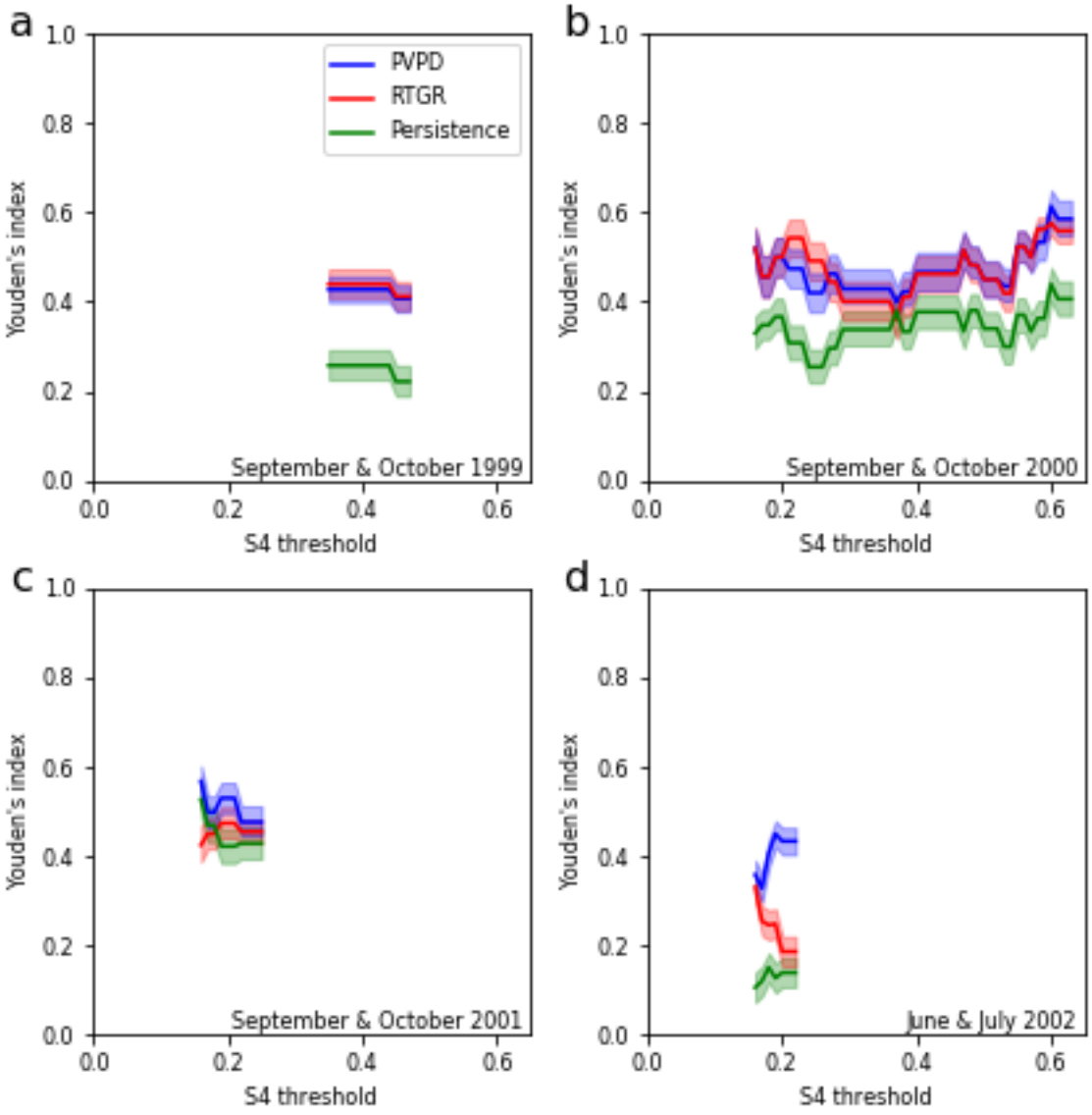

Figure 51. Maximum YIs at Vanimo in September and October 1999 (a), 2000 (b), and 2001 (c), and in June and July 2002 (d).

2002 are lower than those used for March and April 2000 (Figure 46). The PVPD thresholdsfor September and October 1999 are lower than those used for September and October 2000, which tend to be lower than those used for September and October 2001. The monthly means of the daily total sunspot numbers (MDTSN: Table 6) in March and April 2000 are considerably higher than those for March and April 2001 and 2002. The MDTSNs for September and October 2001 are considerably higher than those for September and October in 1999 and 2000.

MDTSNs for October 1999 and September and October 2000 are similar. However, the MDTSN for September 1999 is considerably lower. This lends further support to the suggestion that solar activity appears to be an important factor when determining the optimal PVPD threshold to use. It also suggests that the choice of PVPD threshold may be dependent on whether the equinoctial months are in the spring or autumn as, for example, the September and October 2001 PVPD thresholds are lower than the March and April 2000 PVPD thresholds despite having slightly higher MDTSNs.

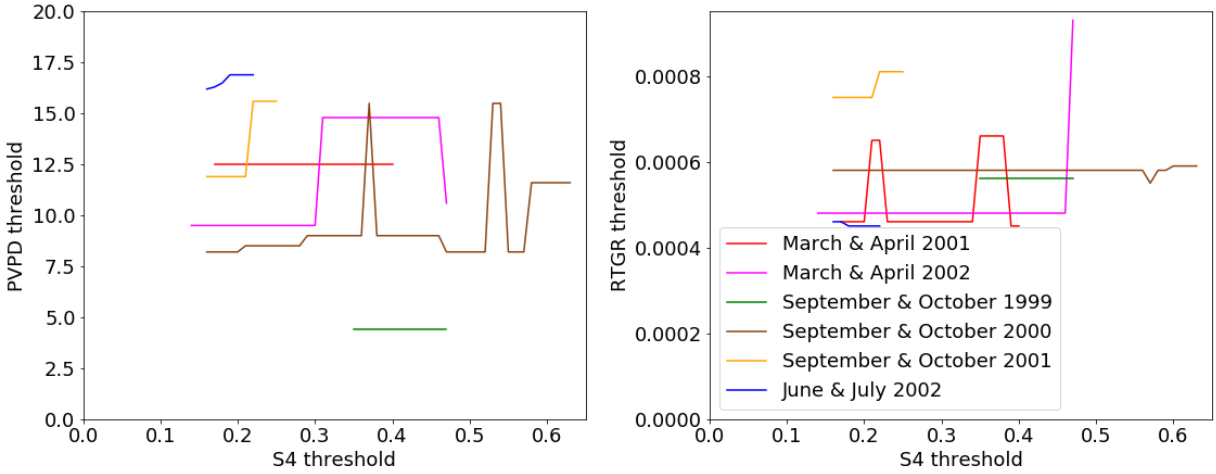

Figure 52. PVPD (left) and RTGR (right) optimal thresholds used for Vanimo test cases in March and April 2001 and 2002, September and October 1999, 2000, and 2001, and June and July 2002, corresponding to results shown in Figure 50 and Figure 51.

In June and July 2000, 2001, and 2003, and in September and October 2003 each of the three forecasting techniques are unable to outperform 95% of random forecast maximum YIs for any choice of $S4_{90}$ threshold. The poor performance of PVPD and RTGR forecasting during the June and July test cases suggest that these forecasting methods, when using TIE-GCM, may not be suitable for scintillation forecasting during solstitial months. In the September and October 2003 test case the PVPD values are particularly low, with only one PVPD value in this test case

exceeding 10.1 ms^{-1}. This may be due to lower solar activity during this Vanimo test case which has suppressed the equinoctial TIE-GCM daily PVPD values. Also, it may not be a coincidence that the only equinoctial test case which does not demonstrate any obvious forecasting skill includes extremely disturbed solar and geomagnetic conditions (including the Halloween storm). One should bear in mind with these results that TIE-GCM day-to-day variability is only driven by 3 hourly Kp and daily F10.7 solar flux values. However, it would be expected that the inclusion of data assimilation would improve ionospheric specification and, therefore, scintillation forecasting skill. Therefore, we now consider PVPD forecasting skill when using AENeAS (Section 3.6) output to generate PVPD forecasts.

6.4.5. Low-Latitude Scintillation Forecasting with AENeAS

The forecasting skill of the Rayleigh-Taylor growth rate (RTGR) and proxy for vertical plasma drift (PVPD) approaches have been discussed when using TIE-GCM output. PVPD forecasting skill is now considered for a single test case when AENeAS output is used. In this work an independent TIE-GCM simulation is used for each of 32 AENeAS ensemble members. GNSS total electron content (TEC) observations from the Madrigal database are assimilated once in each 15 minute model time step. A direct comparison between PVPD forecasting skill using TIE-GCM and AENeAS can be obtained by using the mean AENeAS electron densities and altitudes for the same latitude, longitude and pressure level across all ensemble members. Vertical linear interpolation provides a single altitude for an electron density of 2×10^{11} e^-/m^3 at a specified location on the magnetic equator. The change in height of this electron density can then provide a maximum PVPD value using the method described in Section 6.3.

Figure 53 demonstrates forecasting skill for a range of $S4_{90}$ thresholds at Vanimo, Papua New Guinea for 56 days in March and April 2000 as discussed in the previous subsection and by Carter, Yizengaw, et al. (2014). Figure 53a and Figure 53b show the area under the ROC curve and the maximum YIs respectively.

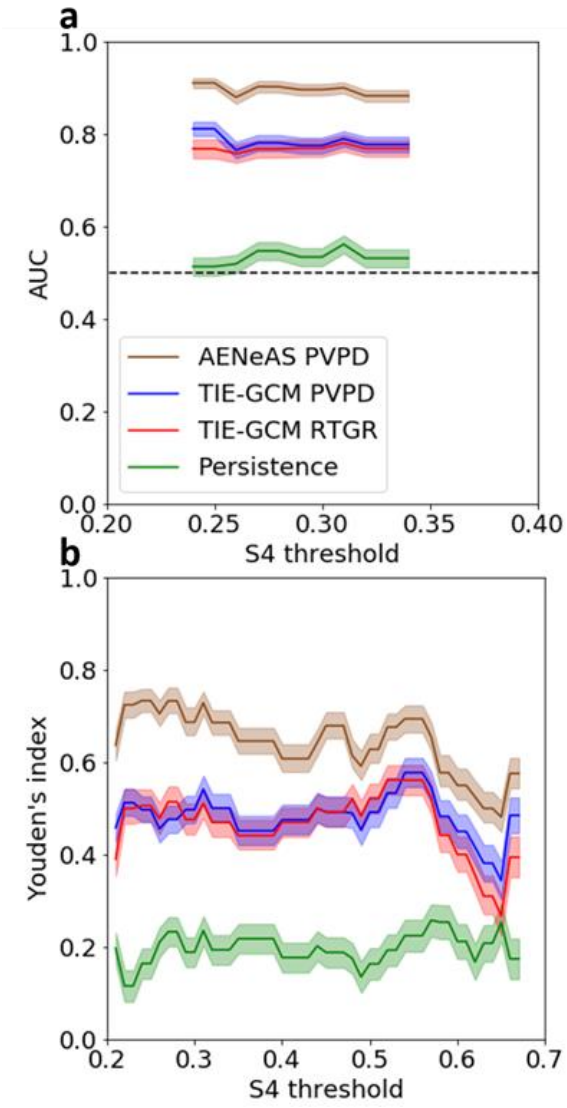

Figure 53. AUCs (a) and maximum YIs (b) for PVPD forecasting with AENeAS (brown) and TIE-GCM (blue), RTGR forecasting with TIE-GCM (red), and persistence forecasting (green) at Vanimo, Papua New Guinea in March and April 2000. Coloured shaded regions represent the range of skill values within the mean and two standard deviations from leave-one-out jackknifing. The horizontal dashed line in (a) represents a model with no skill.

Figure 53 clearly shows that in this test case, for all considered $S4_{90}$ thresholds using both AUCs and maximum YIs, AENeAS PVPD forecasting (brown) consistently outperforms TIE-GCM PVPD (blue) and RTGR (red) forecasting and persistence forecasting (green). However, the use of AENeAS output provides a further distinct advantage over TIE-GCM when used for PVPD forecasting: the ability to use the ensemble to generate probabilistic forecasts.

7. PROBABILISTIC FORECASTING OF LOW-LATITUDE SCINTILLATION

7.1. Methods

Probabilistic forecasts of low-latitude scintillation can provide a clearer understanding of whether strong scintillation will occur than deterministic forecasts, as probabilistic forecasts provide information about the uncertainty of an event. Therefore, probabilistic forecasts provide end-users with greater insight when determining whether action will need to be taken to mitigate scintillation effects.

Using the AENeAS (Section 3.6) ensemble mean to generate proxy for vertical plasma drift (PVPD) forecasts has demonstrated an improvement in forecasting skill when compared to PVPD forecasting with a single TIE-GCM simulation (Section 6.4.5); however, the availability of output from each ensemble member provides an opportunity to generate a probabilistic forecast of low-latitude scintillation. Using the approach discussed in Section 6.3, the maximum PVPD can be determined for each ensemble member to produce an ensemble of PVPD values. One simple method to provide a probabilistic forecast would be to use the proportion of ensemble members for which the PVPD value is above the PVPD threshold as the probability of strong scintillation occurring (a frequentist approach). However, this approach can only produce reasonable probabilistic estimates if many ensemble members are available and the forecasted event is not climatologically rare (Joliffe & Stephenson, 2012). A method which requires a smaller number of ensemble members is to use the ensemble of PVPD values to estimate the probability density function (PDF) of the PVPD speed at a chosen time and location. For each PVPD ensemble member a Gaussian PDF is produced with mean equal to the PVPD value and a fixed standard deviation (SD). The estimated overall PVPD PDF is the

normalised sum of these PDFs. This method is referred to as kernel density estimation (KDE), using a Gaussian kernel (Figure 54). Kernels with other distributions could also be chosen; however, Gaussian kernels are commonly used when determining the PDF of a variable unless the variable is bounded, e.g. a variable which is restricted to non-negative values such as precipitation (Wang & Bishop, 2005). As PVPD values are unbounded, and in the absence of information to suggest that an alternative kernel would be more effective, Gaussian kernels will be used for the KDE.

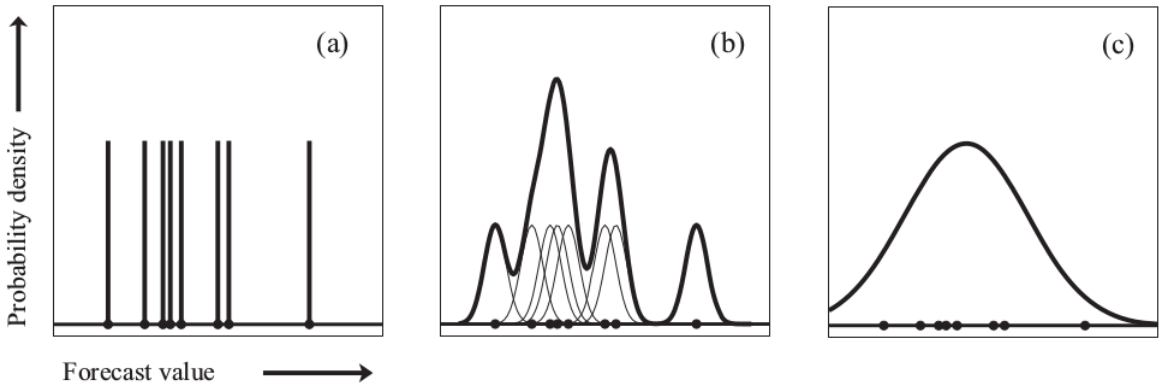

Figure 54. Cartoon of methods to estimate the probability density function (PDF) from an ensemble of values. (a) Frequentist approach: use the proportion of sample values above/below the chosen threshold to determine the probability that a randomly selected value is above/below the threshold, (b) Kernel density estimation with a Gaussian kernel: create a PDF by taking the normalised sum of Gaussian distributions, each of which has mean equal to an ensemble value, and (c) PDF fitting: fit a PDF which is representative of the sample of ensemble values (Joliffe & Stephenson, 2012).

The choice of standard deviation (SD) for the set of Gaussian distributions is an important factor as it can significantly affect the final PVPD PDF. If the SD is too small the resulting PDF will

be too dependent on each ensemble member output value, effectively producing a spike at each output value (i.e. as the SD tends to zero the PVPD PDF approaches the frequentist distribution). This does not take into account that the ensemble member PVPDs are only samples from the underlying unknown PDF. If the SD is too large then information from the individual PVPD values about the underlying distribution will be lost. To find a SD which avoids these issues, j evenly spaced SD values between (e.g.) zero and ten (zero not included) are tested. Leave-one-out cross-validation determines the best SD to use in the following way:

1) k ensemble members are used to generate k PVPD values. Select one PVPD value to be the test set. The remaining $(k-1)$ PVPD values are the training set.

2) From the set of j SDs, $\mathrm{SD}_i (i \in 1, \dots, j)$ is used as the KDE SD, thereby generating j PVPD PDFs using the $(k-1)$ PVPD values in the training set.

3) Find the probability density of the test set value in each of the PVPD PDFs. These densities provide a likelihood function of SDs which would produce the test set value.

4) Repeat steps one to three $(k-1)$ times so each PVPD value has been used as the test set value. k likelihood functions have now been produced.

5) The product of the k likelihoods associated with $\mathrm{SD}_i (i \in 1, \dots, j)$ provide the likelihood that the PVPD PDF generated using SD_i would produce the k PVPD values. The SD with the greatest of these combined likelihoods is chosen as the SD to be used for the KDE of the final PVPD PDF with all k PVPD values.

Some examples of PVPD PDFs which could be generated in this way using 32 AENeAS ensemble members are displayed in Figure 55.

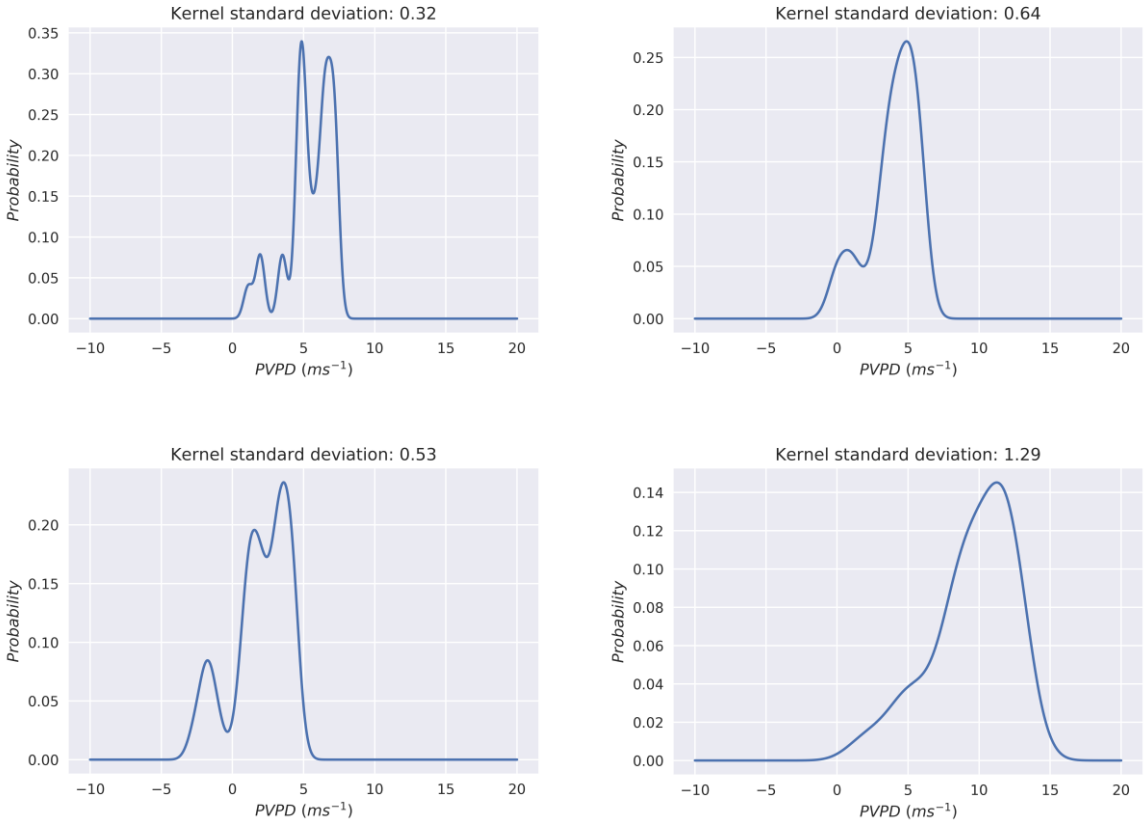

Figure 55. Examples of PVPD PDFs created using kernel density estimation with a Gaussian kernel. PDFs have been selected from within a seven hour period in August 2011.

The PVPD PDF can then be used to estimate the probability that a PVPD is greater than a chosen threshold, $\mathrm{P}(\mathrm{PVPD} > \mathrm{PVPD}_{\mathrm{thresh}})$, by determining the proportion of the area under the PDF curve which is above the PVPD threshold. The probability of strong scintillation occurring during the subsequent night, $\mathrm{P}(\mathrm{S4} > \mathrm{S4}_{\mathrm{thresh}})$, can be determined using the law of total probability (Kolmogorov, 1950):

$$\begin{aligned} \mathrm{P}(\mathrm{A}) &= \mathrm{P}(\mathrm{A} \cap \mathrm{B}) + \mathrm{P}(\mathrm{A} \cap \mathrm{B}^{\mathrm{C}}) \\ &= \mathrm{P}(\mathrm{A} \mid \mathrm{B})\mathrm{P}(\mathrm{B}) + \mathrm{P}(\mathrm{A} \mid \mathrm{B}^{\mathrm{C}})\mathrm{P}(\mathrm{B}^{\mathrm{C}}), \end{aligned} \tag{7.1}$$

for events A and B, where B^C is the complement of B (i.e. $P(B^C) = 1 - P(B)$, the probability that event B does not occur) and $P(A \mid B)$ is the conditional probability that event A will occur given that event B has occurred. Therefore,

$$\begin{aligned} P(S4 > S4_{thresh}) = {} & P(S4 > S4_{thresh} \mid PVPD > PVPD_{thresh}) \\ & \times P(PVPD > PVPD_{thresh}) \\ & + P(S4 > S4_{thresh} \mid PVPD \leq PVPD_{thresh}) \\ & \times P(PVPD \leq PVPD_{thresh}) . \end{aligned} \tag{7.2}$$

Anderson et al. (2004) reported that the maximum five minute average S4 between sunset and sunrise was found to be greater than 0.5 on 90% of days with observed PVPDs greater than 20 ms^{-1} and less than 0.5 on 85% of days with PVPDs less than 20 ms^{-1}. Using these values, the probability that the maximum five minute average S4 is greater than 0.5 is given by

$$\begin{aligned} P(S4 > 0.5) &= P(S4 > 0.5 \mid PVPD > 20\ ms^{-1}) \\ &\quad \times (PVPD > 20\ ms^{-1}) \\ &\quad + P(S4 > 0.5 \mid PVPD \leq 20\ ms^{-1}) \\ &\quad \times P(PVPD \leq 20\ ms^{-1}) \\ &= 0.9\ P(PVPD > 20\ ms^{-1}) \\ &\quad + (1 - 0.85)[1 - P(PVPD > 20\ ms^{-1})] \\ &= 0.15 + 0.75\ P(PVPD > 20\ ms^{-1}) , \end{aligned} \tag{7.3}$$

where $\mathrm{P}(\mathrm{PVPD} > 20\ \mathrm{ms}^{-1})$ is determined from the PVPD PDF. However, as discussed in the previous chapter, these thresholds and forecast success rates are likely to vary under differing conditions such as location, season and solar activity (e.g. Smith et al., 2016).

A dummy example of a global forecast of the strongest scintillation which would be observed between sunset and sunrise for all locations which are currently post-sunset or for which sunset will occur within the next six hours is shown in Figure 56. Following discussion with the Met Office Space Weather Operations Centre (MOSWOC) steps have been taken to provide maps of low-latitude scintillation which are consistent with existing Met Office space weather forecasting tools. To this end a four-colour system is used to show when the likelihood of strong scintillation is forecasted to be less than 25%, between 25% and 50%, between 50% and 75%, or greater than 75%. The timestamp for the forecast is displayed in the lower left-hand corner of the plot (as in other MOSWOC images). For ease of use, meridian lines and the magnetic equator are shown. Since the forecasts cover a six-hour lead-time there are regions which are in daylight for the total period of the forecast. This region remains white in the forecast plot to show that no forecast has been provided for this region. High latitude regions also remain white as scintillation forecasts are not provided for these areas. Although this example is consistent with existing Met Office space weather tools, the output can be adapted for other users. For example, if an action was only deemed to be safe if the probability of strong scintillation was below 25%, an operator may be under the mistaken impression that the probability was below 25% in one location but the probability was above 25% a few metres away. The displayed probabilities are representative of the strong scintillation probability at a TIE-GCM grid point longitude, extending 2.5 degrees east of each grid point to capture the eastward motion of equatorial plasma bubbles. An alternative visualisation could include a greater number of

segmentations of probabilities (i.e. number of colours included in the colourbar) or providing a smoothed colour scheme with interpolation between TIE-GCM longitudes.

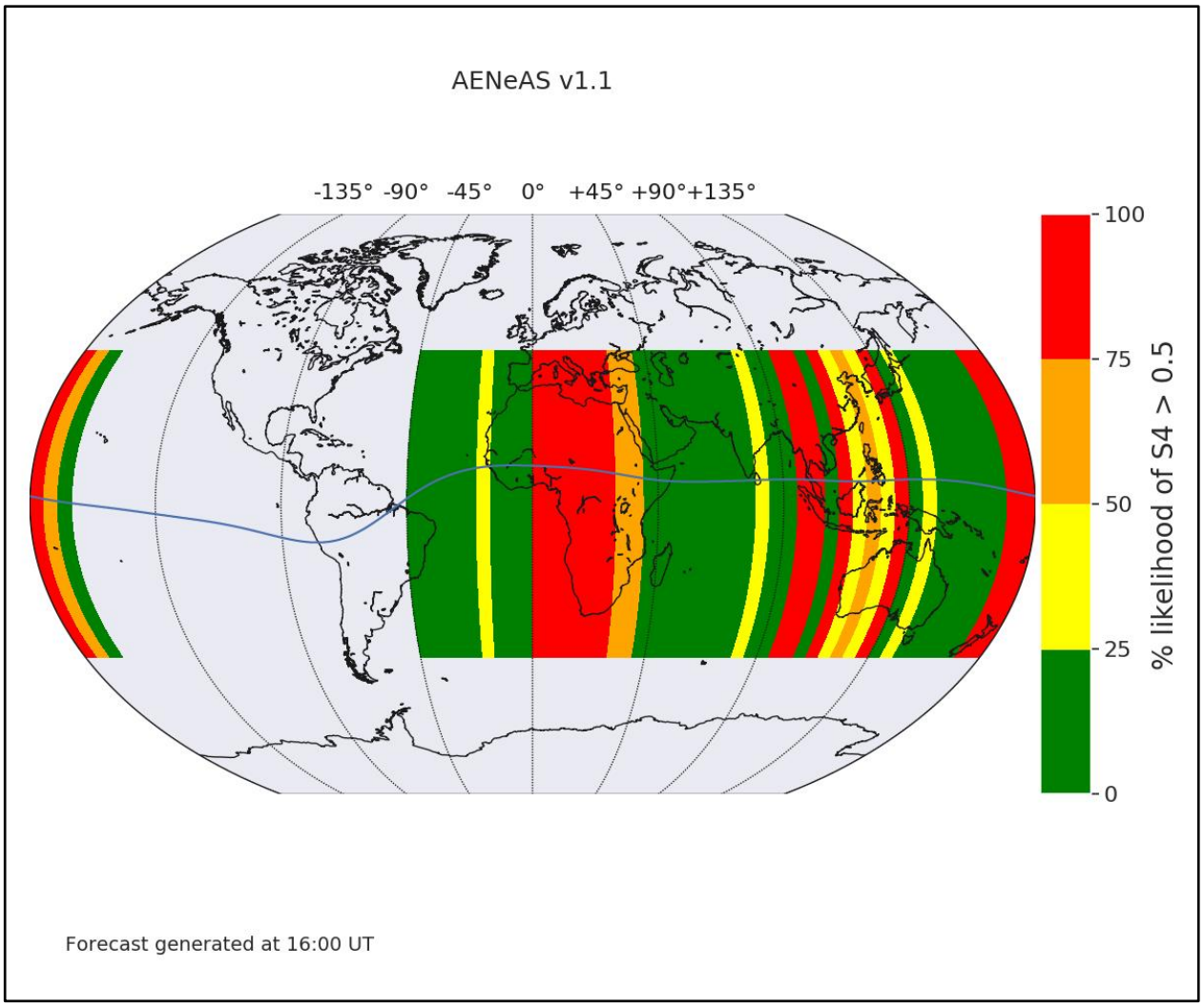

Figure 56. Plot of low latitude scintillation forecast for 16:00 - 22:00 UT on 8 March 2000. Colours represent the likelihood of the five-minute average S4 exceeding 0.5 during the current/upcoming evening. Note that the forecast does not make a prediction of latitudinal extent, only whether scintillation is likely to be observed at low latitudes.

7.2. Improving the Forecast: Temporal Resolution and Latitudinal Extent

PVPD forecasting has provided forecasts in a similar format to those provided by Carter et al. (e.g. 2014) and Anderson et al. (e.g. 2004), i.e. forecasts of whether strong scintillation will occur at a location in a 24-hour period or between sunset and sunrise. It is understood that, particularly during equinoctial months (at locations where the magnetic equator is roughly parallel to the geographic equator), equatorial plasma bubbles (EPBs) tend to form during the hours shortly after sunset (Woodman & La Hoz, 1976). Once formed, EPBs tend to drift eastwards. Therefore, scintillation observed late at night can be due to EPBs generated at locations to the west of the observation site. The all-night forecast is, therefore, trying to provide a prediction of whether EPBs have been generated anywhere in an extended region to the west of the observation site. To move away from the all-night forecast, we instead consider the PVPD value as an indicator of whether an EPB will be generated at that longitude. By considering a time window of, for example, three hours after sunset in which the bubble could be formed, the bubble location can then be propagated forwards using an estimation of EPB drift speed. However, if using this approach, the temporal extent of the bubble's ability to produce scintillation must also be considered. Determining the latitudinal extent of the EPB will also produce more informative forecasts.

In a study by Sridharan et al. (2014) the magnetic latitudinal range of scintillation over Trivandrum was found to correlate closely to observations of h'F at 19:30 LT (Figure 57). A correlation was also found for the duration of a scintillation event and the h'F at 19:30 LT (Figure 58). The parabolic nature of this relationship was explained as being due to the correlation between ion-neutral collisions and plasma scale length (L) with h'F. A strong linear relationship between equinoctial PVPD speed observations and h'F has been noted by Redmon

et al. (2010), as shown in Figure 59. Therefore, under the assumption that the relationship between h'F and the latitudinal and temporal extent of scintillation events is also present at other locations, the PVPD speed at a location on the magnetic equator can be used to estimate the probability of EPB generation, the longevity of the EPB and the latitudinal extent of scintillation.

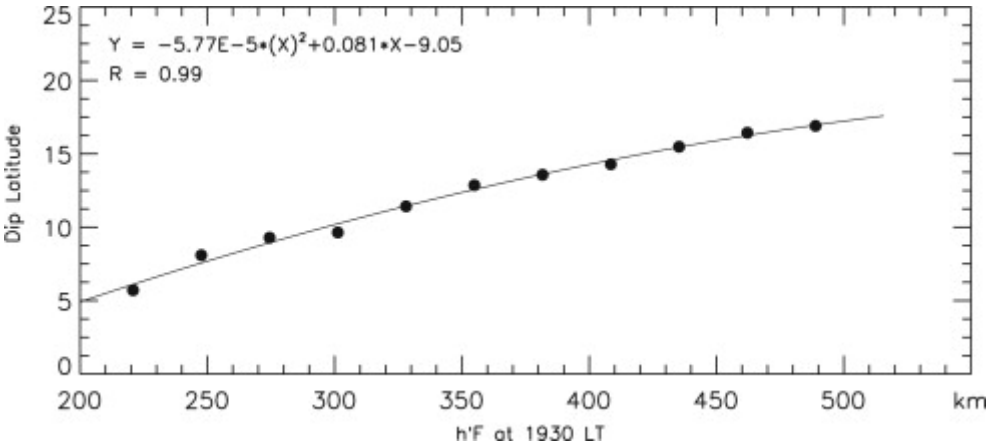

Figure 57. Relationship between Trivandrum h'F observations at 19:30 LT and the magnetic latitudinal extent of scintillation observations (Sridharan et al., 2014).

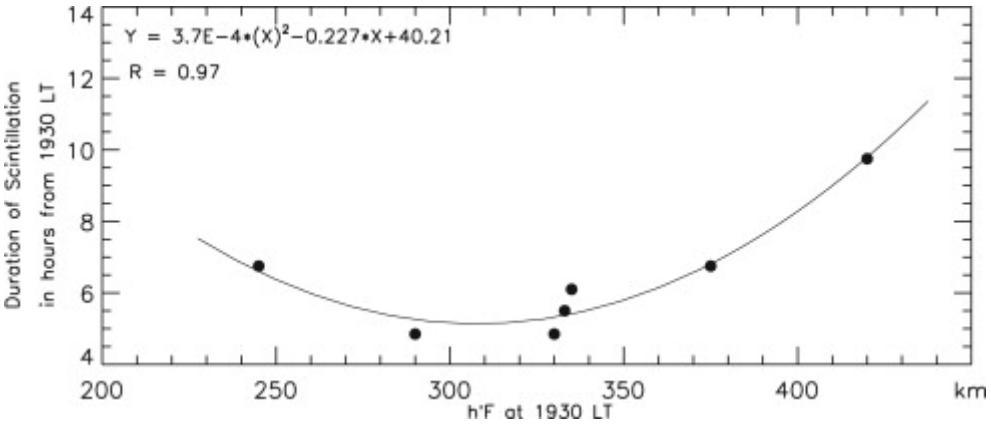

Figure 58. Relationship between Trivandrum h'F observations at 19:30 LT and scintillation event duration (Sridharan et al., 2014).

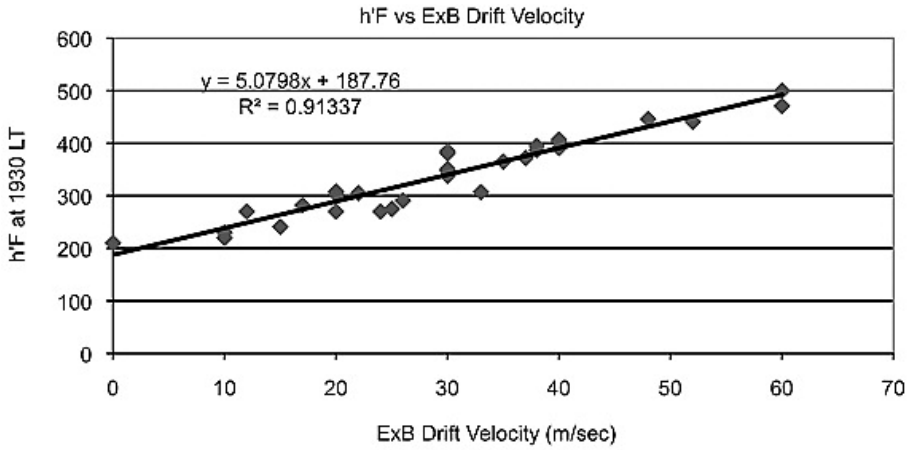

Figure 59. h'F and PVPD speeds observed for 30 randomly selected, equinoctial, geomagnetically quiet days between 2002 and 2005 (Redmon et al., 2010).

Sridharan et al. (2014) adopted an estimated zonal drift speed of 80 ms^{-1}. However, Bagiya et al. (2015) suggested that this may decrease throughout the night. 80 ms^{-1} eastward drift corresponds to approximately 2.5° longitude per hour at low latitudes. Probabilities of EPB generation can therefore be shifted eastward at the rate of one grid point per hour for 2.5° longitudinal resolution (or one grid point every two hours for 5° resolution) to generate the probability of strong scintillation being observed due to EPB generation at the specified location. EPB generation tends to commence within a few hours of sunset. The strong scintillation period could, therefore, be considered as the three hours following sunset. However, it may be reasonable to restrict this EPB generation period to the times for which PVPD values exceed the PVPD threshold subject to a short delay to allow bubble formation to take place.

As EPB formation periods may be greater than one hour, it is possible that a location could experience scintillation effects at a given time due to EPBs generated at more than one location.

The probability that strong scintillation occurs at a given location as a result of one or more of these drifting irregularities can now be calculated. If there are two events, $E_1$and E_2, which could produce strong scintillation at a given location at a given time, the probability of strong scintillation $P(S)$ is given by

$$P(S) = P(E_1) + P(E_2) - P(E_1 \cap E_2)\,, \tag{7.4}$$

where $P(E_1 \cap E_2)$ is the intersection of $E_1$and E_2, i.e. the probability that event E_1 and event E_2 both occur. As the number of contributing events increases the number of terms in this calculation increases due to the need to calculate all possible probability intersections. If, however, the probability that strong scintillation and events $E_1$and E_2 do not occur ($P(S')$, $P(E_1{}')$, and $P(E_2{}')$ respectively) are considered instead, the probability that scintillation does not occur is given by:

$$\begin{aligned} 1 - P(S) &= P(S') \\ &= P(E_1') \cdot P(E_2') \\ &= \big(1 - P(E_1)\big) \cdot \big(1 - P(E_2')\big)\,. \end{aligned} \tag{7.5}$$

This method can be used to combine the probabilities of any number *n* of contributing events, i.e.

$$P(S') = P(E_1') \cdot P(E_2') \cdot P(E_3') \ldots P(E_n') \tag{7.6}$$

Once all contributing events have been considered the probability of strong scintillation at a specified longitude and time is given by:

$$P(S) = 1 - P(S') \,. \tag{7.7}$$

The duration of plasma irregularities must be estimated to determine which EPB generation events contribute to the probability of observing strong scintillation at a specified time and longitude. The relationship between h'F and latitudinal and temporal extent demonstrated by Sridharan et al. (2014), whilst only tested in the Indian sector, in the absence of any further data, can be applied more broadly. Thresholds can therefore be established which correspond to various irregularity durations to determine the number of timesteps an EPB generation event should contribute to scintillation observation predictions. Scaling factors (F) can be calculated from the PVPD probability density function using

$$\mathrm{F} = \frac{\mathrm{P(PVPD} > \mathrm{T)}}{\mathrm{P(PVPD} > 20\ \mathrm{ms^{-1}})}\,, \tag{7.8}$$

where T is the new PVPD threshold. Once the irregularity duration has exceeded the duration associated with a PVPD of 20 $\mathrm{ms^{-1}}$ (5.5 hours) the probability of strong scintillation associated with an EPB generation event is scaled by the appropriate scaling factor for each subsequent time step. In the same manner PVPD thresholds can be established for latitudinal extent from the magnetic equator. Scaling factors are calculated in the same way for latitudinal extent to generate low-latitude scintillation forecasts which vary with time, latitude and longitude. An example plot of such a forecast is shown in Figure 60. Note the variation in

latitudinal extent of high likelihood of strong scintillation over Africa. As latitudinal extent is relevant to this style of forecast, reference latitudes are provided.

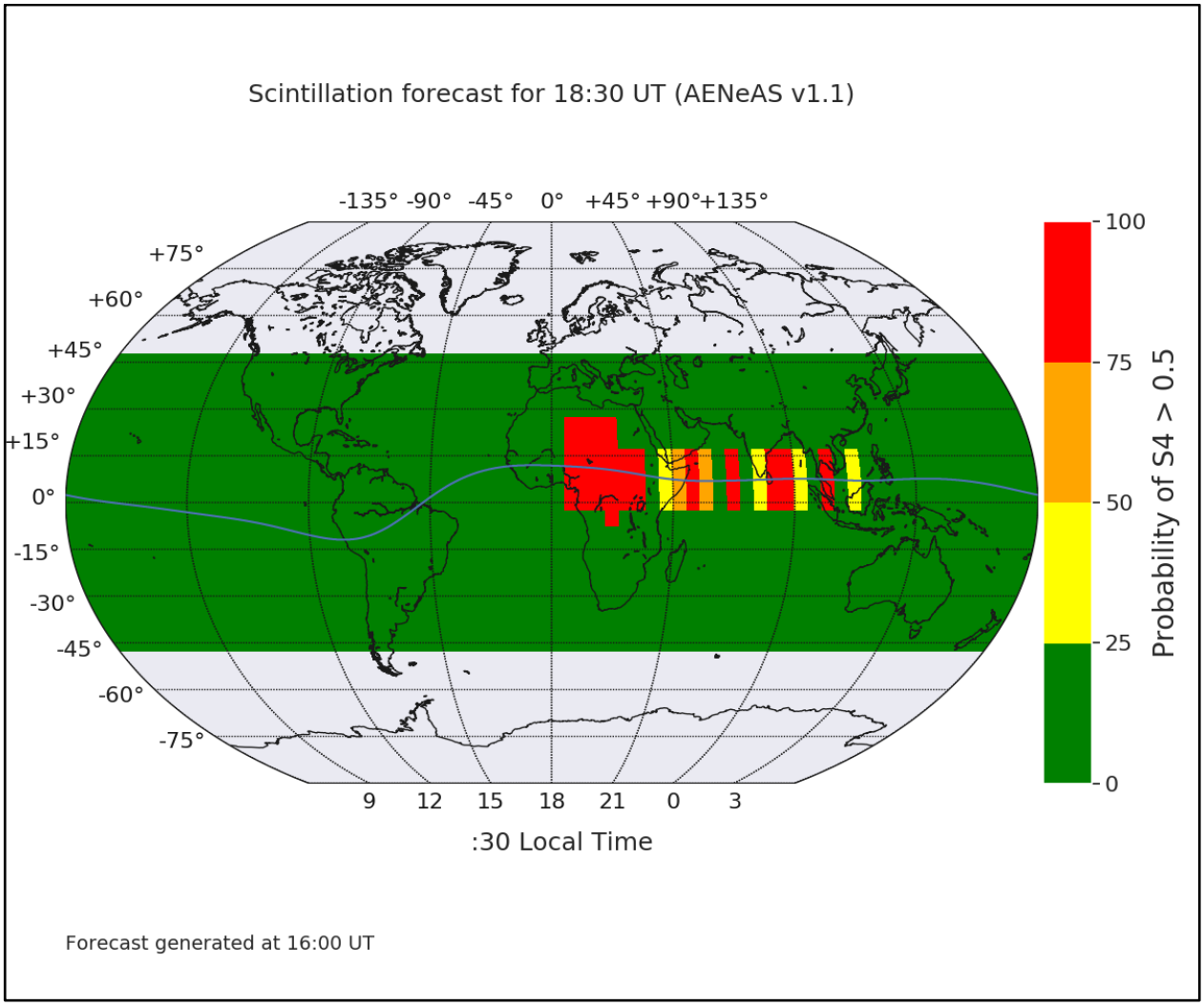

Figure 60. Example of low latitude scintillation forecast for 18:30 UT generated at 16:00 UT. Unlike Figure 56 the forecast now includes predictions of latitudinal extent and is for one specified time rather than the whole evening.

Work on probabilistic low latitude scintillation forecasting is ongoing. The described method will be developed further as part of the Space Weather Instrumentation, Measurement, Modelling and Risk (SWIMMR) project (NERC Grants on the Web, 2020), with a view to

operational use within MOSWOC. This will involve determining global PVPD thresholds, which are likely to be described as a function (or functions) of longitude, season, and solar activity. Investigation will also be required to determine whether the relationships between h'F and the latitudinal extent (Figure 57) or duration (Figure 58) of scintillation events are valid at locations other than Trivandrum. It is possible that, if such relationships exist at other longitudes, these relationships may take different forms or have different coefficients at locations other than Trivandrum. Once these relationships at other longitudes (and, possibly, season and solar activity) have been determined, validation of this probabilistic low-latitude forecasting method can be undertaken though comparisons of probabilistic forecasts to scintillation observations. A metric such as the Brier Score (Brier, 1950) can be used to determine whether the proposed approach demonstrates forecasting skill and, therefore, the suitability of this forecasting approach for global low-latitude scintillation forecasts in an operational setting.

8. IMPROVING AENEAS PERFORMANCE BY INTRODUCING LOWER BOUNDARY VARIABILITY

In Sections 6 and 7 output from ionospheric models was used to provide forecasts of ionospheric scintillation. As demonstrated in Section 6.4.5, improving the ionospheric specification by using the AENeAS data assimilation model (rather than the physics-based TIE-GCM model) improved the accuracy of the scintillation forecasts. Furthermore, improved ionospheric specification (e.g. by using AENeAS rather than a climatological model) would increase the accuracy of ray-tracing for modelling of over-the-horizon radar (OTHR) systems (e.g. increase the accuracy of modelling within Section 5). Improved ray-tracing accuracy would be particularly important in an operational OTHR system, for aspects such as coordinate registration. Therefore, we now consider the AENeAS model, specifically a method to improve the model performance. As discussed in Section 3.6, an important consideration for improving the capability of AENeAS for ionospheric nowcasting and forecasting is whether ensemble members are orthogonal and can span the range of state spaces possible for the real ionosphere-thermosphere system. AENeAS incorporates a Monte Carlo approach to randomly select F10.7, hemispheric power, and cross-tail potential values from predetermined probability distributions to drive TIE-GCM when propagating ensemble members forward in time. However, the lower boundary conditions (LBCs) remain identical for each ensemble member. In this chapter perturbations will be applied to the Global Scale Wave Model (GSWM) output currently used for AENeAS (and, therefore, TIE-GCM) LBCs. It will be shown that perturbing TIE-GCM LBCs can produce perturbations at higher altitudes, including changes to the peak electron density (N_{max}) and corresponding altitude (h_{max}). A method for producing random perturbations to TIE-GCM LBC horizontal winds will be described. Intuitively, the addition of further variability between ensemble members should increase the likelihood that ensemble

members are orthogonal. It shall also be demonstrated that the range of possible ionospheric conditions for ensemble members is increased when LBC horizontal wind perturbations are included.

8.1. TIE-GCM Lower Boundary Forcing

TIE-GCM lower boundary forcing has previously been shown to influence TIE-GCM ionospheric behaviour (e.g., Pedatella, 2016). As well as neutral temperatures and horizontal wind velocities, aspects such as **E×B** vertical drift velocity and TEC can vary considerably depending on lower boundary values. Geomagnetic activity is understood to be a major influence on the ionospheric peak electron density. However, conditions at lower altitudes may exert a comparable influence (Rishbeth and Mendillo, 2001). Pedatella (2016) explored the change in the TIE-GCM ionospheric response to a geomagnetic storm when the lower boundary conditions were adjusted. Sudden stratospheric warming (SSW) events are known to impact ionospheric conditions (e.g., Mošna et al., 2021). Pedatella's new lower boundary zonal mean climatology, planetary waves, and tidal variability were based on simulations of a SSW event in January 2013. The temporally varying solar and geomagnetic forcing were based on conditions during the Halloween storm of 2003. Although the SSW forcing was extreme, using the SSW lower boundary conditions compared to the GSWM lower boundary showed that the TEC response could vary by up to 100% during Halloween storm conditions. This suggests that changes to AENeAS lower boundary conditions can be used to change ionospheric and thermospheric conditions at higher altitudes.

8.2. Homogeneous Global Lower Boundary Perturbations

As an initial demonstration of the potential impact of lower boundary perturbations, homogeneous global perturbations are applied to LBC horizontal wind speeds. An example of the unperturbed lower boundary wind velocities from GSWM are provided in Figure 61.

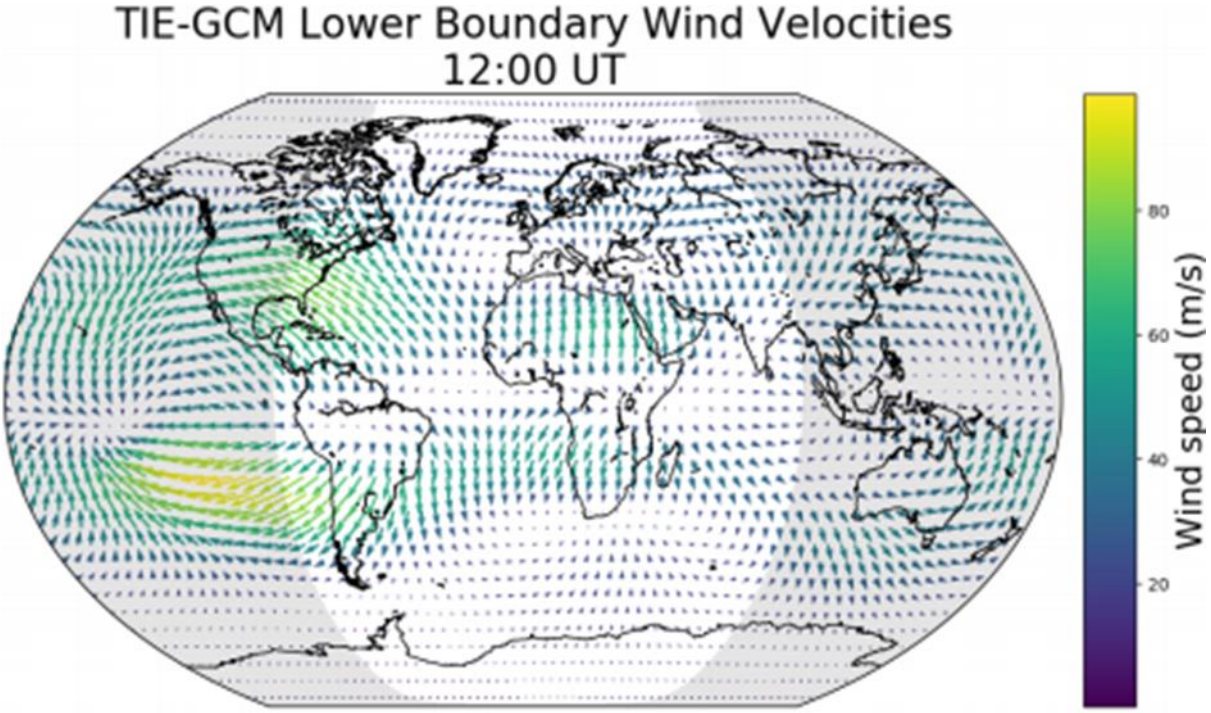

Figure 61. TIE-GCM lower boundary wind velocities corresponding to GSWM output for 12:00 UT on 21 March. Arrow size and colour represent the magnitude of the wind speed. The shaded region represents night-time. 5° latitude-longitude resolution is shown for clarity, however, the overall behaviour is representative of 2.5° resolution with diurnal and semi-diurnal migrating and non-migrating tides.

Initially, wind velocity magnitudes are increased or decreased by a fixed proportion without changing wind directions, to determine changes that can be caused to ionospheric conditions due to changes in wind speeds alone, without changing global wind flow. Five-day simulations were initiated at 0:00 UT on 21 March 2002 using identical initial conditions to unperturbed

simulations, but with altered lower boundary horizontal wind conditions. An example of electron density profile variation induced by extreme lower boundary wind perturbations is shown in Figure 62 for a 200% increase in lower boundary wind velocities. The global hmF2

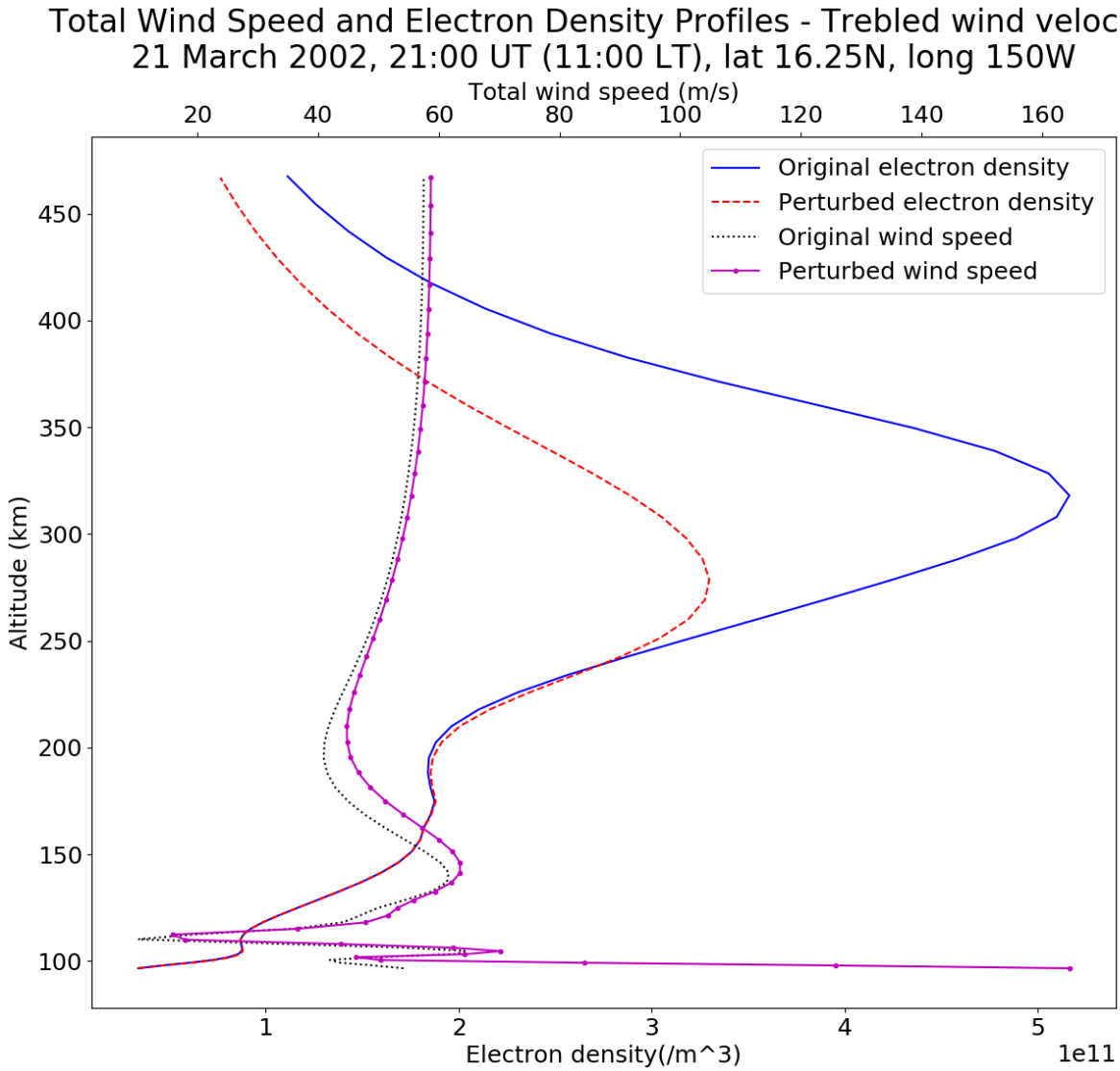

Figure 62. Electron density (lower axis) and wind speed (upper axis) variation 9 hours after simulation start time due to increase of lower boundary wind speeds by 200%. Electron densities are shown with (dashed red line) and without (solid blue line) lower boundary perturbation and wind speeds are shown with (purple solid dotted line) and without (black dotted line) lower boundary perturbation.

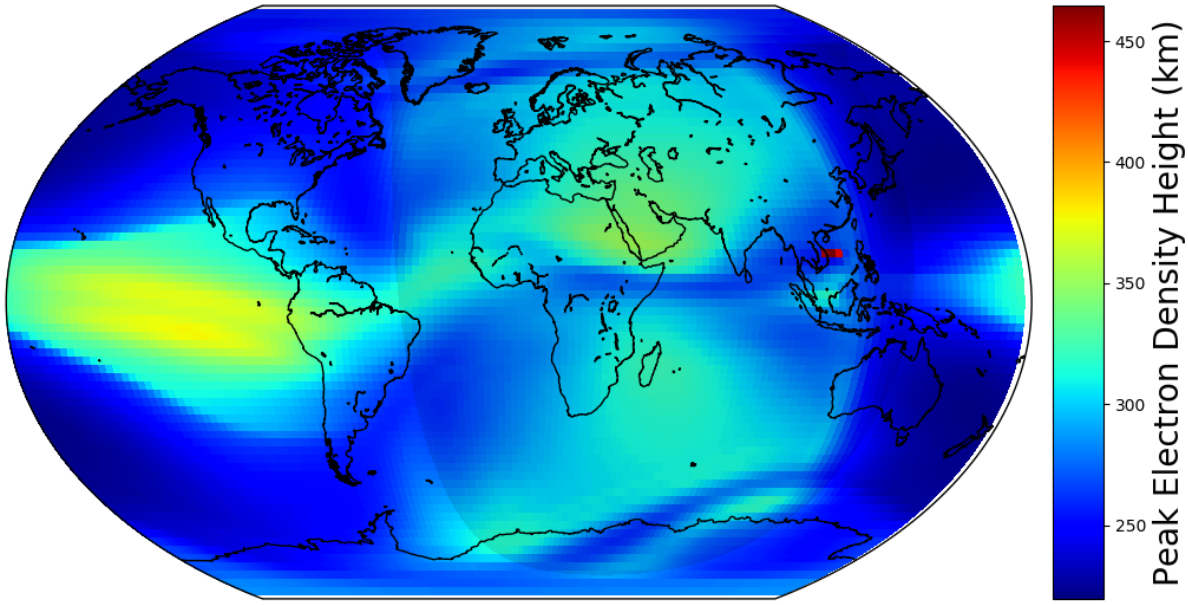

Figure 63. Global hmF2 at 21:00 UT on 21 March 2002 from TIE-GCM simulation with start time 0:00 on 21 March 2002. F10.7 is fixed at 70 sfu. Shaded region indicates night-time.

map corresponding to the simulation time in Figure 62 is shown in Figure 63. We see that in this extreme (and unphysical) case the electron density profile in Figure 62 has changed significantly with large reductions in NmF2 and hmF2. The change in wind speed reduces very swiftly as altitude increases from the lower boundary. This suggests that the observed electron density variation is due to conditions impacted by lower boundary winds close to the lower boundary rather than due to the increased wind speeds propagating up from the lower boundary. Indeed, the most significant changes to hmF2 and NmF2 are focussed on the region close to the magnetic equator, due to changes in wind speeds which are generating the dynamo electric field. hmF2 is decreased at the equatorial ionisation crests and the region in which the plasma density decreases (directly to the north and south of the crests) has a steeper gradient, as seen in the blue region on the left-hand side of Figure 64. The enhancement of the eastward neutral wind close to the magnetic equator in the evening sector drives more plasma upward via **E×B**

drift during and following the pre-reversal enhancement, resulting in the enhanced night-time hmF2 seen in the red region in the centre of Figure 64.

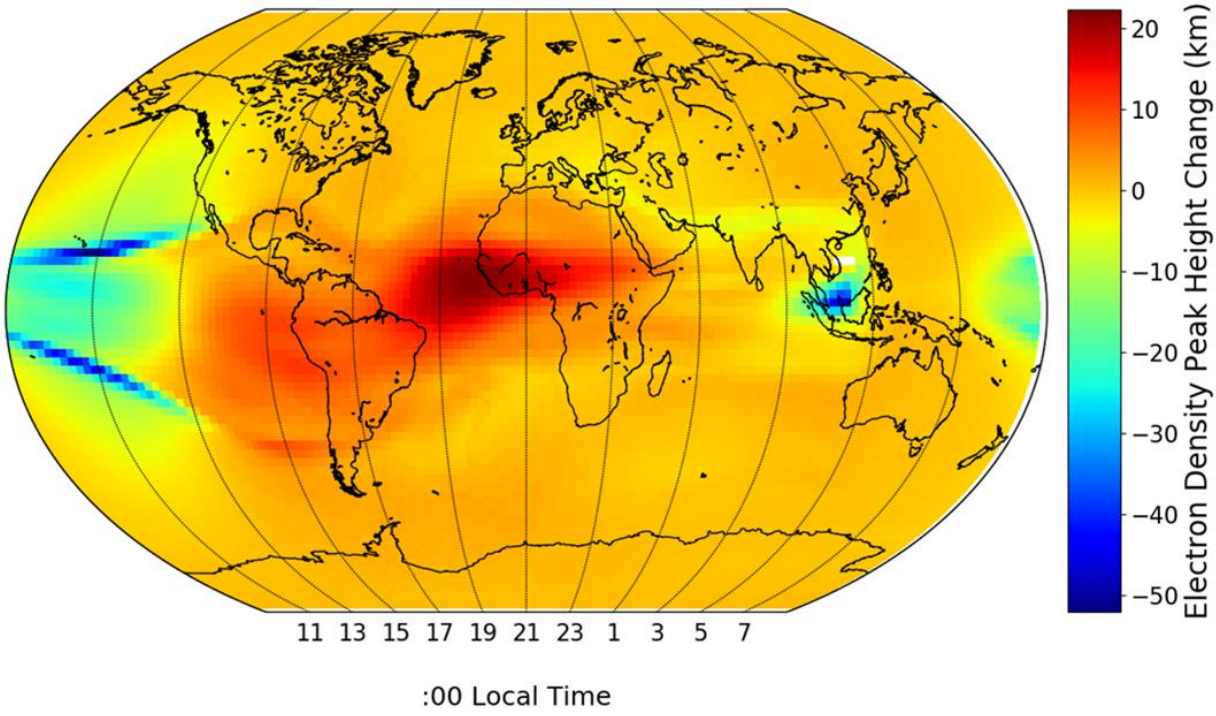

Figure 64. Global changes in hmF2 due to a 200% increase in lower boundary winds corresponding to electron density profiles in Figure 62. The location of the electron density profiles in Figure 62 is in the upper dark blue region on the left-hand side (latitude 16.25N, longitude 150W).

The percentage of 2.5° latitude-longitude grid points with hmF2 shifts greater than 5 km (~1-2%) during a five-day simulation (with output time step of 30 minutes) are shown in Figure 65 for a range of global homogenous wind speed perturbations. An increase in perturbation magnitude results in an increased number of hmF2 shifts greater than 5 km. Wind speed increases primarily produce downwards hmF2 shifts of 5 km or greater, whereas wind speed decreases produce a greater number of upwards hmF2 shifts. Global homogenous temperature fluctuations were also investigated. However, global temperature increases or decreases of

more than 20 K tended to result in model simulations crashing, due to atmospheric density features moving a distance greater than one grid cell within the default time step (Dorrian & Elvidge, 2020). Temperature changes with magnitude small enough to avoid breaking the model produced a smaller number of significant hmF2 shifts than 25% increases or decreases of wind speeds. Global temperature decreases tended to produce a greater number of significant hmF2 increases rather than decreases. Temperature increases produced a greater number of hmF2 decreases.

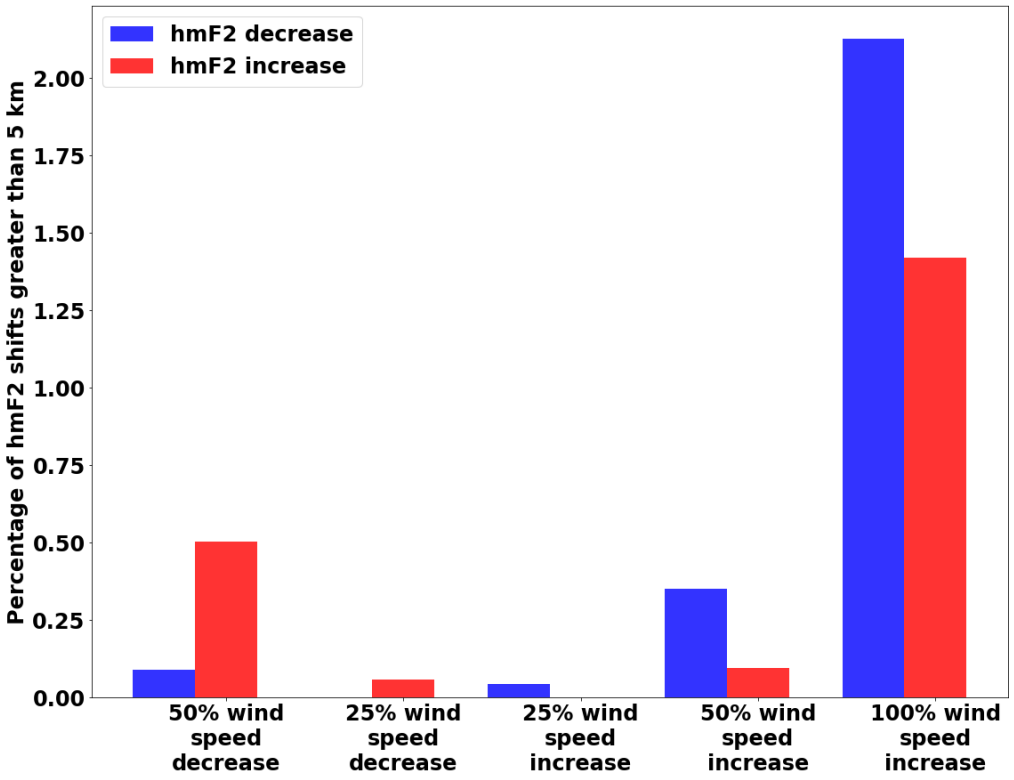

Figure 65. Percentage of hmF2 shifts greater than 5 km for homogeneous global wind speed perturbations. 21-26 March with F10.7 = 70 (representing solar minimum).

Homogeneous perturbations demonstrate that changes to LBCs can produce ionospheric variability at higher altitudes. However, local variability in the LBCs would provide

perturbations which are likely to be less unphysical than the large global changes considered so far. Intuitively, it would also seem sensible that incorporating local variability in LBC perturbations would be more likely to produce orthogonal ensemble members for AENeAS. TIE-GCM stability appears to be more sensitive to lower boundary temperature perturbations than wind perturbations. This can be overcome by reducing the TIE-GCM model time step size. However, this reduction in model stability would not be desirable for operational use as other factors can also contribute to model instability, such as sudden large changes to the geomagnetic driver values. Therefore, the focus in this work will be on perturbations of TIE-GCM lower boundary horizontal winds. A method which incorporates local variability through the use of spherical harmonic functions will now be discussed.

8.3. Lower Boundary Perturbations Generated Using Spherical Harmonics: Method

Spherical harmonics can be used to introduce lower boundary wind perturbations which vary both globally and locally. A spherical harmonic function is a continuous complex function over the surface of a sphere. The spherical harmonic function is defined by parameters l and m where $l \geq |m|$. $|m|$ can be considered to represent the number of evenly spaced longitudinal circles passing through both poles for which the real/imaginary part is equal to zero. The number of circles parallel to the equator for which the real/imaginary part is equal to zero is given by $l - |m|$. The spherical harmonic function, Y_l^m, is given by

$$Y_l^m(\theta, \phi) = \sqrt{\frac{(2l+1)(l-m)!}{4\pi(l+m)!}} e^{im\theta} P_l^m \cos\phi \,, \qquad (8.1)$$

where θ and ϕ are the longitude and colatitude (90° - latitude) respectively and P_l^m is a Legendre function. Examples of the real part of spherical harmonic functions with $0 \leq l \leq 3$ are shown in Figure 66.

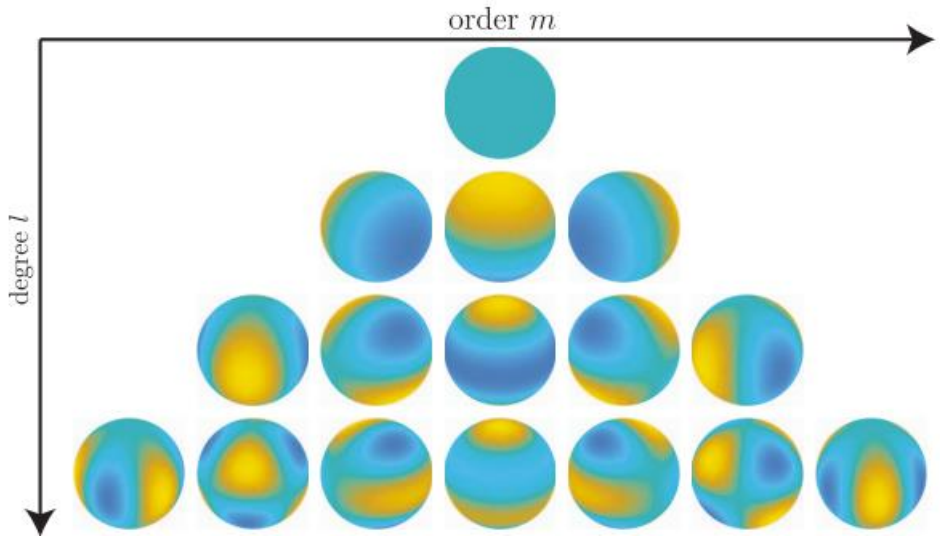

Figure 66. Spherical harmonic functions (real part) with values of l from zero (top) to three (bottom). Spherical harmonic functions with $|m| \leq l$ are shown with m=0 in the central column. For each spherical harmonic function, high values are shown in yellow and low values are shown in blue (Pfaff et al., 2017).

Spherical harmonic functions are used to increase and decrease the zonal and meridional neutral wind at each grid point on the lower boundary. As spherical harmonic output is complex it can be used to perturb lower boundary wind speeds in two dimensions. In this work the real component corresponds to zonal wind speed perturbations and the imaginary component corresponds to meridional wind speed perturbations. As discussed, the parameters l and m define the behaviour of the spherical harmonic function. In this work TIE-GCM is used with 2.5° resolution. Therefore, to permit local perturbations such that neighbouring longitudinal

grid points can oscillate in opposite directions, spherical harmonic functions will be considered for which values of l and m can take values with magnitude of up to 72. As $l \geq |m|$, random values of l are drawn from the range [3, 72]. The minimum value within the range is chosen to avoid large global wave structures dominating the global perturbations. m is subsequently drawn randomly from the range $[-l,\ l]$. Scaled spherical harmonic wind values (w_s) are determined by:

$$w_s = l^{-0.5} w\ , \tag{8.2}$$

where w is the unscaled spherical harmonic wind values. To generate perturbations which have varying local structures, the final perturbations are generated by summing multiple scaled spherical harmonic functions. Ideally, the perturbations encompass both large and small scale structures, thereby generating variability between ensemble members. By trial and error, the sum of 40 scaled spherical harmonic functions generated using the described method were found to generate variability in structure size. The process used to generate perturbation matrices is described further in Figure 67. Figure 68 and Figure 69 show examples of different structure sizes which can be generated using the described method.

So far, only perturbations of hmF2 and NmF2 following changes to lower boundary winds have been considered. However, hmF2 output from TIE-GCM is known to occasionally have errors, particularly at high latitudes (NCAR High Altitude Observatory, 2016). For example, at some locations (such as auroral regions) the peak electron density may be in the E region, and at some of these locations the TIE-GCM hmF2 value may correspond to the E region peak. Therefore, to avoid errors which may suggest variability due to lower boundary perturbations which is not

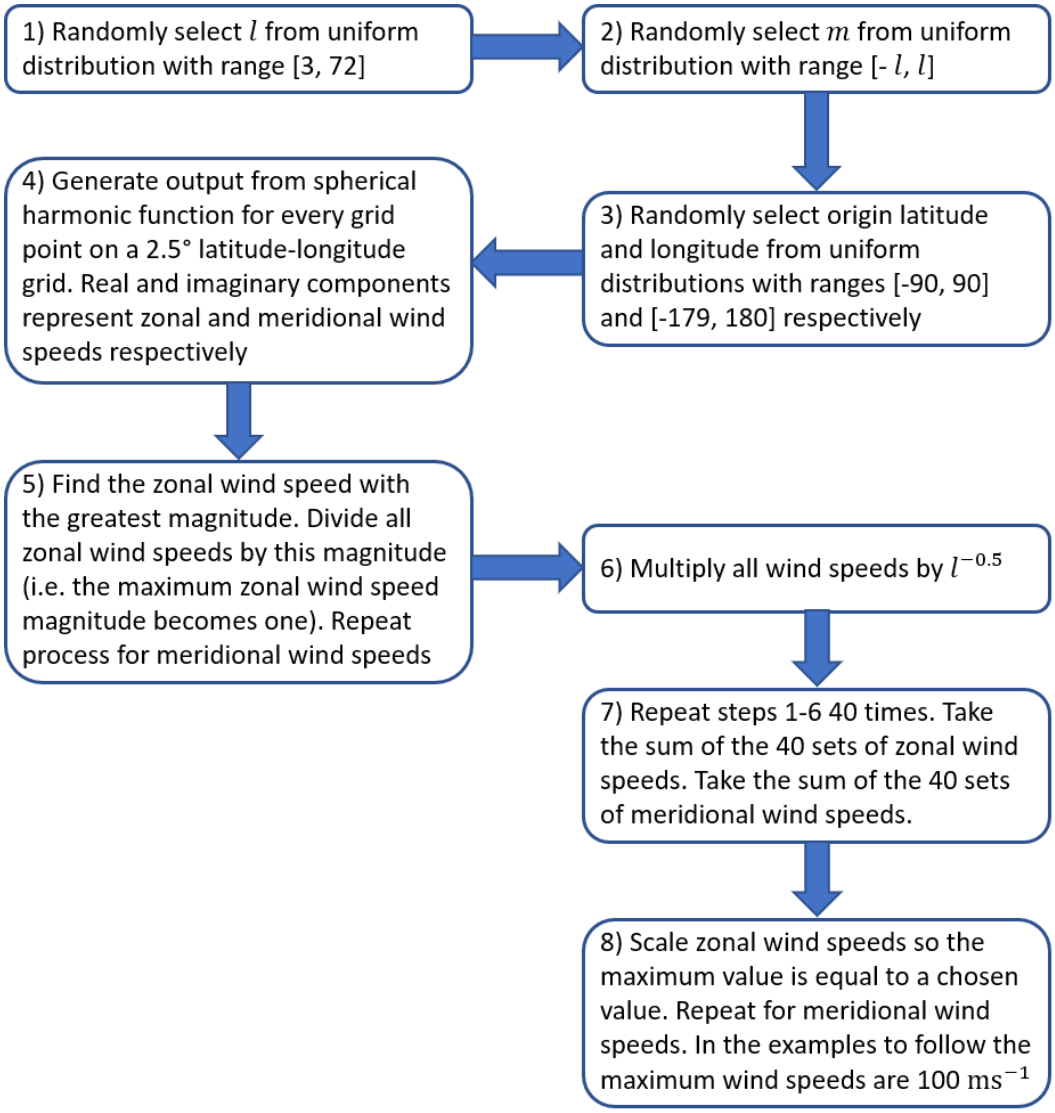

Figure 67. Flow chart describing the method used to create perturbation matrices.

present, N_{max} and h_{max} will be considered for further testing instead of hmF2 and NmF2. N_{max} and h_{max} are the peak electron density on the electron density profile and the height associated with the peak electron density respectively. N_{max} and h_{max} are determined by fitting a Chapman function (equation 3.3) to the highest electron density value (and associated altitude) on the vertical grid at a latitude-longitude point, including two electron density and altitude values immediately above and below the highest electron density value (i.e., the Chapman

function is fitted to five points). In auroral regions the peak electron density may occur in the

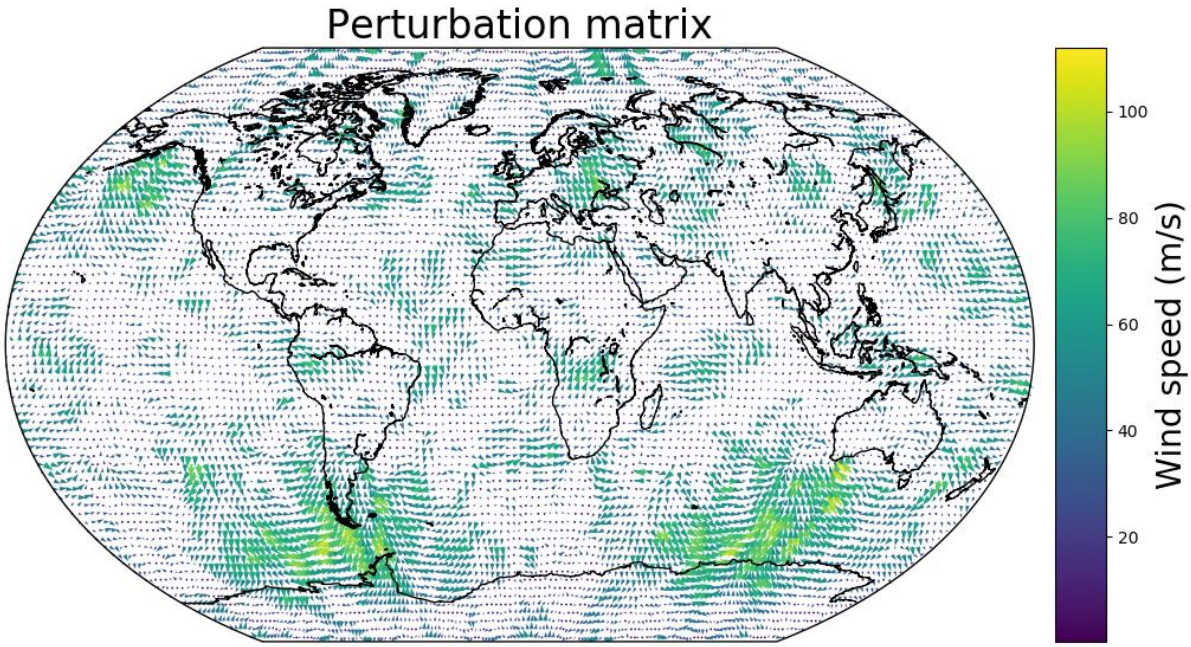

Figure 68. Example of perturbation matrix. Arrow size and colour represent the magnitude of the wind speed. Note two large continent sized perturbations in the southern hemisphere.

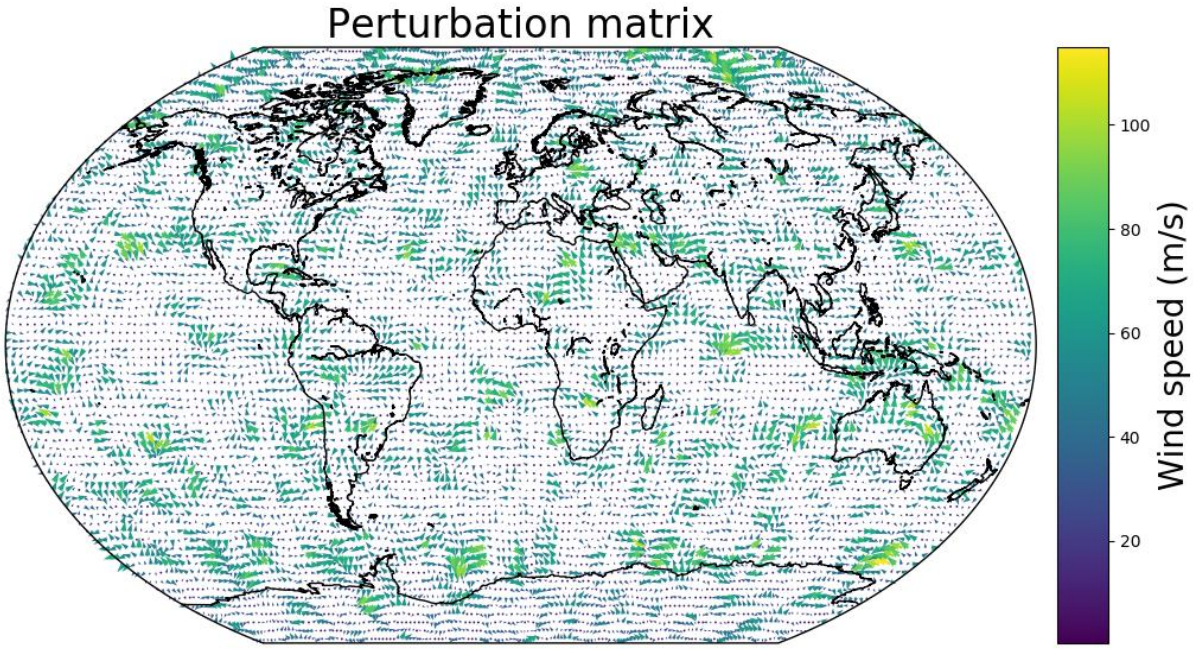

Figure 69. Example of perturbation matrix. Note the lack of extremely large structures which were present in Figure 68.

E region. Therefore, large scale changes to h_{max} at high latitudes should be considered with caution, as this may be due to the boundary between locations with E region and F region peak electron densities shifting by one (or more) latitude or longitude grid space.

8.4. Lower Boundary Perturbations Generated Using Spherical Harmonics: Results

Perturbation matrices generated using the random spherical harmonic method have been used to demonstrate the increase in size of the possible sample space for ensemble members when LBC perturbations are incorporated. First, the minimum and maximum h_{max} and N_{max} values are obtained for each 2.5° latitude-longitude grid point, for every 10 minute time step in a 24-hour day, and over a wide range of environmental conditions without perturbing the LBCs (i.e. using GSWM output for LBCs). 192 combinations of test scenario conditions are considered, using every combination of the environmental conditions listed in Table 7.

Table 7. Values used for the date, solar activity, hemispheric power and cross-tail potential when determining minimum and maximum values of hmF2 and NmF2 for unperturbed LBCs.

Test case environmental condition	Values used
Date	21 March, 21 June, 21 September, 21 December
F10.7	70, 160, 250
Hemispheric power	11.96, 39.07, 109.87, 300 (corresponding to Kp = 0, 3, 6 and 9: equation 3.31)
Cross-tail potential	15.0, 67.2, 133.8, 214.8 (corresponding to Kp = 0, 3, 6 and 9: equation 3.32)

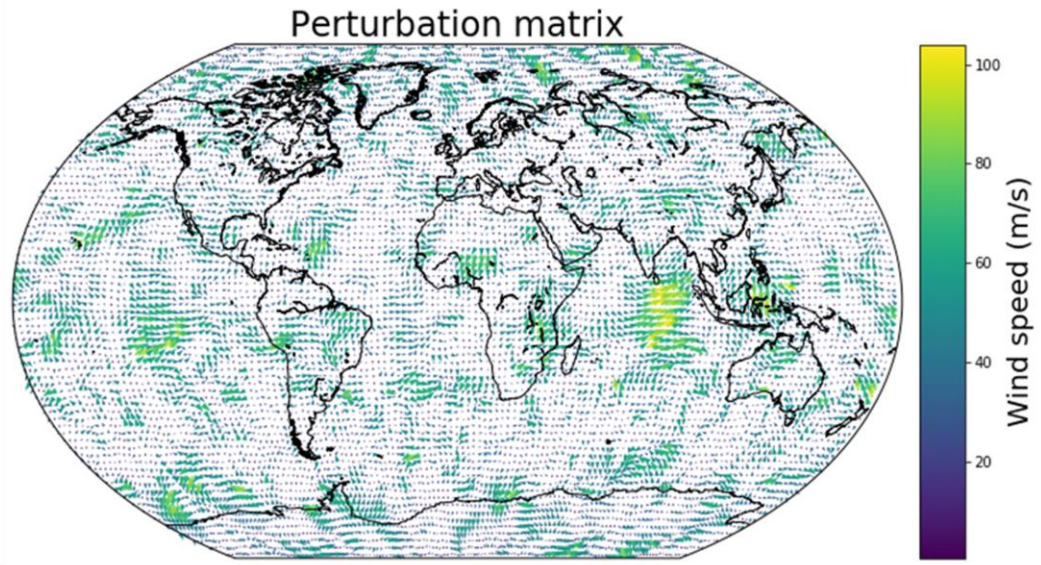
Perturbation matrix
100
80
60
40
20
Wind speed (m/s)

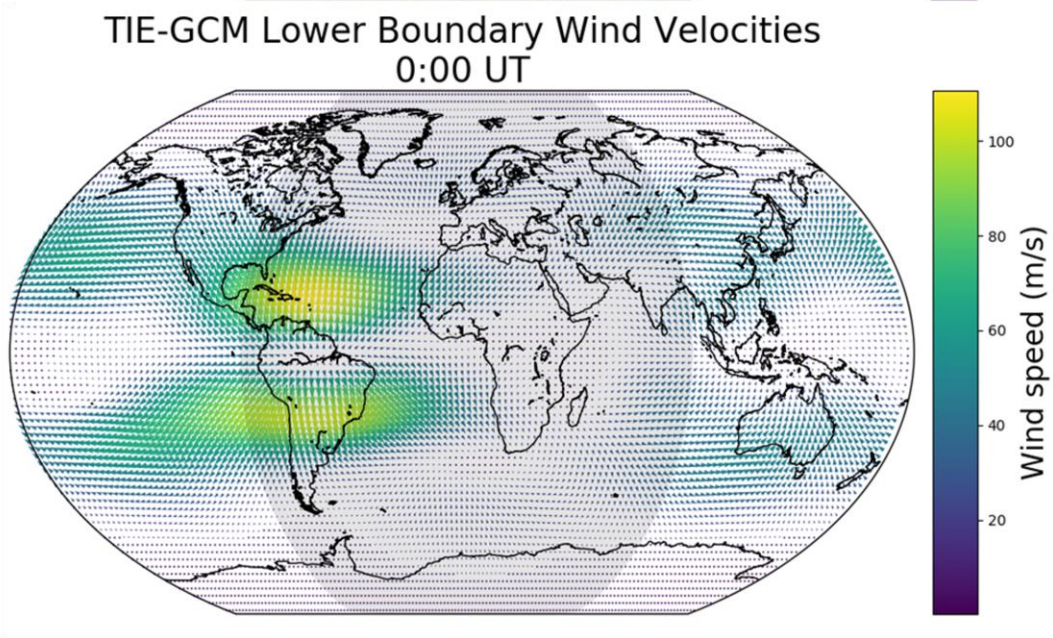
TIE-GCM Lower Boundary Wind Velocities
0:00 UT
100
80
60
40
20
Wind speed (m/s)

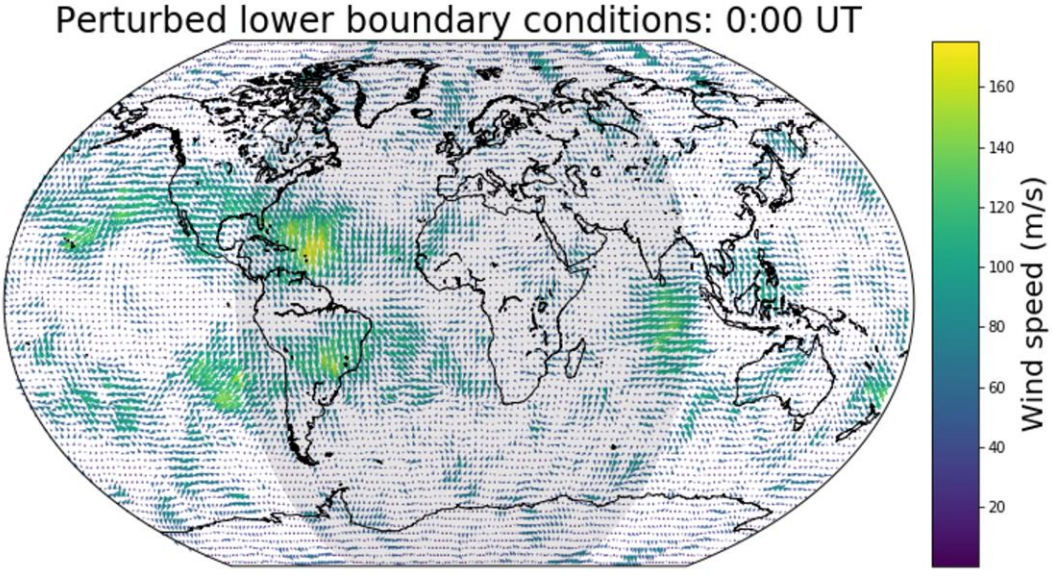
Perturbed lower boundary conditions: 0:00 UT
160
140
120
100
80
60
40
20
Wind speed (m/s)

Figure 70. Arrow size and colour represent the magnitude of the wind speed. Top: *Randomly generated perturbation matrix used for analysis. Note the large structure at low-latitudes in the sunrise sector*. Middle: *GSWM output for lower boundary horizontal winds at 0:00 UT in mid-March. The shaded region indicates night-time locations on the ground. Bottom: Perturbed lower boundary horizontal winds for mid-March at 0:00 UT generating by summing the perturbation matrix and GSWM output. Note the region of increased wind speed east of central America, due to perturbation matrix winds with the same direction as the winds with the greatest speed in GSWM output. The perturbation matrix shifts longitudinally by 15° per hour to keep structures stationary in relation to the day-night terminator.*

A comparison between the minimum unperturbed N_{max} and h_{max} values (across 192 test cases) and the minimum N_{max} and h_{max} values from the 21 June test case with F10.7 = 70, hemispheric power = 300, cross-tail potential = 214.8 (hemispheric power and cross tail potential corresponding to Kp = 9), and perturbed LBCs is shown in Figure 71. This perturbed test case is chosen as it demonstrates significant decreases in N_{max} and h_{max} when compared to unperturbed test cases. TIE-GCM output is with 2.5° latitude-longitude resolution. However, for ease of comparison, 10-minute output across a 24-hour day is binned according to local time in one-hour bins. The minimum N_{max}/h_{max} value across the 192 test cases is considered. Regions in which the perturbed test case do not produce lower N_{max}/h_{max} values than all 192 test cases are shown in white. If the perturbed test case does provide lower N_{max} and h_{max} values than the minimum values from the 192 test cases, the difference between these values is shown according to the colourbar. The proportional changes are also shown for the perturbed

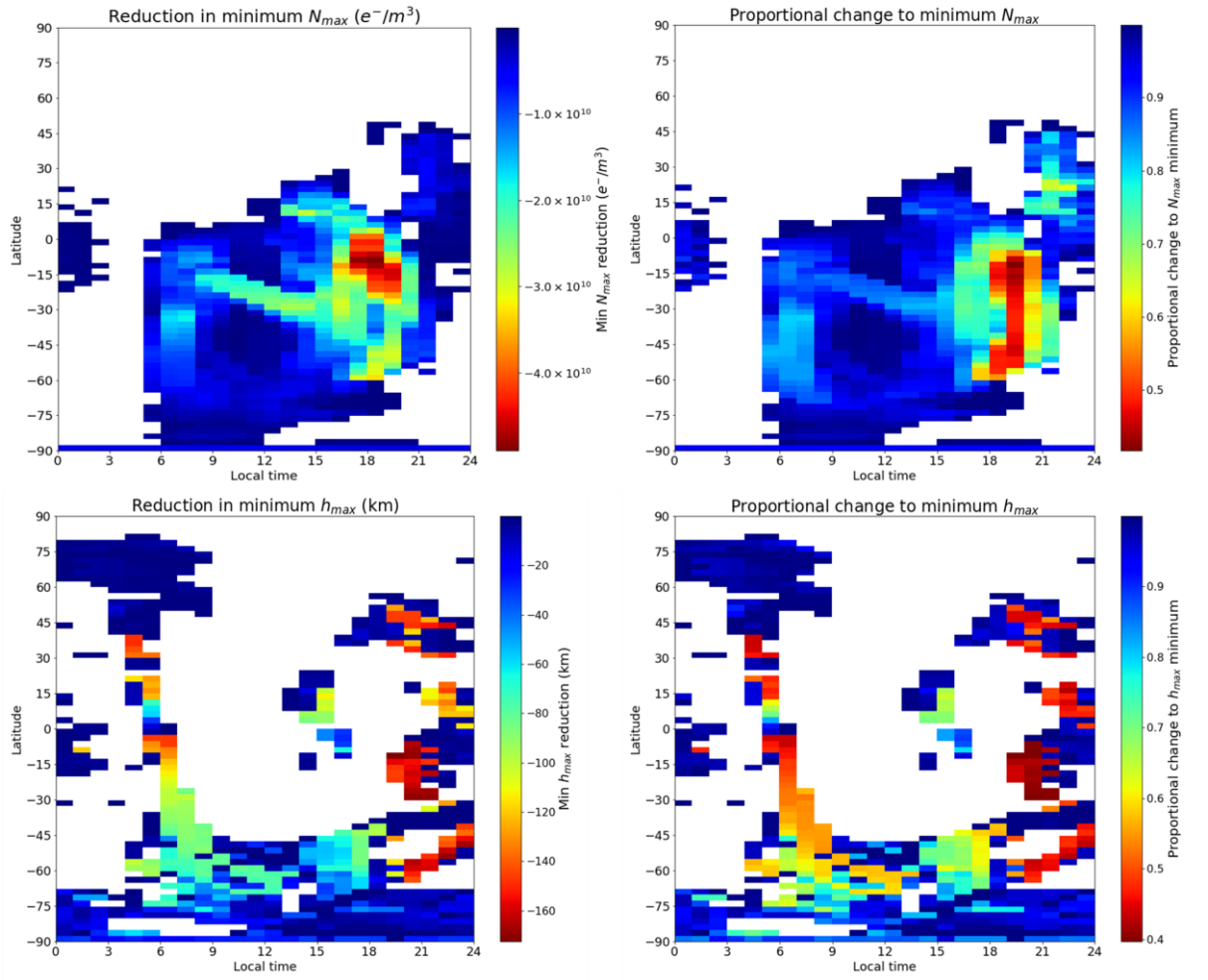

Figure 71. The reduction in N_{max} (top left) and h_{max} (bottom left) for the 21 June test case with F10.7 = 70, hemispheric power = 300, cross-tail potential = 214.8, and the lower boundary wind perturbations shown in Figure 70*, compared to the lowest N_{max} and h_{max} values across all 192 test cases with unperturbed lower boundaries. Also shown are the proportional values of the single perturbed test case N_{max} (top right) and h_{max} (bottom right) values compared to the lowest N_{max} or h_{max} values from 192 unperturbed test cases (e.g. if the perturbed N_{max} value is equal to 90% of the lowest unperturbed N_{max} value, the proportional value is 0.9).*

test case when compared to the lowest values from 192 unperturbed test cases. For example, if the perturbed N_{max} or h_{max} value was equal to 90% of the lowest unperturbed value, the proportional value would be 0.9. The most significant N_{max} value reductions occur at low

latitudes between 1700 and 2000 LT. However, reductions in excess of 25% are observed in the southern hemisphere at most latitudes up to 60°S between 1700 and 2000 LT, and are present at some latitudes between 1600 and 2200 LT. Similar proportional reductions can be seen in a smaller region in the northern hemisphere between 2000 and 2300 LT. N_{max} reductions of around 50% can be observed in the southern hemisphere between 1800 and 2000 LT. N_{max} reductions of up to 15% can also be observed at southern hemisphere mid latitudes in the early morning. The most significant changes to h_{max} occur around sunrise (due to delayed uplift of the ionosphere following sunrise) and post sunset. Some southern hemisphere higher latitudes show significant h_{max} reductions throughout the day. However, some of these reductions are caused by slight movement of the auroral region, in which TIE-GCM peak electron densities do not occur in the F region.

The N_{max} and h_{max} changes for all 192 perturbed LBC test cases are now considered, comparing the minimum and maximum N_{max} (Figure 72) and h_{max} (Figure 73) values across all perturbed cases with the minimums and maximums from the 192 unperturbed cases. Small reductions in the minimum N_{max} can be produced in almost all regions and local times (Figure 72), apart from during the night at one northern hemisphere polar latitude (86.25°N). Significant proportional reductions (up to 25%) are seen for the minimum N_{max} at low latitudes throughout the night. The regions with the greatest proportional reductions in the minimum N_{max} are in similar locations to those for the single test case considered in Figure 71, although the size of this region has increased. Significant changes to the minimum N_{max} can also be observed at auroral latitudes, particularly in the morning and late afternoon/early evening sectors. The perturbed lower boundary winds are also able to generate N_{max} values which are greater than those produced by 192 unperturbed test cases. Small increases to the maximum N_{max} are

present at all locations apart from locations close to the equator and at high latitudes in the northern hemisphere, with the most significant increases occurring at low and mid latitudes during the morning. Proportional increases to the maximum N_{max} are less extreme than reductions to the minimum N_{max}, with few locations experiencing N_{max} increases greater than 15%. Test cases with perturbed lower boundary winds are able to produce lower h_{max} values than unperturbed test cases at all locations and UTs (Figure 73). The most significant reductions

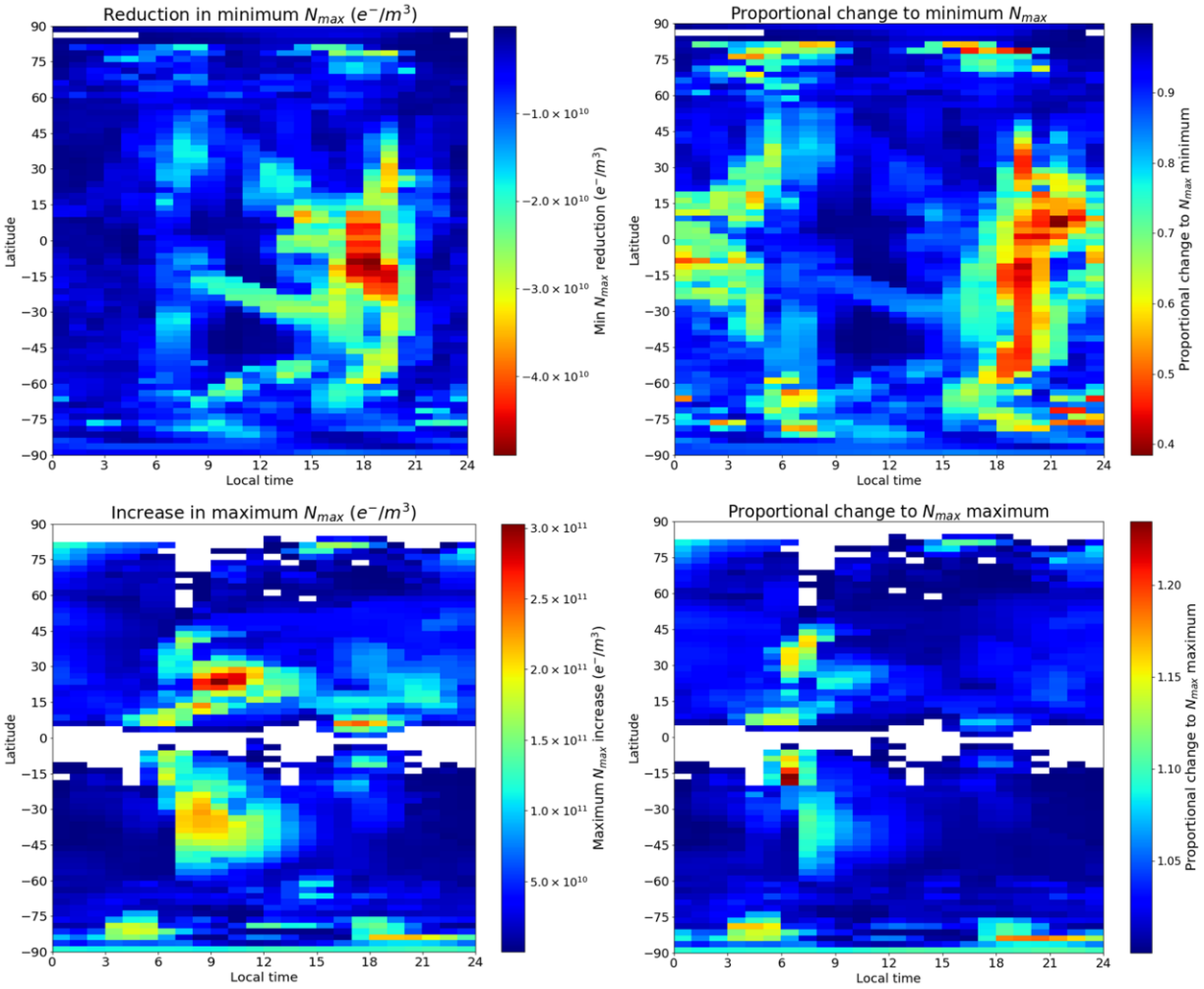

Figure 72. Differences (left) and proportional changes (right) between minimum (top) and maximum (bottom) N_{max} values from 192 unperturbed test cases and the minimum (top) and maximum (bottom) N_{max} values from 192 test cases with the lower boundary wind perturbations shown in Figure 70.

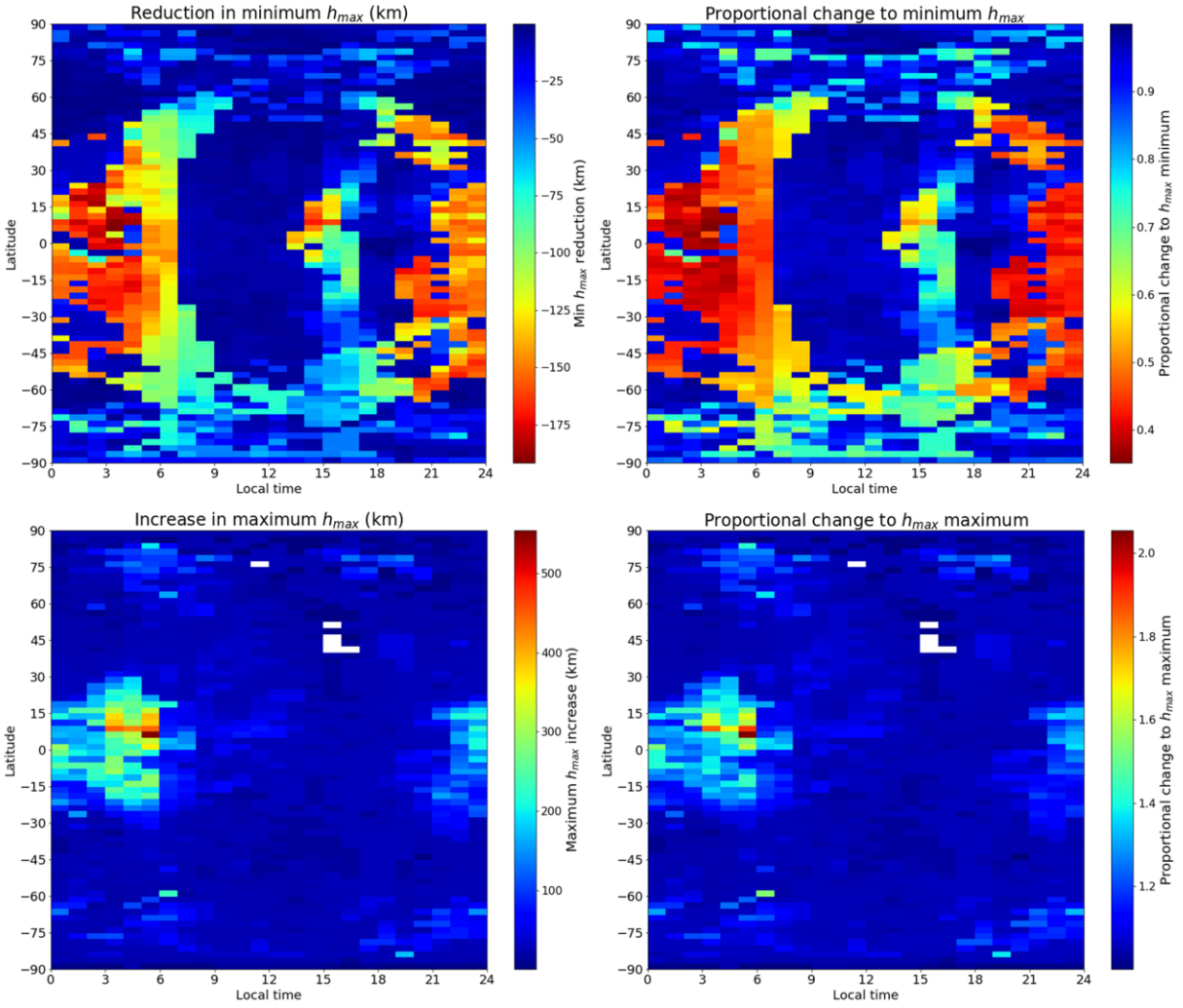

Figure 73. Differences (left) and proportional changes (right) between minimum (top) and maximum (bottom) h_{max} values from 192 unperturbed test cases and the minimum (top) and maximum (bottom) h_{max} values from 192 test cases with the lower boundary wind perturbations shown in Figure 70.

(50 km or greater) in h_{max} (compared to the minimum unperturbed values) occur throughout the night and during the late afternoon at lower latitudes, and extends to higher latitudes around the hours of sunrise and sunset. There are also significant h_{max} reductions at high latitudes throughout the 24-hour day. However, a contributing factor to these reductions may be the transition from a F region peak to an E region peak shifting to neighbouring grid cells. Perturbed

lower boundary test cases can also generate h_{max} values greater than the maximum h_{max} values from all unperturbed test cases. h_{max} increases are observed at almost all latitudes and UTs, with the most extreme increases (200 km or greater) occurring between 2300 and 0600 UT at low latitudes.

8.5. Lower Boundary Perturbations: Discussion and Future Work

The application of a perturbation matrix to GSWM lower boundary horizontal winds has generated peak electron densities and corresponding heights which are beyond the range generated by unperturbed test cases for the same set of model conditions. Therefore, the inclusion of lower boundary perturbations increases the sample space spanned by AENeAS ensemble members. However, it should be noted that under some test case conditions extreme changes to h_{max} and N_{max} can be produced by disrupting wind flow close to the terminators, thereby impacting the uplift and downwelling of plasma in the sunrise and sunset sectors. If all ensemble members include this terminator wind disruption, similar ionospheric conditions could be generated across all ensemble members. Therefore, the range of AENeAS ensemble backgrounds may be mapped to a different subsection of the total sample space rather than increasing the sample space size. This may result in a loss of orthogonality across ensemble members rather than the desired increase.

The method described for generating the perturbation matrix includes scaling of the matrix values so that the peak zonal and meridional wind speeds are equal to 100 ms^{-1}. Future work may include setting the peak wind speeds equal to a value drawn from a probability distribution (e.g., an exponential probability distribution). This would avoid significant disruption to

terminator wind flow across a large number of ensemble members, while still increasing variability across AENeAS ensemble members (compared to all ensemble members having unperturbed LBCs). An alternative solution could include damping of wind perturbations within the sunrise and sunset sectors.

9. CONCLUSIONS

Within this work ionospheric models have been used to test the concept of a multistatic over-the-horizon radar (MOTHR) and to forecast low-latitude scintillation. Furthermore, lower boundary wind perturbations have been used to drive additional variability between ensemble members for an ensemble data assimilation ionospheric model, which is used to support high frequency (HF) communications for aviation and ionospheric environmental forecasts. The additional variability between ensemble members has the potential to improve ionospheric specification, which could in turn improve scintillation forecasting skill and over-the-horizon radar (OTHR) modelling accuracy.

Using 2D numerical ray tracing and an empirical ionospheric model (FIRIC; Section 3.4) with continuous electron densities and gradients, a comparison of over-the-horizon radar sensitivity has been performed for a pseudo-monostatic and a multistatic OTHR configuration. Use of a multistatic configuration permits the calculation of target velocities (rather than radial speeds) from a single radar sweep, and makes it harder for targets to be hidden in clutter when the signal from the illuminated region can be detected by multiple receivers. The multistatic configuration requires the simultaneous detection of a target by a pseudo-monostatic receiver and (at least) one of two bistatic receivers located in arbitrarily selected locations. A comparison was performed to determine the region of coverage and sensitivity possible for each configuration when multiple frequencies could be selected. The coverage area for the multistatic configuration was very similar to the monostatic coverage area. The multistatic configuration has slightly poorer sensitivity than the monostatic configuration, particularly in the regions for which the monostatic sensitivity is highest. However, this loss of sensitivity is not severe (< 10 dB m^2), and targets with radar cross sections of ~ -10 dB m^2 can still be detected at some

locations. A comparison is also considered for the sensitivity and coverage which is possible across a range of ionospheric conditions, including low and high solar activity, midnight and midday, during March, June, September, and December. The same behaviour is observed as for the previous test case; the coverage area is similar for the multistatic and monostatic configurations, and the drop in sensitivity for the multistatic configuration is not severe. Targets with a RCS of 5 dB m^2 or more can still be observed by the multistatic configuration at most locations within the coverage area across all 16 considered test cases. These results suggest that a MOTHR configuration has performance comparable to the monostatic configuration with an acceptable level of sensitivity loss. However, as the multistatic configuration includes a pseudo-monostatic receiver, a multistatic configuration could still be used in a pseudo-monostatic mode when necessary for increased sensitivity. Analysis within this work has assumed that transmitters and receivers have a homogeneous gain of 0 dB. Future work could include the incorporation of improved (and more realistic) antenna designs. This will impact results due to differences in the antenna and array gain patterns when transmitting or receiving to different directions with respect to the orientation of the array.

A novel approach to forecast low-latitude ionospheric scintillation using output from an ionospheric model (TIE-GCM; Section 3.5) has been described and implemented. A proxy for vertical plasma drift (PVPD) at the magnetic equator is used to predict whether strong scintillation will be observed in the subsequent evening at low-latitude locations with a similar longitude. This method was compared to an existing method which uses Rayleigh-Taylor growth rates (RTGRs) determined from TIE-GCM output to predict low-latitude scintillation. Test cases were reproduced from previous RTGR forecasting case studies. Additional test cases were also considered, for all periods in which the Ionospheric Scintillation Monitor in Vanimo,

Papua New Guinea was operational and scintillation was observed reasonably regularly. RTGR forecasting requires a greater number of model outputs at a far greater number of locations than PVPD forecasting. Despite this, in almost all test cases for which either PVPD or RTGR forecasting demonstrated forecasting skill (by outperforming at least 95% of forecasts which are sequences of random numbers), PVPD forecasting matched or outperformed RTGR forecasting (and outperformed persistence forecasting) when suitable PVPD and RTGR thresholds are known. PVPD performance was also considered for one test case when PVPD values were generated using a data assimilation ionospheric model (AENeAS; Section 3.6), using the mean of the ensemble of PVPD values. Forecasting skill was shown to improve significantly when using PVPD forecasting with AENeAS compared to PVPD or RTGR forecasting with TIE-GCM.

A method to use the ensemble of PVPD values from AENeAS to generate probabilistic forecasts has been described. Probabilistic PVPD forecasting work is ongoing, and will be developed further with a view to operational use within the UK Met Office Space Weather Operations Centre. Appropriate PVPD thresholds will need to be determined for longitudes which have not yet been considered, which may be dependent on factors such as season and solar activity. A possible method for developing scintillation forecasts for specified times and including the latitudinal spread of irregularities has been discussed. However, the success of this method will be dependent on whether the previously described relationships between h'F and the latitudinal extent or duration of scintillation events (Sridharan et al., 2014) are observed for locations other than Trivandrum, or whether alternative relationships can be determined.

The forecasting skill of PVPD forecasting and OTHR modelling are dependent on the accuracy of the ionospheric specification. The success of ionospheric specification with AENeAS is, in part, dependent on variability between ensemble members. Following the assimilation of observations, ionospheric conditions are propagated forward using TIE-GCM. TIE-GCM is driven by solar (F10.7 solar flux) and geomagnetic (Kp) indices. However, the lower boundary conditions specified using output from the Global Scale Wave Model (Hagan et al., 1993) are only dependent on the day of year and time of day. The effects at higher altitudes of homogeneous perturbations to TIE-GCM lower boundary horizontal wind speeds (scaling) have been discussed, and larger homogeneous wind speed changes have been shown to produce a greater proportion of significant hmF2 changes than small wind changes. These hmF2 changes demonstrate that perturbations to TIE-GCM lower boundary conditions can impact modelled conditions at higher altitudes, including in the F region. Perturbations to lower boundary temperatures were found to impact the model stability, so the remaining focus was on perturbations to lower boundary winds. A method to generate lower boundary wind perturbations which include local variations was introduced, in which global perturbations are produced using the sum of scaled randomly generated spherical harmonic functions. This method was shown to generate small-scale structures, and is also capable of generating large-scale structures which are present in some, but not all, global perturbations (thereby adding additional variability between global perturbations). The addition of a global perturbation to lower boundary winds was shown to produce electron density peak values and heights which could not be produced by unperturbed TIE-GCM simulations with a wide range of solar and geomagnetic conditions. Therefore, the addition of locally varying lower boundary wind perturbations was shown to increase the range of possible ionospheric conditions which ensemble members could take. However, care needs to be taken to ensure that this does not

result in all ensemble members being mapped to the same region of the total state space, as this may reduce the area of the state space which can be represented rather than increasing it. To avoid this, a randomly generated scaling of the global perturbation may be beneficial, so similar large-scale changes to ionospheric conditions are only seen in a small subset of ensemble members.

10. FUTURE WORK

In Section 8 it was demonstrated that the methodology described therein was able to increase the size of the sample space of ionospheric conditions. However, it has not been explicitly demonstrated that this improves the accuracy of AENeAS output. An obvious approach to demonstrate whether AENeAS ionospheric specification is improved would be to determine AENeAS output for the same environmental conditions both with and without perturbed lower boundary conditions (LBCs). Model output could then be compared directly with ionospheric observations from instrumentation, such as ionosondes.

Section 6 showed that a proxy for vertical plasma drift (PVPD) determined using output from a physics-based model could be used for scintillation forecasting. However, the forecasting skill was shown to significantly improve when using output from the Advanced Ensemble electron density (Ne) Assimilation System (AENeAS) rather than the physics-based model, due to the improvement in ionospheric specification. Therefore, if the accuracy of ionospheric specification with AENeAS is improved further by including perturbed LBCs, adding perturbed LBCs would improve the accuracy of PVPD scintillation forecasting. AENeAS output both with and without perturbed LBCs could be used to generate proxy for vertical plasma drift (PVPD) values. Comparisons with scintillation observations using the methodology of Sections 6 and 7 could then determine whether the perturbed LBCs improve scintillation forecasting skill when using the PVPD forecasting method.

Over-the-horizon radar (OTHR) simulations were used in Section 5 to demonstrate the viability of a multistatic OTHR. However, the same methodology could be used to determine the expected coverage and frequency management for an operational OTHR system. Furthermore,

ray-tracing through output from an ionospheric model can be used for coordinate registration in an operational system. In Section 5, output from a climatological ionospheric model was used for ray-tracing. A climatological ionospheric model was suitable for the analysis within Section 5; however, effective coordinate registration for an operational OTHR requires ionospheric specification with a high level of accuracy, particularly for bistatic configurations (as the transmitter-target ray path is distinct from the target-receiver ray path). Use of an ionospheric data assimilation model (such as AENeAS) would improve ionospheric specification (compared to a climatological model) and, therefore, increase the accuracy of coordinate registration. Furthermore, if the accuracy of ionospheric specification with AENeAS is improved with the addition of perturbed LBCs (using the methodology of Chapter 8), the accuracy of ray-tracing and, therefore, coordinate registration will increase further. Propagation paths produced by ray-tracing through AENeAS output, both with and without perturbed LBCs, could be compared to observations of HF skywave transmissions to determine whether ray-tracing accuracy is improved.

The forecasting skill of PVPD forecasting was demonstrated in Section 6 by comparing PVPDs with Global Positioning System scintillation observations. However, plasma irregularities within the ionosphere can impact radio propagation for a wide range of transmission frequencies, including HF. OTHR transmissions scattered by plasma irregularities can result in unwanted radar echoes, referred to as ionospheric clutter (Jangal et al., 2009; Thayaparan & MacDougall, 2004). Therefore, PVPD forecasting could be used to predict the nights on which an OTHR is more likely to be impacted by low-latitude ionospheric clutter. Furthermore, if PVPD forecasting can be developed using the approach described in Section 7.2 (predicting plasma irregularity duration and latitudinal extent to forecast the occurrence of scintillation at

a chosen time and location), PVPD forecasting could be used to provide accurate predictions of target positions or look angles for which OTHR surveillance may be impacted by low-latitude ionospheric clutter at a chosen time. Therefore, the combined topics of focus within this work could potentially contribute to accurate frequency management, coordinate registration and low-latitude ionospheric clutter mitigation for an operational monostatic, bistatic or multistatic OTHR system.

LIST OF REFERENCES

Abdu, M. A., Alam Kherani, E., Batista, I. S., De Paula, E. R., Fritts, D. C., & Sobral, J. H. A. (2009). Gravity wave initiation of equatorial spread F/plasma bubble irregularities based on observational data from the SpreadFEx campaign. *Annales Geophysicae*, *27*(7), 2607–2622. https://doi.org/10.5194/angeo-27-2607-2009

Altadill, D., Torta, J. M., & Blanch, E. (2009). Proposal of new models of the bottom-side B0 and B1 parameters for IRI. *Advances in Space Research*, *43*(11), 1825–1834. https://doi.org/10.1016/j.asr.2008.08.014

Altadill, D., Magdaleno, S., Torta, J. M., & Blanch, E. (2013). Global empirical models of the density peak height and of the equivalent scale height for quiet conditions. *Advances in Space Research*, *52*(10), 1756–1769. https://doi.org/10.1016/j.asr.2012.11.018

Anderson, D. N., Forbes, J. M., & Codrescu, M. (1989). A fully analytic, low- and middle-latitude ionospheric model. *Journal of Geophysical Research: Space Physics*, *94*(A2). https://doi.org/10.1029/ja094ia02p01520

Anderson, David N., Reinisch, B., Valladare, C., Chau, J., & Veliz, O. (2004). Forecasting the occurrence of ionospheric scintillation activity in the equatorial ionosphere on a day-to-day basis. *Journal of Atmospheric and Solar-Terrestrial Physics*, *66*(17), 1567–1572. https://doi.org/10.1016/J.JASTP.2004.07.010

Anderson, S. J. (1995). *US5440312A*. United States.

Angling, M. J., Elvidge, S., & Healy, S. B. (2018). Improved model for correcting the ionospheric impact on bending angle in radio occultation measurements. *Atmospheric Measurement Techniques*, *11*(4), 2213–2224. https://doi.org/10.5194/amt-11-2213-2018

Appleton, E. V. (1927). The existence of more than one ionised layer in the upper atmosphere [2]. *Nature*. https://doi.org/10.1038/120330a0

Appleton, E. V. (1932). Wireless studies of the ionosphere. *Institution of Electrical Engineers - Proceedings of the Wireless Section of the Institution*, *7*(21), 257–265. https://doi.org/10.1049/pws.1932.0027

Appleton, E. V. (1933). On two methods of ionospheric investigation. *Proceedings of the Physical Society*, *45*(5), 673–688. https://doi.org/10.1088/0959-5309/45/5/306

Appleton, E. V. (1946). Two anomalies in the ionosphere. *Nature*, *157*(3995), 691. https://doi.org/10.1038/157691a0

Appleton, E. V., & Beynon, W. J. G. (1940). The application of ionospheric data to radio-communication problems: Part I. *Proceedings of the Physical Society*, *52*(4), 518–533. https://doi.org/10.1088/0959-5309/52/4/311

Australian Bureau of Meteorology Space Weather Services. (2022). Ionospheric Scintillation. Retrieved June 26, 2022, from https://www.sws.bom.gov.au/World_Data_Centre/1/11

Azzarone, A., Bianchi, C., Pezzopane, M., Pietrella, M., Scotto, C., & Settimi, A. (2012). IONORT: A Windows software tool to calculate the HF ray tracing in the ionosphere. *Computers and Geosciences*, *42*, 57–63. https://doi.org/10.1016/j.cageo.2012.02.008

Bagiya, M. S., Sridharan, R., Sunda, S., Jose, L., Pant, T. K., & Choudhary, R. (2014). Critical assessment of the forecasting capability of L-band scintillation over the magnetic equatorial region – Campaign results. *Journal of Atmospheric and Solar-Terrestrial Physics*, *110–111*, 15–22. https://doi.org/10.1016/J.JASTP.2014.01.012

Bagiya, M. S., Sridharan, R., Sunda, S., Jose, L., Pant, T. K., & Choudhary, R. (2015). Impact of the perturbation zonal velocity variation on the spatio/temporal occurrence pattern of L band scintillation-A case study. *Journal of Geophysical Research: Space Physics*, *120*(7), 5882–5889. https://doi.org/10.1002/2015JA021322

Balan, N., Bailey, G. J., & Jayachandran, B. (1993). Ionospheric evidence for a nonlinear relationship between the solar e.u.v. and 10.7 cm fluxes during an intense solar cycle. *Planetary and Space Science*, *41*(2), 141–145. https://doi.org/10.1016/0032-0633(93)90043-2

Barlow, E. J. (1949). Doppler Radar. *Proceedings of the IRE*, *37*(4), 340–355. https://doi.org/10.1109/JRPROC.1949.231638

Barrick, D. E. (1971). First-Order Theory and Analysis of MF /HF / VHF Scatter from the Sea. *IEEE Transactions on Antennas and Propagation*, *20*(1). https://doi.org/10.1109/TAP.1972.1140123

Basler, R. P. (1997). OTH radar system design. In *IEEE National Radar Conference - Proceedings* (pp. 223–226).

Basu, S., Kudeki, E., Basu, Su., Valladares, C. E., Weber, E. J., Zengingonul, H. P., et al. (1996). Scintillations, plasma drifts, and neutral winds in the equatorial ionosphere after sunset. *Journal of Geophysical Research: Space Physics*, *101*(A12), 26795–26809. https://doi.org/10.1029/96JA00760@10.1002/(ISSN)2169-9402.MISETA1

Basu, Santimay, MacKenzie, E., & Basu, S. (1988). Ionospheric constraints on VHF/UHF communications links during solar maximum and minimum periods. *Radio Science*, *23*(3), 363–378. https://doi.org/10.1029/RS023i003p00363

Bates, D. R., & Massey, H. S. W. (1946). The basic reactions in the upper atmosphere. I. *Proceedings of the Royal Society of London. Series A. Mathematical and Physical Sciences*, *187*(1010). https://doi.org/10.1098/rspa.1946.0078

Bazin, V., Molinie, J. P., Munoz, J., Dorey, P., Saillant, S., Auffray, G., et al. (2006). A general presentation about the OTH-Radar NOSTRADAMUS. In *IEEE National Radar Conference - Proceedings* (pp. 634–642). https://doi.org/10.1109/RADAR.2006.1631867

Béniguel, Y., Forte, B., Radicella, S. M., Strangeways, H. J., Gherm, V. E., & Zernov, N. N. (2004). Scintillations effects on satellite to Earth links for telecommunication and navigation purposes. *Annals of Geophysics*, *47*(2-3 SUPPL.).

Bent, R. B., Llewellyn, S. K., & Walloch, M. K. (1972). *Description and Evaluation of the Bent Ionospheric Model. Volume I. Final report, 28 June--27 October 1972* (No. AD-753081; SAMSO-TR-72-239 (Vol. 1))

Bilitza, D. (2004). A correction for the IRI topside electron density model based on Alouette/ISIS topside sounder data. *Advances in Space Research*, *33*(6), 838–843. https://doi.org/10.1016/j.asr.2003.07.009

Bilitza, D. (2018). IRI the International Standard for the Ionosphere. *Advances in Radio Science*, *16*, 1–11. https://doi.org/10.5194/ars-16-1-2018

Bilitza, D., Sheikh, N. M., & Eyfrig, R. (1979). Global Model for the Height of the F2-Peak Using M3000 Values From the CCIR Numerical Map. *Telecommunication Journal*, *46*(9), 549–553.

Bilitza, D., Radicella, S. M., Reinisch, B. W., Adeniyi, J. O., Gonzalez, M. E. M., Zhang, S. R., & Obrou, O. (2000). New B0 and B1 models for IRI. *Advances in Space Research*, *25*(1), 89–95. https://doi.org/10.1016/S0273-1177(99)00902-3

Bilitza, Dieter. (2018). IRI the International Standard for the Ionosphere. *Advances in Radio Science*, *16*, 1–11. https://doi.org/10.5194/ars-16-1-2018

Brace, L. H., & Theis, R. F. (1981). Global empirical models of ionospheric electron temperature in the upper F-region and plasmasphere based on in situ measurements from the atmosphere explorer-c, isis-1 and isis-2 satellites. *Journal of Atmospheric and Terrestrial Physics*, *43*(12), 1317–1343.

Breit, G., & Tuve, M. A. (1926). A test of the existence of the conducting layer. *Physical Review*, *28*(3), 554–575. https://doi.org/10.1103/PhysRev.28.554

Brier, G. W. (1950). Verifications of forecasts expressed in terms of probability. *Monthly Weather Review*, *78*(1), 1–3. https://doi.org/10.1175/1520-0493(1950)078<0001:vofeit>2.0.co;2

Briggs, B. H., & Parkin, I. A. (1963). On the variation of radio star and satellite scintillations with zenith angle. *Journal of Atmospheric and Terrestrial Physics*, *25*(6), 339–366. https://doi.org/10.1016/0021-9169(63)90150-8

Carter, B. A., Yizengaw, E., Retterer, J. M., Francis, M., Terkildsen, M., Marshall, R., et al. (2014). An analysis of the quiet time day-to-day variability in the formation of postsunset equatorial plasma bubbles in the Southeast Asian region. *Journal of Geophysical Research: Space Physics*, *119*(4), 3206–3223. https://doi.org/10.1002/2013JA019570

Carter, B. A., Retterer, J. M., Yizengaw, E., Groves, K., Caton, R., McNamara, L., et al. (2014). Geomagnetic control of equatorial plasma bubble activity modeled by the TIEGCM with *Kp*. *Geophysical Research Letters*, *41*(15), 5331–5339. https://doi.org/10.1002/2014GL060953

Carter, B. A., Retterer, J. M., Yizengaw, E., Wiens, K., Wing, S., Groves, K., et al. (2014). Using solar wind data to predict daily GPS scintillation occurrence in the African and Asian low-latitude regions. *Geophysical Research Letters*, *41*(23), 8176–8184. https://doi.org/10.1002/2014GL062203

Cervera, M. A., & Harris, T. J. (2014). Modeling ionospheric disturbance features in quasi-vertically incident ionograms using 3-D magnetoionic ray tracing and atmospheric gravity waves. *Journal of Geophysical Research: Space Physics*, *119*(1), 431–440. https://doi.org/10.1002/2013JA019247

Chen, J., Bennett, J. A., & Dyson, P. L. (1990). Automatic fitting of quasi-parabolic segments to ionospheric profiles with application to ground range estimation for single-station location. *Journal of Atmospheric and Terrestrial Physics*, *52*(4), 277–288. https://doi.org/10.1016/0021-9169(90)90095-5

Chen, J., Bennett, J. A., & Dyson, P. L. (1992). Synthesis of oblique ionograms from vertical ionograms using quasi-parabolic segment models of the ionosphere. *Journal of Atmospheric and Terrestrial Physics*, *54*(3–4), 323–331. https://doi.org/10.1016/0021-9169(92)90011-9

Coleman, C. J. (1997). On the simulation of backscatter ionograms. *Journal of Atmospheric and Solar-Terrestrial Physics*, *59*(16). https://doi.org/10.1016/S1364-6826(97)00038-2

Coleman, C. J. (1998). A ray tracing formulation and its application to some problems in over-the-horizon radar. *Radio Science*, *33*(4), 1187–1197. https://doi.org/10.1029/98RS01523

Coleman, Christopher J. (2008). Ionospheric Ray-Tracing Equations and their Solution. *The Radio Science Bulletin*, *325*(325), 17–23.

Costa, E., De Paula, E. R., Rezende, L. F. C., Groves, K. M., Roddy, P. A., Dao, E. V., & Kelley, M. C. (2011). Equatorial scintillation calculations based on coherent scatter radar and C/NOFS data. *Radio Science*, *46*(2). https://doi.org/10.1029/2010RS004435

Courtier, P. (1998). The ECMWF implementation of three-dimensional variational assimilation (3D-Var). I: Formulation. *Quarterly Journal of the Royal Meteorological Society*, *124*(550), 1783–1807. https://doi.org/10.1256/smsqj.55001

Croft, T. A., & Hoogansian, H. (1968). Exact Ray Calculations in a Quasi-Parabolic Ionosphere With No Magnetic Field. *Radio Science*, *3*(1), 69–74. https://doi.org/10.1002/rds19683169

Crombie, D. D. (1955). Doppler spectrum of sea echo at 13.56 Mc./s. [3]. *Nature*. https://doi.org/10.1038/175681a0

Daley, R. (1991). *Atmospheric data analysis* (No. 2). Cambridge university press.

Dang, T., Zhang, B., Lei, J., Wang, W., Burns, A., Liu, H. L., et al. (2021). Azimuthal averaging-reconstruction filtering techniques for finite-difference general circulation models in spherical geometry. *Geoscientific Model Development*, *14*(2), 859–873. https://doi.org/10.5194/gmd-14-859-2021

Danilov, A. D., & Smirnova, N. V. (1995). Improving the 75 to 300 km ion composition model of the IRI. *Advances in Space Research*, *15*(2), 171–177. https://doi.org/10.1016/S0273-1177(99)80044-1

Danilov, A. D., & Yaichnikov, A. P. (1985). A new model of the ion composition at 75 to 1000 km for IRI. *Advances in Space Research*, *5*(7), 75–79. https://doi.org/10.1016/0273-1177(85)90360-6

Danilov, A. D., Rodevich, A. Y., & Smirnova, N. V. (1995). Problems with incorporating a new D-region model into the IRI. *Advances in Space Research*, *15*(2), 165–168. https://doi.org/10.1016/S0273-1177(99)80042-8

Davies, K., Watts, J. M., & Zacharisen, D. H. (1962). A study of F 2 -layer effects as observed with a Doppler technique . *Journal of Geophysical Research*, *67*(2). https://doi.org/10.1029/jz067i002p00601

Davis, C. (1996). The ionogram. Retrieved June 26, 2022, from https://www.ukssdc.ac.uk/ionosondes/ionogram_interpretation.html

Dorrian, G., & Elvidge, S. (2020). *MIE5 Final Report Part 2 – Model Testing*.

Du, Z. (2020). Forecasting the Daily 10.7 cm Solar Radio Flux Using an Autoregressive Model. *Solar Physics*, *295*(9). https://doi.org/10.1007/s11207-020-01689-x

DuCharme, E. D., Petrie, L. E., & Eyfrig, R. (1973). A method for predicting the F1 layer critical frequency based on the Zurich smoothed sunspot number. *Radio Science*, *8*(10), 837–839. https://doi.org/10.1029/RS008i010p00837

Dyson, P. L., & Bennett, J. A. (1988). A model of the vertical distribution of the electron concentration in the ionosphere and its application to oblique propagation studies. *Journal of Atmospheric and Terrestrial Physics*, *50*(3), 251–262. https://doi.org/10.1016/0021-9169(88)90074-8

Eccles, W. H. (1912). On the diurnal variations of the electric waves occurring in nature, and on the propagation of electric waves round the bend of the earth. *Proceedings of the Royal Society of London. Series A, Containing Papers of a Mathematical and Physical Character*, *87*(593). https://doi.org/10.1098/rspa.1912.0061

Elvidge, S. (2019). Ionosphere-thermosphere data assimilation models and the potential of RO. In *Radio Occultation Science Advisory Group Meeting 6*. Frankfurt.

Elvidge, S. (2022). *ROM SAF CDOP-3 Visiting Scientist Report 39: Ionospheric 1D-Var Retrieval Assessment*.

Elvidge, S., & Angling, M. J. (2019). Using the local ensemble Transform Kalman Filter for upper atmospheric modelling. *Journal of Space Weather and Space Climate*, *9*, A30. https://doi.org/10.1051/swsc/2019018

Emmert, J. (2010). Properties of Earth's Upper Atmosphere. Retrieved August 13, 2021, from https://www.nasa.gov/image-article/properties-of-earths-upper-atmosphere/

Evensen, G. (1994). Sequential data assimilation with a nonlinear quasi-geostrophic model using Monte Carlo methods to forecast error statistics. *Journal of Geophysical Research*, *99*(C5). https://doi.org/10.1029/94jc00572

Eyre, J. R. (1989). Inversion of cloudy satellite sounding radiances by nonlinear optimal estimation. I: Theory and simulation for TOVS. *Quarterly Journal of the Royal Meteorological Society*, *115*(489), 1001–1026. https://doi.org/10.1002/qj.49711548902

Fabrizio, G. A. (2013). *High frequency over-the-horizon radar: fundamental principles, signal processing, and practical applications*. McGraw-Hill Education.

Fabrizio, G. A. (2019). High frequency over-the-horizon radar. In *2019 IEEE Radar Conference, RadarConf 2019*. https://doi.org/10.1109/RADAR.2019.8835812

Farley, D. T. (1960). A theory of electrostatic fields in the ionosphere at nonpolar geomagnetic latitudes. *Journal of Geophysical Research*, *65*(3), 869–877. https://doi.org/10.1029/jz065i003p00869

Fejer, B. G., de Paula, E. R., González, S. a., & Woodman, R. F. (1991). Average vertical and zonal F region plasma drifts over Jicamarca. *Journal of Geophysical Research*, *96*(June 1988), 13901. https://doi.org/10.1029/91JA01171

Fejer, B. G., Scherliess, L., & de Paula, E. R. (1999). Effects of the vertical plasma drift velocity on the generation and evolution of equatorial spread F. *Journal of Geophysical Research: Space Physics*. https://doi.org/10.1029/1999ja900271

Folkestad, K. (1968). Exact Ray Computations in a Tilted Ionosphere With No Magnetic Field. *Radio Science*, *3*(1), 81–84. https://doi.org/10.1002/rds19683181

Forootan, E., Kosary, M., Farzaneh, S., & Schumacher, M. (2023). Empirical Data Assimilation for Merging Total Electron Content Data with Empirical and Physical Models. *Surveys in Geophysics*. https://doi.org/10.1007/s10712-023-09788-7

Forte, B., & Radicella, S. M. (2005). Comparison of ionospheric scintillation models with experimental data for satellite navigation applications. *Annals of Geophysics*, *48*(3), 505–514.

Fox, M. W., & McNamara, L. F. (1988). Improved world-wide maps of monthly median foF2. *Journal of Atmospheric and Terrestrial Physics*, *50*(12), 1077–1086. https://doi.org/10.1016/0021-9169(88)90096-7

Friedrich, M., & Torkar, K. M. (2001). FIRI: A semiempirical model of the lower ionosphere. *Journal of Geophysical Research: Space Physics*, *106*(A10), 21409–21418. https://doi.org/10.1029/2001ja900070

Friedrich, M., Pock, C., & Torkar, K. (2018). FIRI-2018, an Updated Empirical Model of the Lower Ionosphere. *Journal of Geophysical Research: Space Physics*, *123*(8), 6737–6751. https://doi.org/10.1029/2018JA025437

Galkin, I. A., Khmyrov, G. M., Kozlov, A. V., Reinisch, B. W., Huang, X., & Paznukhov, V. V. (2008). The ARTIST 5. In *AIP Conference Proceedings* (Vol. 974, pp. 150–159). AIP. https://doi.org/10.1063/1.2885024

Gordon, N. J., Salmond, D. J., & Smith, A. F. M. (1993). Novel approach to nonlinear/non-gaussian Bayesian state estimation. *IEE Proceedings, Part F: Radar and Signal Processing*, *140*(2), 107–113. https://doi.org/10.1049/ip-f-2.1993.0015

Groves, K. M., Basu, S., Weber, E. J., Smitham, M., Kuenzler, H., Valladares, C. E., et al. (1997). Equatorial scintillation and systems support. *Radio Science*, *32*(5), 2047–2064. https://doi.org/10.1029/97RS00836

Gulyaeva, T. L. (1987). Progress in ionospheric informatics based on electron-density profile analysis of ionograms. *Advances in Space Research*, *7*(6), 39–48. https://doi.org/10.1016/0273-1177(87)90269-9

Gunn, R. (1930). On the anomalous rotation of the sun. *Physical Review*, *35*(6), 635–642. https://doi.org/10.1103/PhysRev.35.635

Guo, L., Deng, W., Yao, D., Yang, Q., Ye, L., & Zhang, X. (2021). A knowledge-based auxiliary channel stap for target detection in shipborne HFSWR. *Remote Sensing*, *13*(4), 1–18. https://doi.org/10.3390/rs13040621

Hagan, M. E., & Forbes, J. M. (2003). Migrating and nonmigrating semidiurnal tides in the upper atmosphere excited by tropospheric latent heat release. *Journal of Geophysical Research: Space Physics*, *108*(A2). https://doi.org/10.1029/2002JA009466

Hagan, M. E., Forbes, J. M., & Vial, F. (1993). Numerical investigation of the propagation of the quasi-two-day wave into the lower thermosphere. *Journal of Geophysical Research*, *98*(D12), 23193. https://doi.org/10.1029/93jd02779

Hamel, P., Sambou, D. C., Darces, M., Beniguel, Y., & Hélier, M. (2014). Kriging method to perform scintillation maps based on measurement and GISM model. In *Radio Science* (Vol. 49, pp. 746–752). Wiley-Blackwell. https://doi.org/10.1002/2014RS005470

Hapgood, M. (2017). Satellite navigation—Amazing technology but insidious risk: Why everyone needs to understand space weather. *Space Weather*, *15*(4), 545–548. https://doi.org/10.1002/2017SW001638@10.1002/(ISSN)2333-5084.SCISOC1

Hapgood, M., Angling, M. J., Attrill, G., Bisi, M., Cannon, P. S., Dyer, C., et al. (2021). Development of Space Weather Reasonable Worst-Case Scenarios for the UK National Risk Assessment. *Space Weather*, *19*(4). https://doi.org/10.1029/2020SW002593

Hargreaves, J. K. (1992). *The Solar-Terrestrial Environment*. *The Solar-Terrestrial Environment*. https://doi.org/10.1017/cbo9780511628924

Hartree, D. R. (1929). The Propagation of Electromagnetic Waves in a Stratified Medium. *Mathematical Proceedings of the Cambridge Philosophical Society*, *25*(1), 97–120. https://doi.org/10.1017/S0305004100018600

Haselgrove, C. B., & Haselgrove, J. (1960). Twisted ray paths in the ionosphere. *Proceedings of the Physical Society*, *75*(3), 357–363. https://doi.org/10.1088/0370-1328/75/3/304

Haselgrove, J. (1957). Oblique ray paths in the ionosphere. *Proceedings of the Physical Society. Section B*, *70*(7), 653–662. https://doi.org/10.1088/0370-1301/70/7/302

Haselgrove, J. (1963). The Hamiltonian ray path equations. *Journal of Atmospheric and Terrestrial Physics*, *25*(7), 397–399. https://doi.org/10.1016/0021-9169(63)90173-9

Hays, P. B., Abreu, V. J., Dobbs, M. E., Gell, D. A., Grassl, H. J., & Skinner, W. R. (1993). The high-resolution Doppler imager on the upper atmosphere research satellite. *Journal of Geophysical Research*, *98*(D6). https://doi.org/10.1029/93jd00409

Headrick, J. M., & Skolnik, M. I. (1974). Over-the-Horizon Radar in the HF Band. *Proceedings of the IEEE*, *62*(6). https://doi.org/10.1109/PROC.1974.9506

Hedin, A. E., Spencer, N. W., & Killeen, T. L. (1988). Empirical global model of upper thermosphere winds based on Atmosphere and Dynamics Explorer satellite data. *Journal of Geophysical Research*, *93*(A9), 9959. https://doi.org/10.1029/ja093ia09p09959

Hedin, Alan E. (1987). MSIS-86 Thermospheric Model. *Journal of Geophysical Research*, *92*(A5), 4649. https://doi.org/10.1029/ja092ia05p04649

Holdsworth, D. A., Mulder, K., & Turley, M. D. E. (2022). Jindalee Operational Radar Network: New Growth from Old Roots. In *Proceedings of the IEEE Radar Conference*. https://doi.org/10.1109/RadarConf2248738.2022.9764214

Hough, S. S. (1897). On the application of harmonic analysis to the dynamical theory of the tides. — Part I. On laplace's "oscillations of the first species" and the dynamics of ocean currents. *Philosophical Transactions of the Royal Society of London. Series A, Containing Papers of a Mathematical or Physical Character*, *189*, 201–257. https://doi.org/10.1098/rsta.1897.0009

Hough, S. S. (1898). On the application of harmonic analysis to the dynamical theory of the tides.—Part II. On the general integration of Laplace's dynamical equations. *Philosophical Transactions of the Royal Society of London. Series A, Containing Papers of a Mathematical or Physical Character*, *191*, 139–185. https://doi.org/10.1098/rsta.1898.0005

Huang, C. S., & Hairston, M. R. (2015). The postsunset vertical plasma drift and its effects on the generation of equatorial plasma bubbles observed by the C/NOFS satellite. *Journal of Geophysical Research: Space Physics*. https://doi.org/10.1002/2014JA020735

Hunt, B. R., Kostelich, E. J., & Szunyogh, I. (2007). Efficient data assimilation for spatiotemporal chaos: A local ensemble transform Kalman filter. *Physica D: Nonlinear Phenomena*, *230*(1–2), 112–126. https://doi.org/10.1016/j.physd.2006.11.008

ISO. (2009). Space systems - Space environment (natural and artificial) - The Earth's ionosphere model: international reference ionosphere (IRI) model and extensions to the plasmasphere.

ITU. (2019). *Radio Noise, Recommendation ITU-R P372-14, International Telecommunications Union, Geneva.*

Jangal, F., Saillant, S., & Hélier, M. (2009). Ionospheric clutter mitigation using one-dimensional or two-dimensional wavelet processing. *IET Radar, Sonar and Navigation*, *3*(2). https://doi.org/10.1049/iet-rsn:20070095

Joliffe, I., & Stephenson, D. (eds.). (2012). Forecast Verification: A Practitioner's Guide in Atmospheric Science. *Second Edition*. John Wiley & Sons.

Jones, R. M., & Stephenson, J. J. (1975). A versatile three-dimensional ray tracing computer program for radio waves in the ionosphere. *OT Report 75-76*, (October), 185.

Jones, W. B., & Gallet, R. M. (1962). Representation of diurnal and geographic variations of ionospheric data by numerical methods. *Journal of Research of the National Bureau of Standards, Section D: Radio Propagation*, *66D*(4), 419. https://doi.org/10.6028/jres.066d.043

Kalman, R. E. (1960). A new approach to linear filtering and prediction problems. *Journal of Fluids Engineering, Transactions of the ASME*, *82*(1), 35–45. https://doi.org/10.1115/1.3662552

Kelly, M. A., Comberiate, J. M., Miller, E. S., & Paxton, L. J. (2014). Progress toward forecasting of space weather effects on UHF SATCOM after Operation Anaconda. *Space Weather*, *12*(10), 601–611. https://doi.org/10.1002/2014SW001081

Kil, H., Paxton, L. J., & Oh, S. J. (2009). Global bubble distribution seen from ROCSAT-1 and its association with the evening prereversal enhancement. *Journal of Geophysical Research: Space Physics*. https://doi.org/10.1029/2008JA013672

King-Hele, D. G., & Walker, D. M. C. (1977). Upper-atmosphere zonal winds: Variation with height and local time. *Planetary and Space Science*, *25*(4), 313–336. https://doi.org/10.1016/0032-0633(77)90048-4

Kintner, P. M., Ledvina, B. M., & De Paula, E. R. (2007). GPS and ionospheric scintillations. *Space Weather*, *5*, 9003. https://doi.org/10.1029/2006SW000260

Kolmogorov, A. N. (1950). *Foundations of the theory of probability*. (N. Morrison, Ed.). Chelsea Publishing Company.

de La Beaujardière, O. (2004). C/NOFS: a mission to forecast scintillations. *Journal of Atmospheric and Solar-Terrestrial Physics*, *66*(17), 1573–1591. https://doi.org/10.1016/J.JASTP.2004.07.030

Landeau, T., Gauthier, F., & Ruelle, N. (1997). Further improvements to the inversion of elevation-scan backscatter sounding data. *Journal of Atmospheric and Solar-Terrestrial Physics*, *59*(1). https://doi.org/10.1016/1364-6826(95)00167-0

Lassen, H. (1926). Über die Ionisation der Atmosphäre und ihren Einflußauf die Ausbreitung der kurzen elektrischen Wellen der drahtlosen Telegraphie. *Zeitschrift Für Hochfrequenztechnik*, *28*, 109.

Lee, H. G., Kim, K., & Kim, J. (2011). On the long time simulation of the Rayleigh-Taylor instability. *International Journal for Numerical Methods in Engineering*, *85*(13), 1633–1647. https://doi.org/10.1002/nme.3034

Lee, I. T. (2013). *Assimilation of radio occultation data observed by FORMOSAT-3/COSMIC into a coupled Thermosphere/Ionosphere model*. National Central Univ., Zhongli, Taoyuan, Taiwan.

de Lima, G. R. T., Stephany, S., de Paula, E. R., Batista, I. S., Abdu, M. A., Rezende, L. F. C., et al. (2014). Correlation analysis between the occurrence of ionospheric scintillation at the magnetic equator and at the southern peak of the Equatorial Ionization Anomaly. *Space Weather*, *12*(6), 406–416. https://doi.org/10.1002/2014SW001041

Lin, C. Y., Matsuo, T., Liu, J. Y., Lin, C. H., Huba, J. D., Tsai, H. F., & Chen, C. Y. (2017). Data Assimilation of Ground-Based GPS and Radio Occultation Total Electron Content for Global Ionospheric Specification. *Journal of Geophysical Research: Space Physics*, *122*(10). https://doi.org/10.1002/2017JA024185

Lindzen, R. S., & Chapman, S. (1969). *Atmospheric tides. Thermal and gravitational* (Vol. 15). Springer Science & Business Media.

Liu, L. B., Wan, W. X., Chen, Y. D., & Le, H. J. (2011). Solar activity effects of the ionosphere: A brief review. *Chinese Science Bulletin*. https://doi.org/10.1007/s11434-010-4226-9

Liu, Z., Gao, Y., & Skone, S. (2005). A study of smoothed TEC precision inferred from GPS measurements. *Earth, Planets and Space*, *57*(11), 999–1007. https://doi.org/10.1186/BF03351880

Makarevich, R. A., Crowley, G., Azeem, I., Ngwira, C., & Forsythe, V. V. (2021). Auroral E-Region as a Source Region for Ionospheric Scintillation. *Journal of Geophysical Research: Space Physics*, *126*(5). https://doi.org/10.1029/2021JA029212

Martyn, D. (1956). Processes Controlling Ionization Distribution in the F2 Region of the Ionosphere. *Australian Journal of Physics*, *9*(1), 161. https://doi.org/10.1071/ph560161

Martyn, D. F. (1935). The propagation of medium radio waves in the ionosphere. *Proceedings of the Physical Society*, *47*(2), 323–339. https://doi.org/10.1088/0959-5309/47/2/311

Martyn, D. F. (1953). Electric currents in the ionosphere - Ionization drift due to winds and electric fields. *Philosophical Transactions of the Royal Society of London. Series A, Mathematical and Physical Sciences*, *246*(913), 306–320. https://doi.org/10.1098/rsta.1953.0018

Materassi, M., Coster, A. J., Forte, B., & Skone, S. (Eds.). (2019). *The Dynamical Ionosphere: A Systems Approach to Ionospheric Irregularity*. Elsevier.

Mayr, H. G., Mengel, J. G., Talaat, E. R., Porter, H. S., & Chan, K. L. (2005). Mesospheric non-migrating tides generated with planetary waves: I. Characteristics. *Journal of Atmospheric and Solar-Terrestrial Physics*, *67*(11), 959–980. https://doi.org/10.1016/j.jastp.2005.03.002

Mitra, S. K., & Syam, P. (1935). Absorbing layer of the ionosphere at low height [2]. *Nature*. https://doi.org/10.1038/135953b0

Mošna, Z., Edemskiy, I., Laštovička, J., Kozubek, M., Koucká Knížová, P., Kouba, D., & Siddiqui, T. A. (2021). Observation of the ionosphere in middle latitudes during 2009,

2018 and 2018/2019 sudden stratospheric warming events. *Atmosphere*, *12*(5). https://doi.org/10.3390/atmos12050602

Nava, B., Coïsson, P., & Radicella, S. M. (2008). A new version of the NeQuick ionosphere electron density model. *Journal of Atmospheric and Solar-Terrestrial Physics*, *70*(15), 1856–1862. https://doi.org/10.1016/j.jastp.2008.01.015

NCAR High Altitude Observatory. (2016). *TIEGCM Documentation Release 2.0*. Retrieved August 20, 2022, from https://www.hao.ucar.edu/modeling/tgcm/tiegcm2.0/userguide/html/index.html

NERC Grants on the Web. (2020). *Space Weather Instrumentation, Measurement, Modelling and Risk: Ionosphere (SWIMMR-I)*. Retrieved April 16, 2022, from https://gotw.nerc.ac.uk/list_full.asp?pcode=NE%2FV002643%2F1

Norman, R. J., & Cannon, P. S. (1997). A two-dimensional analytic ray tracing technique accommodating horizontal gradients. *Radio Science*, *32*(2), 387–396. https://doi.org/10.1029/96RS03200

Norman, Robert J., Le Marshall, J., Carter, B. A., Wang, C. S., Gordon, S., & Zhang, K. (2012). A new pseudo three-dimensional segment method analytical ray tracing (3-D SMART) technique. *IEEE Transactions on Antennas and Propagation*, *60*(12), 5818–5824. https://doi.org/10.1109/TAP.2012.2214194

Nugent, L. D., Elvidge, S., & Angling, M. J. (2021). Comparison of Low-Latitude Ionospheric Scintillation Forecasting Techniques Using a Physics-Based Model. *Space Weather*, *19*(7). https://doi.org/10.1029/2020SW002462

Oberheide, J., Forbes, J. M., Zhang, X., & Bruinsma, S. L. (2011). Climatology of upward propagating diurnal and semidiurnal tides in the thermosphere. *Journal of Geophysical Research: Space Physics*, *116*(11). https://doi.org/10.1029/2011JA016784

Ott, E. (1978). Theory of Rayleigh-Taylor bubbles in the equatorial ionosphere. *Journal of Geophysical Research*. https://doi.org/10.1029/ja083ia05p02066

Parrish, D. F., & Derber, J. C. (1992). The National Meteorological Center's spectral statistical-interpolation analysis system. *Monthly Weather Review*, *120*(8), 1747–1763. https://doi.org/10.1175/1520-0493(1992)120<1747:TNMCSS>2.0.CO;2

Pedatella, N. M. (2016). Impact of the lower atmosphere on the ionosphere response to a geomagnetic superstorm. *Geophysical Research Letters*, *43*(18), 9383–9389. https://doi.org/10.1002/2016GL070592

Peirce, C. S. (1884). The numerical measure of the success of predictions. *Science*, *ns-4*(93), 453–454. https://doi.org/10.1126/science.ns-4.93.453-a

Pfaff, F., Kurz, G., & Hanebeck, U. D. (2017). Filtering on the unit sphere using spherical harmonics. In *IEEE International Conference on Multisensor Fusion and Integration for Intelligent Systems* (Vol. 2017-November). https://doi.org/10.1109/MFI.2017.8170417

Pignalberi, A., Pezzopane, M., & Rizzi, R. (2018). Modeling the Lower Part of the Topside Ionospheric Vertical Electron Density Profile Over the European Region by Means of Swarm Satellites Data and IRI UP Method. *Space Weather*, *16*(3), 304–320. https://doi.org/10.1002/2017SW001790

Plendl, H. (1932). Concerning the influence of the eleven-year solar activity period upon the propagation of waves in wireless telegraphy. *Proceedings of the Institute of Radio Engineers*, *20*(3), 520–539. https://doi.org/10.1109/JRPROC.1932.227588

Priyadarshi, S. (2015). A Review of Ionospheric Scintillation Models. *Surveys in Geophysics*, *36*(2), 295–324. https://doi.org/10.1007/s10712-015-9319-1

Qian, L., Burns, A. G., Emery, B. A., Foster, B., Lu, G., Maute, A., et al. (2014). The NCAR TIE-GCM: A Community Model of the Coupled Thermosphere/Ionosphere System. In

Modeling the Ionosphere-Thermosphere System (Vol. 9780875904, pp. 73–83). https://doi.org/10.1002/9781118704417.ch7

Quenouille, M. H. (1949). Problems in Plane Sampling. *The Annals of Mathematical Statistics*, *20*(3), 355–375.

Rajesh, P. K., Lin, C. C. H., Chen, C. H., Chen, W. H., Lin, J. T., Chou, M. Y., et al. (2017). Global equatorial plasma bubble growth rates using ionosphere data assimilation. *Journal of Geophysical Research: Space Physics*, *122*(3), 3777–3787. https://doi.org/10.1002/2017JA023968

Rawer, K. (1982). Replacement of the present sub-peak plasma density profile by a unique expression. *Advances in Space Research*, *2*(10), 183–190. https://doi.org/10.1016/0273-1177(82)90387-8

Rayleigh. (1882). Investigation of the Character of the Equilibrium of an Incompressible Heavy Fluid of Variable Density. *Proceedings of the London Mathematical Society*, *s1-14*(1), 170–177. https://doi.org/10.1112/plms/s1-14.1.170

Redmon, R. J., Anderson, D., Caton, R., & Bullett, T. (2010). A Forecasting Ionospheric Real-time Scintillation Tool (FIRST). *Space Weather*, *8*(12). https://doi.org/10.1029/2010SW000582

Retterer, J. M. (2010). Forecasting low-latitude radio scintillation with 3-D ionospheric plume models: 1. Plume model. *Journal of Geophysical Research: Space Physics*, *115*(A3). https://doi.org/10.1029/2008JA013839

Rezende, L. F. C., de Paula, E. R., Stephany, S., Kantor, I. J., Muella, M. T. A. H., de Siqueira, P. M., & Correa, K. S. (2010). Survey and prediction of the ionospheric scintillation using data mining techniques. *Space Weather*, *8*(6). https://doi.org/10.1029/2009SW000532

Richmond, A. D., Matsushita, S., & Tarpley, J. D. (1976). On the production mechanism of electric currents and fields in the ionosphere. *Journal of Geophysical Research*, *81*(4), 547–555. https://doi.org/10.1029/ja081i004p00547

Richmond, A. D., Ridley, E. C., & Roble, R. G. (1992). A thermosphere/ionosphere general circulation model with coupled electrodynamics. *Geophysical Research Letters*, *19*(6), 601–604. https://doi.org/10.1029/92GL00401

Rishbeth, H. (1971). Polarization fields produced by winds in the equatorial F-region. *Planetary and Space Science*, *19*(3), 357–369. https://doi.org/10.1016/0032-0633(71)90098-5

Rossby, C. (1939). Relation between variations in the intensity of the zonal circulation of the atmosphere and the displacements of the semi-permanent centers of action. *Journal of Marine Research*, *2*, 38–55.

Sartori, J. T. D. (2021). Oblique Incidence Ionospheric Sounding: A Bibliometric Research. *URSI Radio Science Letters*, *3*. https://doi.org/10.46620/21-0010

Schunk, R., & Nagy, A. (2009). *Ionospheres: physics, plasma physics, and chemistry*. Cambridge university press.

Schunk, R. W., Gardner, L., Scherliess, L., & Zhu, L. (2012). Problems associated with uncertain parameters and missing physics for long-term ionosphere-thermosphere forecasting. *Radio Science*, *47*(3). https://doi.org/10.1029/2011RS004911

Schwabe, H. (1844). Sonnen — Beobachtungen im Jahre 1843. *Astronomische Nachrichten*, *21*(15), 234–235. https://doi.org/10.1002/asna.18440211505

Scotto, C., Radicella, S. M., & Zolesi, B. (1998). An improved probability function to predict the F1 layer occurrence and L condition. *Radio Science*, *33*(6), 1763–1765. https://doi.org/10.1029/98RS02637

Shubin, V. N. (2015). Global median model of the F2-layer peak height based on ionospheric radio-occultation and ground-based Digisonde observations. *Advances in Space Research*, *56*(5), 916–928. https://doi.org/10.1016/j.asr.2015.05.029

Skolnik, M. (1990). *Radar Handbook. Second Edition*. *McGraw-Hill* (Vol. 53).

Smith, J. M., Rodrigues, F. S., Fejer, B. G., & Milla, M. A. (2016). Coherent and incoherent scatter radar study of the climatology and day-to-day variability of mean F region vertical drifts and equatorial spread F. *Journal of Geophysical Research A: Space Physics*. https://doi.org/10.1002/2015JA021934

Smith, N. (1937). Extension of normal-incidence ionosphere measurements to oblique-incidence radio transmission. *Journal of Research of the National Bureau of Standards*, *19*(1), 89. https://doi.org/10.6028/jres.019.052

Smith, N. (1939). The Relation of Radio Sky-Wave Transmission to Ionosphere Measurements. *Proceedings of the IRE*, *27*(5), 332–347. https://doi.org/10.1109/JRPROC.1939.228397

Sousasantos, J., Kherani, E. A., & Sobral, J. H. A. (2017). An alternative possibility to equatorial plasma bubble forecasting through mathematical modeling and Digisonde data. *Journal of Geophysical Research: Space Physics*, *122*(2), 2079–2088. https://doi.org/10.1002/2016JA023241

Sridhar, M., Venkata Ratnam, D., Padma Raju, K., Sai Praharsha, D., & Saathvika, K. (2017). Ionospheric scintillation forecasting model based on NN-PSO technique. *Astrophysics and Space Science*, *362*(9), 166. https://doi.org/10.1007/s10509-017-3144-6

Sridharan, R., Bagiya, M. S., & Sunda, S. (2012). A novel method based on GPS TEC to forecast L band scintillations over the equatorial region through a case study. *Journal of Atmospheric and Solar-Terrestrial Physics*, *80*, 230–238. https://doi.org/10.1016/J.JASTP.2012.02.007

Sridharan, R., Bagiya, M. S., Sunda, S., Choudhary, R., Pant, T. K., & Jose, L. (2014). First results on forecasting the spatial occurrence pattern of L-band scintillation and its temporal evolution. *Journal of Atmospheric and Solar-Terrestrial Physics*, *119*, 53–62. https://doi.org/10.1016/J.JASTP.2014.06.015

Sultan, P. J. (1996). Linear theory and modeling of the Rayleigh-Taylor instability leading to the occurrence of equatorial spread F. *Journal of Geophysical Research: Space Physics*, *101*(A12), 26875–26891. https://doi.org/10.1029/96ja00682

Sunda, S., Yadav, S., Sridharan, R., Bagiya, M. S., Khekale, P. V., Singh, P., & Satish, S. V. (2017). SBAS-derived TEC maps: a new tool to forecast the spatial maps of maximum probable scintillation index over India. *GPS Solutions*, *21*(4), 1469–1478. https://doi.org/10.1007/s10291-017-0625-6

Tanna, H. J., Karia, S. P., & Pathak, K. N. (2013). A study of L band scintillations during the initial phase of rising solar activity at an Indian low latitude station. *Advances in Space Research*, *52*(3), 412–421. https://doi.org/10.1016/J.ASR.2013.03.022

Thayaparan, T., & MacDougall, J. (2004). *The role of ionospheric clutter in mid-latitude and arctic regions for the assessment of HFSWR surveillance*. Defence Research Establishment Ottawa.

Themens, D. R., Reid, B., & Elvidge, S. (2022). ARTIST Ionogram Autoscaling Confidence Scores: Best Practices. *URSI Radio Science Letters*, *4*. https://doi.org/10.46620/22-0001

Thomason, J., Skaggs, G., & Lloyd, J. (1979). *A global ionospheric model*. Naval Research Laboratory.

Thomason, J. F. (2003). Development of over-the-horizon Radar in the United States. In *2003 Proceedings of the International Conference on Radar, RADAR 2003* (pp. 599–601). https://doi.org/10.1109/RADAR.2003.1278809

Tonks, L., & Langmuir, I. (1929). Oscillations in ionized gases. *Physical Review*, *33*(2), 195–210. https://doi.org/10.1103/PhysRev.33.195

Třísková, L., Truhlík, V., & Šmilauer, J. (2003). An empirical model of ion composition in the outer ionosphere. *Advances in Space Research*, *31*(3), 653–663. https://doi.org/10.1016/S0273-1177(03)00040-1

Truhlik, V., Bilitza, D., & Triskova, L. (2012). A new global empirical model of the electron temperature with the inclusion of the solar activity variations for IRI. *Earth, Planets and Space*, *64*(6), 531–543. https://doi.org/10.5047/eps.2011.10.016

Truhlik, V., Bilitza, D., & Triskova, L. (2015). Towards better description of solar activity variation in the International Reference Ionosphere topside ion composition model. *Advances in Space Research*, *55*(8), 2099–2105. https://doi.org/10.1016/j.asr.2014.07.033

Tsunoda, R. T. (2010). On seeding equatorial spread F during solstices. *Geophysical Research Letters*. https://doi.org/10.1029/2010GL042576

De Voogt, A. H. (1953). The Calculation of the Path of a Radio-Ray in a Given Ionosphere". *Proceedings of the IRE*, *41*(9), 1183–1186. https://doi.org/10.1109/JRPROC.1953.274455

Wang, X., & Bishop, C. H. (2005). Improvement of ensemble reliability with a new dressing kernel. *Quarterly Journal of the Royal Meteorological Society*, *131*(607), 965–986. https://doi.org/10.1256/qj.04.120

Washburn, T. W. (1971). *Discrete echoes in ionospherically propagated ground backscatter*. Stanford Research Institute.

Wise, J. C. (2004). Summary of recent australian radar developments. *IEEE Aerospace and Electronic Systems Magazine*, *19*(12), 8–10. https://doi.org/10.1109/MAES.2004.1374061

Woodman, R. F. (1970). Vertical drift velocities and east- west electric fields at the magnetic equator. *J Geophys Res*, *75*(31), 6249–6259. https://doi.org/10.1029/ja075i031p06249

Woodman, R. F., & La Hoz, C. (1976). Radar observations of F region equatorial irregularities. *Journal of Geophysical Research*, *81*(31), 5447–5466. https://doi.org/10.1029/JA081i031p05447

Yee, J. H., Talaat, E. R., Christensen, A. B., Killeen, T. L., Russell, J. M., & Woods, T. N. (2003). TIMED Instruments. *Johns Hopkins APL Technical Digest (Applied Physics Laboratory)*.

Yeh, K. C., & Liu, C. H. (1982). Radio Wave Scintillations in the Ionosphere. *Proceedings of the IEEE*, *70*(4), 324–360. https://doi.org/10.1109/PROC.1982.12313

Yokoyama, T. (2017). A review on the numerical simulation of equatorial plasma bubbles toward scintillation evaluation and forecasting. *Progress in Earth and Planetary Science*, *4*(1). https://doi.org/10.1186/s40645-017-0153-6

Youden, W. J. (1950). Index for rating diagnostic tests. *Cancer*, *3*(1), 32–35. https://doi.org/10.1002/1097-0142(1950)3:1<32::AID-CNCR2820030106>3.0.CO;2-3

Zawdie, K. A., Drob, D. P., Siskind, D. E., & Coker, C. (2017). Calculating the absorption of HF radio waves in the ionosphere. *Radio Science*, *52*(6), 767–783. https://doi.org/10.1002/2017RS006256